

Surface analysis of thermionic dispenser cathodes

Citation for published version (APA):

Cortenraad, H. M. R. (2000). *Surface analysis of thermionic dispenser cathodes*. [Phd Thesis 1 (Research TU/e / Graduation TU/e), Applied Physics]. Technische Universiteit Eindhoven. <https://doi.org/10.6100/IR539337>

DOI:

[10.6100/IR539337](https://doi.org/10.6100/IR539337)

Document status and date:

Published: 01/01/2000

Document Version:

Publisher's PDF, also known as Version of Record (includes final page, issue and volume numbers)

Please check the document version of this publication:

- A submitted manuscript is the version of the article upon submission and before peer-review. There can be important differences between the submitted version and the official published version of record. People interested in the research are advised to contact the author for the final version of the publication, or visit the DOI to the publisher's website.
- The final author version and the galley proof are versions of the publication after peer review.
- The final published version features the final layout of the paper including the volume, issue and page numbers.

[Link to publication](#)

General rights

Copyright and moral rights for the publications made accessible in the public portal are retained by the authors and/or other copyright owners and it is a condition of accessing publications that users recognise and abide by the legal requirements associated with these rights.

- Users may download and print one copy of any publication from the public portal for the purpose of private study or research.
- You may not further distribute the material or use it for any profit-making activity or commercial gain
- You may freely distribute the URL identifying the publication in the public portal.

If the publication is distributed under the terms of Article 25fa of the Dutch Copyright Act, indicated by the "Taverne" license above, please follow below link for the End User Agreement:

www.tue.nl/taverne

Take down policy

If you believe that this document breaches copyright please contact us at:

openaccess@tue.nl

providing details and we will investigate your claim.

Surface Analysis of Thermionic Dispenser Cathodes

PROEFSCHRIFT

ter verkrijging van de graad van doctor aan de Technische Universiteit Eindhoven, op gezag van de Rector Magnificus, prof.dr. M. Rem, voor een commissie aangewezen door het College voor Promoties in het openbaar te verdedigen op vrijdag 8 december 2000 om 16.00 uur

door

René Cortenraad

geboren te Maastricht

Dit proefschrift is goedgekeurd door de promotoren:

prof.dr. H.H. Brongersma

en

prof.dr. V.G. Glebovsky

Copromotor:

dr. A.W. Denier van der Gon

Printed at the Universiteitsdrukkerij, Eindhoven University of Technology

CIP-DATA LIBRARY TECHNISCHE UNIVERSITEIT EINDHOVEN

Cortenraad, René

Surface analysis of thermionic dispenser cathodes / René Cortenraad. – Eindhoven:
Technische Universiteit Eindhoven, 2000. – Proefschrift.

ISBN 90-386-1689-9

NUGI 812

Trefw.: oppervlaktefysica / lage-energy ionen verstrooiing / neutralisatie / kathode

Subject headings: surface physics / low-energy ion scattering / charge exchange / cathodes

“Whether the general public will be enough interested in television to make it possible to commercialise home sets for television is still to be seen.”

Ernst Alexanderson, 1935
(television pioneer)

aan mijn ouders

The work described in this thesis has been performed at the Department of Physics of the Eindhoven University of Technology, the Netherlands, and was supported by Philips Research (Aachen, Germany and Blackburn, United Kingdom) and Philips Display Components (Eindhoven, the Netherlands).

Contents

1. General Introduction	1
1.1 Does vacuum conduct electricity?	1
1.2 Thermionic dispenser cathodes	2
1.3 Scope of the thesis	3
1.4 Surface analysis using ion scattering	4
1.5 Outline of the thesis	6
2. Influence of Analyser Transmission and Detection Efficiency on the Energy Dependence of Low-Energy Ion Scattering Signals	9
2.1 Introduction	10
2.2 Experimental	10
2.3 LEIS signal intensity	11
2.4 Analyser transmission	13
2.5 Channelplate efficiency	16
2.6 Other types of analysers	20
2.6.1 Standard CMA	20
2.6.2 Hemispherical analyser	20
2.7 Discussion	21
2.7.1 Charge exchange studies	21
2.7.2 Quantitative surface analysis	25
2.8 Conclusions	27
3. Growth, Characterisation and Surface Cleaning Procedures of High-Purity W Single Crystals	31
3.1 Introduction	32
3.2 Growth of W single crystals	32
3.3 Crystal characterisation	34
3.4 Cleaning and characterisation of the crystal surface	37
3.5 Conclusions	40
4. Crystal-Face Dependence of Low-Energy Ion Scattering Signals	43
4.1 Introduction	44
4.2 Experimental	44
4.3 Results	45
4.3.1 Ion scattering experiments	45
4.3.2 Ion scattering simulations	47
4.3.3 Influence of surface roughness and disorder	49
4.4 Discussion and conclusions	50

5. Work Function Dependent Neutralisation of Low-Energy Noble Gas Ions	53
5.1 Introduction	54
5.2 Neutralisation mechanisms	54
5.2.1 Auger neutralisation	55
5.2.2 Collision-induced neutralisation	56
5.2.3 Resonant neutralisation	56
5.2.4 Neutralisation probability	57
5.3 Experimental	57
5.3.1 Set-up	57
5.3.2 Methods of inducing the work function change	58
5.3.3 Characteristic velocity method	59
5.4 Results and discussion	60
5.4.1 Evidence for work function dependent neutralisation	60
5.4.2 Characteristic velocity versus work function	61
5.4.3 Auger versus collision-induced neutralisation	63
5.4.4 Resonant neutralisation at low work functions	65
5.4.5 Macroscopic work function versus local potential	67
5.4.6 Scattering from adatoms and substrate atoms	69
5.5 Conclusions	70
6. On the Quantification of the Surface Composition of Low-Work Function Surfaces using Low-Energy Ion Scattering	75
6.1 Introduction	76
6.2 Experimental	76
6.3 Results and discussion	77
6.4 Guidelines for quantification	82
6.5 Conclusions	83
7. Surface Analysis of Thermionic Dispenser Cathodes	87
7.1 Introduction	88
7.2 Experimental	88
7.3 Results and discussion	91
7.3.1 The outermost atomic layer	91
7.3.2 Ion scattering at low work functions	93
7.3.3 Coverage versus work function	95
7.3.4 The role of the surface oxygen	99
7.3.5 The role of the cathode substrate	100
7.4 Conclusions	102

8. Dynamic Behaviour of Thermionic Dispenser Cathodes under Ion Bombardment	105
8.1 Introduction	106
8.2 Experimental	108
8.3 Results and discussion	108
8.3.1 The dynamic equilibrium	108
8.3.2 The sputtering process	110
8.3.3 The resupply process	113
8.3.4 Coverage and emission at dynamic equilibrium	117
8.3.5 Ion bombardment induced substrate damage	120
8.3.6 Ion bombardment in oxygen background	123
8.4 Conclusions	124
Summary	129
Samenvatting	131
Publications	133
Dankwoord	135
Curriculum Vitae	137

1

General Introduction

1.1 Does vacuum conduct electricity?

Up to the beginning of the twentieth century the main objective of science was to discover natural laws. Science in those days was mainly curiosity-driven. The work of the scientists started by making a hypothesis based on existing laws established by previous experiments or by the work of others, and through making carefully controlled experiments a new theory was derived. The usefulness of the thus derived theory was weighed by its ability to predict the results of further experiments or theories. The gradual shift of the emphasise from the curiosity-driven science to the application-driven science started in the beginning of the twentieth century. However, turning a fundamental discovery into an application for the benefit of mankind takes time, and most applications in use today find their roots in a fundamental question posted by a scientist years, decades, or even centuries, ago.

The fundamental question whether vacuum conducts electricity was posted in 1854, and formed the cradle for an electronic device that every human in the developed world comes into contact with almost every day: the cathode-ray tube as used in television-sets. In that year Heinrich Geissler created the first man-made vacuum by blowing a glass tube and pumping it out with his newly constructed vacuum pump [1]. In an era where electricity was the main topic of science, it was only natural to see whether the vacuum could conduct electricity. Using the “Geissler tube”, shown in figure 1.1a, it was concluded that current could flow between the cathode and the anode, and that this current was carried by mysterious “cathode rays”. Over the next decades the Geissler tube as developed into the cathode-ray tube. Figure 1.1b shows a cathode-ray tube as created by Max Dieckmann in 1906. This design is very similar to the cathode-ray tubes used in television-sets of the present time, only the deflection plates have been replaced by deflection coils. Over the next few decades the basic cathode-ray tube was developed into a working television-set, mainly due to the efforts of Vladimir Zworykin and David Sarnoff [1].

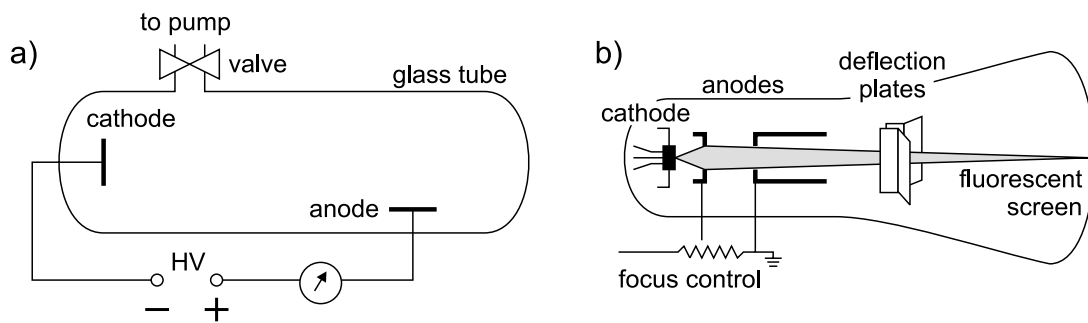


Figure 1.1. Schematic representation of the Geissler tube constructed in 1854 (a), and the cathode-ray tube constructed in 1906 (b).

1.2 Thermionic dispenser cathodes

Since the pioneering days of the cathode-ray tube, oxide cathodes have been employed as electron sources [2,3]. The cathode consists of a thick layer of the oxides of the earth alkali elements (Ba, Sr, Ca), and has a low work function of approximately 1.2 eV. Due to its low work function the oxide cathode can deliver a continuous electron emission density of the order of $1 \text{ A}\cdot\text{cm}^{-2}$ at an operating temperature of 700-800°C. However, the oxide cathode is unsuited for applications requiring higher emission densities due to its semiconductor nature. With the introduction of large high-quality tubes and high-definition television, the demand arose for higher emission densities, exceeding the capabilities of the oxide cathodes. Emission densities above the limit of oxide cathodes can be obtained from thermionic dispenser cathodes, which were developed by Levi in the 1950s [4]. Figure 1.2a shows a dispenser cathode unit as used in cathode-ray tubes. The electron emission originates from a porous W matrix with a diameter of 1 mm, which is indicated in the figure by the arrow. This porous matrix consists of pressed and sintered W granulates with dimensions of the order of $10 \mu\text{m}$, and is impregnated with a BaO-containing compound [5]. Figure 1.2b presents a secondary electron microscope image of the matrix, revealing the individual W granulates and the impregnated pores. During cathode operation the impregnate reacts with the W matrix, and Ba

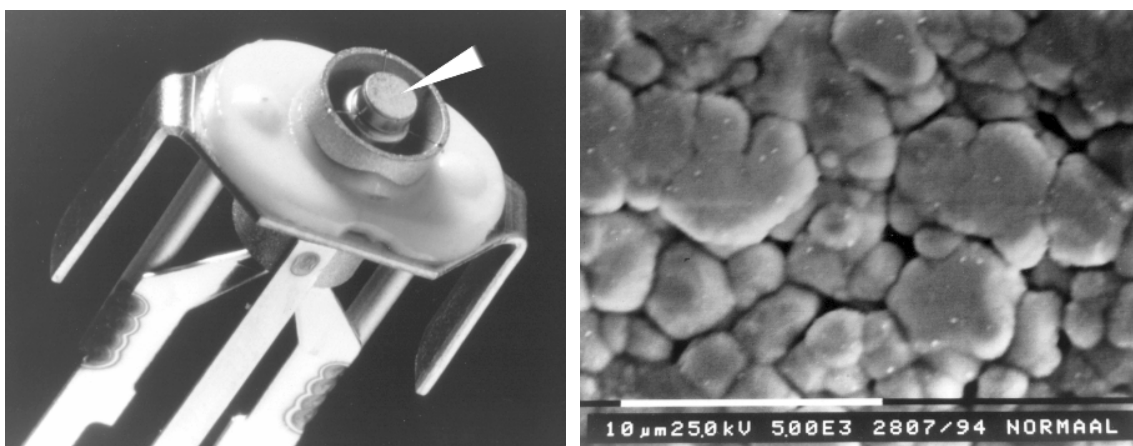


Figure 1.2. (a) Photograph of a thermionic dispenser cathode unit. (b) Secondary electron microscope image of the porous matrix, revealing the individual granulates and the impregnated pores.

and O segregate to the surface forming an electropositive Ba-O dipole layer with a work function of approximately 2 eV. To compensate for the higher work function compared to the oxide cathode, the basic dispenser cathode (B-type cathode) is operated at a temperature of 1030°C, which yields an electron emission density of several $\text{A}\cdot\text{cm}^{-2}$.

Further enhancement of the electron emission density has been achieved by coating the surface of the W matrix by a refractory metal layer (e.g. Os, Re, Ir) with a thickness of the order of 300-500 nm [6,7]. Because of the unexpected large emission enhancement due to this coating these top-layer cathodes were referred to as “Magic” or M-type cathodes. The latest development in cathode design is the use of a Ba-scandate complex in the cathode coating, which results in extremely large emission densities of more than $300 \text{ A}\cdot\text{cm}^{-2}$ [6]. An overview of the improvement of the emission capabilities of thermionic cathodes during the twentieth century is given in figure 1.3 [6]. Despite the obtainable high emission densities of the top-layer cathodes, the exact mechanism of the emission enhancement due to the various top-layer cathodes is not completely understood, and hinders further improvement of the cathodes.

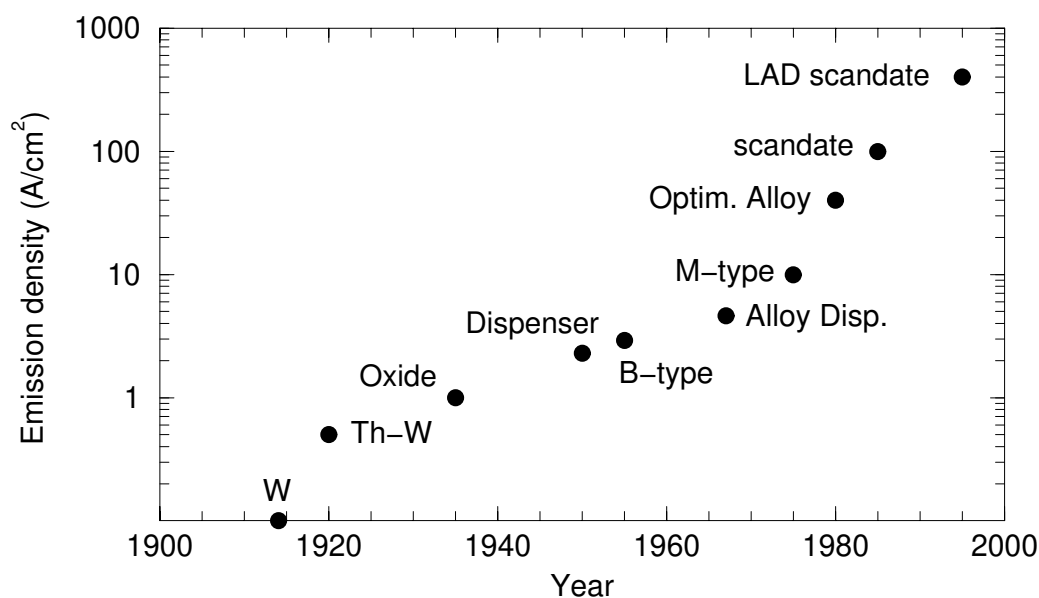


Figure 1.3. Progress of the electron emission densities of thermionic cathodes during the twentieth century (temperature of 1030°C).

1.3 Scope of the thesis

The objective of this thesis was to study the surface properties of real thermionic dispenser cathodes as used in cathode-ray tubes. The work was performed in a collaboration with Philips Research Labs (Aachen and Blackburn) and Philips Display Components (Eindhoven). Through surface analysis of various (top-layer) dispenser cathodes by means low-energy ion scattering (LEIS) and Auger electron spectroscopy (AES), the relation between the electron emission capabilities and the surface properties of the cathodes was investigated. The insights gained in this work contribute to the understanding of the operation of dispenser cathodes, and help to understand the influence of the substrates of the top-layer cathodes on the emission capabilities.

Furthermore, the dynamic behaviour of the dispenser cathodes during bombardment by ionised residual gases has been analysed. The residual gas atoms present in the cathode-ray tube can be ionised by the high-density electron beam. Due to the electric fields present in the tube, these ions are accelerated onto the cathode surface where they sputter away the Ba-O complex and damage the cathode substrate [8,9]. In order to maintain a constant Ba-O coverage during cathode operation, a dynamic equilibrium exists between the removal and the resupply processes of the Ba and O atoms. This dynamic behaviour of the cathodes during ion bombardment has been analysed, and a model has been derived that describes the surface coverage and electron emission during the bombardment, and includes the influence of the cathode temperature and the incident ion flux. The insights from these studies can help to improve the ion bombardment resistivity of dispenser cathodes.

The emphasis in this thesis is on the use of low-energy ion scattering for the surface analysis. In the ion scattering noble gas ions are used to probe the outermost atomic layer of the surface. The surface sensitivity is obtained because of the high neutralisation probability of the noble gas ions during the interactions with the surface atoms [10,11,12]. However, in the course of the investigations it has become evident that the neutralisation probability of the ions strongly depends on the work function. In order to correctly interpret the ion scattering signals, this work function dependence has to be understood, and therefore a substantial part of the work for this thesis was devoted to understanding the neutralisation of noble gas ions at low work functions. The insights from these investigations are used for the quantitative analysis of the surface composition of the low-work function cathodes. These insights are of course not limited for application to cathodes, but are of relevance to all ion scattering studies of low-work function systems.

This thesis also serves as an example to demonstrate how surface science nowadays is capable of analysing complex industrial systems. Since the 1960s there has been a virtual explosion in the level of research on solid surfaces due to the introduction and development of UHV techniques. However, in the first decades following the availability of the UHV techniques, the field of surface science has mainly focussed on fundamental processes at well-ordered surfaces. Now, the field of surface science has come of age, and is indeed capable of tackling real industrial problems. Moreover, this work also demonstrates the interplay between application-driven and curiosity driven research; although the neutralisation mechanisms of noble gas ions were studied to be able to perform the surface analysis of the cathodes (i.e. application-driven research), these investigations could also have been performed purely to gain more understanding of the neutralisation mechanisms of noble gas ions (i.e. curiosity-driven research).

1.4 Surface analysis using ion scattering

Before the outline of this thesis is presented in the next section, here a brief demonstration is given of the influence of the work function on the surface analysis of the cathodes using low-energy ion scattering. The purpose of this section is to emphasise that knowledge about the neutralisation mechanisms of noble gas ions at low-work function surfaces is essential in order to perform an accurate ion scattering analysis of dispenser cathodes. The basic principles of low-energy ion scattering will not be discussed here because many excellent reviews are available in the literature [13,14,15,16,17].

Figure 1.4 presents LEIS spectra of a top-layer dispenser cathode with an Os(80%)/Ru(20%) coating and a work function of 1.85 eV. The ion scattering was performed using Ne^+ ions with

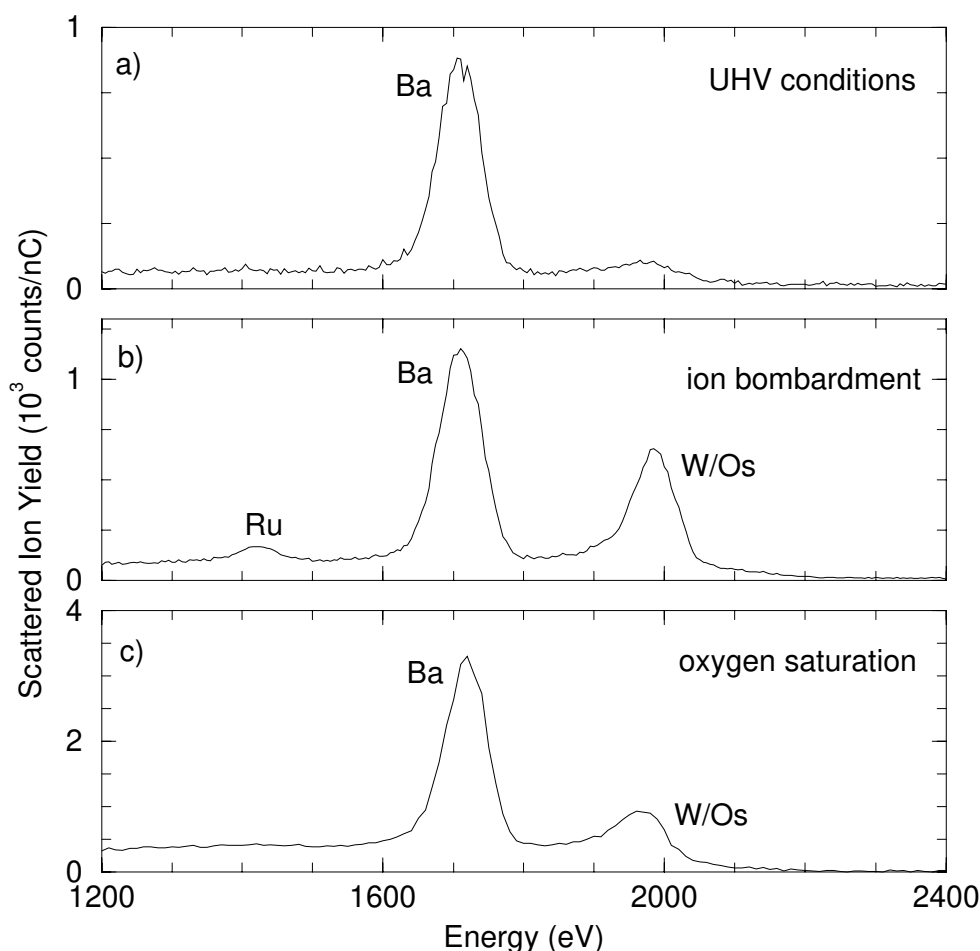


Figure 1.4. LEIS spectra using 3 keV Ne^+ ions for an Os/Ru dispenser cathode: (a) cathode operation in UHV, (b) cathode operation during ion bombardment, and (c) the cathode saturated with oxygen at room temperature.

an initial energy of 3 keV, and the spectra shown represent mass spectra of the outermost atomic layer of the cathode under different conditions. Figure 1.4a shows a spectrum of the cathode during operation at 1030°C in UHV, obtained using a very low ion flux in order not to influence cathode operation. The spectrum shows only a distinct Ba peak, and no clear peaks due to the substrate atoms. This indicates that only Ba atoms are present in the outermost atomic layer of the cathodes, and that the surface is covered by the Ba-O complex. When the cathode is exposed to a high-flux ion bombardment, peaks due to substrate atoms are clearly visible in the spectrum (figure 1.4b). Since in LEIS only the outermost atoms are probed, this indicates that the substrate is incompletely covered by the Ba-O complex due to the ion bombardment. This is schematically illustrated in figure 1.5, which shows that the substrate atoms can only be probed by the incident ions if no Ba and O atoms are present on top. Despite the Ba-O complex removal, the Ba signal intensity has increased compared to operation in UHV without ion bombardment. The increase in signal is caused by an increase in the work function associated with the removal of the Ba-O dipoles. This work function increase results in a decrease in the neutralisation probability of the noble gas ions. Therefore, a larger fraction of the incident ions survives the interactions with the surface as an ion, and consequently this yields a higher ion scattering signal despite the lower Ba density.

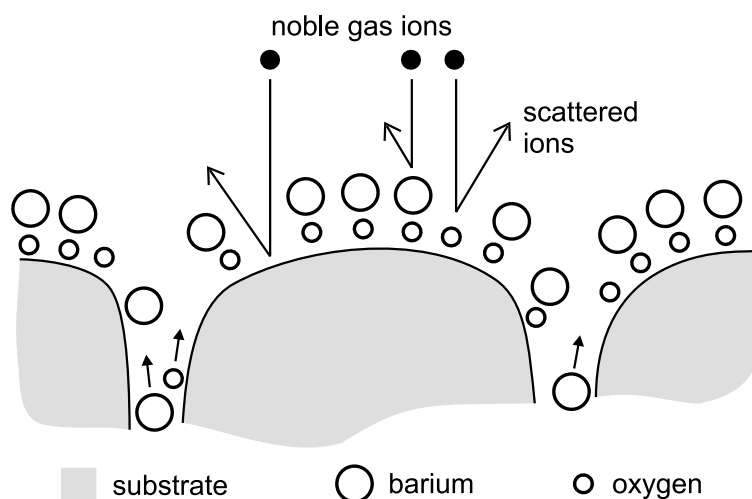


Figure 1.5. Schematic interpretation of the ion scattering analysis of the cathodes. Only the outermost atoms are probed by the incident ions.

An even more dramatic demonstration of the influence of the work function on the ion scattering signal is shown in figure 1.4c. Here, the cathode is saturated with oxygen at room temperature, which does not change the Ba density but does increase the work function to approximately 5 eV due to oxygen poisoning of the Ba-O dipoles. As under the ion bombardment, the work function increase results in a decrease of the neutralisation probability of the ions, and consequently the ion scattering signal increases by approximately a factor of 4 despite an unchanged Ba density.

From the examples in figure 1.4 it is evident that the work function strongly influences the neutralisation probability of the ions, and thus the measured ion scattering signal. When comparing the surface composition of various cathodes with different work functions, the influence of the work function as demonstrated in figure 1.4 is also present. An accurate surface analysis of dispenser cathodes therefore requires detailed knowledge of the influence of the work function on the neutralisation probability in order to correctly interpret the ion scattering signals.

1.5 Outline of the thesis

In order to describe the outline of this thesis it is most convenient to start with the final chapters 7 and 8, where the results are presented of the surface analysis of the thermionic dispenser cathodes during operation in UHV and during ion bombardment, respectively. In chapter 7 the relation between the surface composition and the electron emission of the various top-layer cathode is described, and it will be explained how the emission capabilities are determined by the substrate material. In subsequent chapter 8, the dynamic behaviour of the dispenser cathodes during the ion bombardment is described, where the emphasis will be on the Ba-O removal and resupply processes during the bombardment. A model to describe the surface coverage and electron emission during the ion bombardment will be presented. In the discussions in chapter 7 and 8, the role of the oxygen on the cathode surface is discussed in detail, and it will become apparent that the importance of the oxygen has been underestimated in the majority of papers dealing with dispenser cathodes reported in the literature.

The continuous red thread that runs through the preceding chapters is the accurate investigation of the cathodes. Although the LEIS technique is widely used for quantitative compositional analysis of many different types of surfaces, and hundreds of papers appear in the literature each year, ion scattering studies of low-work function systems are sporadic. Moreover, systematic investigations of the work function dependence of the neutralisation probability of noble gas ions are also absent in the literature. Therefore, prior to the surface analysis of the dispenser cathodes, a systematic investigation of this work function dependence was performed using cathode model systems, consisting of sub-monolayers of Ba atoms adsorbed on W substrates. In chapter 5 the results of these model investigations are presented, where the focus is on discussing the neutralisation mechanisms for noble gas ions at low work functions. In chapter 6 it is subsequently discussed how these neutralisation mechanisms can influence the quantification of the surface composition using ion scattering, and it is demonstrated how to correct for the influence of the work function. The discussions in chapter 5 and 6 are not focussed on cathodes, but are of importance to all ion scattering studies of low-work function surfaces.

The neutralisation investigations were performed using high-purity W single crystalline substrates with well-ordered surface structures. The growth and characterisation procedures of the W crystals with different crystallographic orientations are discussed in chapter 3. The surface cleaning procedures required to obtain well-ordered crystalline surfaces free from contaminants and impurities are also discussed. In addition to using the W crystals as substrates in the neutralisation investigations, the crystals were also used to investigate the influence of the crystal orientation on the signal intensity in LEIS. As will be shown in chapter 4, the structure of the surface influences the number of surface atoms that are probed by the incident ions. For quantitative analysis of the surface composition of the cathodes, or other surfaces, the relation between the signal intensity and the number of atoms probed by the ions has to be known.

In this thesis a strong emphasis exists on investigating and discussing the neutralisation probability of noble gas ions. The neutralisation investigations of the model systems and the real cathodes were performed using the characteristic velocity method, in which the neutralisation probability of the ions is deduced from the dependence of the LEIS signal on the incident energy of the ions. In order to correctly derive the neutralisation probability from the energy dependence of the LEIS signal, knowledge about the energy dependencies of the instrument, such as the analyser transmission and the detection efficiency, is essential. Therefore, in chapter 2 a thorough investigation and the instrumental energy dependencies of the set-up used in this work is presented.

The chapters of this thesis have been prepared for individual publication in devoted scientific journals. Therefore, each of the following chapters can be read independently. Accordingly, some overlap between the chapters is unavoidable.

References

- 1 D.E. Fisher, M.J. Fisher, "Tube, the invention of television", Counterpoint, Washington, 1996.
- 2 J.P. Blewett, *J. Appl. Phys.* 10 (1939) 668.
- 3 S. Yamamoto, *J. Vac. Soc. Japan* 40 (1997) 423.
- 4 R.O. Jenkins, *Vacuum* 19 (1984) 353.
- 5 R.E. Thomas, J.W. Gibson, G.A. Haas, R.H. Abrahams, *IEEE Trans. Elec. Dev.* 37 (1990) 850.
- 6 G. Gaertner, P. Geittner, H. Lydtin, A. Ritz, *Appl. Surf. Sci.* 111 (1997) 11.
- 7 P. Zalm, A.J.A. van Stratum, *Philips Tech. Rev.* 27 (1966) 69.
- 8 G. Gaertner, P. Geittner, D. Raasch, A. Ritz, D.U. Wiechert, *Appl. Surf. Sci.* 146 (1999) 12.
- 9 G. Gaertner, P. Geittner, D. Raasch, D.U. Wiechert, *Appl. Surf. Sci.* 146 (1999) 22.
- 10 H.H. Brongersma, P.M. Mul, *Surf. Sci.* 35 (1973) 393.
- 11 H.H. Brongersma, T.M. Buck, *Nucl. Instr. and Meth.* 149 (1978) 569.
- 12 H. Niehus H, W. Heiland, E. Taglauer, *Surf. Sci. Rep.* 17 (1993) 213.
- 13 D.P. Woodruff, T.A. Delchar, "Modern Techniques of Surface Science", Cambridge University Press, Cambridge, 1994.
- 14 J.C. Riviere, "Surface Analytical Techniques", Clarendon Press, Oxford, 1990.
- 15 A.W. Czanderna, D.M. Hercules, *Ion Spectroscopies for Surface Analysis*", Plenum Press, New York, 1991.
- 16 J. Rabalais, "Low Energy Ion-Surface Interactions", John Wiley & Sons, Chichester, 1994.
- 17 V. Bortolani, N.H. March, M.P. Tosi, "Interaction of Atoms and Molecules with Solid Surfaces", Plenum Press, New York, 1990.

Influence of Analyser Transmission and Detection Efficiency on the Energy Dependence of Low-Energy Ion Scattering Signals



Abstract

The signal intensity in low-energy ion scattering depends, among others, on the kinetic energy of the scattered ions. The measured energy dependence is a combination of the intrinsic energy dependence, determined by the ion-sample interaction, and the instrumental energy dependence. The intrinsic energy dependence is often exploited to obtain information on the charge transfer processes taking place between the ions and the sample surface. The resulting information is of relevance both for quantitative surface analysis as well as for obtaining a fundamental understanding of charge transfer processes. For a correct determination of the intrinsic energy dependence it is crucial that the energy dependencies of the analyser transmission and the ion detection efficiency of the instrument are accurately known.

In this paper we outline how these energy dependencies may be obtained, and we present the results for the cylindrical mirror analyser and micro-channelplate based detector in our set-up. The discussions about the energy dependencies are not specific for our set-up, but can be directly applied to other cylindrical mirror analysers and channelplate-based detectors. In addition, the similarities and differences with other types of analysers are briefly discussed. The implications of uncertainties in these energy dependencies for charge-exchange studies and quantitative compositional surface analysis are treated in detail.

2.1 Introduction

Low-Energy Ion Scattering (LEIS) using noble gas ions is capable of probing the outermost atomic layer of a wide range of different materials. LEIS investigations have been reported on many different types of solid surfaces (e.g. metals [1], oxides [2], polymers [3,4]), and even on liquid surfaces [5]. The investigations are not limited to well-ordered flat (single crystal) systems, but can also give valuable information about the outermost layers of complex real industrial systems such as catalysts [6,7,8], polymer LEDs [9], and thermionic dispenser cathodes [10,11].

In addition to compositional analysis of the outermost atomic layer, LEIS is also used for fundamental investigations of ion-solid interactions, such as charge exchange processes that occur during the interaction between the ion and surface atom(s) [12]. In many applications, both for compositional analysis and charge exchange studies, the influence of the initial ion energy on the LEIS signal intensity is important. The energy dependence of the LEIS signal is the subject of this paper. The work presented and discussed here is not focused on the investigation of a particular system, but is of relevance to all studies where energy dependent LEIS measurements are performed.

The energy dependence of the measured LEIS signal can be divided into the intrinsic energy dependence and the instrumental energy dependence. The intrinsic energy dependence is exclusively determined by the energy dependencies of the physical parameters involved in the ion-target interaction, i.e. the scattering cross-section and the neutralisation mechanism(s). The instrumental energy dependencies are introduced through the measurement method, and include the energy dependencies of the analyser transmission and the ion detection efficiency. It is surprising that, although several hundred LEIS papers appear in the literature each year, a thorough investigation of these energy dependencies and a discussion of the consequences for the interpretation of LEIS signals is strikingly absent. In this paper we report on the investigation of the instrumental energy dependencies of the cylindrical mirror analyser (CMA) and channelplate-based detector in our set-up. We present and discuss methods to investigate the energy dependencies of the analyser transmission (section 2.4) and detection efficiency (section 2.5). Although the investigations focus on the instrumental energy dependencies of the analyser and detector in our set-up, the methods outlined may be applied to other instruments. An overview of the similarities and differences with other types of commonly used analysers is therefore given (section 2.6). Finally, we conclude by discussing the implications of errors in the instrumental energy dependence on the interpretation of charge exchange studies and on a quantitative analysis of the composition of the outermost atomic layer (section 2.7).

2.2 Experimental

In the LEIS set-up MiniMobis [13] a monoenergetic beam of noble gas ions with an initial energy range of 1-5 keV is directed perpendicular onto the sample surface (see figure 2.1a). Ions that are backscattered over an angle of $\theta=136^\circ$ are energy analysed by a CMA. The ion beam is produced by a differentially pumped ion source, which is positioned directly above the CMA. The resulting beam is mass analysed by a Wien-filter and is focused and controlled by a set of Einzel-lenses, with the final lens mounted inside the CMA.

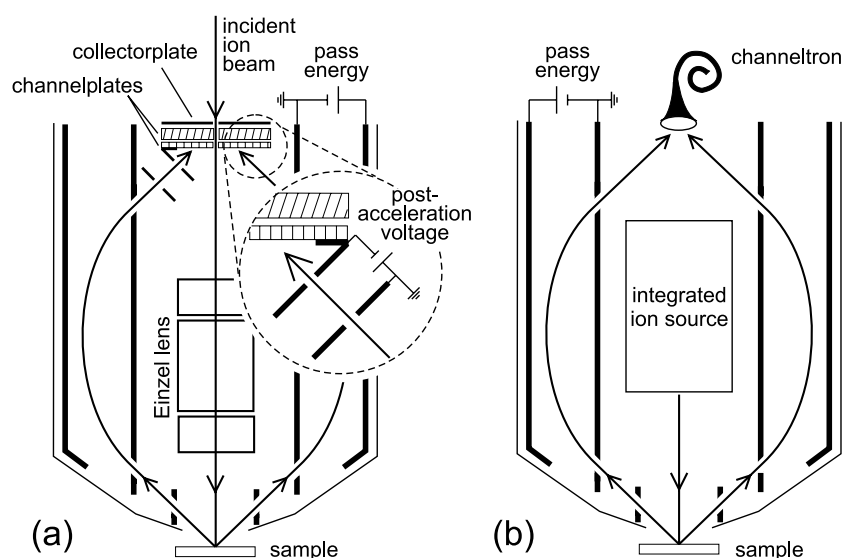


Figure 2.1. Schematic of the cylindrical mirror analyser, as used in our set-up (a), and for a standard system (b). In our system the incident ion beam is directed perpendicular to the surface, and ions that are backscattered over an angle of $\theta=136^\circ$ are detected by the channelplates. After the energy selection the ions are accelerated by the post-acceleration voltage (0-1000V) to increase the kinetic impact energy on the channelplates (see circular inset). In a standard CMA usually an integrated ion source is used, and the detection is performed by a single channeltron. A variable post-acceleration is not standard for a regular system.

Ions that pass the CMA energy selection slits are detected by a set of two micro-channelplates stacked in Chevron configuration [14,15]. The first channelplate has a channel orientation perpendicular to the surface, and a thickness of 0.5 mm (Philips G12-36/0). Electrons leaving the first plate are accelerated by a 100 V potential difference to the second plate, which is mounted at a distance of 0.5 mm behind the first plate. The second channelplate has a channel orientation 13° off the surface normal and a thickness of 1.0 mm (Philips G12-36/13/DT/LR). The charge cloud generated by the channelplates is accelerated by a 200 V potential onto a Cu collector, which feeds the charge pulse into the acquisition electronics that are operating in pulse-counting mode.

The channelplates operate in saturated mode for a channelplate operating voltage of approximately 3000 V, applied between the front of the first plate and the backside of the second plate. The operation voltages of the individual plates, which are applied between the front and back of each plates, have a ratio of 2:3 for the first and second plate respectively. The front of the first channelplate can be put at a negative potential (0-1000V) to post-accelerate the ions after passing the last energy selection slits, and thus increase the kinetic impact energy of the ions on the channelplate surface (see figure 2.1a).

2.3 LEIS signal intensity

Before we come to the investigation of the instrumental energy dependencies we will first direct our attention to the definition of the LEIS signal intensity. As we will show later, the choice for the use of the peak area or the peak height as a measure for the signal intensity influences the correction for the analyser transmission. It should be noted that numerous LEIS

studies have been reported in the literature where the signal intensity is used without specification whether the peak area or the peak height is used.

Ions with an initial energy E_i that scatter from surface species k in the scattering direction θ have a final energy E_f [16]. Due to (in)elastic energy losses the peak at E_f has a finite width, which is expressed in the intrinsic energy distribution $I_k(E)$ of the peak [17,18]. The total ion yield $Y_k(E_i)$ for ions with energy E_i scattering from species k with density n_k is given by integration of $I_k(E)$ over the intrinsic peak:

$$Y_k(E_i) = \int_{peak} I_k(E) dE = \frac{d\sigma_k}{d\Omega}(E_i) \cdot P_k^+(E_i) \cdot n_k \quad (2.1)$$

The total ion yield is thus proportional to the differential scattering cross-section $d\sigma_k/d\Omega$, the ion fraction P_k^+ , and the surface density n_k . The ion fraction is the probability of the incident ion to leave the surface as an ion after the interaction with its scattering partner, and is assumed to be constant over the energy range covered by the peak of species k . The ion yield Y_k in eq. (2.1) is normalised for the ion flux, and the influence of surface roughness is omitted here because it is not relevant for the discussion [19].

When performing a LEIS experiment the measured LEIS peak corresponding to species k is a convolution of the intrinsic energy distribution $I_k(E)$ and the instrumental energy dependence $\eta'(E, E_f)$. Here, $\eta'(E, E_f)$ expresses the dependence on energy E for a fixed pass energy E_f . We assume that the instrumental energy dependence varies slowly across the energy range of the intrinsic peak. The measured LEIS signal intensity $S_k(E_i)$ after integration of the peak area from species k is thus given by:

$$S_k(E_i) = \int (I_k(E) * \eta'(E, E_f)) dE = \int \eta'(E, E_f) dE \cdot \int I_k(E) dE = \eta(E_f) \cdot Y_k(E_i) \quad (2.2)$$

Here, we have used the general property of the convolution operation that the area of the convolution is equal to the product of the areas of the convoluted functions [20]. The effective instrumental energy dependence for the peak at energy E_f is defined as $\eta(E_f) = \int \eta'(E, E_f) dE$. The instrumental energy dependence $\eta(E_f)$ is a combination of the energy dependencies of the analyser transmission $T(E_f)$ and the ion detection efficiency $\varepsilon(E_f)$, which both depend on the final energy E_f of the scattered ions. Therefore, the instrumental energy dependence depends only on the final energy of the ions, and is independent of the initial energy or the scattering species. The measured signal intensity $S_k(E_i)$ of species k is found by substitution of eq. (2.1) in eq. (2.2) and using the instrumental energy dependence $\eta(E_f) = T(E_f) \cdot \varepsilon(E_f)$:

$$S_k(E_i) = T(E_f) \cdot \varepsilon(E_f) \cdot \frac{d\sigma_k}{d\Omega}(E_i) \cdot P_k^+(E_i) \cdot n_k \quad (2.3)$$

This equation shows the separate parameters that combine to form the energy dependence of the measured LEIS signal. The energy dependencies of the ion fraction [12] and the differential scattering cross-section [21,22] are determined by the ion-target combination. (The scattering cross-section will further be denoted as σ_k). The energy dependencies of the analyser transmission $T(E_f)$ and ion detection efficiency $\varepsilon(E_f)$ are in principle different for each instrument.

2.4 Analyser transmission

The transmission of a CMA is proportional to the selected pass energy: the width of the energy transmission window ΔE scales with the pass energy E , i.e. $\Delta E/E$ is a constant. To determine how this transmission influences the measured LEIS intensity, we have to distinguish between using the peak area or the peak height as signal intensity. In addition, we have to consider the energy dependence of the intrinsic peak, i.e. the nature of the contributions to the finite peak width. Most effects contributing to the intrinsic peak width can be divided into two categories [23,24]: those that scale with the kinetic energy of the ion (E), and those that scale with the square root of the ion energy (\sqrt{E}). Effects that scale with E include the spread in energy and angle of the incident ion beam, and the spread in scattering angle θ of the accepted ions due to finite width of the primary selection slits. The ‘‘Doppler shift’’ due to scattering of thermally vibrating surface atoms [25] scales with \sqrt{E} , as do the inelastic energy losses due to electronic excitations [26,27]. For convenience in the discussion we will refer to the effects that scale with E and \sqrt{E} as elastic and inelastic effects respectively.

Let us first consider the influence of the analyser transmission on the measured peak area by taking a closer look at eq. (2.2). The signal intensity $S_k(E_i)$ is defined as the area of the convolution $I_k(E) * \eta'(E, E_f)$, which implicitly means that we use the area of the measured peak as a measure for the signal intensity. The area of the measured peak $S_k(E_i)$ is equal to the area of the intrinsic peak $Y_k(E_i)$, multiplied by the area of the transmission window $\int \eta'(E, E_f) dE$. The width of transmission window scales with the final energy of the peak, and therefore the area of the transmission window also scales with the final energy of the peak. The correction for the analyser transmission when the peak area is used as a measure for the signal intensity is thus given by $T(E_f) = c \cdot E_f$, where the constant c includes the solid angle of the analyser.

The influence of the transmission on the measured peak height can not be deduced as straightforward as for the measured peak area. Instead, we will use the simulations in figure 2.2 to show that the energy dependence of the measured peak height depends on the analyser resolution and the peak broadening details. In the simulations a distinction is made between elastic and inelastic peak broadening. In addition, high and low analyser resolutions were simulated, where the width of the transmission window ΔE is relatively small and relatively large compared to the peak width respectively. For all four figures (2.2a-d) the two top peaks (thick solid curves) represent intrinsic peaks of the same species, but using different initial energies E_i and $\beta \cdot E_i$. We assumed that the cross-section and the ion fraction are the same for both peaks. Therefore, the areas of the intrinsic peak A are identical for both peaks, while the width is different due to the energy dependence of the peak broadening effects. The transmission windows are shown as rectangles. The measured peaks (dashed curves) were obtained by a convolution of the intrinsic peaks with the corresponding transmission windows. The measured peak area and peak height are denoted as A^m and h^m respectively.

First consider the low resolution limit (figures 2.2b and 2.2d). For both elastic and inelastic broadening the intrinsic peak falls completely within the transmission window. As a result, the measured peak height is independent of the final energy and the peak broadening details. In the high resolution limit the elastic and inelastic effects have to be considered separately. Starting with pure elastic broadening (figure 2.2a) we see that the widths of the intrinsic peak and of the transmission window both scale with the final energy. Consequently, the fraction of the intrinsic peak within the transmission window is independent of the final energy. The height of the measured peak for pure elastic broadening is, therefore, independent of the final

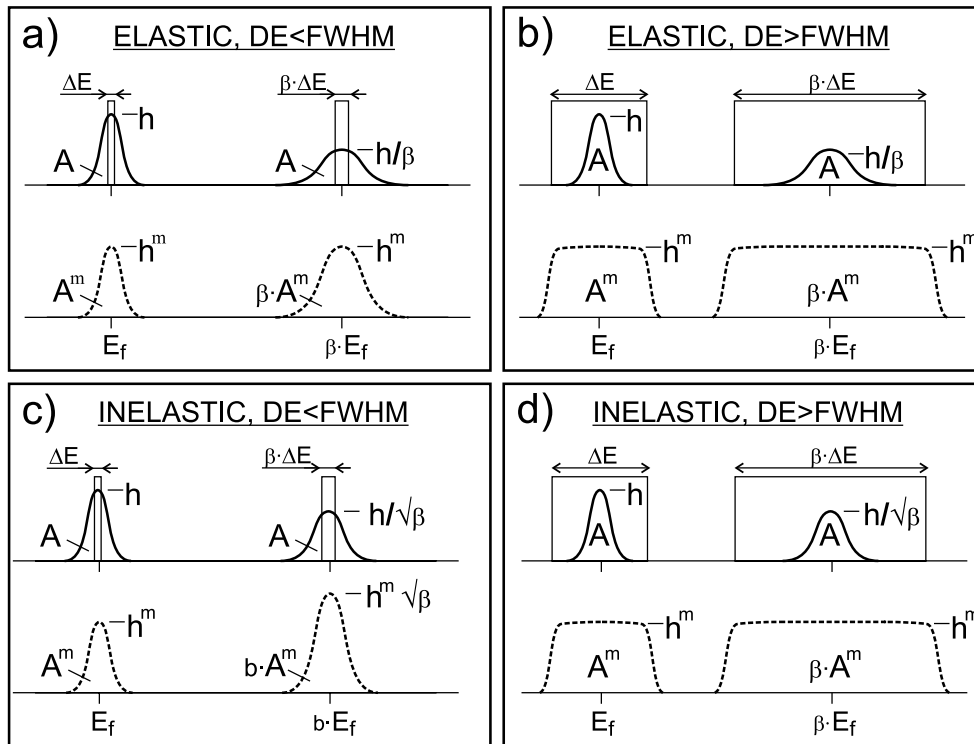


Figure 2.2. The transformation of the intrinsic peak to the measured peak by the analyser transmission. The top and bottom graphs show purely elastic ($FWHM \sim E$) and inelastic ($FWHM \sim \sqrt{E}$) peak broadening respectively. The left ($\Delta E < FWHM$) and right ($\Delta E > FWHM$) graphs show a high and low analyser resolution respectively. For all four separate situations two peaks of the same species are shown, using initial energies $E_{i,1}$ and $E_{i,2} = \beta \cdot E_{i,1}$. The final energies of these peaks are E_f and $\beta \cdot E_f$ respectively. The thick solid curves represent the intrinsic peaks, and the dashed curves represent the measured peaks.

energy of the peak ($h^m = \text{constant}$). For pure inelastic broadening (figure 2.2c) the peak width scales with $\sqrt{E_f}$ and the width of the transmission window scales with E_f . Effectively, the fraction of the peak within the transmission window scales with $\sqrt{E_f}$. The measured peak height for pure inelastic broadening, therefore, scales with $\sqrt{E_f}$. For our CMA (which has a resolution comparable to the standard available analysers) the resolution is such that the transmission window width is smaller than the peak width. Therefore, the experimental conditions mostly resemble figures 2.2a and 2.2c. The correction for the analyser transmission when the peak height is used thus depends on the fraction of the intrinsic peak within the transmission window, which is determined by the peak broadening details. Therefore, we define $T(E_f) = c \cdot f(E_f)$, where $f(E_f)$ represents the fraction of the intrinsic peak within the transmission window. For purely elastic broadening $f(E_f)$ is constant and for purely inelastic broadening $f(E_f)$ is proportional to $\sqrt{E_f}$.

Based on the considerations above we have to redefine eq. (2.3), where the use of the peak area or the peak height as a measure for the signal intensity has to be considered separately. Consequently, we come to the following relations for the energy dependence of the LEIS signal intensity, using the peak area $S_k^A(E_i)$ and peak height $S_k^h(E_i)$ respectively:

$$S_k^A(E_i) = c \cdot E_f \cdot \varepsilon(E_f) \cdot \sigma_k(E_i) \cdot P_k^+(E_i) \cdot n_k \quad (2.4a)$$

$$S_k^h(E_i) = c \cdot f(E_f) \cdot \varepsilon(E_f) \cdot \sigma_k(E_i) \cdot P_k^+(E_i) \cdot n_k \quad (2.4b)$$

Here we have substituted $T(E_f)=c \cdot E_f$ and $T(E_f)=c \cdot f(E_f)$ for the correction for the analyser transmission respectively. Obviously, using the peak area is the preferred method, since this does not require information on the peak broadening details. However, since the peak height is also frequently used in literature, we will show here how the fraction $f(E)$ may be determined experimentally.

In practice the peak width is determined by a combination of elastic and inelastic effects. Let $\Delta E_{elas}(E)$ and $\Delta E_{inelas}(E)$ be the contributions from the elastic and inelastic effects to the total peak width $\Delta E_{total}(E)$. The energy dependence of the total peak width $\Delta E_{total}(E)$ is given by:

$$\Delta E_{total}(E) = \sqrt{(\Delta E_{elas}(E))^2 + (\Delta E_{inelas}(E))^2} = \sqrt{(C_{elas} \cdot E)^2 + (C_{inelas} \cdot \sqrt{E})^2} \quad (2.5)$$

Here we used $\Delta E_{elas}(E)=C_{elas} \cdot E$ and $\Delta E_{inelas}(E)=C_{inelas} \cdot \sqrt{E}$ for the energy dependencies of the separate components, where the constants C_{elas} and C_{inelas} represent a measure for the magnitude of the elastic and inelastic effects respectively. At each particular energy, the fraction of the LEIS peak within the transmission window $f(E)$ can be found by dividing the width of the transmission window by the peak width $\Delta E_{total}(E)$. The energy dependence of the fraction is thus given by $f(E) \sim E/\Delta E_{total}(E)$.

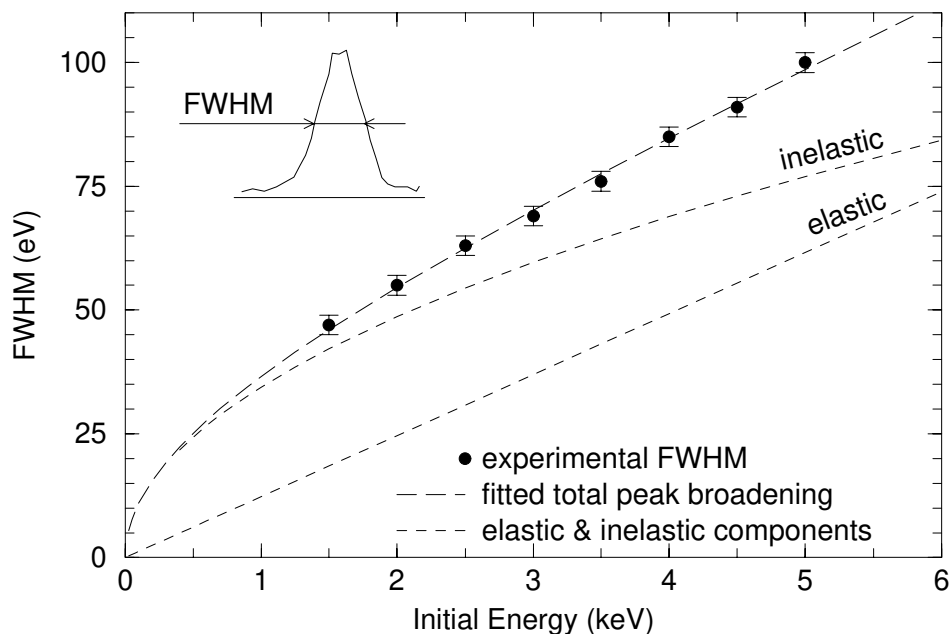


Figure 2.3. The FWHM of the LEIS peaks versus the initial energy. The data is taken from a Ne^+ investigation of Ba atoms on a tungsten based thermionic cathode. The data-points have been fitted with eq. (2.5), where C_{elas} and C_{inelas} are used as fitting parameters. Also shown are the elastic and inelastic broadening components, with $C_{elas}=1.23 \cdot 10^{-2}$ and $C_{inelas}=1.09 \text{ eV}^{1/2}$ as derived from the fit.

The relative broadening contributions are hard to predict theoretically, but can be derived experimentally by plotting the peak width versus the ion energy for a certain ion-target combination. Figure 2.3 shows an example for Ne^+ ions scattered from Ba atoms in the outermost layer of a thermionic cathode [10,13,28]. The experimentally determined peak width (FWHM) is plotted as a function of the initial ion energy and is fitted using eq. (2.5), with C_{elas} and C_{inelas} as fitting parameters (long dashed curve). The separate contributions of the elastic and inelastic peak broadening components are also shown (dashed curves). Once the energy dependence of the peak width has been determined, the energy dependence of $f(E)$ can be deduced and the correction for the analyser transmission on the peak height can be performed. For example, in figure 2.3 the fraction of the peak within the analyser window for an initial energy of 1.5 keV and 5 keV is deduced as $f(E)=0.10$ and $f(E)=0.16$ respectively. Here we used $\Delta E/E=0.005$ for the resolution of our analyser, which has been determined from the width of the elastic scattering peak in Auger electron spectroscopy.

2.5 Channelplate efficiency

The detection efficiency of the scattered ions depends on the creation of secondary electrons by the initial ion impact on the channelplate surface, and on the ability of the channelplates to convert these initial secondary electrons into a charge pulse on the collector. The former creation process is a statistical process that depends, among others, on the kinetic energy of the ions [29,30]. The latter charge multiplication process depends on the configuration of the channelplates, and the voltage applied across the plates [14,31]. In addition, it is important to note that ageing of the channelplates can deteriorate the charge multiplication process. Here, we have investigated the energy dependence of the detection efficiency for different noble gas ions (He^+ , Ne^+ , and Ar^+). In the following we will focus on Ar^+ ions scattered from a tungsten crystal to demonstrate the approach used to determine the channelplate detection efficiency. The results for He^+ and Ne^+ ions are summarised and compared to Ar^+ at the end of the section. The tungsten crystal preparation and cleaning details have been reported elsewhere [32] (see chapter 3).

The dependence of the detection efficiency on the kinetic impact energy was investigated by using a post-acceleration voltage to vary the kinetic energy of the ions after they have passed the final selection slit (see figure 2.1). This enabled us to vary the impact energy of the ions on the surface of the channelplate without affecting other parameters, such as the scattering cross-section and ion fraction. By measuring the LEIS signal as a function of the post-acceleration voltage, the influence of the energy dependence of the detection efficiency is investigated. For a fixed initial energy the post-acceleration voltage is varied between 0-1000 V, resulting in an equally wide range over which the influence of the impact energy on the LEIS signal is studied. To investigate the detection efficiency over a wider impact energy range different initial energies were used, each covering a 1000 eV wide impact energy range. Figure 2.4 demonstrates this approach for a channelplate voltage of 3000 V, where the four lower line segments show the measured signal (left axis) as a function of the impact energy for a fixed initial energy. The absolute difference in signal between the separate segments is caused by the change in ion fraction, cross-section and transmission associated with the change in initial energy. The change in signal as a function of the impact energy within each segment is only due to the detection efficiency. It is assumed that the channelplate efficiency varies smoothly with impact energy over the whole range investigated. Therefore the partially overlapping segments were individually scaled (as indicated by the arrows) and pasted

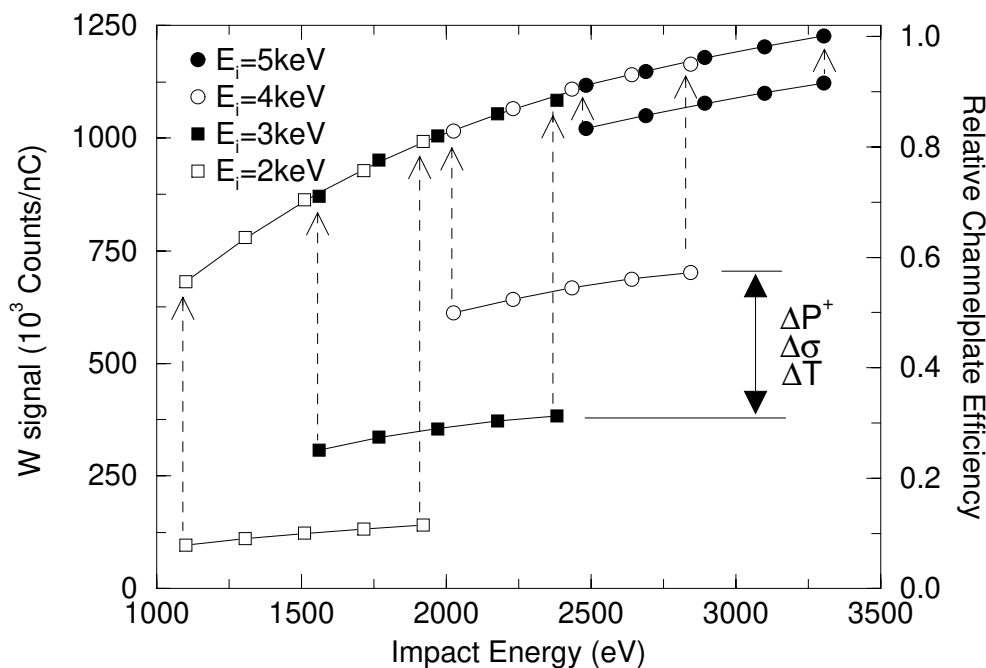


Figure 2.4. The detection efficiency as a function of the impact energy for a channelplate voltage of 3000 V (Ar^+ ions scattered from W). The lower separate segments represent the LEIS signal as measured (left axis), where the lowest signal is observed for $E_i=2$ keV due to the small ion fraction. The data-points in each segment are measured with a post-acceleration voltage of 200 V, 400 V, 600 V, 800 V, and 1000 V (from left to right). Scaling the segments to form a smooth curve, and normalising to $E_i=5000$ eV and $V_{pa}=1000$ V, gives the relative channelplate efficiency (right axis).

together to form a smooth curve over the whole impact energy range (upper curve). This curve represents the change in channelplate detection efficiency as a function of the impact energy on the channelplate surface. Since we can not determine the absolute detection efficiency with this approach, the curve represents the detection efficiency relative to the highest impact energy used in our investigation, measured at $E_i=5$ keV and $V_{pa}=1000$ V (right axis). Using this procedure, relative detection efficiency curves have been determined for different channelplate voltages along the saturation curve. A saturation curve shows how the measured signal depends on the applied channelplate voltage. In figure 2.5 these efficiency curves are presented for channelplate voltages between 2650 V and 3150 V with steps of 35 V. The inset in the figure shows a saturation curve for a constant impact energy of 1250 eV, where the position of the efficiency curves along the saturation curves becomes clear. The dependence of the detection efficiency on the impact energy diminishes with increasing applied channelplate voltage, i.e. shifting from unsaturated to saturated channelplates. Here, unsaturated channelplates serve to simulate aged channelplates that can no longer be operated in the saturated mode. However, it should be emphasised that even with channelplates operating in the saturated mode, a clear dependence of the detection efficiency on the impact energy is still present.

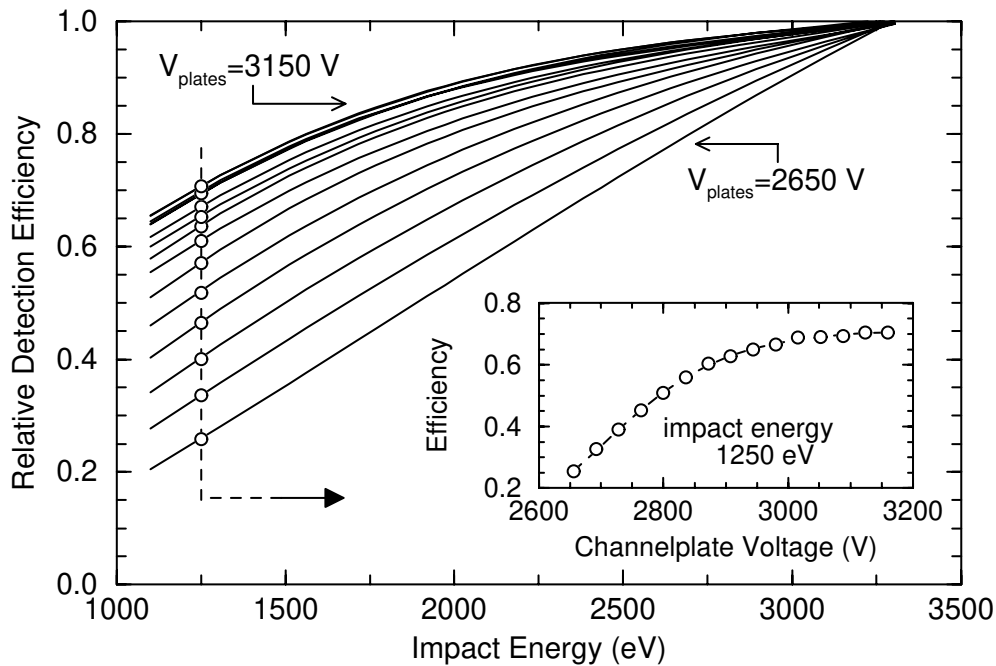


Figure 2.5. The relative channelplate efficiency curves as in figure 2.4 for different channelplate voltages. The bottom and top curve were determined for a channelplate voltage of 2650 V and 3150 V respectively. The difference in channelplate voltage between the individual curves is 35 V. The channelplates are operating in saturated mode for channelplate voltages larger than 2900 V. The inset shows the efficiency for an impact energy of 1250 eV as a function of the channelplate voltage.

In the method outlined above the post-acceleration voltage was varied to investigate the detection efficiency. Under standard LEIS conditions the post-acceleration voltage is fixed at the maximum voltage of 1000 V for maximum detection efficiency. As a preparation for the detection efficiency investigations, the influence of a variable post-acceleration on the LEIS signal was investigated. These studies revealed that for unsaturated channelplates in combination with low impact energies the post-acceleration voltage influenced the LEIS signal. Due to the influence of the variable post-acceleration the detection efficiency was underestimated approximately 10-20% for low channelplate voltages ($V_{pa} < 2750\text{eV}$) in combination with low impact energies ($E_{impact} < 1500\text{eV}$). No influence was observed for saturated channelplates or high impact energies. In the results presented above the influence of the variable post-acceleration was corrected for. We emphasise that the influence of the post-acceleration was brought about because of our approach to investigate the detection efficiency, and does not affect regular LEIS experiments where the post-acceleration voltage is fixed.

The observed energy dependence of the detection efficiency on the impact energy can be described by secondary electron emission theory. The electron creation upon impact is a statistical process which obeys the Poisson distribution, where the probability $P(n)$ for n electrons to be emitted for a certain secondary electron yield γ is given by [33,34]:

$$P(n) = \frac{\gamma^n \cdot \exp(-\gamma)}{n!} \quad (2.6)$$

Secondary electron emission is a combination of kinetic and potential electron emission mechanisms [29]. The kinetic electron emission depends on the kinetic impact energy of ions on the channelplate surface. The potential electron emission is independent of the energy and can occur for example by an Auger neutralisation process of the impacting ion. The secondary electron yield due to kinetic emission is in first order proportional to the kinetic impact energy of the ion on the surface [29,35]. Thus we define $\gamma = c_1 \cdot E_{\text{impact}} + c_2$, where constants c_1 and c_2 are determined by the type of ion, the channelplate properties (e.g. channelplate material), and the exact impact details (e.g. impact angle).

Let us now assume that, when the channelplates are operated in saturated mode, the electron multiplication process is efficient enough so that the creation of a single secondary electron during the ion impact on the channelplate surface is sufficient for the ion to be detected. Using eq. (2.6) the dependence of the detection efficiency on the impact energy can be expressed as [34]:

$$\varepsilon = P(n \geq 1) = 1 - \exp(-\gamma) = 1 - \exp(-c_1 \cdot E_{\text{impact}} - c_2) \quad (2.7)$$

The comparison between the secondary electron emission theory and the experimentally determined efficiency curves for saturated channelplates is presented in figure 2.6. In the inset

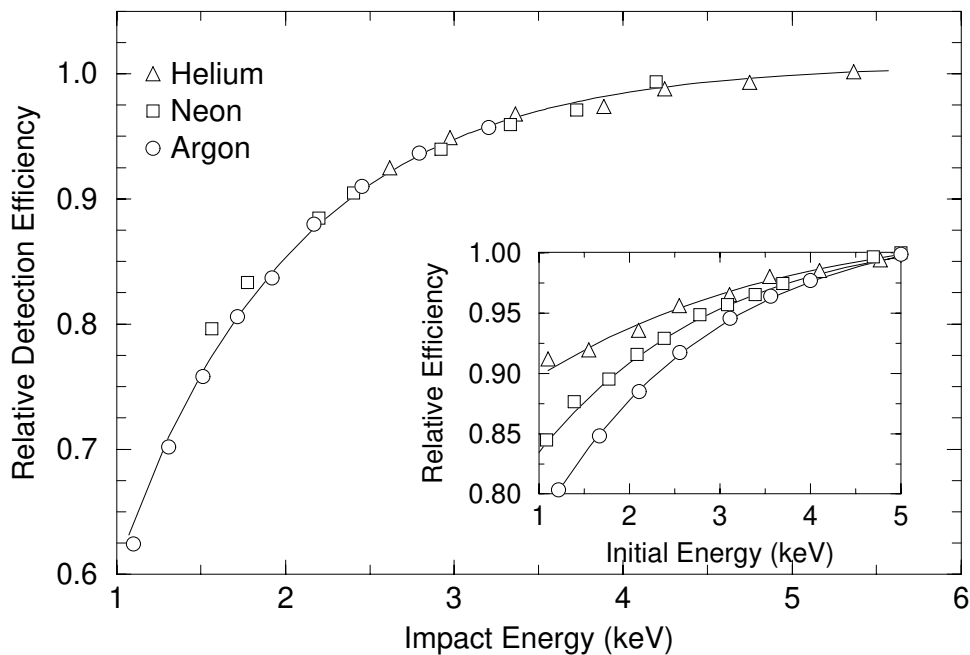


Figure 2.6. The relative detection efficiencies for He^+ , Ne^+ , and Ar^+ with the channelplates in saturated mode. The solid lines are fits to the data-points using eq. (2.7). The separate curves for He^+ , Ne^+ , and Ar^+ are scaled to form a smooth curve. The inset shows the separate curves as a function of initial energy, to show that for a fixed initial energy the efficiency decreases with increasing ion mass.

in figure 2.6 the relative detection efficiency is shown versus the initial energy for the different ions, demonstrating a decreasing detection efficiency with increasing ion mass. However, this is only an indirect effect of the ion mass, because an increase in ion mass results in a decrease in final energy, and therefore, also in a decrease in impact energy. The main panel in figure 2.6 shows the detection efficiency versus the impact energy on the channelplate surface, where the same data is used as in the inset. Here the individual relative efficiency curves of the different ions have been scaled and pasted together to form a smooth overall efficiency curve as a function of the impact energy. The solid line is a fit with the secondary electron emission theory in eq. (2.7), where the constants c_1 and c_2 are used as a fitting parameter. It is clear that the emission theory describes the data quite well. Note that other investigations have suggested a square root energy dependence of the electron yield ($\gamma \sim \sqrt{E_{\text{impact}}}$) [35]. This results in different fitting parameters c_1 and c_2 , but yields equally good fits of our experimental data. Thus, we can conclude that the energy dependence of the detection efficiency is similar for the different ion types, which agrees with the experimental observation that for these ions the energy dependence of the secondary electron yield is approximately the same [29,35].

2.6 Other types of analysers

2.6.1 Standard CMA

Thus far, we have focused on the CMA used in our LEIS set-up as shown in figure 2.1. Also shown in figure 2.1 is the layout of a standard CMA with integrated ion source. In this type of configuration the ion beam is produced inside the CMA and the detection is usually performed by a single channeltron. Although our system is home-built, it is in principle equal to the standard analysers, and has a comparable energy resolution. Therefore, the discussions and conclusions concerning the energy dependence of the correction for the analyser transmission are directly applicable to the standard CMA.

The investigation of the ion detection efficiency was performed using a variable post-acceleration voltage. The observations and conclusions about the dependence of the detection efficiency on the impact energy and operation voltage are similar for channelplates and channeltrons. However, the details of the configuration and state of the detector determine the exact shape of detection efficiency curves, as was shown in figure 2.5. If a variable post-acceleration is available in the set-up, the energy dependence of the detection efficiency can be determined as demonstrated. Unfortunately, a variable post-acceleration is by no means standard in a regular CMA, which implies that the detection efficiency can not be investigated by the applied method. If no post-acceleration can be performed the impact energies on the detector surface are not very large. For low initial energies, or large ion masses, the impact energies are in the regime where the detection efficiency depends strongly on the impact energy.

2.6.2 Hemispherical analyser

The hemispherical analyser (HA), a standard tool in X-ray photoelectron spectroscopy (XPS), can also be used for ion scattering spectroscopy. The HA can be operated in an identical manner as a CMA, with a variable pass energy. In this mode, the discussions and conclusions concerning the energy dependence of the CMA analyser transmission can be directly applied to this type of analyser. Note that because the HA is used for XPS, it generally has a better energy resolution than the standard CMA. For the energy dependence of the detection efficiency the same way of reasoning applies as with the standard CMA.

The HA can also be operated with a fixed pass energy. A variable acceleration (or deceleration) of the ions is performed before the energy selection slits, so the selected ions always enter the electrostatic deflection area with the same kinetic energy. The advantage of this mode is that the width of the energy window, the analyser transmission, and the impact energy on the detector do not depend on the final energy of the scattered ions. However, if energy dependent measurements are performed where the initial energy of the ions is varied, the same pass energy must be used for the whole initial energy range. In this mode, care must be taken that the variable acceleration (or deceleration) voltages do not have any influence on the ion trajectories. Any (de)focusing effects before the selection slits can change the opening angle of the analyser and change the analyser transmission. As a result, the analyser transmission is no longer constant, and a correction is required. Therefore, for operation in the constant pass-energy mode, great care must be exerted in the design of the beam optics in order to guarantee a constant transmission through the input lens system.

2.7 Discussion

2.7.1 Charge exchange studies

A widely used approach to characterise the neutralisation behaviour of the incident ions is the characteristic velocity model. In this model it is assumed that the probability for an incident ion to survive the interactions with the surface as an ion, is determined by the rate of charge exchange, and by the velocity of the ion. The dependence of the ion fraction P_i^+ on the ion velocity v is given by [36,37,38,39,40,41]:

$$P_k^+ = e^{-v_c \frac{1}{v}} \quad (2.8)$$

The characteristic velocity v_c is a measure for the neutralisation rate and depends on the electronic interaction details of the ion-target combination. The exact definition of the ion velocity depends on the charge exchange processes involved. For noble gas ion scattering it is commonly believed that the basic neutralisation mechanism is an Auger process to the ground state of the ion. Therefore, the effective ion velocity is often defined as $1/v = 1/v_i^\perp + 1/v_f^\perp$, where v_i^\perp and v_f^\perp denote the velocities of the ion before and after the interaction normal to the surface [36,37]. For alkali ion scattering the neutralisation occurs through a resonant electron transfer from the surface to the ground state of the ion [41]. For the resonant charge transfer only the outgoing velocity is important and thus $1/v = 1/v_f^\perp$ is more appropriate [41,42]. Some neutralisation studies also indicate the existence of a neutralisation mechanism that takes place during the close encounter between the ion and its scattering partner [43]. For this very local mechanism the ion velocity is used, rather than the velocity normal to the surface. Although the definition of v depends on the neutralisation mechanism involved, the discussion below applies independent on the particular choice of v . (Note however that the characteristic velocity model can not be applied to core-level resonant neutralisation that takes place for some ion-target combinations, like e.g. He⁺-Pb [44]).

The characteristic velocity v_c is derived experimentally by measuring the LEIS signal as a function of the ion velocity. This can be accomplished by varying the initial energy of the ion, while keeping the incident and scattering angle fixed [45,46,47]. An alternative approach is to keep the initial energy and scattering angle fixed, and vary the incident [48] or outgoing angle [45,49]. In the latter approach the neutralisation on the outgoing trajectory can be investigated

separately [45,49]. However, this method can not be applied for local neutralisation mechanisms. For the investigation of the neutralisation probability along the complete trajectory, varying the initial energy is the most straightforward method that requires the least complicated instrumentation. We will focus on this method because it is possible for all mechanisms.

In order to derive the characteristic velocity, the measured LEIS signal has to be corrected for the energy dependence of the transmission, the detection efficiency, and the cross-section. Substituting the model for the ion fraction in eq. (2.3) then gives:

$$\frac{S_k(E_i)}{T(E_f) \cdot \varepsilon(E_f) \cdot \sigma_k(E_i)} = n_k \cdot e^{-v_c \cdot \frac{1}{v}} \quad (2.9)$$

By taking the natural logarithm, the relation between the characteristic velocity and all the energy dependent factors involved is shown more clearly:

$$\ln[S_k(E_i)] - \{\ln[T(E_f)] + \ln[\varepsilon(E_f)] + \ln[\sigma_k(E_i)]\} = \ln[n_k] - v_c \cdot \frac{1}{v}(E_i) \quad (2.10)$$

From this equation it follows that, in order to correctly derive the characteristic velocity from the energy dependence of the measured LEIS signal, the functions $T(E_f)$, $\varepsilon(E_f)$, and $\sigma_k(E_i)$ have to be known exactly. To demonstrate the implications of an error in any of these energy dependencies we will determine the characteristic velocity with and without a correction for the detection efficiencies. Subsequently, the characteristic velocity is determined from the peak area and peak height using the correction for the transmission from eq. (2.4a) and eq. (2.4b) respectively.

We have derived the characteristic velocity for Ar^+ ions scattered from W as a function of the applied channelplate voltage, with and without a correction for the previously derived detection efficiencies. In figure 2.7 the filled circles show the characteristic velocity without a correction for the detection efficiency. The channelplate voltage directly influences the energy

	$v_c \text{ He}^+$ (10^5 m/s)	$v_c \text{ Ne}^+$ (10^5 m/s)	$v_c \text{ Ar}^+$ (10^5 m/s)
Corrected for detection efficiency	2.52	1.50	1.45
No efficiency correction ($V_{\text{plates}}=3100\text{V}$)	2.72 (+8%)	1.60 (+7%)	1.57 (+8%)
No efficiency correction ($V_{\text{plates}}=2600\text{V}$)	3.86 (+53%)	2.28 (+52%)	2.04 (+41%)

Table 2.1. The characteristic velocity v_c (in 10^5 m/s) for He^+ , Ne^+ and Ar^+ ions scattered from W. The first row shows the v_c after a correction for the detection efficiency. The second and third row show the v_c without the efficiency correction for a channelplate voltage of 3100V and 2600V respectively. The peak area is used as signal intensity and a correction is performed for the transmission and cross-section. The percentages between brackets give the overestimation compared to the corrected values. See also figure 2.7.

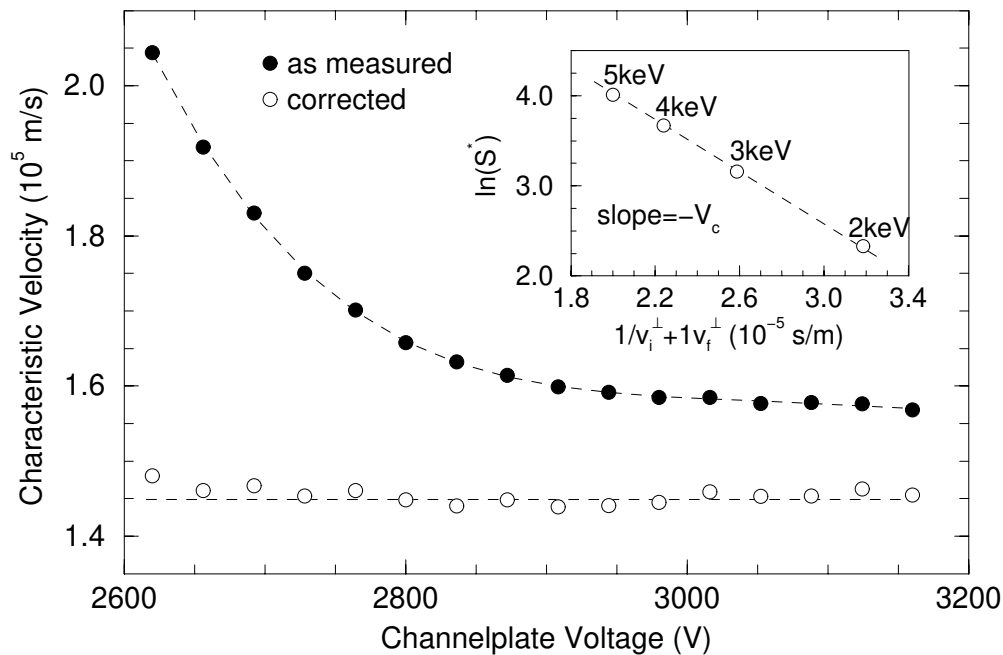


Figure 2.7. The characteristic velocity of Ar^+ ions scattered from W as a function of the channelplate voltage. The peak area is used as signal intensity and a correction is performed for the transmission and cross-section. The interaction time is defined as $1/v_i^\perp + 1/v_f^\perp$, where v_i^\perp and v_f^\perp denote the velocity of the ion before and after the interaction normal to the surface. The inset shows an example of a $\ln(S^*)$ versus $1/v_i^\perp + 1/v_f^\perp$ plot. Here, S^* is the LEIS signal corrected for the transmission and the cross-section. A similar behaviour is observed for He^+ and Ne^+ , and an overview of the overestimation of the characteristic velocities is given in table 2.1.

dependence of the detection efficiency, and therefore influences the energy dependence of the measured signal (see figure 2.5). For low channelplate voltages, the detection efficiency at low initial ion energies is much smaller than the detection efficiency at high initial ion energies. The signal at low initial energies is thus underestimated compared to high initial energies. This leads to a steeper energy dependence of the measured signal, which is interpreted as a neutralisation effect and leads to an overestimation of the characteristic velocity. Because the dependence of the detection efficiency on the impact energy increases with decreasing channelplate voltage, the overestimation of the characteristic velocity also increases with decreasing channelplate voltage.

Figure 2.7 also shows the characteristic velocity after correcting the measured signals at different initial energies with the above derived detection efficiencies (open circles). After the correction the characteristic velocity has become a constant parameter independent of the experimental settings, confirming the validity of the derived efficiency curves and the correction method. Comparing the values for the characteristic velocity before and after the efficiency correction, the overestimation can be as large as 50% for low channelplate voltages, or old channelplates that can not reach saturation anymore. It is important to note that even for channelplates in saturated mode an overestimation of the derived characteristic velocity is observed if no correction is performed for the detection efficiency. Although figure 2.7 only

shows the results for Ar^+ ions, a similar behaviour is observed for Ne^+ and He^+ ions. An overview of the overestimation of the characteristic velocities for the different ions is given in table 2.1.

An error in the energy dependence of the analyser transmission correction also results in an incorrectly derived characteristic velocity. In figure 2.8 the characteristic velocity is determined for Ne^+ ions scattered from the Ba atoms in the outermost layer of a thermionic cathode [10,13,28] using the peak area (filled circles) and peak height (open circles) as signal intensities. The correction for the analyser transmission for the peak height is derived from figure 2.3, with the constants $C_{elas}=1.23 \cdot 10^{-2}$ and $C_{inelas}=1.09 \text{ eV}^{1/2}$. The characteristic velocities determined from the peak area ($v_c=(2.55 \pm 0.03) \cdot 10^5 \text{ m/s}$) and peak height ($v_c=(2.55 \pm 0.04) \cdot 10^5 \text{ m/s}$) are identical when the correct energy dependence for the transmission correction is used. Also shown in figure 2.8 by the dashed lines are the characteristic velocities using the peak height in combination with an analyser correction for pure elastic ($v_c=(2.77 \pm 0.05) \cdot 10^5 \text{ m/s}$) and pure inelastic ($v_c=(2.37 \pm 0.03) \cdot 10^5 \text{ m/s}$) peak broadening, by using $T(E_f)=f(E_f)=1$ and $T(E_f)=f(E_f)=\sqrt{E_f}$ respectively. Clearly the additional step required when the peak height is used can lead to a significant error in the derived characteristic velocity if the elastic and inelastic contributions to the peak broadening are not correctly determined.

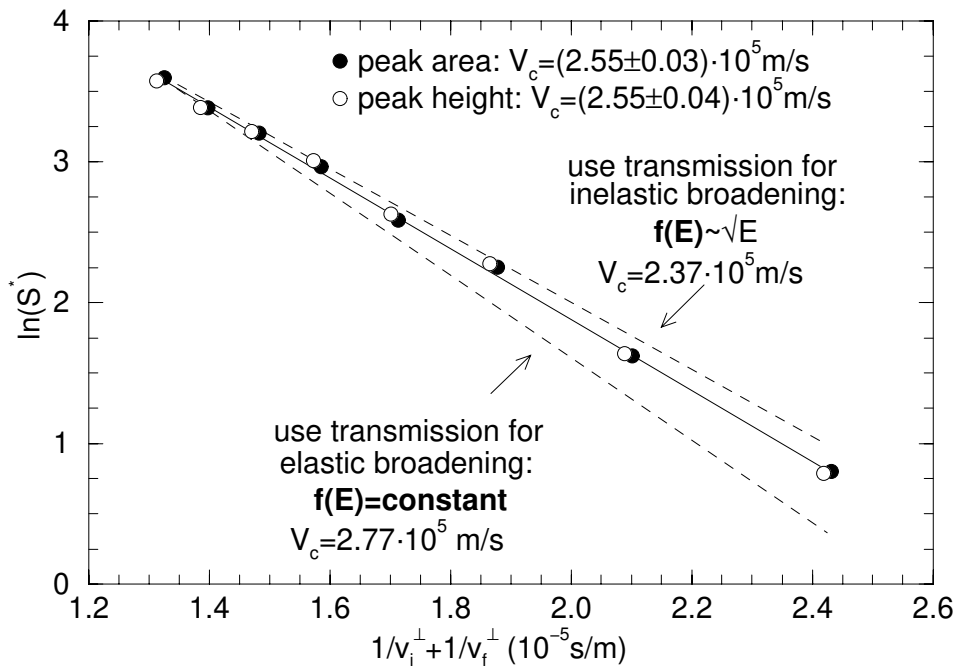


Figure 2.8. The influence of the transmission correction of the investigation of the characteristic velocity. The characteristic velocity is determined for Ne^+ scattered from Ba atoms (as in figure 2.3). Here, S^* is the LEIS signal corrected for the transmission and the cross-section. The velocities v_i and v_f denote the velocities of the ion before and after the interaction, and $1/v_i^\perp + 1/v_f^\perp$ is proportional to the interaction time. The transmission correction for the peak height is performed using C_{elas} and C_{inelas} from figure 2.3. The dashed lines show the fit to the data point where the peak height is used in combination with a transmission correction for purely elastic and inelastic effects.

Errors in the energy dependencies of $T(E_f)$, $\varepsilon(E_f)$, or $\sigma_k(E_i)$ lead to an incorrect characteristic velocity, and the corresponding neutralisation probability. However, in comparative neutralisation studies the introduced error is not always as large as demonstrated in figure 2.7 and figure 2.8. To compare the neutralisation probabilities of a certain ion scattering from species k and l , the ratio of ion fractions can be expressed as:

$$\frac{P_k^+}{P_l^+} = \frac{e^{-v_c^k \frac{1}{v}}}{e^{-v_c^l \frac{1}{v}}} = e^{-(v_c^k - v_c^l) \frac{1}{v}} = e^{-\Delta v_c \frac{1}{v}} \quad (2.11)$$

This shows that the absolute difference in characteristic velocity Δv_c is the essential parameter to characterise the neutralisation difference between species k and l . This result has a positive consequence for neutralisation studies where the same species is investigated in different situations, for example in studies of the influence of the workfunction on the charge exchange of a fixed ion-target combination [50]. If for different workfunctions the characteristic velocity is investigated under identical experimental conditions, the factors $\ln[T(E_f)]$, $\ln[\varepsilon(E_f)]$, and $\ln[\sigma_k(E_i)]$ in eq. (2.10) remain unchanged. When the absolute difference Δv_c is determined, these factors, and any errors therein, are subtracted out of the equation. The ratio of ion fractions is, therefore, unaffected by any error in the energy dependent factors. Note that the conclusion is only valid because the same species is investigated in a different (chemical) environment with the same experimental conditions, and the LEIS peaks are found at the same final energy. This is not the case when the neutralisation behaviour is experimentally compared for different elements, and Δv_c is used to express the neutralisation difference [47]. Since the LEIS peaks are found at different final energies, the factors $T(E_f)$ and $\varepsilon(E_f)$ are not equal. The potential error in Δv_c due to an error in $T(E_f)$ or $\varepsilon(E_f)$ increases with an increasing difference in the final energies of the involved species.

2.7.2 Quantitative surface analysis

Quantitative information about the composition of the outermost atomic layer can not be extracted from a single measurement. Therefore the basis of any quantification is the comparison of LEIS signals. The ratio of signals for scattering from species k and l is given by:

$$\frac{S_k(E_i^k)}{S_l(E_i^l)} = \frac{T(E_f^k) \cdot \varepsilon(E_f^k) \cdot \sigma(E_i^k) \cdot P_k^+(E_i^k) \cdot n_k}{T(E_f^l) \cdot \varepsilon(E_f^l) \cdot \sigma(E_i^l) \cdot P_l^+(E_i^l) \cdot n_l} \quad (2.12)$$

Here, the energies E_i^k , E_f^k and E_i^l , E_f^l are used for species k and l respectively. Using eq. (2.12) as a basis, we will discuss the implications of an error in the instrumental energy dependencies on a quantitative analysis. These implications depend on the required quantification strategy. The discussion below is therefore divided into 4 quantification strategies, starting with the most straightforward method using reference samples, and expanding to situations that require a more elaborate method.

1) A straightforward quantitative analysis can be performed if for the species to be quantified a reference sample with a known surface density is at hand, and no matrix effects are present. In the absence of matrix effects the neutralisation probability, and therefore the ion fraction

P^+ , is the same for scattering from the sample under investigation and from the reference sample. If both samples are measured under identical experimental conditions, T , ε , and σ are identical. Consequently, eq. (2.12) is reduced to $n_k = (S_k/S_{ref}) \cdot n_{ref}$, where S_{ref} is the measured reference signal and n_{ref} is the elemental density of the reference sample. Any possible error in the energy dependencies factors $T(E_f)$, $\varepsilon(E_f)$, and $\sigma(E_i)$ is therefore divided out, and does not affect the quantitative analysis.

2) Quantification with reference samples of the same species in the presence of matrix effects, requires an investigation of the neutralisation probabilities on the sample of interest and on the reference sample. To correct for the matrix effects, the characteristic velocities are determined on both samples and the resulting ion fractions are substituted in eq. (2.12). The ratio of ion fractions from both samples can also be expressed as shown in eq. (2.11), where species k and l represent the sample of interest and the reference sample respectively. This shows that the absolute difference in characteristic velocity Δv_c between the sample of interest and the reference sample is the essential factor for the matrix effects correction. The absolute difference Δv_c is unaffected by any error in $T(E_f)$, $\varepsilon(E_f)$, or $\sigma(E_i)$ when both samples are measured under identical experimental conditions. A quantitative surface analysis using references sample with the same species is, therefore, unaffected by any error in the energy dependencies.

3) An analysis of the composition of a sample containing multiple species in the outermost layer (e.g. binary alloy), can be performed without the use of reference samples. In this case the different species are found at different final energies, where $T(E_f)$ and $\varepsilon(E_f)$ are not identical. From eq. (2.12) it is obvious that an error in these energy dependencies will result in an incorrect quantitative analysis. An additional error can be introduced when correcting for the neutralisation probabilities of the different species. For different species the characteristic velocity difference Δv_c is influenced by an error in the energy dependencies (see previous section on charge exchange studies). Note that this situation is identical to quantification with the use of reference samples that consist of a different species than the sample of interest. We can conclude that if no reference sample of the appropriate species is at hand, a correct quantitative analysis can only be performed if all energy dependencies are known.

4) The dual-isotope surface composition (DISC) method was introduced by Ackermans et al. [51,52] to quantify the surface composition of a sample containing multiple species without the use of reference samples. In principle this method is identical to the previous discussed methods of determining the characteristic velocity by measuring the LEIS signal as a function of the initial ion energy. The special feature of this method is that at every initial energy a measurement using $^4\text{He}^+$ and $^3\text{He}^+$ ions is performed. The signal ratio $S_k(^3\text{He})/S_k(^4\text{He})$ is used to determine the characteristic velocity, instead of the directly measured absolute LEIS signal. From an experimental point of view the advantage is that the ratio $S_k(^3\text{He})/S_k(^4\text{He})$ can be determined by, either using a mixed $^3\text{He}/^4\text{He}$ beam, or by merely changing the noble gas in the ion source. If no mass filter is used, the beam optics do not have to be adjusted. This approach has the advantage that, if the ion beam does not have the same configuration at the different initial energy settings, it only influences the absolute measured LEIS signal but not the ratio $S_k(^3\text{He})/S_k(^4\text{He})$. However, because of the difference in the final energies for $^4\text{He}^+$ and $^3\text{He}^+$ ions, the ratio is influenced by an error in $T(E_f)$, or $\varepsilon(E_f)$. Therefore, a correct quantitative analysis using the DISC method requires the instrumental energy dependencies to be known.

2.8 Conclusions

The energy dependence of the signal intensity in low-energy ion scattering is defined by the combined energy dependencies of the analyser transmission $T(E_i)$, detection efficiency $\varepsilon(E_i)$, scattering cross-section $\sigma_k(E_i)$ and ion fraction $P_k^+(E_i)$. The energy dependencies of the cross-section and ion fraction are determined by the physical parameters involved in the ion-target interaction. However, the energy dependencies of the analyser transmission and detection efficiency are determined by the characteristics of the LEIS set-up, and have to be investigated for the set-up in-situ. In this paper we have reported on the investigations of these instrumental energy dependencies. Although the investigations were focused on our set-up, the discussions can be directly applied to other cylindrical mirror analysers and channelplate- or channeltron-based detectors.

The transmission of the cylindrical mirror analyser is proportional to the pass energy. However, the correction for this transmission depends on whether the peak area or peak height is used as a measure for the signal intensity. For the peak area the transmission correction is straightforward, and proportional to the final energy of the peak. When the peak height is used, the correction depends on the details of the peak broadening effects. Using the peak height therefore requires the investigation of the contributions of elastic and inelastic energy losses to the finite peak width.

The detection efficiency of the scattered ions depends on the kinetic impact energy of the ion and on the applied operation voltage. The energy dependence of the detection efficiency is determined by the dependence of the kinetic electron emission on the impact energy of the ions on the channelplate surface. Because this dependence of the electron yield on the impact energy is approximately the same for He^+ , Ne^+ and Ar^+ ions, the detection efficiency is determined by the impact energy and is independent of the ion mass. The dependence of the detection efficiency on the impact energy can be explained using secondary electron emission theory.

Correct knowledge of the instrumental energy dependencies is important when charge-exchange mechanisms are studied, or when a quantitative surface analysis is performed with LEIS. In charge-exchange studies the dependence of the ion fraction on the kinetic energy can be used to study the charge exchange mechanisms between the ion and target atom(s). To correctly derive the energy dependence of the ion fraction from the measured LEIS signals, the energy dependencies of the analyser transmission, detection efficiency, and scattering cross-section have to be exactly known. Any errors in these energy dependencies will result in an incorrectly derived energy dependence of the ion fraction and the derived neutralisation probability. It should be emphasised that this can lead to an incorrect interpretation of the neutralisation mechanism(s) and can cause difficulties comparing experimental and theoretical studies.

The consequences of an error in the instrumental energy dependencies on a quantitative surface analysis depend on the details of the applied quantification strategy. If reference samples with a known surface density are at hand, consisting of the same species as the sample of interest, the quantification is unaffected by any errors in the instrumental energy dependencies. The quantification of the surface composition of a sample containing multiple species, can be performed without the use of reference samples. However, in this situation, an error in the involved energy dependencies will result in an error in the derived surface composition.

Acknowledgements

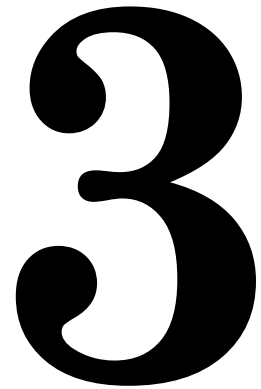
We would like to thank the participants of the Human Capital & Mobility program (CHRX-CT94-0479) on comparison of elemental LEIS sensitivities at different set-ups for the discussions leading to this work [53].

References

- 1 H. Niehus, W. Heiland, E. Taglauer, Surf. Sci. Rep. 17 (1993) 213.
- 2 H.H. Brongersma, P.A.C. Groenen, J.-P. Jacobs, in *Science of Ceramic Interfaces II*, Material Science Monographs 81, Ed. J. Nowotny (Elsevier Science B.V., Amsterdam 1994), p 113.
- 3 T.G. Vargo, J.A. Gardella, R.L. Schmitt, K.J. Hook, T.J. Hook, L. Salvati, *Low-Energy Ion Scattering Spectrometry of Polymer Surface Composition and Structure*, in Surface Characterisation of Advanced Polymers. Ed. L. Sabbatini, P.G. Zambonin, 1993.
- 4 P. Bertrand, Y. De Puydt, Nucl. Instr. and Meth. B78 (1993) 181.
- 5 G. Andersson, H. Morgner, Surf. Sci. 405 (1998) 138.
- 6 P. Delichere, K.E. Bere, M. Abon, Appl. Cat. A172 (1998) 295.
- 7 B.A. Horrell, D.L. Cocke, Catal. Rev.-Sci. Eng. 29 (1987) 447.
- 8 H.H. Brongersma, R.A. van Santen, *Fundamental aspects of heterogeneous catalysis studied by particle beams*, NATO ASI series B 265, (Plenum Press, New York, 1991).
- 9 M.P. de Jong, D.P.L. Simons, M.A. Reijme, L.J van Ijzendoorn, A.W. Denier van der Gon, M.J.A. de Voigt, H.H. Brongersma, R.W. Gymer, Synth. Met., accepted for publication.
- 10 C.R.K. Marrian, A. Shih, G.A. Haas, Appl. Surf. Sci. 24 (1985) 372.
- 11 A.W. Denier van der Gon, M.F.F.K. Jongen, H.H. Brongersma, U. van Slooten, A. Manenschijn, Appl. Surf. Sci. 111 (1997) 64.
- 12 Woodruff DP, Nucl. Instr. and Meth. 1982; **194**: 639.
- 13 R. Cortenraad, A.W. Denier van der Gon, H.H. Brongersma, G. Gaertner, A. Manenschijn, Appl. Surf. Sci. 146 (1999) 69.
- 14 J.L. Wiza, Nucl. Instr. and Meth. 162 (1979) 587.
- 15 W.B. Colson, J. McPherson, F.T. King, Rev. Sci. Instr. 44 (1973) 1694.
- 16 H. Niehus, R. Spitzl, Surf. Interf. Anal. 17 (1991) 287.
- 17 W. Heiland, E. Taglauer: *Inelastic Ion-Surface Collisions*, Eds H.H. Tolk, J.C. Tully (Academic Press, New York, 1977), p. 27.
- 18 W. Heiland, A. Naermann, Nucl. Instr. and Meth. B78 (1993) 20.
- 19 J.-P. Jacobs, S. Reijne, R.J.M. Elfrink, S.N. Mikhailov, H.H. Brongersma, M. Wutting, J. Vac. Sci. Technol. A12 (1994) 2308.
- 20 R.M. Bracewell: *The Fourier Transform and Its Applications*, (McGraw-Hill Book Company, New York, 1965), p.111.
- 21 G. Molière, Z. Naturforsch. 2a (1947) 133.
- 22 D.J. O'Connor, J.P. Biersack, Nucl. Instr. and Meth. B15 (1986) 14.
- 23 W. Heiland, E. Taglauer, Nucl. Instr. and Meth. 132 (1976) 535.
- 24 P. Bertrand, Nucl. Instr. and Meth. 170 (1980) 489.

- 25 B. Fastrup, G. Hermann, K.J. Smith, Phys. Rev. A3 (1971) 1591.
- 26 O.B. Firsov, Sov. Phys. JETP 36 (1959) 1076.
- 27 For the electronic excitations we should actually consider the centre of mass energy. However, since the centre of mass energy is directly related to the initial energy, the energy dependent behaviour is the same.
- 28 R.E. Thomas, J.W. Gibson, G.A. Haas, R.H. Abrams, IEEE Trans. Elec. Dev. 17 (1990) 850.
- 29 M. Kaminsky: *Atomic and Ionic Impact Phenomena on Metal Surfaces* (Springer-Verlag, Berlin, 1965), p.300.
- 30 R.S. Gao, P.S. Gibner, J.H. Newman, K.A. Smith, Rev. Sci. Instrum. 55 (1984) 1756.
- 31 Philips Components, *Electron Multiplier Data Handbook* (Book PC12 1991).
- 32 S.N. Ermolov, R. Cortenraad, V.N. Semenov, A.W. Denier van der Gon, S.I. Bozhko, H.H. Brongersma, V.G. Glebovsky, Vacuum 53 (1999) 83.
- 33 P. Varga, H. Winter: *Particle Induced Electron Emission II*. Editor G. Hoehler (Springer-Verlag, Berlin 1992), p.149.
- 34 T. Ashata, M. Onobu, A. Kondo, R. Shimizu, H.J. Kang, Jpn. J. Appl. Phys. 36 (1997) 7427.
- 35 P.C. Zalm, L.J. Beckers, Philips J. Res. 39 (1984) 61.
- 36 H.D. Hagstrum, Phys. Rev. 96 (1954) 336.
- 37 H.D. Hagstrum: *Inelastic Ion-Surface Collisions*, Editors H.H. Tolk, J.C. Tully (Academic Press, New York, 1977), p. 1.
- 38 M. Aono, R. Souda, Nucl. Instr. and Meth. B27 (1987) 55.
- 39 G. Verbist, J.T. Devreese, H.H. Brongersma, Surf. Sci. 233 (1990) 323.
- 40 D.J. Godfrey, D.P. Woodruff, Surf. Sci. 105 (1981) 438.
- 41 R. Brako, D.M. Newns, Rep. Prog. Phys. 52 (1989) 655.
- 42 M.L. Yu, N.D. Lang, Nucl. Instr. and Meth. B14 (1986) 403.
- 43 E.C. Goldberg, R. Monreal, F. Flores, H.H. Brongersma, P. Bauer, Surf. Sci. 440 (1999) L875.
- 44 W. Bloss, D. Hone, Surf. Sci. 72 (1978) 277.
- 45 R.J. MacDonald, P.J. Matin, Surf. Sci. 111 (1981) L739
- 46 L.C.A. van den Oetelaar, S.N. Mikhailov, H.H. Brongersma, Nucl. Instr. Meth. B85 (1994) 420
- 47 S.N. Mikhailov, R.H.M. Elfrink, J.-P. Jacobs, L.C.A. van den Oetelaar, P.J. Scanlon, H.H. Brongersma, Nucl. Instr. and Meth. B93 (1994) 149.
- 48 P. Bertrand, F. Delannay, C. Bulens, J.-M. Streydio, Surf. Sci. 68 (1977) 108
- 49 R.J. MacDonald, D.J. O'Connor, Surf. Sci. 124 (1983) 423
- 50 M. Beckschulte, E. Taglauer, Nucl. Instr. and Meth. B78 (1993) 29.
- 51 P.A.J. Ackermans, *Surface Analysis by Low-Energy Ion Scattering*, Ph.D. thesis, Eindhoven University of Technology, The Netherlands (September 1990).
- 52 P.A.J. Ackermans, M.A.P. Creuwels, H.H. Brongersma, P.J. Scanlon, Surf. Sci. 227 (1990) 361.
- 53 H.H. Brongersma et al., Nucl. Instr. and Meth in Phys. Res. B142 (1998) 377.

Growth, Characterisation, and Surface Cleaning Procedures of High-Purity W Single Crystals



Abstract

High-purity W single crystals have been prepared by the electron-beam floating zone melting technique. The structural quality of these crystals was subsequently improved by application of a strain-annealing technique. X-ray diffraction methods revealed the near-perfect crystallographic structure, and confirmed the absence of first- and second-order subgrains. The observation of the anomalous transmission of X-rays through the thick crystals, also referred to as the Borrmann effect, further substantiated the structural perfection of the crystals.

Well-ordered clean W surfaces free from all contaminants, were obtained by a two-step heating procedure. First, the crystals were heated to 1500 K in an oxygen atmosphere for removal of the carbon impurities. Subsequent flashing to high temperatures (approximately 2500 K) removed the excess oxygen remaining on the surface from the carbon-removal procedure. Low-energy ion scattering and Auger electron spectroscopy confirmed that the cleaning procedures removed all impurities and that the crystal faces exposed only tungsten in the outermost atomic layers. Low-energy electron diffraction patterns showed unreconstructed (1x1) surfaces for the main crystallographic orientations.

3.1 Introduction

Single crystals with a high degree of structural perfection play an important role in surface science. The area of interest for these crystals is twofold: fundamental and applied. From a fundamental point of view, a surface is a rather special kind of defect in the solid state. The bond breaking that takes place when a surface is formed can lead to structural changes, as well as the introduction of localised electronic and vibrational states. Insight in these phenomena is not only of academic interest, but is also relevant for the semiconductor industry, where there is a growing interest in low-dimensional structures. A highly ordered crystallographic surface represents the simplest case of such a low-dimensional structure. Many techniques used for investigations of the various surface properties rely on the periodicity of the surface, and therefore detailed and accurate studies require high-purity crystals with a high degree of structural perfection.

The second area of interest for well-ordered single crystals lies in the modelling of industrial systems. Since the introduction and development of ultra-high-vacuum techniques in the 1960s, there has been a virtual explosion in the level of research on solid surfaces. Since those early days the investigative potential of surface science has matured, and has grown from being able to investigate only relatively simple flat and well-ordered systems, to complex and real industrial systems. However, the complexity of some industrial systems is too large for a one-step analysis of the real system, and the use of a model system is required. Industrial systems like e.g. heterogeneous catalysts [1] or thermionic dispenser cathodes [2,3] have very rough and dynamic surfaces containing multiple species. In these cases, model systems based on flat and well-ordered single crystalline substrates enable more systematic investigations. Thus, although the surface science potential enables the investigation of real industrial systems, well-ordered single crystals are still required for a thorough investigation and understanding of industrial systems.

The present work deals with the growing and characterisation of high-purity W single crystals. The growing techniques used to prepare near-perfect W single crystals are discussed in section 3.2. The degree of structural perfection of these crystals has until now only been achieved for a few single crystals such as silicon and germanium, but not yet for pure metals like tungsten. Subsequently, we present the results of the investigations of the structure of these crystals by means of optical microscopy and X-ray diffraction methods (section 3.3). Following the crystals characterisation, we will discuss the UHV cleaning procedures required to obtain well-ordered surfaces free of all contaminants (section 3.4).

3.2 Growth of W single crystals

In order to prepare W crystals with a high degree of structural perfection, first high-purity W crystals were grown from the melt by electron-beam floating zone melting (EBFZM). Here, we will not discuss the principles of the EBFZM technique, but rather refer to a detailed description by Glebovsky et al. [4,5]. Using the EBFZM technique, single crystals with the three main growing axes [001], [110], and [111] were prepared. The crystallographic orientations of the seed crystals and of the growing axes were determined within an accuracy of 1° by means of Laue X-ray patterns. The EBFZM method is characterised by the presence of high axial temperature gradients of the order of $1000 \text{ K}\cdot\text{cm}^{-1}$ in both the solid phase and the melt [5]. An experimental temperature distribution along the growing axis is shown in figure 3.1, where the position of the melt is indicated. These temperature gradients result in high thermal stresses and are responsible for the substructures and high dislocation densities in the crystals grown by the EBFZM technique, which are further referred to as as-grown crystals.

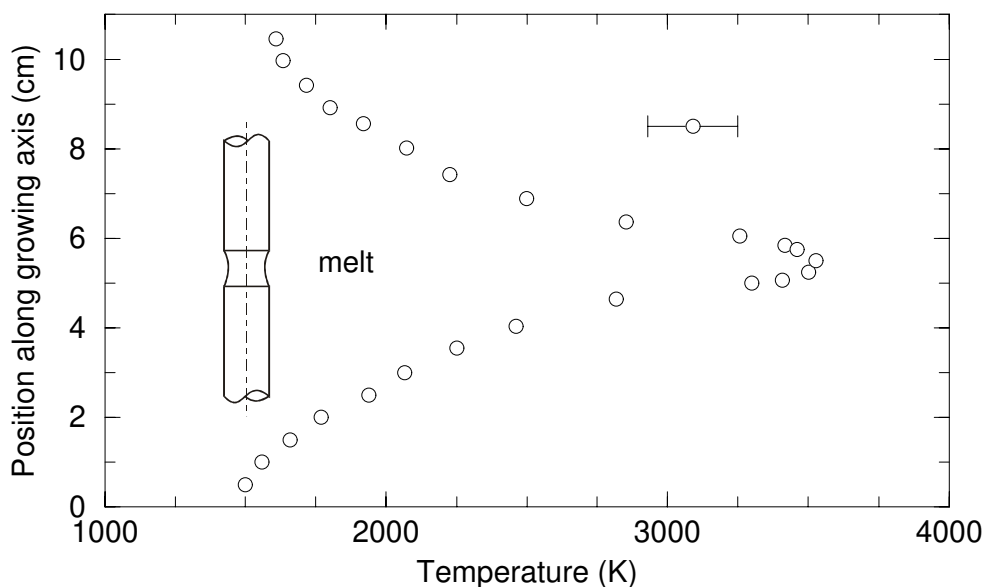


Figure 3.1. Example of the temperature gradient across the crystal during the growth using the EBFZM technique. A gradient of the order of $1000 \text{ K}\cdot\text{cm}^{-1}$ is present near the melt. The dashed line shows the growing axis.

Perfection of the structural quality of the as-grown crystals, and a decrease of the dislocation density was achieved by applying a strain-annealing technique to the as-grown crystals. The crystals grown by the EBFZM method that served as a basis for the strain-annealing technique were first cut to a rectangular size of $15 \times 15 \times 70 \text{ mm}^3$. The thus obtained rectangular W crystals were subsequently cold rolled to realise a 7% size reduction of the crystal. The cold-rolling resulted in total deformation of the crystal structure. Next, the crystals were annealed at a temperature just below the melting point in high vacuum, with temperature gradients no more than several $100 \text{ K}\cdot\text{cm}^{-1}$. To ensure a small temperature gradient, a specially designed furnace based on a defocused e-beam gun was constructed. Here, the specimen served as an anode with a potential of a few kV applied between the tungsten cathode coil and the specimen. During the annealing, the small-angle boundaries and dislocations were collected at the grain boundaries, where the deformation stresses served as a driving force. After annealing, poly-crystals containing large grains were obtained, with the dimensions of the separate grains exceeding 10 mm. Each individual grain had a near-perfect crystal structure free from small-angle boundaries.

From the base crystals prepared by the EBFZM technique, as well as from the base crystals prepared by the strain-annealing technique, W substrates with various crystallographic orientation were cut by spark erosion. The orientations of the desired crystallographic planes were determined within an accuracy of 1° by means of Laue X-ray patterns. After cutting, the obtained W crystals were first polished mechanically to a mirror finish with diamond paste ($1 \mu\text{m}$) and alumina micropolish ($0.05 \mu\text{m}$). A special holder was used for the mechanical polishing, where the orientations of the crystals could be verified by X-ray diffraction methods. The achievable accuracy of the crystallographic orientation depends on the structural perfection of the crystal, as will be explained in section 3.3, and is of the order of 1° for the as-grown (AG) crystals, and better than 0.1° for the strain-annealed (SA) crystals. Following

the mechanical polishing, all crystals were electrochemically polished in an aqueous 2% NaOH solution. The electrochemical polishing removed the damaged surface layer of about 300 μm in depth that remained from the spark erosion and the mechanical polishing. Finally, the crystals were annealed in UHV at a temperature of approximately 2800K by electron bombardment.

3.3 Crystal characterisation

Here we present the result of the investigations of the crystallographic structures of the AG and SA single crystals by means of optical microscopy and X-ray diffraction methods. Since many excellent reviews on X-ray diffraction techniques are available, we will not discuss the details of the applied techniques [6,7]. To demonstrate the difference in the degree of structural perfection between the as-grown crystals and the strain-annealed crystals, the characterisation has been performed for both types of crystals. The substructures of the AG crystals, originating from the high thermal stresses, were revealed by electrolytic etching in a 25% aqueous solution of NH_4OH . The etching exposes the small-angle boundaries that separate the different subgrains. Figure 3.2 shows the subgrain structure of an W(100) AG crystal studied by optical microscopy, where the small-angle boundaries appear as lines. The mean subgrain size is of the order of 500 μm , with the grains slightly elongated in the direction of the growing axes. The etching technique also revealed the dislocations and point defects, which appear as dots in figure 3.2. The dislocation density of the AG crystals can be

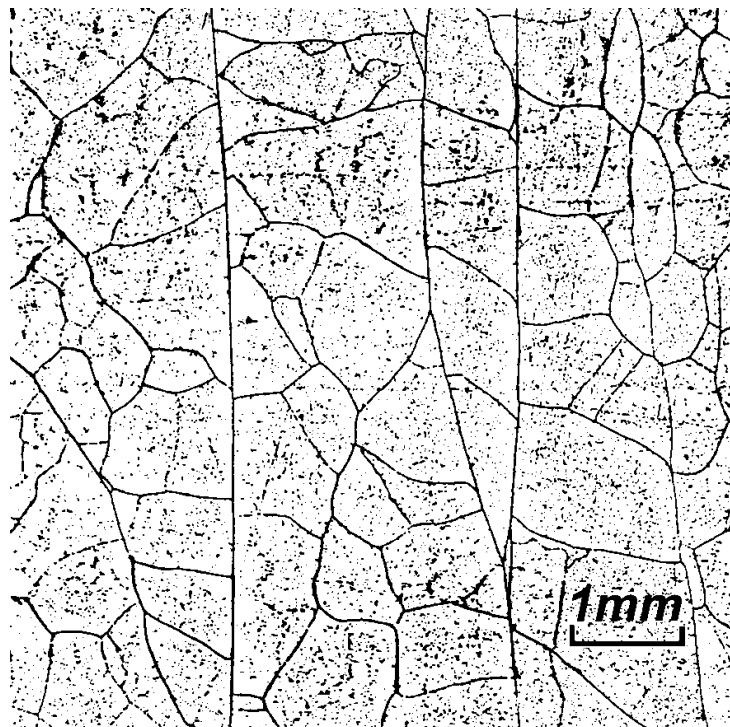


Figure 3.2. The substructures of an AG crystal studied by optical microscopy. Electrolytic etching exposes the small-angle boundaries that separate the different subgrains as lines. The etching technique also reveals the dislocations and point defects, which appear as dots.

derived by this method, and is found to be typically 10^5 - 10^7 cm^{-2} . The exact dislocation density depends on the growing parameters, as has been shown by Glebovsky et al. [5]. Investigation of the substructures of SA crystals is not possible by this etching technique due to the absence of the small-angle boundaries. Therefore, X-ray diffraction techniques were used for a direct comparison of the crystallographic structures of the AG crystals and the SA crystals.

Quantitative information about the misorientation angles of the different subgrains was obtained by the so-called rocking curve technique [7], which is an X-ray diffraction technique based on the principle of Bragg reflection [8]. To measure rocking curves, the angle between the X-ray source and the detector is fixed under the first order Bragg diffraction angle. The crystal is then rotated with respect to the incoming X-ray beam, and the intensity of the diffracted beam is measured as a function of the angle. In figures 3.3a and 3.3b rocking curves are shown for a W(110) AG crystal and a W(110) SA crystal respectively. Note that the AG rocking curve has a scale in angular degrees, while the SA rocking curves have a scale in angular seconds. The rocking curve of the AG crystal clearly shows different subgrains with different orientations as separate peaks, indicated by the arrows in figure 3.3a. The misorientation angle between the different subgrains can be derived from the rocking curve and is of the order of 1° . The degree of structural perfection of the SA crystal compared to the AG crystal becomes apparent by comparing the rocking curves in figures 3.3a and 3.3b. No subgrain structure is visible in the rocking curve for the crystal prepared by the strain-annealing technique. The absence of texture effects, like e.g. preferential growing directions, was verified by measuring rocking curves at three different azimuthal orientations of the crystal, which were separated by 45° . The rocking curves of the crystals are used to determine the exact crystallographic orientation during the mechanical polishing (see section 3.2). The accuracy of the crystallographic orientation is therefore directly related to the width of the rocking curve, and is of the order of 1° and $100''$ for the AG and SA crystals respectively.

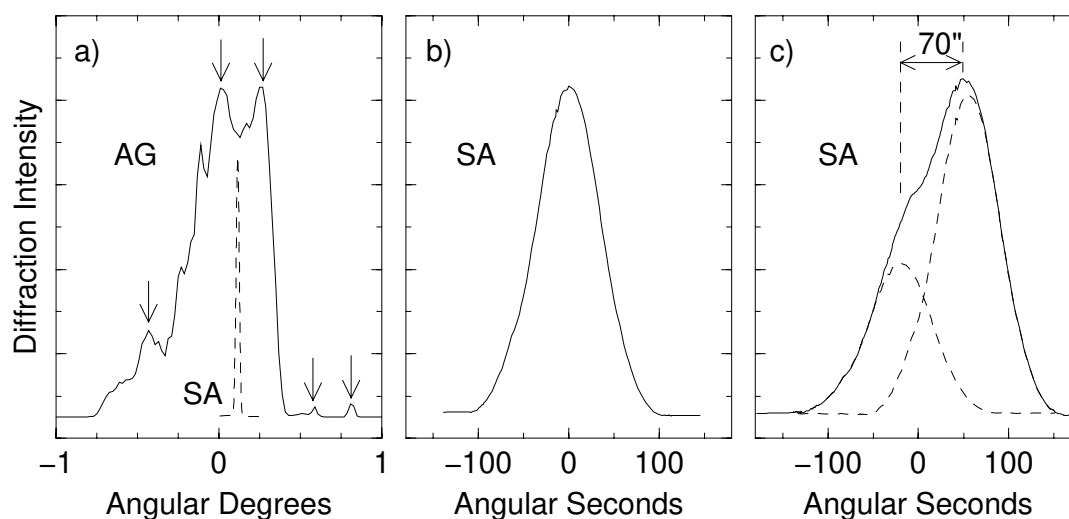


Figure 3.3. Rocking curves of W(110) crystals: (a) as-grown crystal, (b) strain-annealed crystal, (c) strain-annealed crystal with small-angle boundary. Figure 3.3a also shows the rocking curve of the SA crystal taken from figure 3.3b for comparison (dashed curve). The arrows in figure 3a indicate different subgrains. The rocking curve in figure 3c was measured across the small-angle boundary shown in figure 3.4b.

Further comparison of the substructures of the AG crystals and the SA crystals was performed by an additional X-ray diffraction technique: Angular scanning X-ray topography [9]. This method consists of mapping the diffracted X-ray intensity across the crystal under a fixed Bragg geometry. Figures 3.4a and 3.4b show X-ray topography images of a W(110) AG crystal and a W(110) SA crystal respectively. Figure 3.4a clearly shows the different subgrains and small-angle boundaries of the AG crystal as different grey-scales. The topography image of the SA crystals shows no such substructure, and confirms the absence of first- and second-order subgrains. For demonstration purposes we have chosen to show a SA crystal with a small-angle boundary, shown in the top left corner of the crystal (figure 3.4b). The rocking curve measured at this boundary is shown in figure 3.3c. Fitting this curve with two separate rocking curves using a width taken from the SA crystal in figure 3.3b, we learn that the misorientation angle between the two grains is approximately 70 angular seconds.

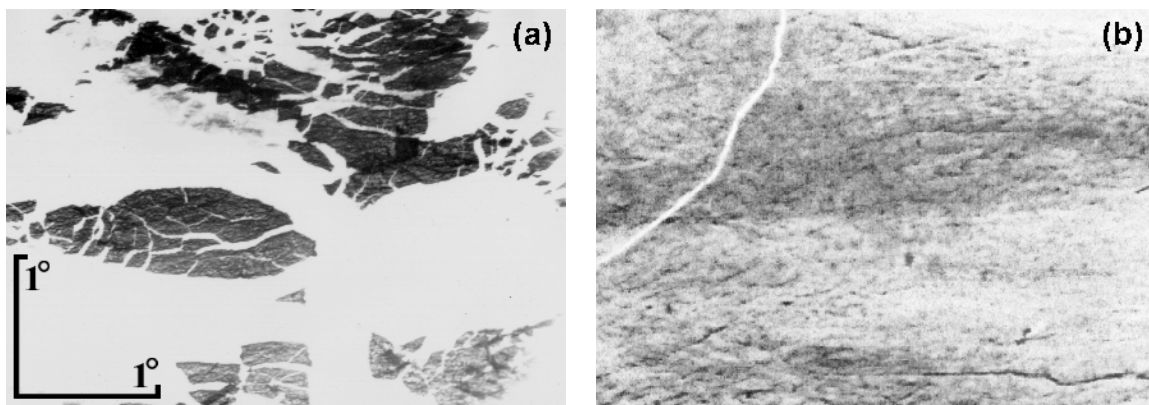


Figure 3.4. Angular scanning X-ray topography images: (a) as-grown crystal, (b) strain-annealed crystal with small-angle boundary in top left corner. Both pictures shown an area of the order of 10 mm^2 . For the AG crystal the different subgrains are shown as different grey-scales. The angular scale indicated in the bottom left of figure 3.4a serves only as a measure for the misorientation angle between the different subgrains.

The structural perfection of the SA crystals enabled the observation of the anomalous transmission of X-rays through the prepared crystals, a phenomenon first observed by Borrmann [7,9]. This so-called Borrmann effect comprises that X-rays can be transmitted through thick crystals in cases where the kinetic X-ray absorption theory does not permit transmission. The transmission is based on the principle of standing Bloch waves in the periodic crystal. For the Borrmann effect to take place, a highly perfect crystal structure is required because otherwise these Bloch waves are adsorbed. Here, we merely state that the Borrmann effect is observed, all the details and results of the X-ray transmission investigations are reported elsewhere [10]. For the standing Bloch waves the average distance between dislocations has to exceed the X-ray extinction length L . For $\text{CuK}\alpha$ radiation the extinction length can be estimated for an ideal dislocation free tungsten crystal as $L=1.7 \text{ }\mu\text{m}$. Consequently, the critical dislocation density for the Borrmann effects is given by $N=1/L^2=3.5 \cdot 10^7 \text{ cm}^{-2}$. The dislocation density derived from the etching technique, as shown in figure 3.2, is estimated as $N=2 \cdot 10^5 \text{ cm}^{-2}$, which is well below the predicted critical value as might be expected since the Borrmann effect is observed. Note that the necessary degree of structural perfection for the Borrmann effect to occur has until now been achieved only for a

few single crystals such as silicon, germanium, and high temperature superconductors. To our knowledge, it is the first time that the Borrmann effect has been observed for pure metals.

3.4 Cleaning and characterisation of the crystal surface

Before these high-purity W single crystals can be used as substrates in studies of surface phenomena, the surfaces need to be well-ordered and free from contaminants. Surface cleaning and characterisation has been performed in the UHV set-up MiniMobis which has a base pressure of $1 \cdot 10^{-10}$ mbar and has been described in detail elsewhere [11,12] (see also chapter 2). The cleaning procedures were monitored with various surface sensitive techniques. Low-energy ion scattering (LEIS) was used for the compositional analysis of the outermost atomic layer [13]. The LEIS investigations were performed using He^+ ions with an initial energy of 5 keV. In addition to LEIS, Auger electron spectroscopy (AES) was used to analyse the surface contaminants, where the information depth is a few monolayers. Structural information about the surface and possible superstructures was obtained by low energy electron diffraction (LEED). For a detailed description of these techniques, see e.g. reference [14]. In the discussion that follows we will demonstrate the surface cleaning procedures taking a strain-annealed W(110) crystal as an example. The results of the LEIS, AES, and LEED investigations at the different required cleaning stages are shown in figures 3.5, 3.6 and 3.7 respectively.

Prior to the cleaning procedures the ion scattering showed almost no tungsten in the outermost atomic layer, indicating that the W surface is to a large extent covered by contaminants (figure 3.5a and 3.5b, bottom curve). Auger analysis showed that only carbon and oxygen contaminant were present (figure 3.6, bottom curve). A significant decrease in the carbon and oxygen contaminants was achieved by sputter cleaning the surface by 3 keV Ar^+ ion bombardment at room temperature. Although the LEIS spectrum after sputtering showed a

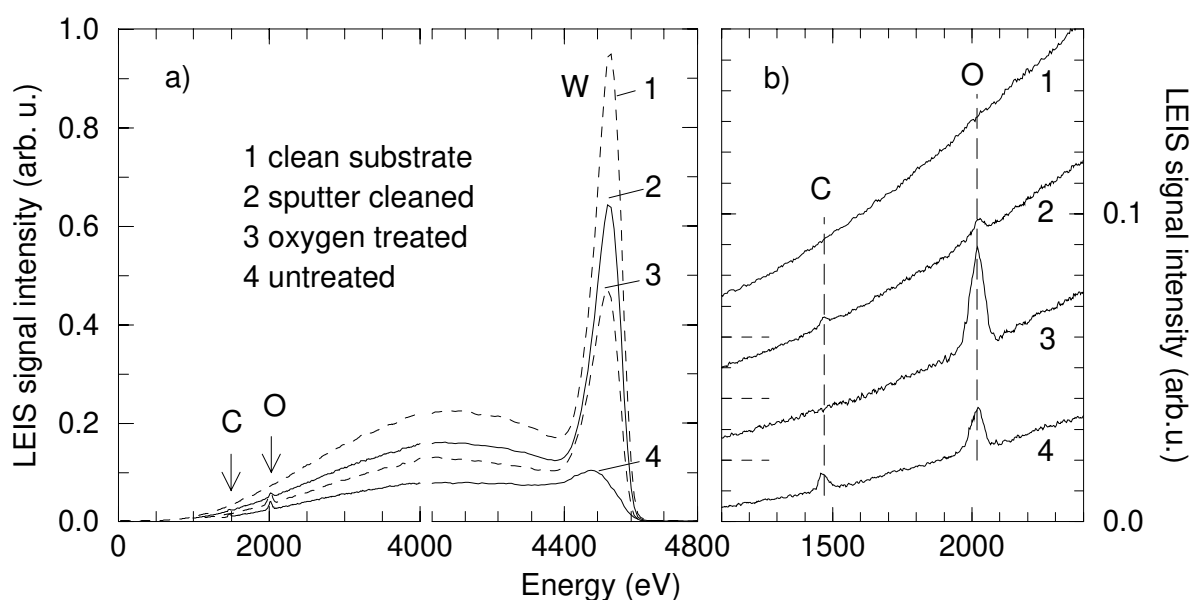


Figure 3.5. LEIS 5 keV He^+ spectra obtained after different cleaning stages of the W(110) crystal: (a) complete energy range, (b) energy range covering only the C and O peaks. The baselines of the spectra in figure 3.5b are indicated by the dashed lines. The AES spectra of the corresponding stages are shown in figure 3.6.

clear W peak, the impurities could not be removed completely. A further disadvantage of sputter cleaning of the surface is that only the impurities in the outermost layer(s) are removed. Any annealing of the substrate to restore the sputtering induced surface disorder resulted in segregation of the carbon impurities from the surface region to the outermost layer. The most effective method to remove the carbon contamination from the outermost layer, and simultaneously deplete the surface region of carbon impurities, is to heat the W crystal in an oxygen atmosphere [15,16]. The carbon depletion was performed in a pre-treatment chamber by heating the crystal by means of electron bombardment at a temperature of approximately 1500 K in 10^{-5} mbar oxygen for several hours. The oxygen reacts with the carbon present on the surface and forms CO-species, which evaporate at this temperature. Removal of the carbon from the outermost layer results in further carbon segregation to the surface, which is subsequently removed by evaporation.

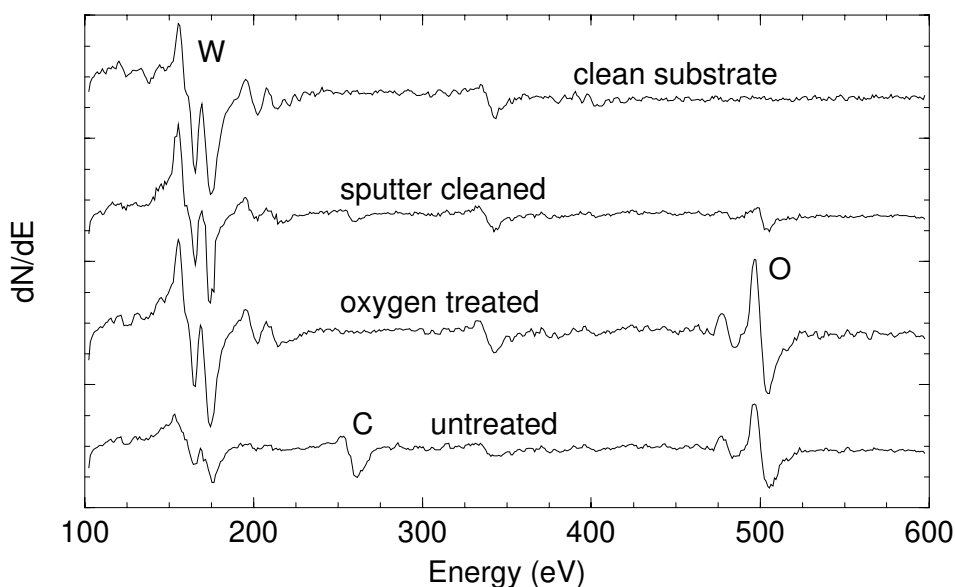


Figure 3.6. The AES spectra at the different cleaning stages of the W(110) crystal. The LEIS spectra of the corresponding stages are shown in figure 3.5.

After the carbon depletion treatment the crystal was flashed in UHV to temperatures in excess of 2500 K to remove the oxygen from the surface [15,16]. Flashing of the crystals was performed in a specially constructed compact e-beam gun, where Philips thermionic dispenser cathodes were used as electron sources [2]. These cathodes have small emitting surfaces with a diameter of 1 mm, but are capable of electron emission densities of more than $100 \text{ A}\cdot\text{cm}^{-2}$ [3]. Compared to the more commonly used e-beam guns based on a W-Re wire, this construction has a low power consumption and minimises heating and degassing of surrounding materials. The carbon and oxygen impurities remaining after the pre-treatment were removed by repetitive cleaning cycles. Each cycle consisted of heating the crystal at 1500 K in $5\cdot 10^{-8}$ mbar O_2 for 30 minutes, followed by flashing to approximately 2500 K in UHV. In the initial cycles, the high temperature flashing resulted in carbon segregation from the remaining bulk impurities. This segregation of the remaining carbon was seen to be a little stronger for the SA crystals compared to the AG crystals due to the difference in growing and

vacuum conditions during the application of the EBFZM and strain-annealing techniques. The carbon that segregated to the surface during the flashing in the initial cycles formed a superstructure on the W(110) substrate (see figure 3.7b) [17,18].

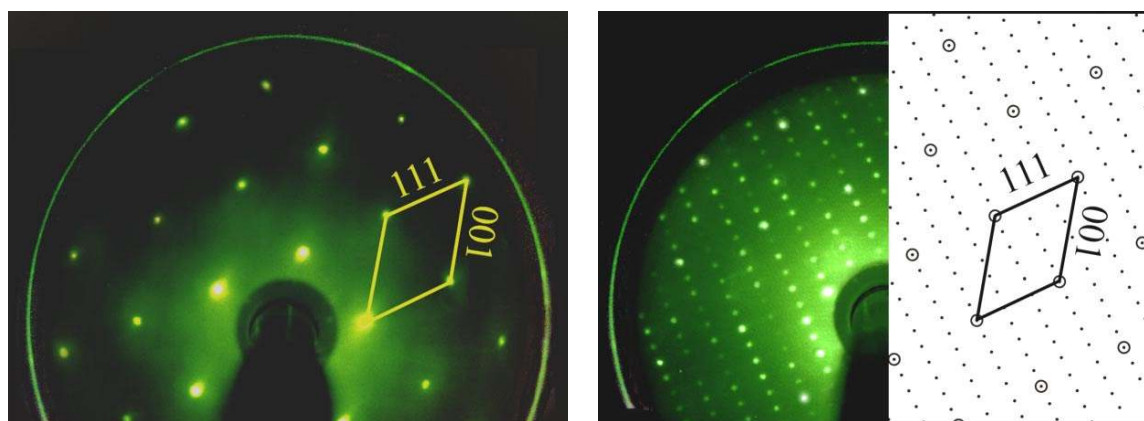


Figure 3.7. LEED patterns of the W(110) crystal at an energy of 300 eV: a) clean unreconstructed W(110), b) carbon $\begin{pmatrix} 0 & 5 \\ 3 & -2 \end{pmatrix}$ superstructure after flashing in the initial cleaning cycles.

After continued cycling the surface region was completely depleted from carbon, and only oxygen was present on the W surface after the oxygen treatment. No more carbon segregated to the surface when the excess oxygen was removed by flashing. Repeated flashing resulted in an oxygen contamination of less than 1% of a monolayer, where one monolayer is defined as the number of W atoms in the outermost layer of the crystal (figure 3.6, top curve). As a reference for the oxygen quantification for both LEIS and AES, the crystal was exposed to an oxygen atmosphere at room temperature. Saturation of the crystal with oxygen results in a (1x1) oxygen superstructure with the corresponding oxygen coverage of 1 monolayer [15,16]. The amount of carbon still present on the surface is below our detection limit and is estimated to be less than 1% of a monolayer, derived from the relative Auger sensitivity of carbon compared to oxygen [19]. Both LEIS and AES can not be used to investigate the presence of hydrogen on the W surface. However, hydrogen desorbs at temperatures of the order of 500-600 K, and is therefore expected to be removed by the high temperature flashing [20]. After cooling down, hydrogen can be adsorbed again because it is the main component of the residual gas in the UHV chamber. From the decrease of the LEIS W signal, it is estimated that the hydrogen adsorption rate is of the order of a few percent of a monolayer per hour. After the cleaning procedures the ion scattering showed only a distinct surface peak at the energy expected for tungsten, confirming that the outermost layer exposed only W atoms (figures 3.5a and 3.5b, top curve). LEED investigations of the clean crystal showed a well-ordered, unreconstructed W(110) surface (figure 3.7a).

The cleaning procedures of high-purity W single crystals have been demonstrated above using a SA W(110) crystal, but other crystallographic orientations showed analogue results. The Auger intensities of the clean W substrates were independent of the crystallographic orientation. However, the ion scattering signal is sensitive to the density of the outermost atomic layer, which differs for the different crystal faces. A demonstration of this sensitivity is given in figure 3.8, where the ion scattering signal is shown across a W bi-crystal. This bi-crystal was prepared by the strain-annealing technique and contains two large grains of

different crystallographic orientations: the (110) and (211) crystal face. The figure shows the intensity of the W signal for a linescan across the grain-boundary of the bi-crystal. It is clearly observed that the more dense packed (110) face results in a higher signal intensity than the less dense packed (211) face. These measurements were performed in a separate setup using a LEIS beam with Gaussian beam profile and a FWHM of only 30 μm [21,22]. The LEIS profile in the grain boundary therefore is a convolution of this beam profile with the actual grain boundary. From figure 3.8 the sensitivity of LEIS to the atomic density of the outermost layer is apparent, as will be discussed in more detail in future work [23] (see chapter 4).

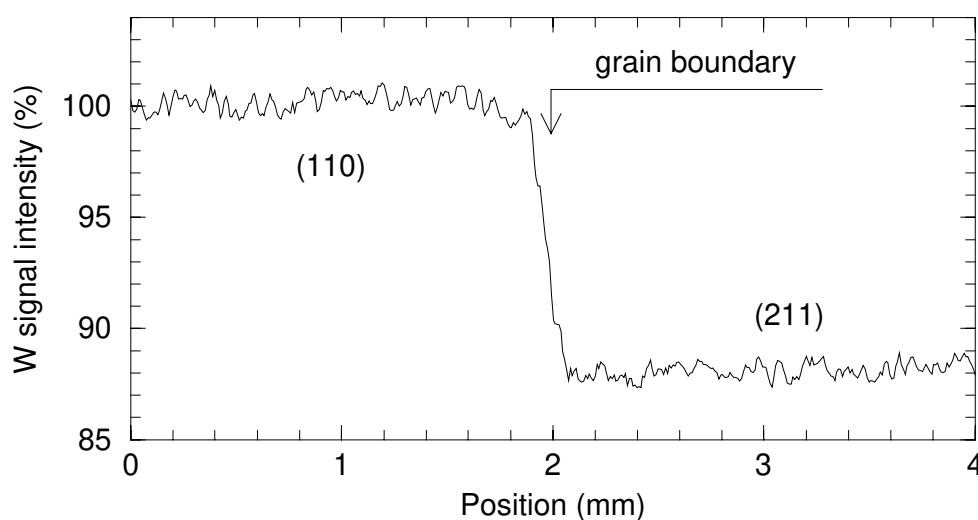


Figure 3.8. LEIS signal intensity across a bi-crystal exposing (110) and (211) faces. The signal is normalised to the closest packed (110) face. The experiment was performed in a separate LEIS set-up equipped with a micro-beam, where the diameter of the incident 3 keV Ne^+ beam was 30 μm for the full width at half maximum. This set-up had a similar scattering geometry: normal incidence and 145° scattering angle.

3.5 Conclusions

In this work the growth, characterisation, and cleaning procedures of high-purity W single crystals were studied. High-purity W crystals were grown by the electron-beam floating zone melting technique. The structural quality of these as-grown crystals was improved by application of a strain-annealing technique. Using different X-ray diffraction methods, the perfection of the crystallographic structure by the strain-annealing procedure has been demonstrated. Rocking curve measurements showed that the small-angle boundaries, present in the as-grown crystals due to the high thermal stresses, were absent in the strain-annealed crystals. Furthermore, angular scanning X-ray topography confirmed the absence of first- and second-order subgrains in these near-perfect crystals. The observation of the anomalous transmission of X-rays through the thick crystals (Borrmann effect) further substantiated the structural perfection of the crystals.

In order to obtain well-ordered surfaces free from all contaminants we applied a two-step cleaning procedure, where the crystals were first heated to 1500 K in an oxygen atmosphere for removal of the carbon impurities. The excess oxygen was subsequently removed by flashing to high temperatures of approximately 2500 K. Low-energy ion scattering and Auger electron

spectroscopy confirmed that the cleaning procedures removed all impurities, and that the crystal faces exposed only tungsten in the outermost atomic layers. Low-energy electron diffraction patterns showed unreconstructed (1x1) surfaces for the main crystallographic orientations.

We therefore conclude that the thus prepared near-perfect W crystals have well-ordered surfaces free from all contaminants, and can be used in fundamental investigations of surface phenomena, or can serve as substrates to model complicated industrial systems.

Acknowledgements

We are very grateful to prof.dr. Vadim Glebovsky and dr. Sergey Ermolov for the preparation of the W crystals and all the further support of this work. In addition we would like to thank Wim Jansen for helping with the micro-beam measurements of the bi-crystal.

References

- 1 J.A. Moulijn, P.W.N.M. van Leeuwen, R.A. van Santen (Eds), "Catalysis, an integrated approach to homogeneous, heterogeneous and industrial catalysis", Elsevier, Amsterdam, 1993.
- 2 R.E. Thomas, J.W. Gibson, G.A. Haas, IEEE Trans. Elec. Dev. 37 (1990) 850.
- 3 G. Gaertner, P. Geittner, H. Lydtin, A. Ritz, Appl. Surf. Sci. 111 (1997) 11.
- 4 V.G. Glebovsky, V.N. Semenov, V.V. Lomeyko, J. Less-Common Metals 117 (1986) 385.
- 5 V.G. Glebovsky, V.N. Semenov, V.V. Lomeyko, J. Crystal Growth 87 (1988) 142.
- 6 J.M. Cowley, "Diffraction Physics", Elsevier, Amsterdam, 1995.
- 7 Z.G. Pinsker, "Dynamical Scattering of X-rays in Crystals", Springer Series in Solid-State Sciences 3, Springer-Verlag, New York, 1978.
- 8 C. Kittel, Introduction to Solid State Physics, 6th edition, John Wiley & Sons, 1986.
- 9 L.H. Schwartz, J.B. Cohen, "Diffraction from Materials", Material Science Series, Academic Press, New York, 1977.
- 10 I.K. Bdikin, S.I. Bozhko, V.N. Semenov, I.A. Smirnova, V.G. Glebovsky, S.N. Ermolov, V.S. Shekhtman, Pisma v. ZhTF 23 (1999) 16 (in russian).
- 11 R. Cortenraad, A.W. Denier van der Gon, H.H. Brongersma, G. Gaertner, A. Manenschijn, Appl. Surf. Sci. 146 (1999) 69.
- 12 R. Cortenraad, A.W. Denier van der Gon, H.H. Brongersma, Surf. Interface Anal. 29 (2000) 524.
- 13 H. Niehus, W. Heiland, E. Taglauer, Surf. Sci. Rep. 17 (1993) 213.
- 14 D.P. Woodruff, T.A. Delchar, "Modern Techniques of Surface Science", E.A. Davis (eds), Cambridge University Press, Cambridge, 1994.
- 15 A. Elbe, G. Meister, A. Goldmann, Surf. Sci. 371 (1997) 438.
- 16 K.E. Johnson, R.J. Wilson, S. Chiang, Phys. Rev. Lett. 71 (1993) 1055.
- 17 R.M. Stern, Appl. Phys. Lett. 5 (1964) 218.
- 18 W.H. Weinberg, R.P. Merrill, Phys. Rev. Lett. 25 (1970) 1198.
- 19 L.E. Davis, N.C. MacDonald, P.W. Palmberg (eds), "Handbook of Auger Electron Spectroscopy", Physical Electronics Industries, 1978.

-
- 20 M. Balden, S. Lehwald, H. Ibach, *Phys. Rev. B* 53 (1996) 7479.
 - 21 A.W. Denier van der Gon, M.A. Reijme, R.F. Rumphorst, A.J.H. Maas, H.H. Brongersma, *Rev. Sci. Instrum.* 70 (1999) 3910.
 - 22 A.W. Denier van de Gon, R. Cortenraad, W.P.A. Jansen, M.A. Reijme, H.H. Brongersma, *Nucl. Instr. and Meth.* 161-163 (2000) 56.
 - 23 R. Cortenraad, S.N. Ermolov, B. Moest, A.W. Denier van der Gon, V.G. Glebovsky H.H. Brongersma, accepted for publication in *Nucl. Instr. Meth. B*.

Crystal-Face Dependence of Low-Energy Ion Scattering Signals



Abstract

Low-energy ion scattering on tungsten single crystals with different crystallographic orientations was performed to analyse the contributions of the different atomic planes to the ion scattering signal. It was found that only for the closest packed crystal face the ion scattering signal originates completely from the outermost atomic plane, while for more open surface structures the deeper planes contribute significantly to the signal. For example, for the W(111) face only 50% of the ion scattering signal is due to ions scattering from the outermost atomic plane.

The influence of ion bombardment on the signal intensity of well-ordered crystalline surfaces was also studied, and it was found that ion bombardment of close-packed high-melting materials (e.g. W) at room temperature leads to a signal decrease of approximately 30% due to the sputter induced roughness and disorder. The mobility of low-melting materials (e.g. Ag) during ion bombardment at room temperature results in a smaller sputter induced roughness and disorder, and a small change in the ion scattering signal (5-10%). Surface cleaning by ion bombardment is a widely applied method, but thus requires a correction for the signal loss due to roughness and disorder when a quantitative analysis is performed.

4.1 Introduction

Low-energy ion scattering (LEIS) is a surface analysis tool which probes the outermost atomic layer of surfaces [1,2,3,4]. This extreme surface sensitivity is obtained due to the high electron affinity of the noble gases used in the ion scattering. Surface analysis using LEIS yields valuable information about the composition of the outermost layer, which is important for e.g. understanding the catalytic properties of surfaces. For a quantitative analysis of the composition of the outermost atomic layer, the ion scattering signals of the surface species under investigation are compared to reference samples of the species with known surface densities. In order to perform an accurate quantification, one has to know exactly how many surface atoms are probed by the incident ions and contribute to the ion scattering signal.

Here, we have investigated the influence of the surface structure on the ion scattering signal intensity using high-purity tungsten single crystals with different crystallographic orientations. The objective was to understand to what extent the deeper atomic planes are probed by the incident ions, depending on the atomic arrangement of the surface. From a combination of ion scattering experiments and simulations, the contributions of the different atomic planes to the ion scattering signal have been deduced for various crystallographic orientations. The insights gained here are used to discuss the implications of the influence of the surface structure on quantitative surface analysis using LEIS. Furthermore, an overview of possible errors in the quantification due to the influence of the surface structure and the cleaning procedures is given.

4.2 Experimental

The high-purity W single crystals used in the ion scattering investigations were grown from the melt by the electron beam floating zone melting (EBFZM) technique [5,6]. A strain-annealing technique was subsequently applied to perfect the structural quality of the crystals [7] (see chapter 3). In order to obtain clean surfaces, all crystals used here were heated at approximately 1500 K in a $5 \cdot 10^{-8}$ mbar oxygen background pressure, removing the carbon impurities from the surface in the form of CO-species [8,9]. The oxygen remaining on the surface was removed by flashing in UHV to temperatures in excess of 2500 K. After the cleaning procedures Auger electron spectroscopy (AES) confirmed that the carbon and oxygen impurities at the surface were below 1% of a monolayer. Low-energy electron diffraction (LEED) investigations showed well-ordered (1x1) diffraction patterns for all the crystallographic orientations.

The LEIS experiments were performed in UHV using a monoenergetic beam of different noble gas ions (He^+ , Ne^+ , and Ar^+) with an initial energy between 1 keV and 5 keV. The incident ions were directed perpendicular onto the surface, and the ions that backscattered over an angle of 136° were energy selected by a cylindrical mirror analyser [10]. All LEIS investigations were performed using an ion dose not exceeding 10^{14} ions $\cdot\text{cm}^{-2}$, to ensure negligible damage to the surface was induced. In the ion scattering, the area of the W peak in the LEIS spectrum was taken as a measure for the signal intensity, and it was found that the absolute signal intensities for the individual crystals were reproducible within 5%. Auger analysis was used to verify that no contamination of the surfaces occurred during the time required for the investigations.

4.3 Results

4.3.1 Ion scattering experiments

The LEIS sensitivity to the crystallographic orientation is demonstrated in figure 4.1, which shows the signal intensity of the W peak across the grain boundary of a bi-crystal exposing the (110) and (211) faces. The signal S is normalised to the LEIS signal of the closest packed (110) face ($S_{110}=100\%$). This figure clearly shows the dependence of the signal intensity on the crystal orientation ($S_{211}=0.88\cdot S_{110}$), and demonstrates the visibility of grain boundaries in ion scattering studies. The difference in signal between the two faces differs from what is expected based on the atomic densities N of the outermost atomic planes ($N_{211}=0.58\cdot N_{110}$). The signal intensity is thus not simply proportional to the atomic density of the outermost atomic plane (see also table 4.1).

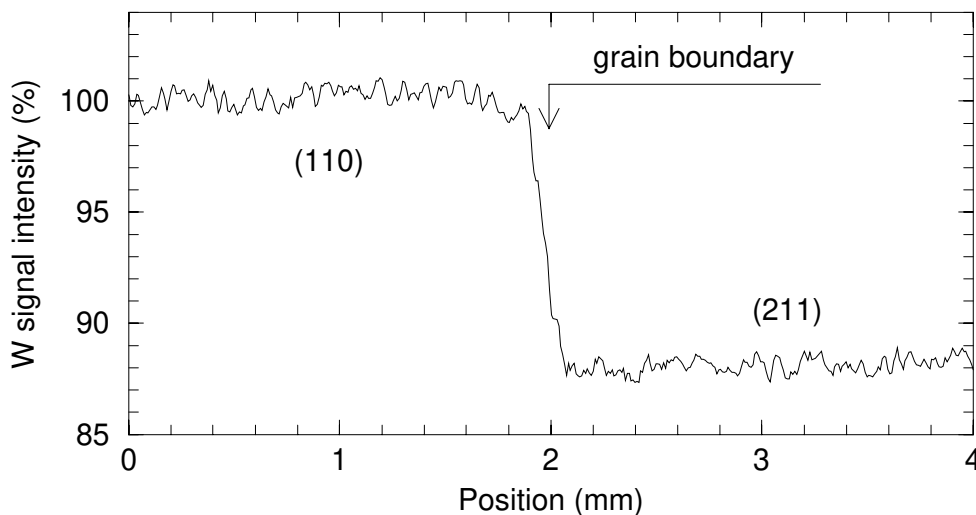


Figure 4.1. LEIS signal intensity across a bi-crystal exposing the (110) and (211) faces. The signal is normalised to the closest packed (110) face ($S_{110}=100\%$). The experiment was performed in a LEIS set-up equipped with a micro-beam, where the diameter of the incident 3 keV Ne^+ beam was 30 μm for the full width at half maximum. This set-up had a similar scattering geometry: normal incidence and 145° scattering angle [11,12].

The dependence of the LEIS signal intensity on the surface structure was further investigated by comparing the signal intensities from different crystallographic orientations. The W signal intensities for the different crystals are plotted in figure 4.2 versus the densities of the outermost atomic planes, which were derived from the lattice constants of the different crystals (see also table 4.1). The signal intensities and the atomic densities are normalised to the closest packed surface ($S_{110}=100\%$, $N_{110}=100\%$). For each crystal and ion type the initial energy was varied between 1 keV and 5 keV, and since no systematic influence of the initial energy was observed, the error bars represent the average for the different energies and for repetitive measurements. The solid line represents the expected signal intensity if only the atoms in the outermost plane contribute to the signal. For crystals with an open surface structure (e.g. W(111)) the measured signal intensity is higher than the solid line due to contributions from the deeper atomic planes. The extent to which the deeper planes contribute

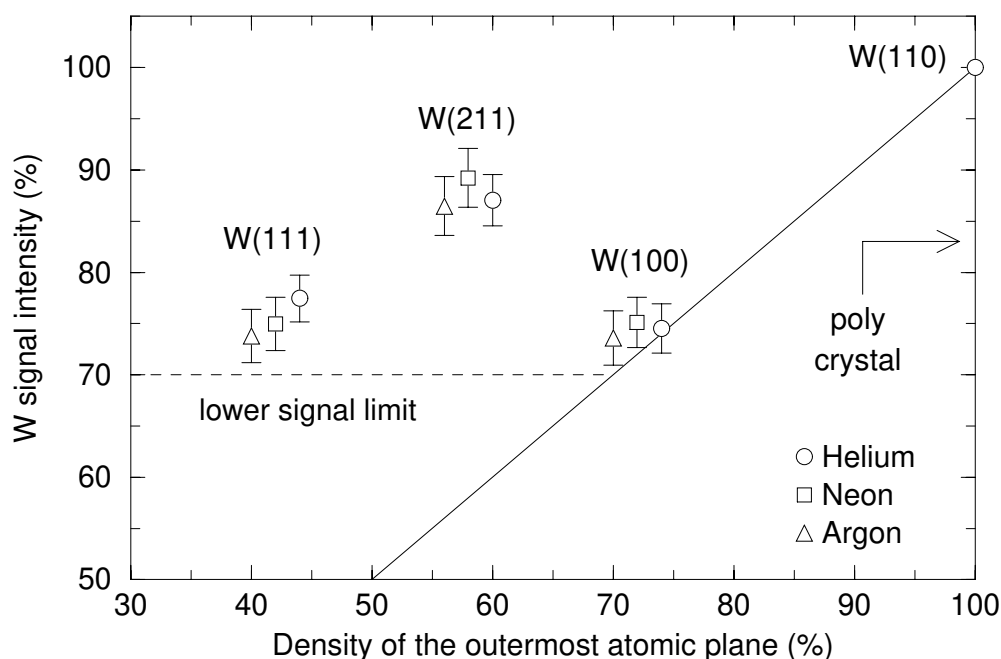


Figure 4.2. LEIS signal intensity for the different W crystals versus the density of the outermost atomic plane. The signals and atomic densities are shown relative to the closest packed W(110) crystal ($S_{110}=100\%$, $N_{110}=100\%$). The symbols for He^+ and Ar^+ are shifted right and left respectively for clarity. The value for the poly-crystal is indicated by the arrow. The solid line shows the expected signal if only the outermost plane contributes to the signal. The dashed line shows the lower limit of the ion scattering signal (see text for explanation).

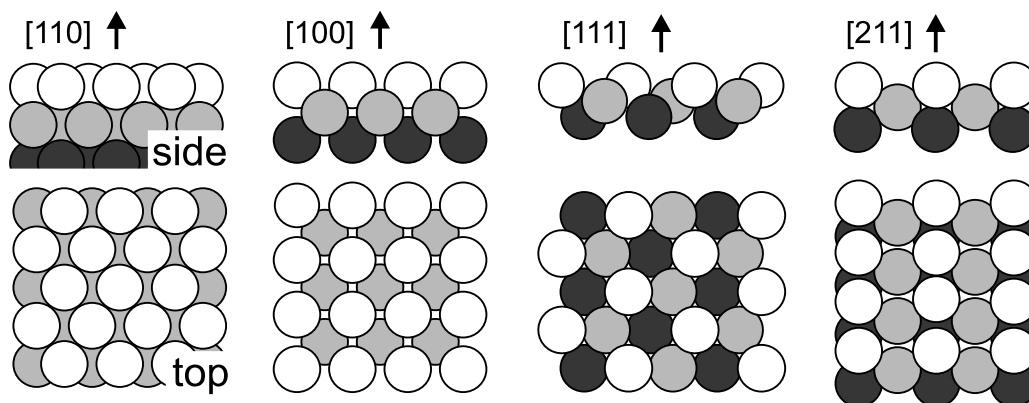


Figure 4.3. Schematic representation of the different crystallographic orientations used in the investigations. For each crystal the upper and lower part represent the side and top view respectively. The lattice parameters are summarised in table 4.1.

to the signal depends on the details of the surface structure, as is evident from the higher signal intensity for the (211) face compared to the signal intensities from the (100) and (111) faces. Figure 4.3 schematically shows the arrangement of the outermost atomic planes of the different crystals used here [13]. Note that no significant differences in the W AES signal intensities were observed for the different crystallographic orientations.

Figure 4.2 also shows the measured signal intensity for a polycrystalline W surface, indicated by the arrow ($S_{poly}=0.83 \cdot S_{110}$). Although the closest packed (110) face has the lowest surface energy, and is therefore expected to be the dominant face at the surface of the poly-crystal, the signal intensity is clearly below the signal of the W(110) single crystal. This lower signal intensity of the poly-crystal compared to the W(110) single crystal is attributed to possible contributions from less dense packed faces, and to signal loss due to the surface roughness caused by variations in the grain orientations off the surface normal [14,15,16].

Crystal surface properties					Results of investigations					
face	a (Å)	b (Å)	ϕ (°)	N ($10^{15}/\text{cm}^2$)	M (%)	S ¹ (%)	S ² (%)	S ³ (%)	L	M ^{IB} (%)
110	2.74	2.74	109	1.41	100	100	-	-	1	74
100	3.16	3.16	90	1.00	74±2	72	2	-	1.03	69
211	2.74	4.47	90	0.82	88±3	58	28	2	1.51	75
111	4.47	4.47	120	0.58	75±3	41	20	15	1.82	71
poly					84±4					71

Table 4.1. Summary of the crystal surface properties and the results of the investigations. a,b: lattice distances, ϕ : lattice angle. N: density of the outermost atomic plane derived from the lattice data. M: measured signal relative to W(110) face. S^{1,2,3}: contributions to the measured signal from the outermost, second, and third atomic plane respectively. L: number of layers effectively probed by the ions. M^{IB}: measured signal after ion bombardment relative to the signal from the undamaged W(110) face.

4.3.2 Ion scattering simulations

In order to differentiate between the contributions from the different atomic planes, ion scattering simulations with an identical geometry were performed. The scattering interactions between the incident ions and the surface atoms were calculated using the SISS-92 computer code, which does not take into account neutralisation effects [17]. However, because the neutralisation probability of the noble gas ions during hard collisions with the surface atoms is very high, we assume that ions which have had multiple interactions with the surface atoms are neutralised. In the simulations we therefore determined the probability that an incident ion has a single elastic collision with an atom in a certain atomic plane, and reaches the detector without scattering from atoms in other atomic planes. Of course, this is an oversimplification of the neutralisation in LEIS, but it gives a good representation of the geometric shadowing and blocking effects occurring on these surfaces. The results are presented in figure 4.4a, which shows the number of ions elastically scattered from the different planes where for each crystal 10^8 ions were directed onto the surface. The number of ions elastically scattered from the outermost atomic plane (filled area) is proportional to the density of the outermost atomic

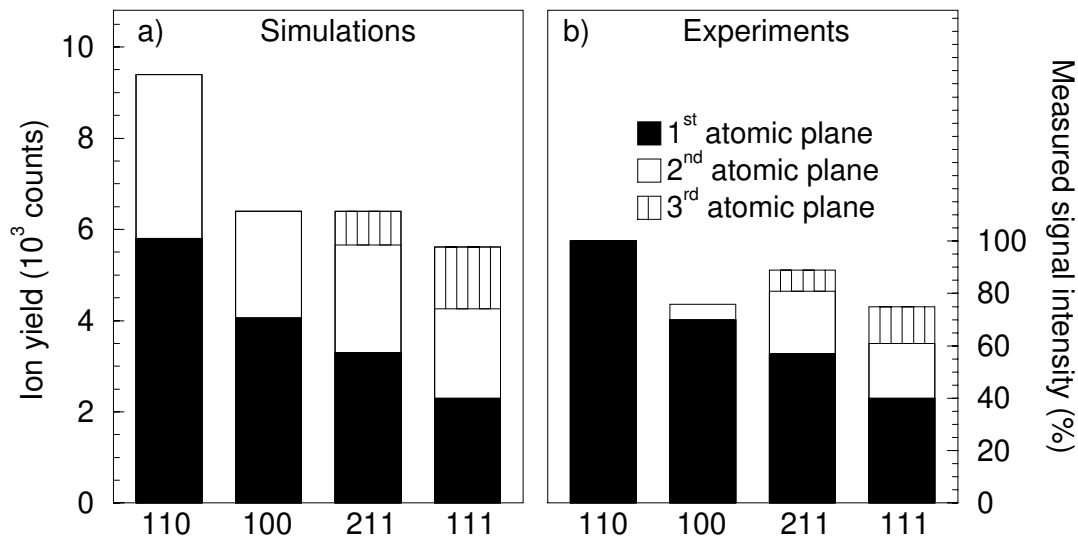


Figure 4.4. Contributions from the different atomic planes derived from the simulations (a) and the experiments (b). For the simulations the number of ions elastically scattered from the indicated planes are shown. For the experiments the relative contributions from the different planes are shown, where the sum of the different planes equals the measured signal as shown in figure 4.2.

plane, as expected. It is evident from the simulations that as the structure becomes more open, the number of atomic planes from which the ions can scatter and contribute to the signal increases. Moreover, the relative contributions from the deeper atomic planes increase with increasing openness.

Because no neutralisation mechanisms were included into the simulations, the closest packed W(110) crystal shows a significant contribution from the second atomic plane. However, ion scattering experiments have shown that for a close packed surface, like the W(110) crystal, the contributions from deeper layers are negligible. Moest et al. [18] concluded from angle resolved ion scattering experiments with similar geometry (normal incidence and 145° scattering angle) that for a Rh(100) crystal with fcc structure the contribution from the second plane is approximately 4%. Similarly, Bergmans et al. [19,20] found that for the somewhat more open (110) fcc structure approximately 10% of the signal originates from the deeper planes. Because the W(110) face is even more close packed than the above mentioned Rh (100) face [13], we assume that all signal for the W(110) face originates from scattering of the outermost atomic plane (i.e. no contribution from 2nd plane).

The visibility of the deeper layers is thus less than indicated in figure 4.4a due to the neutralisation of the ions when passing close to the atoms in the outermost atomic plane. Note that neutralisation can occur at larger distances than the scattering takes place. Figure 4.4b shows the results of combining the experiments with the simulations. Here, the signal intensity for the W(110) crystal originates entirely from the outermost atomic plane. The contributions from the outermost atomic planes for the other crystallographic orientations scale with the densities of the outermost planes. The effective contributions from the second and third atomic planes were decreased such that the sum of the different planes in the figure equalled the measured signal intensity as shown in figure 4.2. The ratios of the contributions

from the second and third planes were taken from the simulations, which results in a slight overestimation of the contribution from the third atomic plane.

We can conclude that for open surfaces the ions scattered from the second, and even the third, atomic planes contribute significantly to the total signal. The results shown in figure 4.4b are also summarised in table 4.1. In addition, the table shows the number of atomic planes effectively seen by the ions, which is derived by dividing the total signal by the contribution from the outermost plane. It is observed that the number of planes L effectively contributing to the LEIS signal increases with decreasing packing density, as can be expected.

4.3.3 Influence of surface roughness and disorder

In the ion scattering experiments above, low ions doses were used in order not to damage the surface structure. A high ion dose induces damage to the structure by sputtering away surface atoms, and can significantly affect the signal intensity due to the creation of roughness and disorder on an atomic scale. To demonstrate the change in the signal intensity caused by the roughness and disorder, the different crystals were exposed to 5 keV Ar^+ ion bombardment at room temperature. LEED investigations during the sputtering revealed that the initially sharp diffraction spots blurred as a function of the applied ion dose, indicating the increase of disorder with increasing dose. The LEIS signal intensity of the backscattered Ar^+ ions is shown in figure 4.5 as a function of the applied ion dose for different crystals. It is observed that the signal intensity decreases with increasing dose, where the signal intensity for the different crystals approaches the same value after a large sputtering dose: $72 \pm 3\%$ of the closest packed (110) face. An identical behaviour is observed for all crystals (see table 4.1). The signal decrease is not caused by contaminations, as was verified by both LEIS and AES.

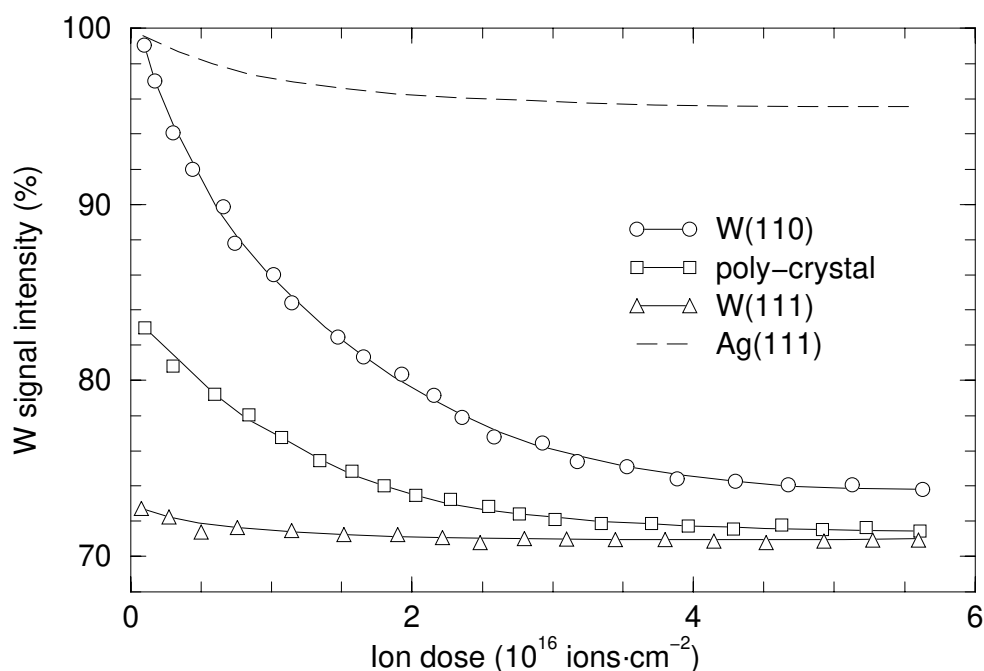


Figure 4.5. The influence of 5 keV Ar^+ ion bombardment on the signal intensity for different crystals. The signal intensity, relative to the undamaged W(110) crystal, is shown versus the applied ion dose. For comparison the result of the low-melting point closest packed Ag(111) crystal is shown (fcc structure).

Therefore, the observed signal decrease is the result of the atomic roughness and disorder induced by the ion bombardment. The ion bombardment destroys the surface structure, and the initial structural differences between the crystals disappear resulting in similar ion scattering signals for all crystals after a large sputtering dose. The signal decrease is the strongest for the W(110) crystal because this is the closest packed structure with the highest ion scattering signal, and thus any change in the atomic arrangement can only result in a signal decrease because of less effective packing.

Due to the high melting point of tungsten the disorder can not be restored at room temperature. The surface structures, and resulting signal intensities, are only restored when the crystals are heated to high temperatures in excess of 2000 K. We emphasise that the influence of the ion bombardment on the signal intensity is not the same for low melting materials, such as e.g. silver. This is demonstrated in figure 4.5, where the result of ion bombardment of the closest packed Ag(111) crystal is shown (dashed line). It is observed that the signal intensity only slightly decreased due to the ion bombardment. LEED investigations confirmed that despite the ion bombardment the surface remained relatively well-ordered. The signal decrease due to sputter induced roughness and disorder thus depends on both the crystallographic orientation and on the melting point of the material.

4.4 Discussion and conclusions

Our results show that the signal intensity in low-energy ion scattering is not straightforward proportional to the density of the outermost atomic plane. This proportionality is only valid for close packed surfaces. For surfaces with open structures the deeper atomic planes can contribute significantly to the ion scattering signals. The contributions from these deeper planes is smaller than the contribution from the outermost atomic plane due to geometric shielding and additional neutralisation. The extent to which the deeper planes contribute to the ion scattering signal is not directly related to the density of the outermost atomic plane, but depends on the atomic arrangement of the surface (see e.g. W(211) in figure 4.2). Comparing the ion scattering signals from the well-ordered crystals and the atomically rough disordered surfaces, it appears that there is a lower limit of the signal intensity in LEIS. This lower limit is approximately 70% of the signal corresponding to the closest packed surface, as is indicated by the dashed line in figure 4.2. Apparently, the balance between the density of the outermost atomic plane and the contributions from deeper planes is such that the total signal intensity is never less than 70% of the maximum obtainable signal.

The insights gained in this study can help to improve the interpretation of ion scattering signals, and therefore can improve the accuracy with which the ion scattering can be used for quantitative analysis. Because no quantitative information can be derived from a single measurement, the use of reference samples with known surface densities forms the basis of quantification. When performing a quantitative analysis, reference samples with well-ordered close packed surfaces are preferred since the signal is proportional to the density of the outermost atomic plane. If only reference samples with well-ordered open surface structures are at hand, the contributions from the deeper planes can be estimated from the insights of this work, using the relation between the number of planes effectively probed and the packing density of the outermost plane (see table 4.1).

Since well-ordered single crystals are often expensive and not easy to come by, polycrystalline substrates are widely used as reference samples for quantification. The surface density of the poly-crystal is then often assumed equal to the density of the closest packed face for the corresponding material. However, the signal intensity from the poly-crystal can be

lower than the signal intensity from the closest packed single crystal due to surface roughness caused by misalignment of the individual grains, and possible contributions from less dense packed faces. The error in the determined relation between the ion scattering signal and the surface density based on the poly crystal can be as large as 20%, as evidenced by the comparison of the W poly-crystal and the W(110) single crystal in figure 4.2.

In addition to the choice of the type of reference sample, the cleaning procedures of the samples also influence the interpretation of the ion scattering signal intensity. The crystals used in this work were cleaned by heating in oxygen and subsequent flashing to high temperatures, which does not affect the crystal structure. However, surface cleaning by ion bombardment is a widely applied technique because of its ease of preparation [21]. Subsequent annealing is often not performed since this leads to segregation of impurities to the surface, i.e. recontamination of the surface. It has been shown here that sputter induced damage results in atomic roughness and disorder and can significantly decrease the ion scattering signal. The extent to which the sputtering influences the ion scattering signal depends on the original surface structure and the melting point of the material. Due to the high-melting point of the W crystals, the ion bombardment of the closest packed W(110) face at room temperature leads to a signal decrease of approximately 30% compared to the well-ordered undamaged crystal. If such a prepared crystal would be used as a reference sample, the error in the quantification is of an identical magnitude. In addition, the extent to which the signal is influenced by the ion bombardment strongly depends on the melting point of the material used. This was demonstrated by the comparison of the ion bombardment of the closest packed W(110) and Ag(111) crystals, where the signal decrease of the Ag(111) crystal was only a few percent due to the larger mobility. Therefore, we conclude that annealing after surface cleaning by ion bombardment is important to restore the sputter induced damaged, especially for high-melting materials. If annealing is not possible, or undesired because of recontamination of the surface by segregation, one can roughly estimate the signal loss from figure 4.5 if the melting point is known.

A final remark should be made about the scattering geometry, which also influences the contributions from the deeper planes. For near perpendicular scattering geometry these contributions are the largest, while for grazing incidence almost no contributions are expected and the signal is proportional to the density of the outermost atomic plane. One might therefore conclude that grazing incidence is the preferred geometry for quantification of open structures. However, one should consider that for grazing incidence the neutralisation of the ions becomes more complicated because more atoms from the outermost atomic plane can become involved in the neutralisation process(es). In general, changes in the neutralisation probability can have a far larger influence (and uncertainty) on the signal intensity than the possible contributions from deeper planes, and grazing incidence is thus not a suited geometry for straightforward quantitative compositional analysis.

Acknowledgements

We are very grateful to prof.dr. Vadim Glebovsky and dr. Sergey Ermolov for the help with the preparation of the W crystals. We also like to thank Barry Moest for the assistance with the ion scattering simulations. In addition, we thank Wim Jansen for the LEIS micro-beam experiments on the bi-crystal.

References

- 1 D.P. Smith, J. Appl. Phys. 38 (1967) 340.
- 2 H.H. Brongersma, P.M. Mul, Chem. Phys. Lett. 14 (1972) 380.
- 3 H. Niehus H, W. Heiland, E. Taglauer, Surf. Sci. Rep. 17 (1993) 213.
- 4 J.W. Rabalais (Ed), *Low Energy Ion-Surface interaction*, Wiley Series in Ion Chemistry and Physics, John Wiley & Sons, 1994.
- 5 V.G. Glebovsky, V.N. Semenov, V.V. Lomeyko, J. Less-Common Metals 117 (1986) 385.
- 6 V.G. Glebovsky, V.N. Semenov, V.V. Lomeyko, J. Crystal Growth 87 (1988) 142.
- 7 R. Cortenraad, S.N. Ermolov, V.N. Semenov, A.W. Denier van der Gon, V.G. Glebovsky, S.I. Bozhko, H.H. Brongersma, to be published in J. Crystal Growth.
- 8 A. Elbe, G. Meister, A. Goldmann, Surf. Sci. 371 (1997) 438.
- 9 K.E. Johnson, R.J. Wilson, S. Chiang, Phys. Rev. Lett. 71 (1993) 1055.
- 10 R. Cortenraad, A.W. Denier van der Gon, H.H. Brongersma, Surf. Int. Anal. 29 (2000) 524.
- 11 A.W. Denier van der Gon, M.A. Reijme, R.F. Rumphorst, A.J.H. Maas, H.H. Brongersma, Rev. Sci. Instrum. 70 (1999) 3910.
- 12 A.W. Denier van de Gon, R. Cortenraad, W.P.A. Jansen, M.A. Reijme, H.H. Brongersma, Nucl. Instr. and Meth. 161-163 (2000) 56.
- 13 J.M. MacLaren, J.B. Pendry, P.J. Rous, *A Handbook of Surface Structures*, Surface Crystallographic Information Service, Reidel Publishing, Dordrecht, 1987.
- 14 G.C. Nelson, J. Appl. Phys. 47 (1976) 1253.
- 15 E. Taglauer, *Ion scattering Spectroscopy*, in Ion Spectroscopies for Surface Analysis, Eds. A.W. Czanderna, D.M. Hercules, Plenum Press, New York, 1991.
- 16 J.-P. Jacobs, S. Reijne, R.J.M. Elfrink, N. Mikhailov, H.H. Brongersma, J. Vac. Sci. Technol. A12 (1994) 2308.
- 17 C.A. Severijns, G. Verbist, H.H. Brongersma, Surf. Sci. 279 (1992) 297.
- 18 B. Moest, P.T. Wouda, A.W. Denier van der Gon, H.H. Brongersma, B.E. Nieuwenhuys, D.O. Boerma, submitted to Surf. Sci.
- 19 R.H. Bergmans, M. van de Grift, A.W. Denier van der Gon, H.H. Brongersma, Surf. Sci. 345 (1996) 303.
- 20 R.H. Bergmans, *Energy and angle resolved ion scattering and recoiling spectroscopy on bimetallic systems*, Ph. D. Thesis, Eindhoven University of Technology, The Netherlands, 1996. (ISBN 90-386-0057-7)
- 21 E. Taglauer, Appl. Phys. A 51 (1990) 238.

Work Function Dependent Neutralisation of Low-Energy Noble Gas Ions



Abstract

We have investigated the work function dependence of the neutralisation of low-energy He^+ , Ne^+ and Ar^+ noble gas ions as used in LEIS. This was done by studying the neutralisation probability of the noble gas ions for scattering from submonolayer coverages of Ba on W(110) and Re(0001) substrates. It was found that the Auger mechanism does not play a significant role for the neutralisation of noble gas ions with an initial energy of 2-5 keV scattered from alkali and earth-alkali elements. The basic neutralisation mechanism for scattering from these elements is collision-induced neutralisation, a mechanism where the neutralisation takes place during the violent collision. The neutralisation probability due to this mechanism is insensitive to work function changes. At low ion energies (<0.5 keV) the collision-induced neutralisation may not be possible, and Auger neutralisation is the dominant mechanism. At work functions below 3-4 eV, resonant neutralisation to the first excited level of the noble gas ions takes place in addition to the collision-induced and Auger neutralisation. The neutralisation behaviour of the noble gas ions due to the resonant neutralisation can be described using the resonant charge exchange theory. Due to the resonant neutralisation, the neutralisation probability for noble gas ions increases exponentially with decreasing work function. This mechanism is only available at low work functions, and the exact work function below which the resonant neutralisation is possible depends on the energy of the first excited level of the ion, when the ion is near the surface at distances where the charge transfer can take place.

5.1 Introduction

Low-Energy Ion Scattering (LEIS) using noble gas ions is a surface analysis technique that only probes the outermost atomic layer of the surface [1,2]. This extreme surface sensitivity is the result of the high neutralisation probability of the noble gas ions during the interaction with the surface atoms. The LEIS technique is widely applied for investigations of the outermost atomic layer of many different types of solid surfaces (e.g. metals [3,4], oxides [5], polymers [6]), liquid surfaces [7,8], and complex real industrial systems like catalysts [9,10], polymer LEDs [11], or thermionic dispenser cathodes [12,13]. Despite the fact that LEIS is widely applied, the neutralisation mechanisms of the noble gas ions have not yet been indisputably established, and are still the subject of many investigations.

The subject of this paper is the work function dependence of the neutralisation of noble gas ions. The neutralisation mechanisms of noble gas ions at low work functions are especially interesting since LEIS studies of low-work function systems have shown a strong influence of the work function on the neutralisation probability [12,13,14,15,16,17]. Several authors have suggested that at low work functions the noble gas ions can be neutralised by a mechanism involving a (resonant) charge transfer to the first excited level of the ion [15,16,18]. However, a systemic investigation of the work function dependence of the noble gas ions at low work functions is absent in the literature. Here, we will show that indeed the noble gas ions can be neutralised by a resonant electron transfer to the first excited levels of the ions, and that the neutralisation behaviour at low work functions can be described by resonant charge exchange theory.

We have investigated the neutralisation behaviour of He^+ , Ne^+ , and Ar^+ noble gas ions over a work function range extending from 6 eV down to 2 eV. The work function changes for these investigations were induced by adsorbing Ba on W(110) and on Re(0001) single crystals. The neutralisation probability for noble gas ions scattered from these systems was determined as a function of the work function using the characteristic velocity method [12,19,20]. From the observed work function dependence of the neutralisation, combined with results from neutralisation studies reported in the literature, the nature of the neutralisation mechanisms is deduced.

In section 5.2 a short overview of the possible neutralisation mechanism for noble gas ions is given [21]. For clarity, in this overview we have already incorporated to some extent the conclusions from our investigations. In the remainder of this paper we present the evidence for these conclusions. The experiments, and the methods used to vary the work function, are described in section 5.3. Subsequently, in section 5.4 we present and discuss the results of our investigations. The main conclusions are summarised in section 5.5.

5.2 Neutralisation mechanisms

In LEIS, noble gas ions are directed onto the surface and those ions that are backscattered from the surface are analysed. Due to the interactions with the surface atoms the ions can be neutralised by several neutralisation mechanisms: Auger neutralisation, collision-induced neutralisation, and resonant neutralisation. Along the ion trajectory each of these mechanisms can occur at a specific interaction distance, which is different for the various mechanisms. The neutralisation along the trajectory can be divided into 3 sections [22,23]: 1) the incoming trajectory, 2) the violent collision, and 3) the outgoing trajectory. Which of the mechanism(s) takes place depends on the ion-target combination, the work function of the system, and on the energy of the ion.

5.2.1 Auger neutralisation

In the Auger neutralisation process an electron is transferred from the metal conduction band of the surface to the ground state of the ion [24,25]. The energy surplus of this transition is used to emit a second electron from the conduction band (see figure 5.1). The Auger neutralisation can take place when there is sufficient overlap between the orbitals of the ion and the surface atoms, which occurs at a distance of approximately 1-2 Å [18,26]. The neutralisation probability depends on the density of electrons available for the transition, and is in first order approximation proportional to the square of the electron density of the target atoms since two electrons are involved in the process [27,28,29]. The transition probability thus depends on the ion-target combination. Furthermore, the neutralisation probability depends on the velocity of the ion: a slow ion spends more time within the spatial region where Auger transitions can take place and therefore has a large neutralisation probability. Since the pioneering work of Hagstrum in the 1950s [24,25], the Auger neutralisation is often assumed to be the dominant neutralisation mechanism for noble gas ions due to the large ionisation potentials of the ground state of the ions (see table 5.1). However, in this paper we show that the Auger process plays no significant role in the neutralisation of noble gas ions with an initial energy of 2-5 keV scattered from alkali and earth-alkali elements. Note that here we only consider small impact parameters that are required for the ions to be backscattered. At large impact parameters the Auger neutralisation can play an important role.

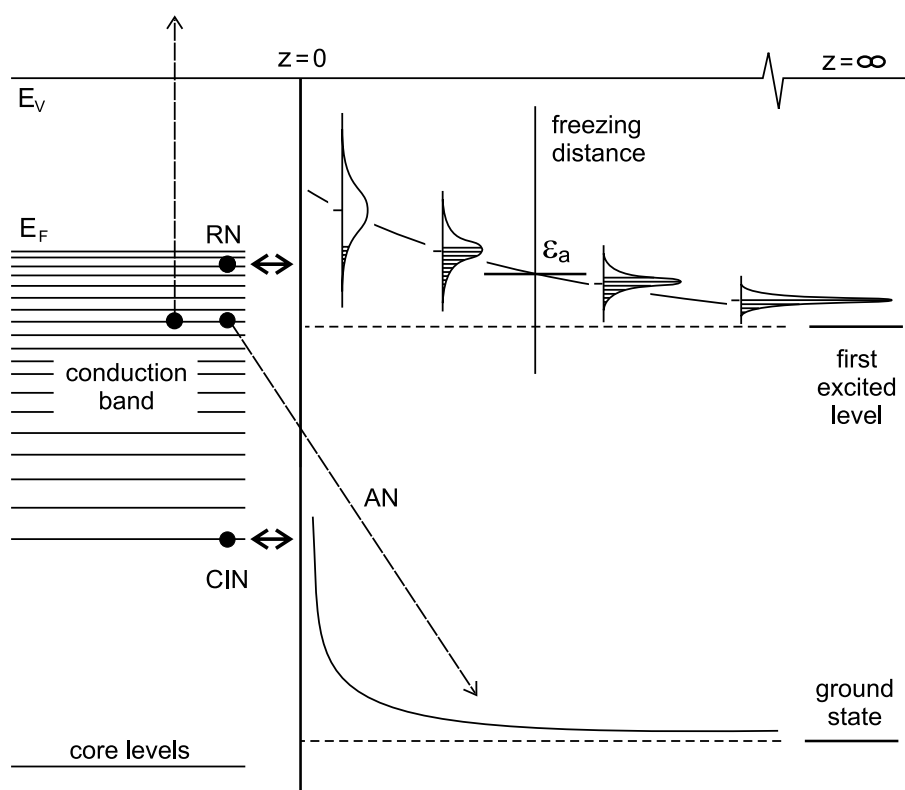


Figure 5.1. Schematic representation of the different neutralisation mechanisms. RN: resonant neutralisation, AN: Auger neutralisation, CIN: collision-induced neutralisation.

5.2.2 Collision-induced neutralisation

Several experimental and theoretical investigations of the neutralisation of noble gas ions have questioned the assumed dominance of the Auger mechanism, and suggested the noble gas ions can also be neutralised during the violent collision between the ion and the target atom [22,23,30,31,32]. Much work on this subject was performed by Boers et al. [23] and later by Souda et al. [30]. For the neutralisation at the close encounter we will use the term collision-induced neutralisation, as introduced by Souda [30].

During the violent collision between the ion and the target atom, the ground state of the ion can be promoted due to the interaction with the core levels of the target atom [33,34,35]. At close distance, of the order of 0.5 \AA , the ground state of the ion is aligned with the bottom of the conduction band, enabling resonant charge exchange between the ground state and the levels at the bottom of the band (see figure 5.1). Consequently, the noble gas ions can be neutralised, and ions that were neutralised by the Auger mechanism on the incoming trajectory can be reionised [18,26,30,35,36]. The probability for collision-induced neutralisation (and reionisation) depends strongly on the ion-target combination, because details of the ground state promotion depend on the energy of the ground state relative to the core levels of the target atom [33,34]. The neutralisation probability furthermore depends on the velocity of the ion, which determines the time available for resonant charge transfer to the ground state.

In this paper we argue that the collision-induced neutralisation is an important neutralisation mechanism for noble gas ions scattered from alkali and earth-alkali elements. Moreover, at high work functions it is the dominant neutralisation mechanisms for these elements. At low work functions additional neutralisation by the resonant neutralisation involving the first excited level of the noble gas ion becomes significant.

5.2.3 Resonant neutralisation

Neutralisation of the noble gas ions is also possible by a resonant electron transfer to the first excited level of the ion; a mechanism similar to the neutralisation mechanism for alkali ions [37,38], for which the energy of the ground state is comparable to the first excited level of the noble gas ions. Although several neutralisation studies have suggested the possibility for this mechanism [15,16,18], here we show the mechanism does indeed take place, but only at low work functions. Moreover, at work functions of the order of 2 eV the resonant neutralisation may become the dominant mechanism for noble gas ions. In this paper we describe the work function dependence of the resonant neutralisation probability using the resonant charge exchange theory, which was developed for alkali ion scattering studies to explain the work function dependence of the neutralisation of the alkali ions.

A brief description of the resonant neutralisation mechanism is given here: When the ion is near the surface, the population of the shifted and broadened level is in equilibrium with the substrate and will become partially occupied up to the Fermi edge (see figure 5.1). Along the outgoing trajectory, the charge exchange rate decreases with increasing distance, and becomes small compared to the rate of level shifting and narrowing. At a distance referred to as the freezing distance the equilibrium is “frozen” (approximately of $2\text{-}4 \text{ \AA}$), and the extend to which the level is filled at this distance determines the charge fraction [39,40]. With increasing velocity of the ions, the freezing distance decreases, and consequently the neutralisation probability decreases. Furthermore, the neutralisation probability is determined by the position of the Fermi edge, and thus depends on the work function.

Due to the resonant neutralisation the noble gas ions are in an excited state as they leave the surface. Deexcitation of the excited noble gas ion cannot take place by a direct transition of the electron to the ground state under the emission of a photon since this is a forbidden

transition. Therefore, deexcitation has to occur through Auger deexcitation or autodetachment [41,42,43,44,45]. The transition rates of these deexcitation processes are approximately one order of magnitude smaller than the transition rates of the resonant charge exchange [41,46]. Therefore, it is expected that the resonant neutralisation to the first excited level can in first order be treated without taking the deexcitation into account.

5.2.4 Neutralisation probability

Despite the fundamental differences between the various mechanisms, the neutralisation probability for each mechanism has a similar dependence on the velocity of the ion. The probability that the incident ion leaves the surface as an ion after the interaction(s) with the surface atom(s) is represented by the ion fraction P^+ , which depends on the ion velocity v according to [21,25,38]:

$$P^+ = \exp(-v_c \cdot 1/v) \quad (5.1)$$

The characteristic velocity v_c is a measure for the neutralisation rate, where the physical parameters that determine the characteristic velocity depend on the type of mechanism. The exact definition of the reciprocal ion velocity $1/v$ depends on the neutralisation mechanism, and whether the interaction involves only the direct scattering partner, or also more neighbouring surface atoms. Auger neutralisation takes place at a distance of approximately 1-2 Å from the scattering partner, and can also involve neighbouring atoms on the incoming and outgoing trajectory. Therefore, the reciprocal ion velocity is defined as $1/v = 1/v_i^\perp + 1/v_f^\perp$, where v_i^\perp and v_f^\perp are the velocities of the ion normal to the surface on the incoming and outgoing trajectory respectively (Hagstrum model) [24,25]. Collision-induced neutralisation involves only the direct scattering partner and the velocities relative to the target atom are used, defining the reciprocal ion velocity as $1/v = 1/v_i + 1/v_f$ (Godfrey-Woodruff model) [20,47,48]. For the resonant neutralisation process involving the first excited level the neutralisation probability is determined at distances of 2-4 Å, and thus like the Auger process for neutralisation by a metal the interaction involves more than one surface atom [38]. Because the neutralisation is determined here on the outgoing trajectory, the reciprocal ion velocity is defined as $1/v = 1/v_f^\perp$. These different definitions of the reciprocal ion velocity imply that the correct choice can only be made once the nature of the mechanism is known. However, independent of this choice the neutralisation behaviour can be described by eq. (5.1), and only the absolute value of the characteristic velocity is influenced by the choice of $1/v$. (Here we have not discussed the quasi-resonant core-level neutralisation that takes place for some ion-target combinations, like e.g. He⁺-Pb [21,49], since it is a rather exceptional process that yields an oscillatory neutralisation behaviour as a function of the velocity.)

5.3 Experimental

5.3.1 Set-up

The neutralisation investigations were performed in the UHV set-up MiniMobis, which has a base pressure of $1 \cdot 10^{-10}$ mbar and is described elsewhere [17,50]. In the set-up instrumentation is available for low-energy ion scattering (LEIS), Auger electron spectroscopy (AES), and low-energy electron diffraction (LEED). The ion scattering was performed using He⁺, Ne⁺ and Ar⁺ noble gas ions with an initial energy between 2 keV and 5 keV. The incident ion beam was directed perpendicular to the surface, and the ions that backscattered over an angle of

136° were energy selected by a cylindrical mirror analyser (CMA) and detected using micro-channelplates. Auger electron spectroscopy was performed with the use of a grazing incidence electron beam, where the electrons were directed onto the surface at an angle of 10° with the surface. The Auger electrons were detected by the same CMA as used for the ion scattering, with a reverse polarity. The work function of the various systems was derived from the onset of the secondary electron emission [51,52,53], where the secondary electrons were created by the AES electron beam. Since this method is a relative work function measurement technique, the clean W(110) substrate was used as a work function reference ($\phi=5.4$ eV [54]). The characterisation and cleaning procedures of the W substrate have been reported elsewhere [55].

5.3.2 Methods of inducing the work function change

In this work we adsorbed different submonolayers of Ba atoms on W(110) and Re(0001) single crystals in order to investigate the neutralisation over a large work function range. The work function change induced by the Ba adsorption is typical for an (earth)alkali-metal system [56,57,58]: at each alkali site the charge donation to the substrate leads to the creation of a dipole antiparallel to the surface dipole, thereby causing a decrease of the work function. Figure 5.2 shows the work function of the Ba/W(110) system as a function of the Ba coverage (open circles), where the Ba coverage is determined by Auger analysis. The Ba coverage was deduced from the Ba(512 eV)/W(169 eV) Auger signal ratio, and calibrated by assigning the work function minimum of $\phi=1.8$ eV to a coverage of $\theta_{Ba}=0.4$ ML [54]. One monolayer corresponds to a Ba density of $6.3 \cdot 10^{14}$ atoms \cdot cm $^{-2}$ for a close packed hexagonal structure. The

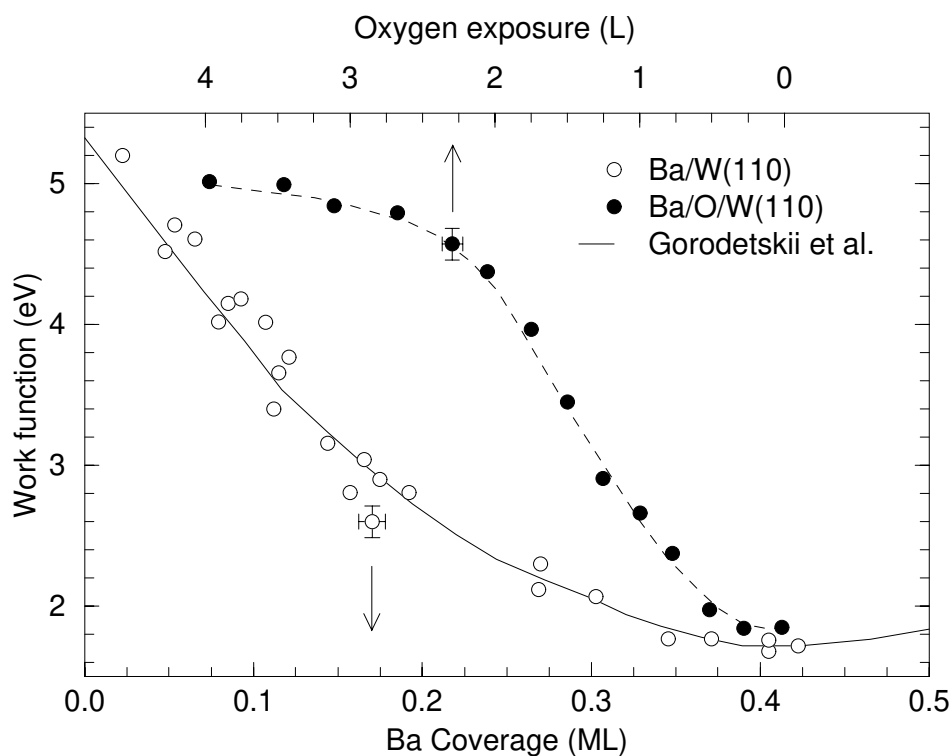


Figure 5.2. The work function of the Ba/W(110) system versus the Ba coverage (open circles). The solid line represents the results of Gorodetskii et al. [59]. The work function of the Ba/O/W(110) system is shown versus the oxygen exposure (filled circles).

accuracy of the coverage and work function measurements is indicated by the error bars in figure 5.2. The solid curve represents the results from Gorodetskii et al. for the work function of the Ba/W(110) system [59]. The work function curve for the Ba/Re(0001) system is not presented but shows a similar dependence on the Ba coverage [60]. For both the Ba/W and the Ba/Re system, the electrostatic repulsion between the different Ba dipoles results in a uniform distribution of the Ba atoms across the substrate [59].

As an alternative method of inducing work function changes, the Ba/W system at a fixed Ba coverage of $\theta_{Ba}=0.4$ ML ($\phi=1.8$ eV) was exposed to an increasing amount of oxygen (0-4 L). The oxygen adsorption leads to depolarisation of the Ba-W dipoles and counteracts the effect of the earth-alkali adsorption [61,62,63]. The oxygen exposure thus increased the work function to a value that is close to that of the clean W(110). Figure 5.2 also shows the work function for the Ba/O/W(110) system as a function of the oxygen exposure (filled circles).

5.3.3 Characteristic velocity method

The characteristic velocity can be derived from the dependence of the measured LEIS signal on the initial energy of the ions. The LEIS signal $S_k(E_i)$ for ions with initial energy E_i scattering from species k is defined as the area of the corresponding peak in the LEIS spectrum, and is proportional to the surface density n_k and the ion fraction $P_k^+(E_i)$ [50]:

$$S_k(E_i) = \varepsilon(E_i) \cdot T(E_i) \cdot \frac{d\sigma_k}{d\Omega}(E_i) \cdot P_k^+(E_i) \cdot n_k \quad (5.2)$$

Here $\varepsilon(E_i)$ and $T(E_i)$ are the ion detection efficiency and the correction for the analyser transmission respectively, which both depend on the energy of the scattered ions [50,64]. The differential scattering cross-section $d\sigma_k/d\Omega(E_i)$ depends on the initial ion energy and can be calculated by a screened Coulomb potential, using e.g. the Molière approximation to the Thomas-Fermi potential [65,66]. The influence of the roughness [67,68] on the LEIS signal is neglected here because well-ordered flat single crystals are used. Combining equations (5.1) and (5.2) we find:

$$\ln \left(\frac{S_k(E_i)}{\varepsilon(E_i) \cdot T(E_i) \cdot \frac{d\sigma_k}{d\Omega}(E_i)} \right) = \ln(n_k) - v_c^k \cdot \frac{1}{v}(E_i) \quad (5.3)$$

This equation shows that the characteristic velocity v_c^k for scattering from species k can be derived from the energy dependence of the LEIS signal after correcting for the energy dependencies of the detection efficiency, analyser transmission, and scattering cross-section. Plotting the logarithm of the corrected signal versus the reciprocal ion velocity yields the characteristic velocity as the slope of the line. The definition of the reciprocal velocity depends on the neutralisation mechanism. Furthermore, at infinite velocity the ion fraction equals unity, and the surface density n_k of the species under investigation can be derived by extrapolating the LEIS signal to infinite velocity.

One should realise that if the instrumental energy dependencies of the set-up are not exactly known, the characteristic velocity cannot be correctly derived. For our LEIS set-up the energy dependencies of the detection efficiency and analyser transmission have been investigated and

reported elsewhere [50]. The consequences of an error in any of these energy dependencies on the derived characteristic velocities are also discussed there.

5.4 Results and discussion

5.4.1 Evidence for work function dependent neutralisation

A demonstration of the influence of the work function on the neutralisation is given in figure 5.3. Here, the ion scattering signal for 2 keV Ne^+ ions scattered from the Ba atoms is shown as a function of the Ba coverage. For low Ba coverages ($\theta_{\text{Ba}} < 0.12$ ML), i.e. high work functions ($\phi > 3.4$ eV), the Ba signal is proportional to the Ba coverage, as expected for a constant neutralisation probability. Above a coverage of $\theta_{\text{Ba}} = 0.12$ ML a deviation from this proportionality is observed, and the Ba signal decreases with increasing Ba coverage. The signal decrease is not due to cluster formation because the Ba adatoms form a uniform layer [58,59], and it is observed that the W substrate signal continuously decreases with increasing Ba coverage. Since the initial energy of the Ne^+ ions was fixed, the detection efficiency, analyser transmission, and scattering cross-section are constant. The observed behaviour can therefore only be explained by a strong continuous decrease of the ion fraction with increasing coverage, where the signal decrease due to the decreasing ion fraction is larger than the signal increase due to the increasing Ba density. Identical trends in the signal intensity versus coverage have been observed for all applied initial energies for He^+ , Ne^+ and Ar^+ ions. Evidently, above a certain Ba coverage, i.e. below a certain work function, an additional neutralisation channel is available.

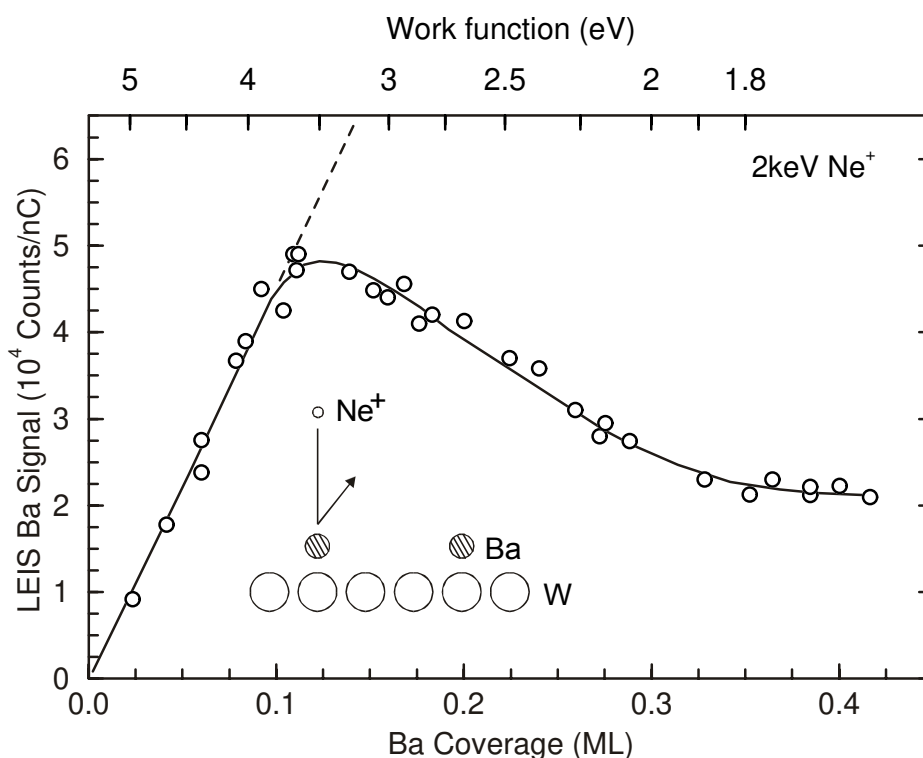


Figure 5.3. The LEIS signal of 2 keV Ne^+ ions scattered from the Ba adatoms as a function of the Ba coverage. The dashed line represent the extrapolation of linear behaviour observed at low coverages.

5.4.2 Characteristic velocity versus work function

Characteristic velocity plots at various fixed work functions are presented in figure 5.4, which shows the Ba signal corrected for the instrumental energy dependencies versus the reciprocal velocity (right ordinate scale). Extrapolation to infinite velocity yields the Ba coverage on the left ordinate scale. Here, the reciprocal velocity was calculated as $1/v=1/v_i+1/v_f$ based on the collision-induced neutralisation, as is explained in section 5.4.3.

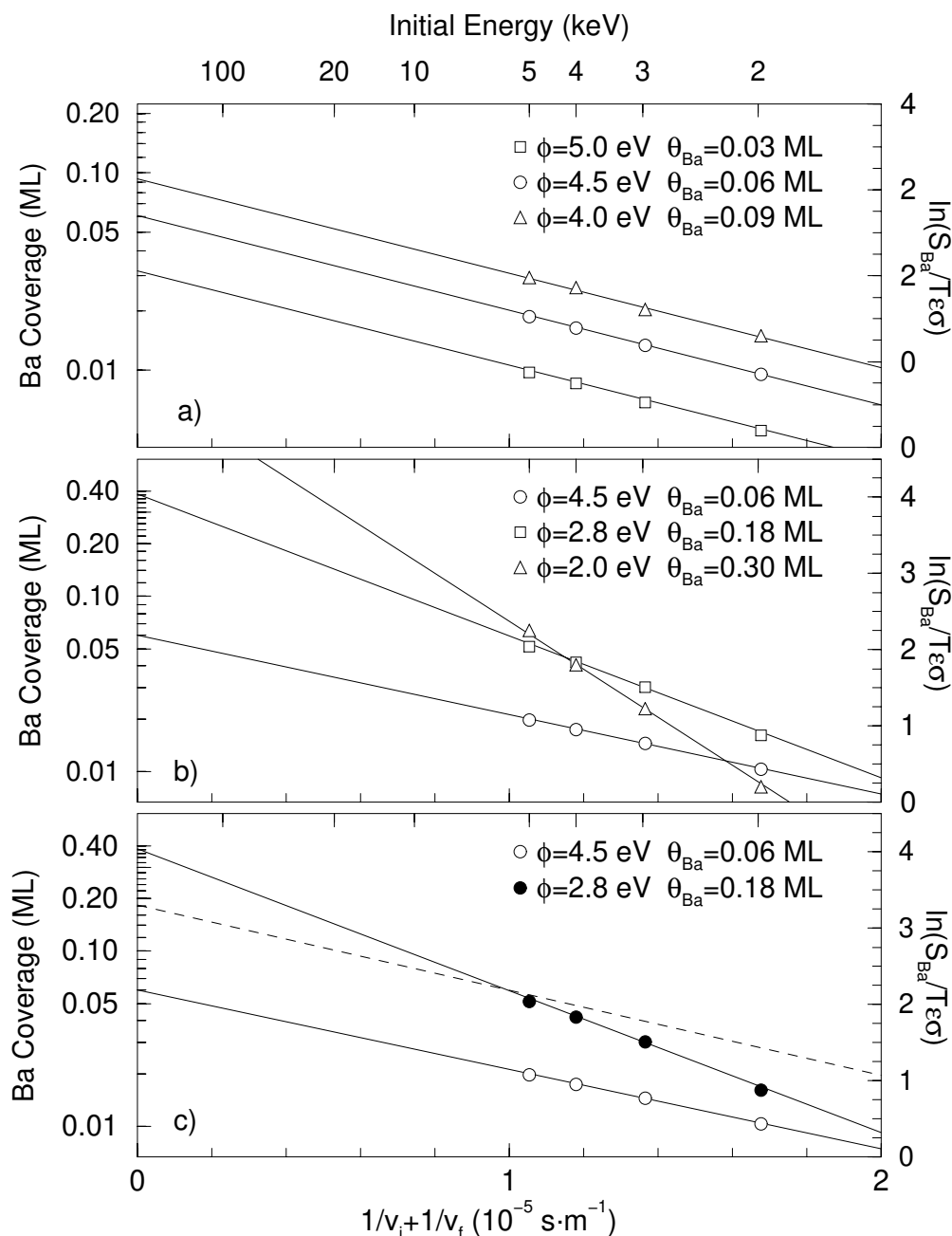


Figure 5.4. Characteristic velocity plots for different work functions. The initial energy scale is shown on the top axis. The solid lines show linear regressions to the data, where the slopes represent the characteristic velocities. (a) high work functions, (b) low work functions, and (c) contribution from resonant neutralisation.

In figure 5.4a (top panel) the characteristic velocity plots are shown for $\phi > 3.4$ eV, where the signal is proportional to the coverage. For these high work functions the characteristic velocity, represented by the slope of the line, is constant. This indicates that at high work functions the noble gas ions are neutralised by a mechanism insensitive to work function changes. In addition, it is found that the extrapolation to infinite velocity gives the correct Ba coverage as calibrated by the Auger analysis.

In figure 5.4b (middle panel) the characteristic velocity plots are shown for $\phi < 3.4$ eV, where the signal decreases with increasing coverage. For comparison, the characteristic velocity plot for a work function of $\phi = 4.5$ eV is also shown. The figure clearly shows that the characteristic velocity increases with decreasing work function. Thus, at low work functions the noble gas ions can be neutralised by a mechanism where the neutralisation probability depends on the work function. Furthermore, it is apparent that the extrapolation to infinite velocity results in an overestimation of the Ba coverage. The explanation for this overestimation is given in section 5.4.4.

The characteristic velocities for Ne^+ ions scattered from the Ba atoms derived from these plots are shown in figure 5.5a versus the work function. The figure shows a constant characteristic velocity plateau at high work functions ($\phi > 3.4$ eV), and a linear increase of the characteristic velocity with decreasing work function at low work functions ($\phi < 3.4$ eV). Similar trends in

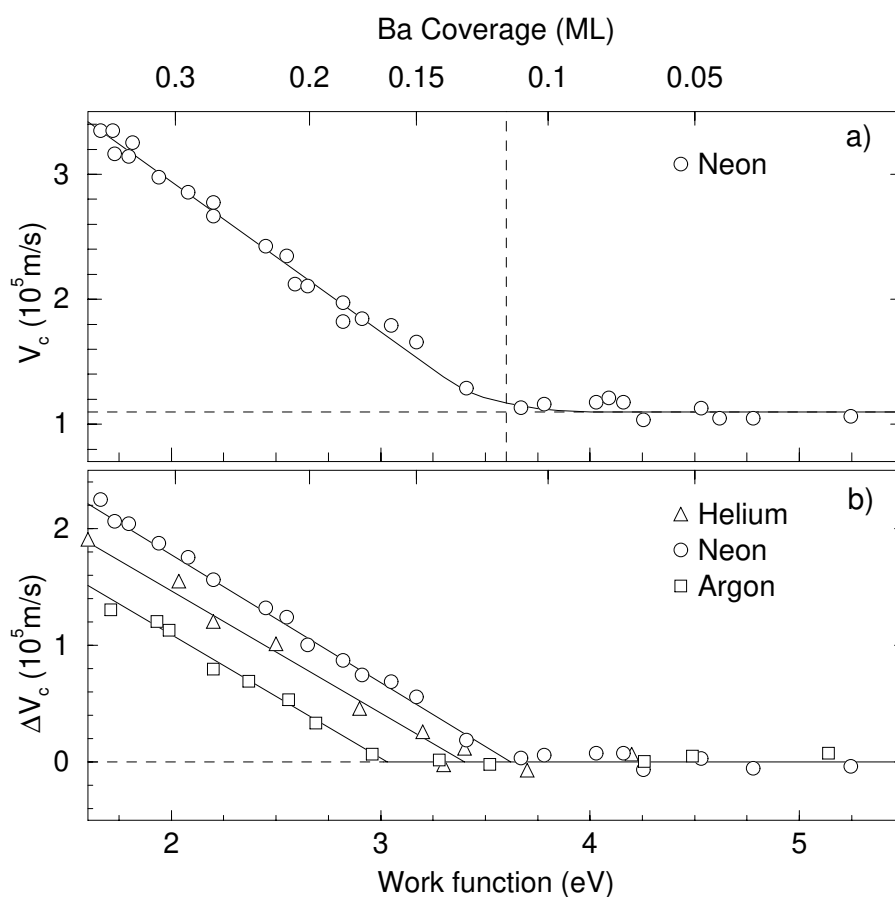


Figure 5.5. (a) The characteristic velocities for Ne^+ ions scattered from the Ba adatoms as a function of the work function. The vertical dashed line represents the onset of the low-work function mechanism. (b) The increase in the characteristic velocity for the different ions relative to the characteristic velocity at high work functions.

the characteristic velocity versus work function curve are observed for the different noble gas ions, only the work function below which the low-work function neutralisation channel is available depends on the ion type. For the different noble gas ions the increase in the characteristic velocity, relative to the constant characteristic velocity plateau observed at high work functions, is shown in figure 5.5b. For example, the Ne^+ curve in figure 5.5b is obtained by subtracting a value of $v_c=1.12\cdot 10^5 \text{ m}\cdot\text{s}^{-1}$ from the entire characteristic velocity curve in figure 5.5a. The characteristic velocity values of the high work function plateau depend on the ion type and thus are different for the He^+ , Ne^+ and Ar^+ ions. These characteristic velocity values are summarised in table 5.1 for the different ions.

	E_g (eV)	E_i (eV)	$\phi_{threshold}$ (eV)	$v_c(\text{Ba})$ ($10^5 \text{ m}\cdot\text{s}^{-1}$)	$v_c(\text{W})$ ($10^5 \text{ m}\cdot\text{s}^{-1}$)
Helium	24.6	4.77	3.2 ± 0.05	4.72 ± 0.15	3.20 ± 0.15
Neon	21.6	4.95	3.4 ± 0.05	1.12 ± 0.11	1.70 ± 0.08
Argon	15.8	4.21	2.9 ± 0.05	0.72 ± 0.08	1.81 ± 0.10

Table 5.1. Overview of the neutralisation results for the different ions scattered from Ba and W atoms. E_g =energy of the ground state. E_i =energy of the first excited level. ϕ_{onset} =work function threshold for low-work function mechanism. $v_c(\text{Ba})$ =characteristic velocity for Ba at $\theta_{\text{Ba}}=0 \text{ ML}$. $v_c(\text{W})$ =characteristic velocity for W at $\theta_{\text{Ba}}=0 \text{ ML}$.

5.4.3 Auger versus collision-induced neutralisation

In this section we discuss the nature of the basic neutralisation mechanism that is available at all work functions. The resonant neutralisation mechanism can only take place at low work functions and is therefore not considered here (see section 5.4.4). The neutralisation of the noble gas ions can thus take place by either Auger neutralisation, or collision-induced neutralisation. Here we show how the relative importance of these mechanisms depends on the place of the target atom in the periodic system. Moreover, we show that for alkali and earth-alkali elements, like Ba, the collision-induced neutralisation is the dominant mechanism in the initial energy range investigated here. We focus on the results for He^+ ions since most of the neutralisation studies that are available in the literature for comparison are for He^+ ions. Figure 5.6 presents the characteristic velocities for He^+ scattered from various targets throughout the periodic system as determined by Mikhailov et al. [31] using an initial energy range of 1-3.5 keV (open symbols). The characteristic velocities for He^+ scattered from the Ba and W atoms in the high work function limit ($\phi > 3.4 \text{ eV}$) are indicated by crosses (x). In addition, figure 5.6 shows the reionisation probabilities for He^+ ions of various target atoms as determined by Souda et al. (closed symbols) [30]. The striking similarity between the reionisation and neutralisation trends across the periodic system strongly suggest that the collision-induced neutralisation plays an important role in the neutralisation of noble gas ions [31]. As discussed in section 5.2 the reionisation involves the same level promotion as the collision-induced neutralisation.

The observed trends for the reionisation have been qualitatively explained by the work of Tsukada et al., who calculated the level promotion of the ground state during the close encounter of He^+ ions and various target atoms [33,34]. These calculations show that for the VIII-II_b elements no or little promotion takes place, while for the elements in the first columns of the periodic system the ground state of the noble gas ions is strongly promoted. Thus, the

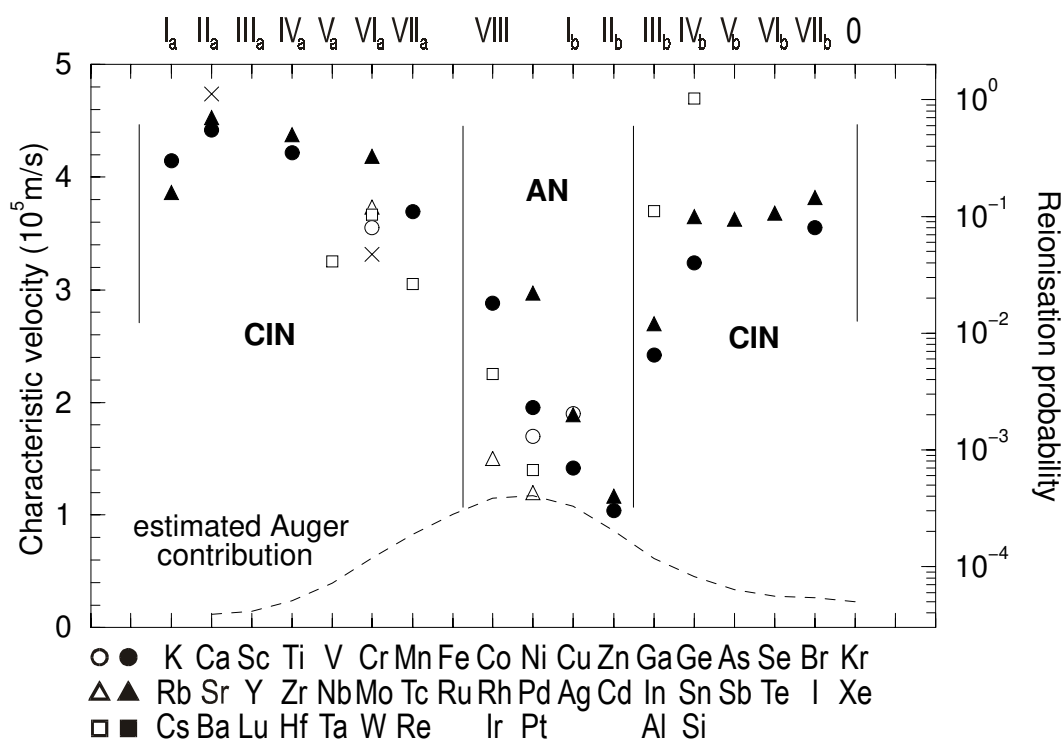


Figure 5.6. The characteristic velocities for He^+ ions scattered from various elements in the periodic table as measured by Mikhailov et al. [31] (open symbols). For comparison, the reionisation probabilities as measured by Souda et al. [30] are also shown (closed symbols). The characteristic velocities for He^+ scattered from Ba and W are indicated by the crosses (x). The dashed line represents the estimated Auger contribution based on the electron density and assuming a dominant Auger neutralisation for Pd.

minimum in the characteristic velocities in figure 5.6 around the VIII-II_b elements is caused by the absence of sufficient promotion, and the resulting absence of collision-induced neutralisation.

Goldberg et al. performed ab initio calculations of the neutralisation of He^+ ions scattered from Pd, and concluded that in this case collision-induced neutralisation is not significant but that Auger neutralisation is dominant [22]. Assuming that the characteristic velocity for Pd in figure 5.6 is completely due to Auger neutralisation, we can estimate the upper limit of the Auger contributions across the periodic system. The Auger neutralisation rate is in first order approximation proportional to the square of the density of electrons available for the transition (see section 5.2). The thus estimated Auger contribution is indicated in figure 5.6 by the dashed curve. The electron density was calculated by dividing the number of valence electrons by the atomic volume.

We conclude that for the neutralisation of He^+ ions backscattered from the Ba adatoms, and all other alkali and earth-alkali elements, the Auger mechanism plays no significant role and the neutralisation thus must be dominated by the collision-induced neutralisation at high work functions. We emphasise that we only claim this conclusion for the initial energies used here. At lower energies (<0.5 keV) the collision-induced neutralisation will often not be possible due to the threshold energy for sufficient promotion, and the neutralisation will be dominated by Auger neutralisation. Furthermore, here we only consider small impact parameters that are required for the ions to be backscattered. At large impact parameters the ground level

promotion is not sufficient for the collision-induced neutralisation to take place, and the Auger neutralisation will be the dominant mechanism.

The dominance of the collision-induced neutralisation here is in agreement with the work function independence of the characteristic velocity. The ground state promotion of the ions is determined by the core levels of the target, and the resulting resonant charge transfer involves the levels at the bottom of the conduction band. The neutralisation probability due to the collision-induced neutralisation is therefore not expected to be sensitive to work function changes. Although the characteristic velocity increases at low work functions, the neutralisation due to the collision-induced mechanism is work function independent over the whole work function range investigated. The contribution of the collision-induced neutralisation is indicated in figure 5.5a by the horizontal dashed line. The characteristic velocity due to the resonant neutralisation at low work functions is superimposed on the characteristic velocity due to the collision-induced neutralisation.

In our work a similar neutralisation behaviour is observed for the He^+ , Ne^+ and Ar^+ ions (see figure 5.5b). This suggests that the collision-induced neutralisation is also the dominant mechanism for Ne^+ and Ar^+ ions. However, definite conclusions can only be made after more results for the neutralisation of these ions from various targets across the periodic system become available (like figure 5.6).

5.4.4 Resonant neutralisation at low work functions

In order to show that the neutralisation of noble gas ions at low work function takes place by resonant neutralisation to the first excited level, we will demonstrate that the neutralisation behaviour observed in this work can be described by the resonant charge exchange theory. We start by deducing that part of the neutralisation probability that is exclusively due to the resonant neutralisation at low work functions. The approach is demonstrated in figure 5.3 for Ne^+ ions. The proportionality between signal and coverage observed for $\theta_{\text{Ba}} < 0.12$ ML is extrapolated to larger coverages as is indicated by the dashed line. The extrapolation is only shown up to $\theta_{\text{Ba}} = 0.15$ ML, but actually extends to a signal intensity of $1.8 \cdot 10^5$ counts/nC for a coverage of $\theta_{\text{Ba}} = 0.4$ ML. This line thus represent the hypothetical ion scattering signal in case the collision-induced and Auger neutralisation would be the only available mechanisms, the resonant neutralisation being absent. The decrease of the measured signal compared to the dashed line is thus ascribed to the resonant neutralisation. The ion fraction due to this mechanism is obtained by dividing the measured signal intensity (solid curve in figure 5.3) by the hypothetical signal intensity (dashed line in figure 5.3). The resulting ion fractions for Ne^+ scattered from Ba are shown in figure 5.7 on a logarithmic scale versus the work function for the different initial energies. It is observed that the ion fraction decreases exponentially with a decreasing work function, where the rate of decrease diminishes with increasing initial energy. Moreover, the work function below which the resonant neutralisation is possible depends on the initial energy of the ions.

These observations can be explained as follows. When the work function is decreased, the Fermi level is raised. The fraction of the broadened first excited level that is filled at the freezing distance thus increases (see figure 5.1). Therefore, the neutralisation probability increases with decreasing work function. Resonant charge exchange theory predicts for the ion fraction [40,69]:

$$P^+ = \exp\left(-C \cdot \frac{|\epsilon_a - \epsilon_F|}{\gamma \cdot v}\right) \quad (5.4)$$

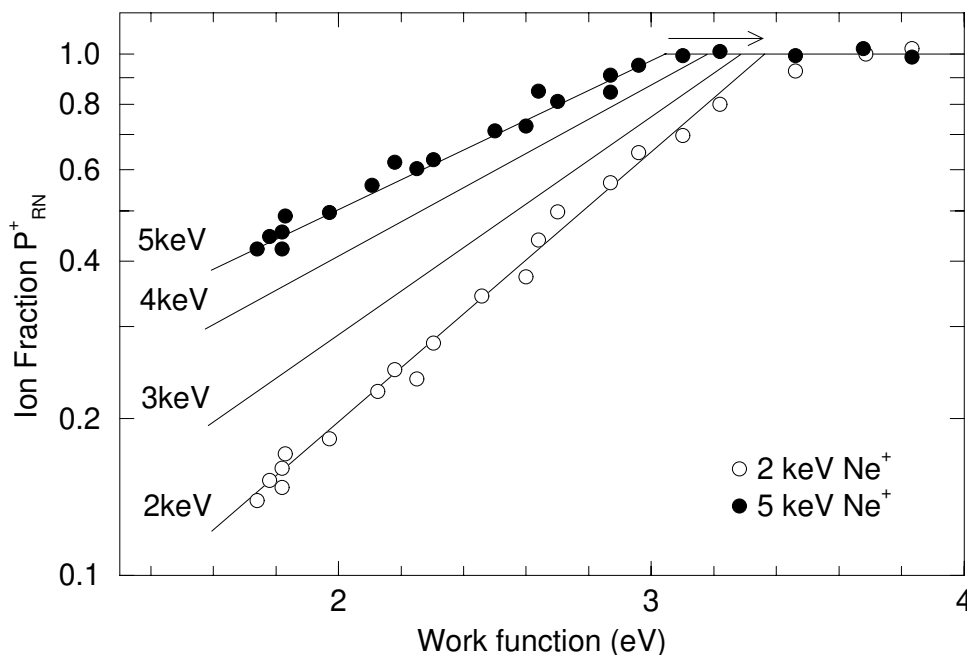


Figure 5.7. Ion fraction exclusively due to the resonant neutralisation mechanism. Note the logarithmic scale of the ion fraction. Only the 2 keV and 5 keV data points are shown for clarity. The arrow indicates the difference in onset of the low-work function mechanism.

Here C is a constant, ε_a is the energy of the first excited state at the freezing distance, and ε_F is the Fermi level of the metal (see figure 5.1). The velocity is defined as $v=v_f^\perp$ because the neutralisation probability is determined on the outgoing trajectory. The decay constant γ describes the decrease of the width $\Delta(z)$ of the first excited level with increasing distance z between the ion and the surface:

$$\Delta(z) = \Delta_0 \cdot e^{-\gamma \cdot z} \quad (5.5)$$

The exponential decrease of the ion fraction with the decreasing work function as observed in figure 5.7 is thus consistent with the theory. Moreover, eq. (5.4) predicts that the characteristic velocity increases linearly with decreasing work function, as was observed in figure 5.5. The increase of the characteristic velocity with decreasing work function is similar for the different ions (see figure 5.5b), which suggests that the decay constants γ are comparable for the ions. Although to our knowledge no reports are available in the literature where the decay constants of the different noble gas ions are compared [70], this similarity is expected since calculations of the level widths for alkali ions show the decay constants are comparable for the various alkali ions [71].

The resonant neutralisation to the first excited level is not possible if the Fermi level is equal to the energy of the excited level when the ion is at rest at infinite distance from the surface (see figure 5.1). This is consistent with figure 5.5, where the work function below which the resonant neutralisation is possible for the different ions is approximately 1.5 eV lower than expected based on the energy of the level at infinite distance from the surface (see table 5.1).

This lower work function compared to the energy of the first excited level is caused by the level shift of the ions near the surface [69,72,73]. The level shift of the first excited levels is of the order of 1-2 eV a few Ångstrom from the surface where the charge state is frozen [24,25]. For resonant neutralisation to take place, the Fermi level has to be near or above the energy of the first excited level at the freezing distance. Hence, the energy ε_a is defined at the freezing distance. For example, if in figure 5.1 the Fermi edge is aligned with the energy of the first excited level when the ion is at infinite distance from the surface (dashed line in figure 5.1), no neutralisation is possible. The difference between the energy of the first excited level and the work function threshold for the resonant neutralisation is similar for the different ions because the level shifts of the ions are comparable at the freezing distance [24,25].

The dependence of the work function threshold on the energy of the ions, as seen in figure 5.7, occurs because the freezing distance decreases with increasing velocity [37,38]. When the freezing distance decreases, the energy ε_a increases, and thus the work function below which the resonant neutralisation can take place decreases. Note that in studies of the neutralisation of alkali ions no clear dependence of the work function threshold for the resonant neutralisation on the energy of the ions is observed at energies well below 1 keV, because the level shift changes very little with distance at large (freezing) distances. The fact that the work function below which the resonant neutralisation is possible depends on the ion energy implies that for a fixed work function the relative importance of the collision-induced neutralisation and resonant neutralisation depends on the energy. This is demonstrated in figure 5.4c, where a characteristic velocity plot is shown for a work function $\phi=2.8$ eV (filled circles). For comparison, the characteristic velocity plot for $\phi=4.5$ eV where only the collision-induced neutralisation is possible is also shown (open circles). The dashed line corresponds to the hypothetical neutralisation behaviour at $\phi=2.8$ eV in the absence of the resonant neutralisation. The decrease of the measured signal compared to the dashed line is caused by the resonant neutralisation. As expected from figure 5.7, at a work function of $\phi=2.8$ eV the resonant neutralisation has a very small influence for an initial energy of 5 keV, but does lead to a significant signal decrease for lower initial energies. Because the relative importance depends on the initial energy, the characteristic velocity method cannot be used to derive the coverage from the extrapolation to infinite velocity; this extrapolation may only be used if the relative importance of the various neutralisation mechanisms is independent of the energy. Figure 5.4c shows that the extrapolation leads to an overestimation of the derived Ba coverage. Note that the extrapolation of the dashed line in figure 5.4c indicates the correct coverage since here only one mechanism is available: collision-induced neutralisation. The implications of these observations for a quantitative compositional surface analysis using LEIS at low-work function systems will be discussed in future work.

We can conclude that at low work functions noble gas ions can be neutralised by a resonant electron transfer to the first excited level of the ion. All observations can be described by the resonant charge exchange theory used for the neutralisation of low-energy alkali ions.

5.4.5 Macroscopic work function versus local potential

Investigations of the resonant neutralisation of low energy alkali ions have shown that the neutralisation probability is governed by the macroscopic work function [69,71,74]. A freezing distance of the order of a few Ångstrom is in agreement with the concept of the macroscopic work function, since at this distance the local potential of the individual atoms is smeared out and the electron distribution is rather smooth. However, most of these alkali studies have used initial ion energies well below 1 keV. To validate whether the concept of the macroscopic work function can be extrapolated to higher initial energies and smaller

freezing distances, or whether the local potential of the atoms starts playing a role, the method of inducing the work function changes was varied. A comparison of the neutralisation behaviour of the Ba/W, Ba/Re, and Ba/O/W systems is shown in figure 5.8, where the characteristic velocities for Ne^+ ions scattered from the Ba adatoms in these different systems are shown versus the work function (see also section 5.3.2). Note that the oxygen in the Ba/O/W system is positioned in the plane between the Ba and W atoms and does not shield the Ba atoms from the incident ions [15,75]. The solid curve in the figure is identical to the curve fitted to the characteristic velocities for Ba in the Ba/W(110) system as shown in figure 5.5a.

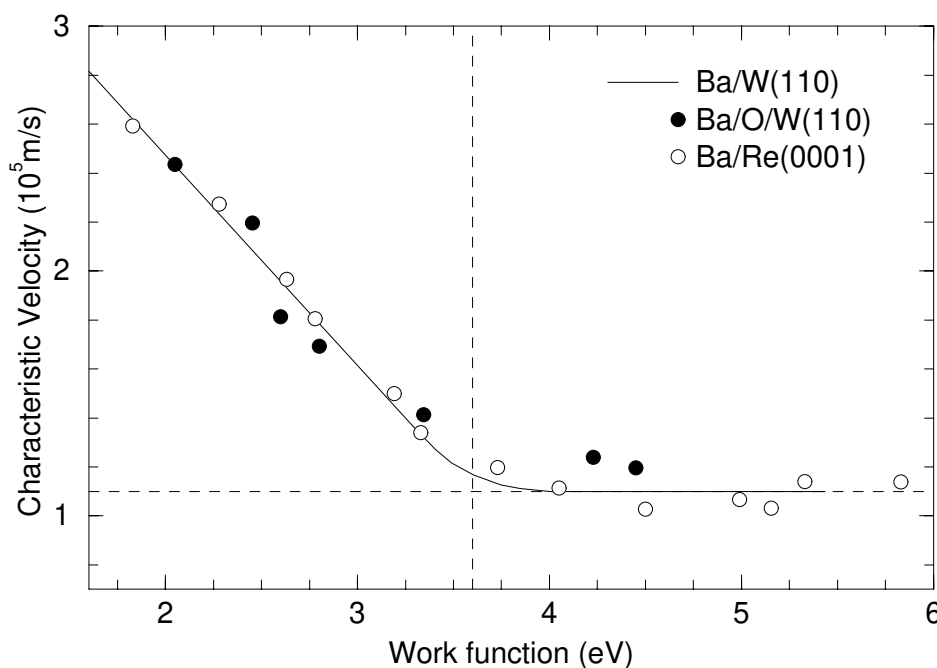


Figure 5.8. Influence of the method of inducing the work function change. The characteristic velocities for Ne^+ ions scattered from Ba in the Ba/O/W(110) and Ba/Re(0001) systems are shown versus the work function. The solid curve is identical to the solid curve fitted to the Ba/W(110) curve in figure 5.5a.

For the different systems, the characteristic velocity shows the same dependence on the work function, independent of the method of inducing the work function changes. However, the local potentials of the Ba atoms at a certain work function are not identical. The work function decrease for the Ba/W system is achieved by increasing the number of Ba-W dipoles, where the dipole strength remains approximately constant up to a coverage of $\theta_{\text{Ba}}=0.3$ ML. In contrast, for the Ba/O/W system the density of the dipoles equals the Ba density at the work function minimum. However, due to the adsorption of oxygen the average dipole strength decreases, and the work function increases. Therefore, for the same macroscopic work function, both systems have different local potentials of the Ba atoms. Similarly, because the work function of the clean Re(0001) substrate is larger than for the clean W(110) substrate ($\phi_{\text{Re}}=6.0$ eV), an identical macroscopic work function for the Ba/W and the Ba/Re system

requires a different dipole arrangement. We can thus conclude that also for noble gas ions at initial energies of a few keV, the neutralisation probability of the resonant mechanism is governed by the macroscopic work function.

5.4.6 Scattering from adatoms and substrate atoms

In a similar manner as for Ba, the neutralisation behaviour has been investigated for noble gas ions scattered from the W substrate atoms not covered by the Ba adatoms in the Ba/W(110) system. Figure 5.9 shows the derived characteristic velocities for Ne^+ ions scattered from the W atoms versus the work function (filled circles). The lower solid curve represents the results for scattering from the Ba adatoms and is reproduced from figure 5.5a. The long-dashed curve represents the expected characteristic velocity versus work function curve for W, where the value of the characteristic velocity at high work functions is taken from the characteristic velocity for clean W. Since the resonant neutralisation is governed by the macroscopic work function and is not influenced by the type of target atom, the resonant neutralisation should be available below the same work function as for Ba. Moreover, the slope of the increase of the characteristic velocity as a function of the work function is also expected to be the same for scattering from Ba and W atoms.

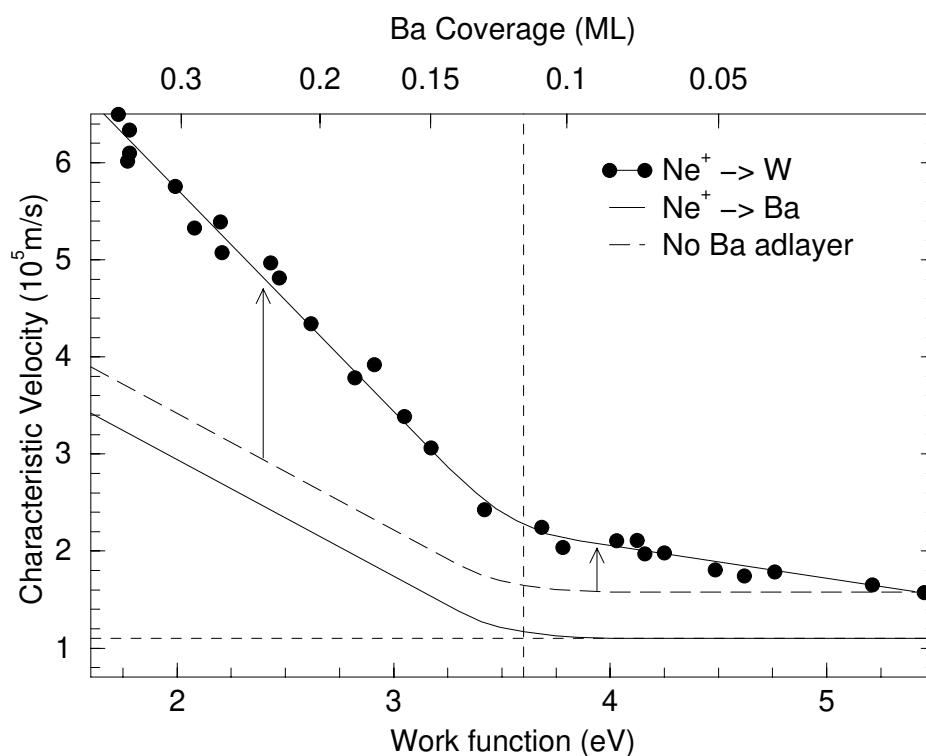


Figure 5.9. The characteristic velocities of Ne^+ ions scattered the W substrate atoms as a function of the work function. The vertical dashed line represents the onset of the low-work function mechanism. The long-dashed curve represent the expected neutralisation behaviour for W on the basis of the Ba investigations, but without the additional neutralisation by the Ba adatoms.

It is obvious in figure 5.9 that, although the resonant neutralisation is possible for $\phi < 3.4$ eV as expected, the slope of the characteristic velocity as a function of the work function is steeper than expected. Apparently, additional neutralisation takes place for scattering from the W substrate atoms compared to the scattering from the Ba adatoms. This increased neutralisation probability occurs because the ions that scatter from the W substrate atoms must traverse through the Ba adlayer on the incoming and outgoing path. An ion that scatters from a W substrate atom, and passes close to a Ba adatom before or after the violent collision with the W atom, can have an additional interaction with the Ba atom. Even though the ion can survive the interaction with the W atom as an ion, the interaction with the Ba adatom can still neutralise the ion. Consequently, if the ion passes at close distance from a Ba adatom, the effective neutralisation probability for the complete trajectory is larger than the expected probability for the single interaction with the W atom. At low Ba coverage the distance between the Ba atoms is large, and only a small fraction of the ions that scatter from the W atoms pass close enough to the Ba atoms to have the additional interaction. With decreasing work function and the associated increasing coverage, the inter-atomic Ba distance decreases, and the fraction of ions that scatter from W and pass at close distance from the Ba adatoms increases. The average additional neutralisation probability due to the Ba adlayer thus increases with increasing coverage and decreasing work function. The arrows in figure 5.9 indicate the increase in the characteristic velocity due to the additional neutralisation by the Ba adlayer. Consequently, the slope of the characteristic velocity versus the work function is steeper for scattering from the substrate atoms than for the adatoms. Moreover, no constant characteristic velocity plateau is observed at high work functions.

The difference in the neutralisation behaviour for scattering from the substrate atoms and from the adatoms has been attributed to additional neutralisation for ions scattering from the substrate atoms due to the presence of the adlayer. The neutralisation details for the interaction between the ion and the substrate atom are thus obscured by the adlayer. The additional neutralisation could be deduced because we separately investigated the neutralisation of the ions scattered from the Ba atoms and the W atoms. In cases where no such differentiation is made, the interpretation of the observed neutralisation behaviour for the substrate atoms is not straightforward.

5.5 Conclusions

In this paper we have investigated the work function dependence of the neutralisation of noble gas ions. This was accomplished by studying the neutralisation probability of He^+ , Ne^+ and Ar^+ ions scattered from Ba atoms on surfaces having different work functions. From the literature it is known that low-energy noble gas ions can be neutralised by different mechanisms: collision-induced neutralisation, Auger neutralisation, and resonant neutralisation. (Exceptional mechanisms, like the quasi-resonant core-level neutralisation, are not considered here.) The distances between the ion and its scattering partner at which the various neutralisation probabilities are determined are characteristic for each mechanism, and are of the order of 0.5 Å, 2 Å, and 4 Å respectively. Along the ion trajectory these different neutralisation mechanisms can thus occur independently. Which mechanism(s) takes place, and what the neutralisation probability due to a particular mechanism is, depends on the ion-target combination, on the work function, and on the initial energy of the ions.

The collision-induced and Auger neutralisation are possible at all work functions. The relative importance of both mechanisms depends strongly on the ion-target combination. Through combining the results of previous neutralisation studies available in the literature, and the

insights from our investigations, we have shown that for noble gas ions scattered from Ba atoms and other (earth) alkali elements the collision-induced neutralisation is the dominant process. We only claim this dominance for the initial energies and small impact parameters used here. At lower energies (<0.5 keV) the collision-induced neutralisation might not be possible because the ground state is insufficiently promoted, and the neutralisation would be dominated by Auger neutralisation. The neutralisation probability due to the collision-induced neutralisation is insensitive to work function changes since the promotion details depend on the core levels of the target atoms. Moreover, since the collision-induced neutralisation takes place during the close encounter between the ion and the target atom, the neutralisation probability is expected to be also insensitive to the scattering geometry.

Resonant neutralisation to the first excited level of the noble gas ions is possible at low work functions. The work function dependence of the neutralisation probability at low work functions is consistent with the resonant charge exchange theory as determined for the work function dependent neutralisation of alkali ions. Although several reports in the literature have suggested the possibility of this mechanism at low work functions, to our knowledge this is the first time that it has actually been shown that resonant neutralisation indeed takes place.

The resonant neutralisation is only possible below a certain work function, and this work function threshold depends on the ionisation potential of the first excited level and on the velocity of the ion. The neutralisation probability due to the resonant mechanism increases exponentially with decreasing work function, while the rate of increase is determined by the velocity of the ion and the decay constant of the level width. In contrast to the Auger and collision-induced neutralisation, the neutralisation probability for this resonant channel is not determined by the specific ion-target combination, but rather is governed by the macroscopic work function. Consequently, the neutralisation probability is determined by the velocity of the ion perpendicular to the surface, and thus depends not only on the energy of the ion but also on the scattering geometry.

Acknowledgements

We would like to thank prof.dr. Peter Bauer and dr. Carmina Monreal for the discussions of the neutralisation mechanisms.

References

- 1 D.P. Smith, J. Appl. Phys. 38 (1967) 340.
- 2 H.H. Brongersma, P.M. Mul, Chem. Phys. Lett. 14 (1972) 380.
- 3 H. Niehus, W. Heiland, E. Taglauer, Surf. Sci. Rep. 17 (1993) 213.
- 4 E. Taglauer, "Ion scattering Spectroscopy", in Ion Spectroscopies for Surface Analysis, Eds. A.W. Czanderna, D.M. Hercules, Plenum Press, New York, 1991.
- 5 H.H. Brongersma, P.A.C. Groenen, J.-P. Jacobs, in *Science of Ceramic Interfaces II*, p. 113-182, Ed. J. Nowotny, Material Science Monographs 81, Elsevier Science B.V., Amsterdam, 1994.

- 6 T.G. Vargo, J.A. Gardella, R.L. Schmitt, K.J. Hook, T.J. Hook, L. Salvati, *Low-Energy Ion Scattering Spectrometry of Polymer Surface Composition and Structure*, in *Surface Characterisation of Advanced Polymers*. Eds. L. Sabbatini, P.G. Zambonin, 1993.
- 7 G. Andersson, M. Morgner, *Surf. Sci.* 405 (1998) 138.
- 8 M. Tassotto, T.J. Gannon, P.R. Watson, *J. Chem. Phys.* 107 (1197) 8899.
- 9 I. Peeters, A.W. Denier van der Gon, M.A. Reijme, P.J. Kooyman, A.M. de Jong, J. van Grondelle, H.H. Brongersma, R.A. van Santen, *J. Catal.* 173 (1998) 28.
- 10 L.C.A. van den Oetelaar, O.W. Nooij, S. Oerlemans, A.W. Denier van der Gon, H.H. Brongersma, *J. Phys. Chem. B* 102 (1998) 3445.
- 11 M.P. de Jong, D.P.L. Simons, M.A. Reijme, L.J. van IJzendoorn, A.W. Denier van der Gon, M.J.A. de Voigt, H.H. Brongersma, R.W. Gymer, *Synth. Met.*, to be published.
- 12 C.R.K. Marrian, A. Shih, G.A. Haas, *Appl. Surf. Sci.* 24 (1985) 372.
- 13 A.W. Denier van der Gon, M.F.F.K. Jongen, H.H. Brongersma, U. van Slooten, A. Manenschijn, *Appl. Surf. Sci.* 111 (1997) 64.
- 14 H.H. Brongersma, W.J. Schouten, *Acta Electronica* 18 (1975) 47.
- 15 M.J. Ashwin, D.P. Woodruff, *Surf. Sci.* 244 (1991) 247.
- 16 M. Beckschulte, E. Taglauer, *Nucl. Instr. Meth. B* 78 (1993) 29.
- 17 R. Cortenraad, A.W. Denier van der Gon, H.H. Brongersma, G. Gaertner, A. Manenschijn, *Appl. Surf. Sci.* 146 (1999) 69.
- 18 R. Souda, M. Aono, *Nucl. Instr. Meth. B* 15 (1986) 114.
- 19 MacDonald RJ, Matin PJ, *Surf. Sci.* 111 (1981) L739
- 20 G. Verbist, J.T. Devreese, H.H. Brongersma, *Surf. Sci.* 233 (1990) 323.
- 21 D.P. Woodruff, *Nucl. Instr. Meth.* 194 (1982) 639.
- 22 L.K. Verhey, B. Poelsema, A.L. Boers, *Nucl. Instr. Meth.* 132 (1976) 565.
- 23 A.L. Boers, *Nucl. Instr. Meth. B* 4 (1984) 98.
- 24 H.D. Hagstrum, *Phys. Rev.* 96 (1954) 336.
- 25 H.D. Hagstrum: *Inelastic Ion-Surface Collisions*, Editors H.H. Tolk, J.C. Tully (Academic Press, New York, 1977), p. 1.
- 26 M. Aono, R. Souda, *Nucl. Instr. Meth. B* 27 (1987) 55.
- 27 W. More, J. Merino, R. Monreal, P. Pou, F. Flores, *Phys. Rev. B* 58 (1998) 7385.
- 28 N. Lorente, R. Monreal, *Surf. Sci.* 370 (1997) 324.
- 29 N. Lorente, R. Monreal, M. Alducin, *Phys. Rev. A.* 49 (1994) 4716.
- 30 R. Souda, T. Aizawa, C. Oshima, Y. Ishizawa, *Nucl. Instr. Meth. B* 45 (1990) 364.
- 31 S.N. Mikhailov, R.J.M. Elfrink, J.-P. Jacobs, L.C.A. van den Oetelaar, P.J. Scanlon, H.H. Brongersma, *Nucl. Instr. Meth. B* 93 (1994) 148.
- 32 E.C. Goldberg, R. Monreal, F. Flores, H.H. Brongersma, P. Bauer, *Surf. Sci.* 440 (1999) L875.
- 33 M. Tsukada, S. Tsuneyuki, N. Shima, *Surf. Sci.* 164 (1985) L811.
- 34 S. Tsuneyuki, M. Tsukada, *Phys. Rev. B* 34 (1986) 5758.
- 35 R. Souda, T. Aizawa, C. Oshima, S. Otani, Y. Ishizawa, *Phys. Rev. B* 41 (1990) 803.
- 36 T.M. Thomas, H. Neumann, A.W. Czanderna, *Surf. Sci.* 175 (1986) L737.
- 37 R. Brako, D.M. Newns, *Rep. Prog. Phys.* 52 (1989) 655.
- 38 J. Los, J.J.C. Geerlings, *Phys. Rep.* 190 (1990) 134.
- 39 E.G. Overbosch, B. Rasse, A.D. Tenner, J. Los, *Surf. Sci.* 92 (1980) 310.
- 40 J.K. Norskov, B.L. Lundqvist, *Phys. Rev. B.* 19 (1979) 5661.
- 41 R.J.A. van den Oetelaar, C.F.J. Flipse, *Phys. Rev. B* 52 (1995) 10807.

- 42 H.D. Hagstrum, P. Petrie, E.E. Chaban, Phys. Rev. B 38 (1988) 10264.
- 43 R. Souda, W. Hayami, T. Aizawa, S. Otani, Y. Ishizawa, Phys. Rev. B 46 (1992) 7315.
- 44 H. Mueller, R. Hausmann, H. Brenten, A. Niehaus, V. Kempfer, Z. Phys. D 28 (1993) 109.
- 45 F. Wieggershaus, S. Krischok, D. Ochs, W. Maus-Friedrichs, V. Kempfer, Surf. Sci. 345 (1996) 91.
- 46 W. Sesselmann, B. Woratschek, J. Kueppers, G. Ertl, Phys. Rev. B 35 (1987) 1547.
- 47 D.J. Godfrey, D.P. Woodruff, Surf. Sci. 105 (1981) 438.
- 48 D.J. Godfrey, D.P. Woodruff, Surf. Sci. 105 (1981) 459.
- 49 W. Bloss, D. Hone, Surf. Sci. 72 (1978) 277.
- 50 R. Cortenraad, A.W. Denier van der Gon, H.H. Brongersma, Surf. Interface Anal. to be published.
- 51 A.P. Janssen, P. Akhter, C.J. Harland, J.A. Venables, Surf. Sci. 93 (1980) 453.
- 52 G. Eng, H.K.A. Kan, Appl. Surf. Sci. 8 (1981) 81.
- 53 H. Oechsner, Fresenius J. Anal. Chem. 355 (1996) 419.
- 54 E. Koch, W. Huisl (eds), "Gmelin Handbook of Inorganic and Organometallic Chemistry, Tungsten Supplement Volume A 6a", Springer-Verlag, Berlin, 1991.
- 55 S.N. Ermolov, R. Cortenraad, V.N. Semenov, A.W. Denier van der Gon, S.I. Bozhko, H.H. Brongersma, V.G. Glebovsky, Vacuum 53 (1999) 83.
- 56 K. Wandelt, "Work function Changes due to Alkali-Metal Adsorption", in "Physics and Chemistry of Alkali Metal Adsorption", Eds. H.P. Bonzel, A.M. Bradshaw, G. Ertl, Elsevier, Amsterdam 1989, p. 25.
- 57 H. Ishida, Phys. Rev. B 38 (1988) 8006.
- 58 E. Wimmer, A.J. Freeman, J.R. Hiskes, A.M. Karo, Phys. Rev. B 28 (1983) 3074.
- 59 D.A. Gorodetskii, Y.P. Melnik, Surf. Sci. 62 (1977) 647.
- 60 D.A. Gorodetskii, A.N. Knysh, Surf. Sci. 40 (1973) 651.
- 61 L.A. Hemstreet, S.R. Chubb, W.E. Pickett, Phys. Rev. B 40 (1989) 3592.
- 62 G.A. Haas, A. Shih, C.R.K. Marrian, Appl. Surf. Sci. 16 (1983) 139.
- 63 B.C. Lamartine, J. v. Czarnecki, T.W. Haas, Appl. Surf. Sci. 26 (1986) 61.
- 64 T. Asahata, M. Onubu, A. Kondo, R. Shimizu, H.J. Kang, Jpn. J. Appl. Phys. 36 (1997) 7427.
- 65 G. Molière, Z. Naturforsch. 2a (1947) 133.
- 66 C.A. Severijns, *Computer Simulation of Low-Energy Ion Scattering*, Ph.D. thesis, Eindhoven University of Technology, The Netherlands (December 1992).
- 67 J.-P. Jacobs, S. Reijne, R.J.M. Elfrink, S.N. Mikhailov, H.H. Brongersma, J. Vac. Sci. Technol. A 12 (1994) 2308.
- 68 G.C. Nelson, J. Appl. Phys. 47 (1976) 1253.
- 69 M.L. Yu, N.D. Lang, Nucl. Instr. Meth. B 14 (1986) 403.
- 70 C.A. Moyer, K. Orvek, Surf. Sci. 114 (1982) 295.
- 71 P. Nordlander, J.C. Tully, Surf. Sci. 211/212 (1989) 207.
- 72 M.L. Yu, N.D. Lang, Phys. Rev. Lett. 50 (1983) 127.
- 73 J.J.C. Geerlings, L.F. Kwakman, J.Los, Surf. Sci. 184 (1987) 305.
- 74 M.L. Yu, Phys. Rev. B 26 (1982) 4731.
- 75 D. Norman, R.A. Tuck, Phys. Rev. Lett. 58 (1987) 519.

On the Quantification of the Surface Composition of Low-Work Function Surfaces using Low-Energy Ion Scattering

6

Abstract

The quantification of the surface composition of low-work function systems using low-energy ion scattering is strongly influenced by resonant neutralisation of the noble gas ions. Below a certain threshold in the work function, resonant neutralisation to the first excited level of the ion is possible, and the neutralisation probability of the ions increases exponentially with decreasing work function. We show how to correct for these matrix effects and perform the quantification using the characteristic velocity method. The discussion and conclusions here are relevant for all ion scattering studies using low-energy noble gas ions on surfaces with a work function below approximately 4 eV.

6.1 Introduction

Low-energy ion scattering (LEIS) using noble gas ions is widely applied for quantitative compositional analysis of the outermost atomic layer of surfaces [1,2,3,4,5]. The list of applications ranges from fundamental studies of surface segregation in alloys, to investigations of real industrial systems like heterogeneous catalysts. A large number of reviews is available in the literature dealing with LEIS on many different types of surfaces [6]. For most systems the neutralisation in LEIS is found to be independent of the environment of the atoms (no matrix effects), and the quantification is straightforward when making use of reference samples of the species of interest with a known surface density. In the absence of matrix effects the neutralisation probability of the ions is identical on the sample under investigation and on the reference sample. Thus, if the samples are measured under identical experimental conditions, the quantification can be performed by comparing the ion scattering signals on both samples.

For systems with low work functions, the quantification of the surface composition is more elaborate. This paper deals with the application of LEIS for a quantitative analysis of surfaces with work functions lower than 3 to 4 eV. Several investigations have demonstrated that at these low work functions the neutralisation probability increases strongly with decreasing work function [7,8,9,10,11]. Recently we have demonstrated that at these low work functions an additional neutralisation mechanism takes place, where the noble gas ions are neutralised by resonant electron transfer to the first excited level of the ions [12] (see chapter 5). There, we described the neutralisation behaviour at low work functions using resonant charge exchange theory [13,14,15,16]. Here, we show how the occurrence of the resonant neutralisation at low work functions influences the quantification. We discuss the application of the characteristic velocity method in order to correct for the work function dependence of the neutralisation probability and perform quantitative LEIS at low-work function surfaces. In this work we used the well studied Ba/W(110) system [17,18] as an example to demonstrate the quantification, but the discussions and conclusions are relevant for LEIS investigations of low-work function systems in general.

6.2 Experimental

The quantification of the surface density of low-work function surfaces was investigated by adsorbing Ba atoms on a W(110) single crystal [12,17,18]. The ion scattering was performed in a UHV set-up with a base pressure of $1 \cdot 10^{-10}$ mbar by directing He^+ , Ne^+ , and Ar^+ ions with an initial energy between 2 keV and 5 keV perpendicular onto the surface [11,19]. The ions that were backscattered from the surface over an angle of 136° were energy analysed by a cylindrical mirror analyser (CMA) and detected using a microchannelplate-based detector. The ion scattering signals were corrected for the transmission of the analyser and the detection efficiency of the channelplates, as reported elsewhere [19]. The area of the Ba peak in the LEIS spectrum was used as a measure for the signal intensity.

The Ba coverage was varied between $\theta_{\text{Ba}} \approx 0$ ML and $\theta_{\text{Ba}} = 0.4$ ML ($1\text{ML} = 6.2 \cdot 10^{14} \cdot \text{atoms} \cdot \text{cm}^{-2}$), resulting in a work function range from $\phi = 5.4$ eV for the clean substrate, down to $\phi = 1.8$ eV for the work function minimum of the Ba/W(110) system. [17,18]. The Ba coverage was also determined by Auger electron spectroscopy (AES), a method insensitive to work function changes, so a validation of the Ba coverage derived by the ion scattering analysis was possible. The area of the Auger Ba peak at 600 eV in the direct electron spectrum was taken as a measure for the Auger signal. The calibration was performed by assigning the work function

minimum of $\phi=1.8$ eV to a coverage of $\theta_{Ba}=0.4$ ML, in agreement with detailed studies of the Ba/W(110) system reported in the literature [12,17,18]. The work functions for the different Ba coverages were derived from the onset of the secondary electron emission, where the secondary electrons were created by the AES electron beam [12,20,21,22].

6.3 Results and discussion

The neutralisation probability of the noble gas ions during the interactions with the surface atoms is expressed using the ion fraction P^+ . The ion fraction represents the probability that an incident ion leaves the surface as an ion after the interactions with the surface. In the characteristic velocity method the ion fraction is defined as $P^+=\exp(-v_c/v)$, where the characteristic velocity v_c is a measure for the neutralisation rate and the ion velocity v represents the time available for the neutralisation [5,10,11,13,23]. The characteristic velocity approach can be used to describe the neutralisation behaviour of the various neutralisation mechanisms for the noble gas ions [12,24]: the Auger neutralisation [23], the collision-induced neutralisation [25], and the resonant neutralisation [13]. The characteristic velocity v_c and the exact definition of the reciprocal velocity $1/v$ depend on the neutralisation mechanism [23,26,27]. In this paper we express the reciprocal velocity as $1/v=1/v_i+1/v_f$, with v_i and v_f the velocities of the ion during the incoming and outgoing trajectory respectively. However, note that the precise definition of the velocity only influences the value of the characteristic velocity, but does not affect the exponential dependence of the ion fraction on the velocity.

The application of the characteristic velocity method to derive the surface density of the species under investigation is based on the property that at infinite velocity no time is available for neutralisation and that the ion fraction thus equals unity ($P^+=1$). The approach is demonstrated in figure 6.1, which illustrates the application of the characteristic velocity using Ne^+ ions for a Ba coverage of $\theta_{Ba}=0.06$ ML (open circles) and for a Ba coverage of $\theta_{Ba}=0.18$ ML (filled circles). Here the ion scattering signal for Ba (S_{Ba}) is shown on the right ordinate scale versus $1/v_i+1/v_f$, which was varied by changing the initial energy of the ions. The measured ion scattering signal was corrected for the energy dependencies of the differential scattering cross-section (σ), the analyser transmission (T), and the detection efficiency (ϵ) [19]. The characteristic velocity v_c is equal to the slope of the linear fit (solid lines). The surface density of the species under investigation, in this case Ba, can be derived by extrapolation to infinite velocity ($P^+=1$). The Ba coverage is thus given by the intersection of the extrapolation with the left ordinate scale, where the coverage was calibrated using the AES analysis. We emphasise that the extrapolation based on the characteristic velocity method only yields the correct surface coverage if the neutralisation rate, i.e. the characteristic velocity v_c , is constant over the velocity range on which the extrapolation is based. If several neutralisation mechanisms occur simultaneously, the individual neutralisation rates of the separate mechanism must be constant, and the characteristic velocities for all mechanisms must be velocity independent.

At low coverages, corresponding to work functions above approximately 4 eV, the neutralisation of the ions scattered from the Ba atoms is dominated by the collision-induced neutralisation mechanism [12]. Since only one mechanism is dominant and the characteristic velocity is velocity independent, the extrapolation to infinite velocity at a work function of $\phi=4.5$ eV gives the correct Ba coverage of $\theta_{Ba}=0.06$ ML (see figure 6.1). Note that for other ion-target combinations the Auger mechanism might be dominant, for example He^+ ions

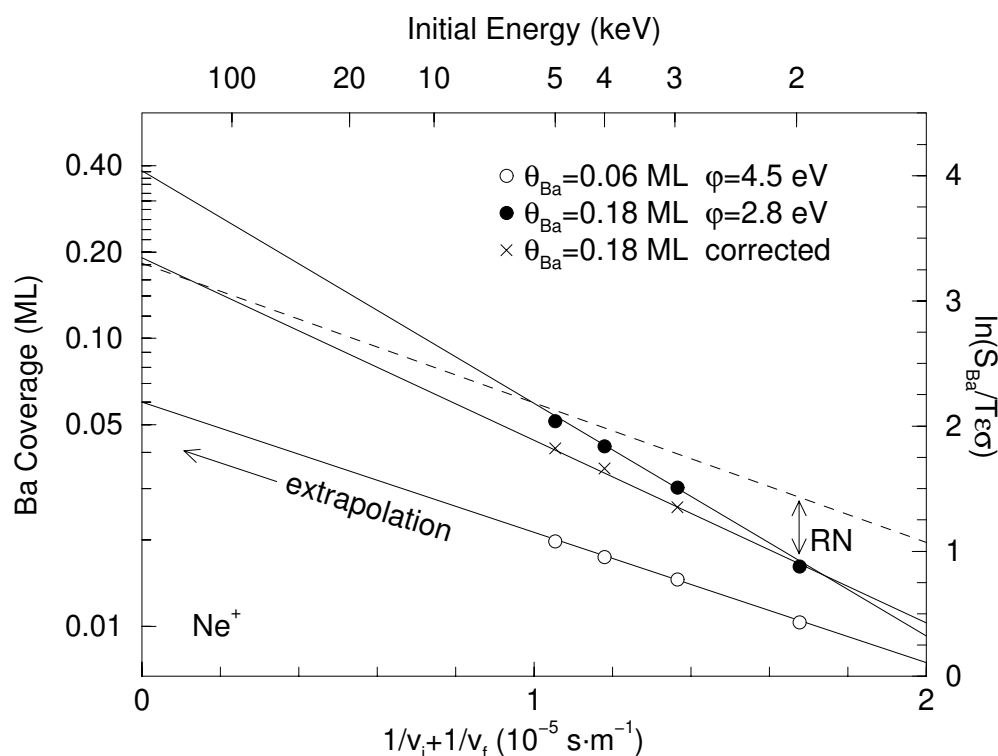


Figure 6.1. Characteristic velocity plots for different Ba coverages: $\theta_{Ba}=0.06$ ML (open circles) and $\theta_{Ba}=0.18$ ML (filled circles). The initial energy scale is shown on the top axis. The solid lines show linear regressions to the data, where the slopes represent the characteristic velocities. The dashed line represent the hypothetical signal in case no resonant neutralisation is possible at $\theta_{Ba}=0.18$ ML ($\phi=2.8$ eV).

scattered from Pd [25]. However, any combination of the collision-induced and Auger neutralisation will yield similar results, if the neutralisation constants (i.e. v_c) for both mechanisms are independent of the velocity.

At a work function of $\phi=2.8$ eV ($\theta_{Ba}=0.18$ ML) resonant neutralisation to the first excited level of the ion takes place in addition to the collision-induced neutralisation. It is evident in figure 6.1 that the extrapolation to infinite velocity results in an overestimation of the Ba coverage: $\theta_{Ba}=0.38$ ML instead of $\theta_{Ba}=0.18$ ML. This overestimation occurs because in the velocity range used here the characteristic velocity of the resonant neutralisation is not constant but depends on the velocity, as we show below and is also discussed in detail elsewhere [12] (see chapter 5). At all coverages and corresponding work functions where resonant neutralisation takes place, the Ba coverage is overestimated when the characteristic velocity method is applied straightforward. For Ne^+ ions figure 6.2 shows the Ba coverages derived from the extrapolation to infinite velocity versus the Ba coverages derived from the Auger analysis (open circles). Also shown are the Ba coverages derived by the characteristic velocity method using He^+ and Ar^+ ions, where only the fitted dashed curves are shown for clarity. The long-dashed line in the figure represents the correct coverage as determined by AES analysis. The work functions below which the resonant neutralisation is possible are marked by the arrows for the Ne^+ , He^+ , and Ar^+ ions (from left to right) [12]. At high work

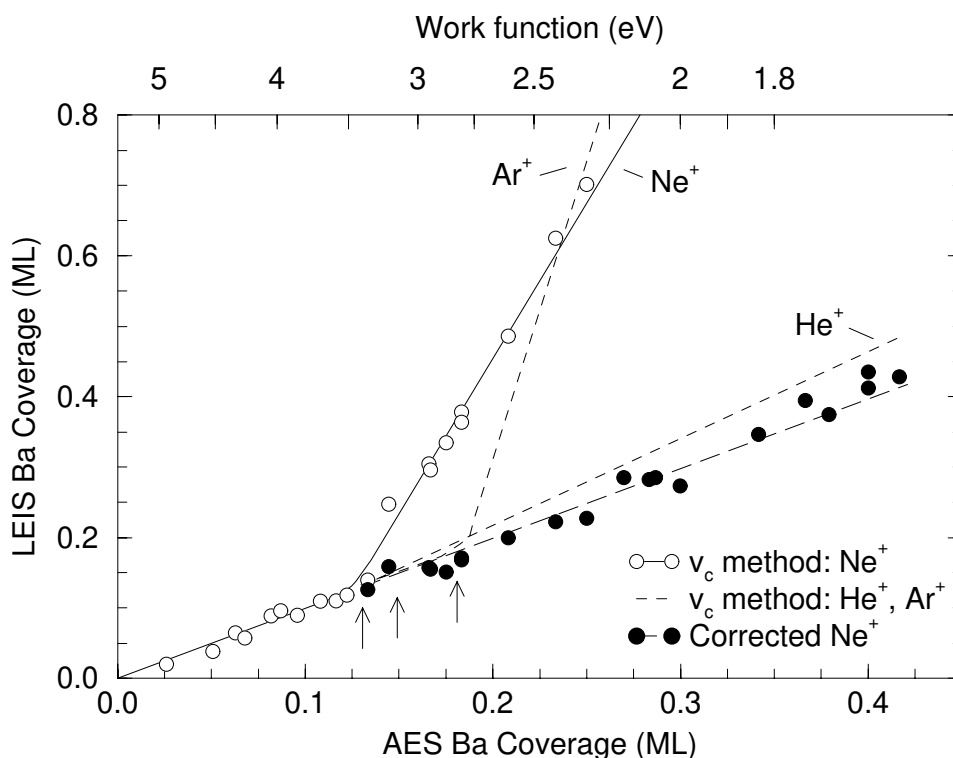


Figure 6.2. The Ba coverage determined by LEIS versus the Ba coverage from the AES analysis. For clarity the data points are only shown for Ne^+ ions: before (open circles) and after (filled circles) the correction for the influence of the resonant neutralisation. The arrows mark the workfunctions below which the resonant neutralisation is possible for the Ne^+ , He^+ and Ar^+ ions (from left to right).

functions, where no resonant neutralisation takes place, the LEIS Ba coverage derived from the extrapolation is within the accuracy of the measurements to the AES Ba coverage. However, when resonant neutralisation to the first excited level takes place it is evident that the characteristic velocity method yields an overestimated coverage, where the degree of overestimation depends on the work function and on the ion type.

To clarify the origin of the overestimation due to the resonant neutralisation we briefly discuss the resonant neutralisation mechanism. In this mechanism the neutralisation probability is determined on the outgoing trajectory [13-16]. Figure 6.3 schematically presents the level shift and level broadening due to the interaction between the first excited level and a metal surface on the outgoing ion trajectory. When the ion is near the surface, the population of the shifted and broadened level is in equilibrium with the substrate and will become partially occupied up to the Fermi edge. When the ion leaves the surface the population increases as long as the equilibrium is maintained. With increasing distance the charge exchange rate decreases, and eventually becomes small compared to the rate at which the level shifts and narrows. At a distance referred to as the freezing distance the equilibrium is “frozen” (approximately 2-4 Å), and the extent to which the level is filled at this distance determines the neutralisation probability and thus the ion fraction.

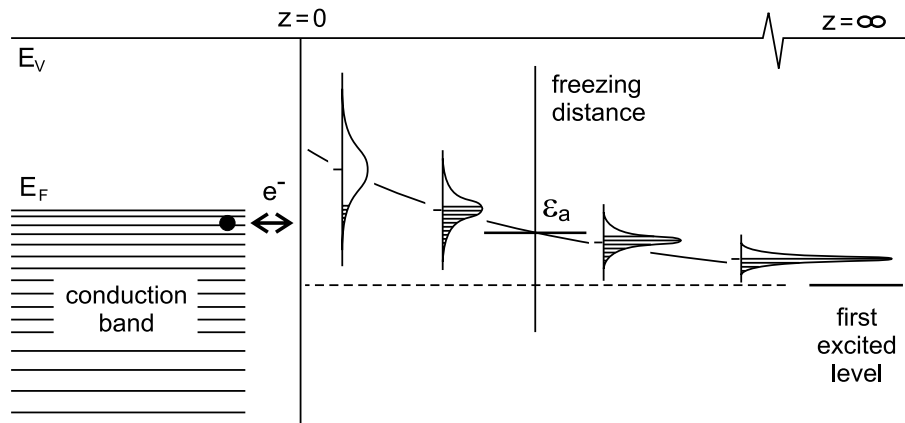


Figure 6.3. Schematic illustration of the fundamentals of the resonant neutralisation. See text for explanation.

Resonant charge exchange theory predicts for the ion fraction P_{RN}^+ [16,28]:

$$P_{RN}^+ = \exp\left(-C \cdot \frac{|\varepsilon_a - \varepsilon_F|}{v}\right) \quad (6.1)$$

Here ε_a is the energy of the first excited level at the freezing distance and ε_F is the Fermi level, where the energy ε_a is higher than the energy of the first excited level at infinite distance due to the level shift. The velocity v represent the velocity of the ion perpendicular to the surface on the outgoing trajectory. The resonant neutralisation is thus only possible when ε_a is above ε_F . However, the freezing distance decreases with increasing velocity of the ions, and consequently ε_a increases with increasing velocity of the ions. This implies that the work function below which the resonant neutralisation is possible depends on the ion velocity. The ion fraction P_{RN}^+ is shown in figure 6.4 for the different initial energies versus the work function, where only the 2 keV and 5 keV data points are shown for clarity. These ion fraction curves are taken from previous investigation [12], where the Ba/W(110) system was used in an identical manner to study the resonant neutralisation mechanism of the noble gas ions at low work functions (see chapter 5). Note that the ion fraction P_{RN}^+ represents the ion fraction in case only resonant neutralisation occurs, and no other neutralisation mechanisms can take place. The exponential decrease of the ion fraction with decreasing work function is consistent with the resonant charge exchange theory described in eq. (1). The constant C in the equation is determined from these results as $C=(0.86\pm 0.03)\cdot 10^5 \text{ m}\cdot\text{s}^{-1}\cdot\text{eV}^{-1}$. It is observed in figure 6.4 that the work function threshold below which the resonant neutralisation takes place decreases with increasing velocity of the ions. This decrease of the work function threshold is due to the decrease of the freezing distance and the related increase of the energy ε_a with increasing velocity. It is exactly this velocity dependence of the energy ε_a which causes the overestimation of the coverage. Due to the resonant neutralisation, the characteristic velocity method cannot be directly applied because the characteristic velocity v_c is equal to $C\cdot|\varepsilon_a - \varepsilon_F|$ in eq. (6.1) and thus depends on the velocity of the ions through the velocity dependence of ε_a .

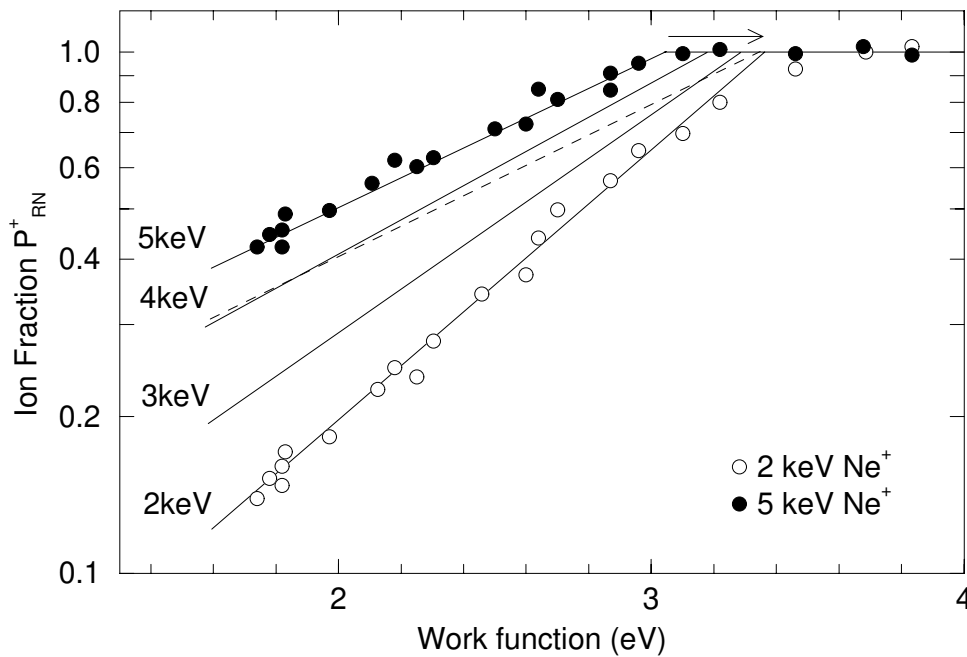


Figure 6.4. Ion fraction for Ne^+ ions exclusively due to the resonant neutralisation mechanism. Note the logarithmic scale of the ion fraction. Only the 2 keV and 5 keV data points are shown for clarity. The dashed line represents the ion fraction for 5 keV after the correction for the velocity dependence of ϵ_a (see text for explanation).

For a more detailed comprehension of the overestimation we analyse the quantification at a coverage $\theta_{Ba}=0.18$ ML having a work function $\phi=2.8$ eV (filled circles in figure 6.1). The dashed line in this figure represents the hypothetical situation when no resonant neutralisation is possible at $\phi=2.8$ eV, and the collision-induced neutralisation is the dominant mechanism. The collision-induced neutralisation is insensitive to work function changes and thus the dashed line has the same slope as the solid line for $\phi=4.5$ eV ($\theta_{Ba}=0.06$ ML). The intersection with the left ordinate corresponds to the correct coverage of $\theta_{Ba}=0.18$ ML. The signal decrease due to the resonant neutralisation is equal to the difference between the measured signal and the dashed line, as is indicated by the vertical arrow for an initial energy of $E_i=2$ keV. Here, the resonant neutralisation is just possible for $E_i=5$ keV ($P^+_{RN}=0.9$), while for $E_i=2$ keV ($P^+_{RN}=0.50$) already a substantial decrease of the ion fraction is observed (see also figure 6.4). Effectively, the characteristic velocity for $E_i=5$ keV is smaller than the characteristic velocity for $E_i=2$ keV, and the extrapolation to infinite velocity leads to an overestimation of the coverage because of this velocity dependence of the characteristic velocity.

To verify that the origin of the overestimation lies in the velocity dependence of the characteristic velocity, we now correct for this velocity dependence. We start by shifting the ion fraction curves for the different energies in figure 6.4 along the work function axis so that the resonant neutralisation has the same work function threshold for all energies. The required shift for $E_i=5$ keV is indicated in figure 6.4 by the arrow, and the dashed line represents the corrected ion fraction curve for 5 keV. The idea behind the shifting of the curves along the work function axis is to artificially make the energy ϵ_a identical for all energies, and thus independent of the velocity. Consequently, the characteristic velocity, which depends on the

factor $C \cdot |\varepsilon_a - \varepsilon_F|$, is constant for a fixed work function and does not depend on the velocity. For example, for $E_i = 5$ keV the ion fraction becomes $P_{RN}^+ = 0.7$ instead of $P_{RN}^+ = 0.9$ before this shift. To correct for the velocity dependence of ε_a , the ion scattering signal in figure 6.1 for $E_i = 5$ keV at a work function of $\varphi = 2.8$ eV was multiplied by a factor $0.7/0.9$. The crosses (x) in figure 6.1 show the measured signal for $\varphi = 2.8$ eV after this correction at all energies. For the crosses the characteristic velocity is independent of the velocity and it is evident that the extrapolation of the corrected signal yields the correct Ba coverage. Applying this method to correct for the velocity dependence of ε_a in the characteristic velocity plots for all coverages where resonant neutralisation is possible ($\varphi < 3.5$ eV) yields the filled circles in figure 6.2 for Ne^+ ions. The agreement between the coverages as determined from the corrected LEIS signals and the AES data confirms the use of the present model for quantification. Although here we only show the correction for Ne^+ ions, identical results were obtained for the He^+ and Ar^+ ions using the same correction procedure. Furthermore, similar investigations for Ne^+ ions scattered from Ba atoms adsorbed on a $\text{Re}(0001)$ crystal [12] also show the present quantification method yields the correct surface density. We thus conclude that if the energy ε_a is independent of the velocity, the characteristic velocity is constant for a fixed work function, and the characteristic velocity method yields the correct coverage.

In figure 6.2 it was observed that the extent of the overestimation of the surface coverage increases with increasing coverage, i.e. decreasing work function. This is due to the increase in the resonant neutralisation with decreasing work function, which means that the relative contribution of the resonant neutralisation to the total neutralisation increases. Hence, the influence of the velocity dependence of the energy ε_a on the quantification increases, and so does the overestimation. A similar way of reasoning explains the difference in the degree of overestimation for the different ions, because the contribution from the resonant mechanism to the total neutralisation is different for the various ions [12]. For example, for He^+ ions the collision-induced neutralisation is the dominant mechanism at all work functions. The resonant neutralisation is a minor contributor even at low work functions and its influence on the quantification is thus small. In contrast, for Ar^+ ions the resonant neutralisation is the dominant mechanism at low work functions, and the velocity dependence of the energy ε_a strongly influences the quantification.

6.4 Guidelines for quantification

Thus far we have focused on investigating the quantification at low work functions for a particular system: Ba adsorbed on W. This knowledge may be directly applied for quantitative analysis of other Ba/W systems under identical scattering conditions. We will report on such application to the quantification of the surface composition of low-work function thermionic Ba dispenser cathodes elsewhere [29] (see chapter 7). However, the results and insights obtained here can be applied in general for the quantification of the surface density of low work function surfaces using the characteristic velocity method. Generalisation of the findings here is simplified by the fact that the neutralisation probability for the resonant neutralisation is determined by the macroscopic work function and by the velocity of the ion as it leaves the surface, and does not depend on the type of target atom [12,13,14]. If the velocity of the ions and the work function of the surface under investigation are known, the ion fraction P_{RN}^+ due to the resonant mechanism can be derived from figure 6.4.

The ion fraction-versus-work function curves in figure 6.4 are not specific for Ne^+ scattered from Ba, but are valid for any combination of target atom, initial ion energy, and scattering geometry that yields that same velocity of the ion as it leaves the surface. Note that the energy

ε_a is independent on the target atom because the level shift a few Ångstroms from the surface is determined by the image force and is thus independent of the target atom. For velocities not exactly equal to those used here, the curves can be found by simple interpolation of the curves given in figure 6.4. The slope of the lines must be inversely proportional to the velocity of the ions (see eq. (6.1)). Once the energy ε_a and the velocity v are known, the ion fraction P_{RN}^+ can be derived by using eq. (6.1) and the here derived constant C .

In order to obtain a similar figure for other ion types all curves have to be shifted along the work function axis, where the required shift is determined by the difference in the energy of the first excited levels of the ions. For example, the energies of the first excited levels for Ne^+ and Ar^+ ions are 4.95 eV and 4.21 eV, respectively. To convert these Ne^+ curves into Ar^+ curves, all curves must be shifted 0.74 eV to a lower work function value. To be more precise, one should correct for the difference in the energies ε_a between the different ions. However, the difference in the energies ε_a is comparable to the difference in energies of the first excited levels at infinite distance, because the shift of the first excited level when the ion is close to the surface is similar for the different ion types [30]. Note that this conversion between ion types is possible because the factor C in eq. (6.1) is similar for the He^+ , Ne^+ , and Ar^+ ions, as is discussed elsewhere [12] (see chapter 5).

Once the ion fraction-versus-work function curves for the system under investigation have been derived, the ion fractions P_{RN}^+ due to the resonant mechanism can be determined for all the energies used in the characteristic velocity plot if the work function for the system is known. The contribution of the resonant neutralisation to the total neutralisation can thus be derived for all initial energies. Moreover, the correction for the velocity dependence of ε_a can then be performed as demonstrated above by shifting the ion fraction curves so that the work function thresholds are identical for all the energies used. The ion fractions P_{RN}^+ before and after the correction for the velocity dependence of ε_a can be determined using eq. (6.1) by substituting the energy ε_a before and after the shift respectively. The ratio of these ion fractions before and after the shift then gives the correction factor of the signal for the velocity dependence of ε_a . With this knowledge the signal intensities in the characteristic velocity plot can be corrected for the influence of the resonant neutralisation as demonstrated in figure 6.1 by the crosses, so the characteristic velocity is independent of the ion velocity and the extrapolation to infinite velocity yields the correct surface density. Of course, this type of quantification is again only possible if the neutralisation constants for the other neutralisation mechanisms do not change over the energy range used. If the relative importance of the other neutralisation mechanisms involved (Auger and/or collision induced) changes over the energy range used, the method will not yield a straight line in the characteristic velocity plots, and this cannot be corrected for by the present correction mechanism for resonant neutralisation.

6.5 Conclusions

The quantification of the surface composition of low-work function systems using low-energy noble gas ion scattering is not straightforward because resonant neutralisation involving the first excited levels of the ions takes place. Application of the characteristic velocity method results in an overestimation of the surface density because due to the resonant neutralisation the characteristic velocity is not constant, but depends on the velocity of the ions. This velocity dependence of the characteristic velocity occurs because the work function threshold of the resonant neutralisation depends on the velocity of the ions. We have presented and discussed a method to correct for the velocity dependence of the characteristic velocity, and have demonstrated that if the resonant neutralisation is possible below the same work function

for all energies, the characteristic velocity method yields the correct surface density of the species under investigation. We have also discussed how the insights from these investigation can be applied for other system, if the work function and the velocity of the ion are known.

The influence of the resonant neutralisation on the quantification, and the extend of the overestimation if no corrections are performed, depend on the relative contribution from the resonant neutralisation to the total neutralisation. Although the resonant neutralisation is governed only by the ion type and the macroscopic work function, the neutralisation rate (i.e. the characteristic velocity) for the Auger and collision-induced neutralisation depend strongly on the ion-target combination [12,31,32,33]. This implies that the relative contribution from the resonant neutralisation thus depends on the ion-target combination. As a rule of thumb, the higher the characteristic velocity for the system at high work functions (in the absence of resonant neutralisation), the lower the influence of the resonant neutralisation on the quantification at low work functions will be.

Finally, we note that in investigations where the neutralisation of alkali ions at initial energies well below 1 keV are studied, a clear velocity dependence of the energy ε_a is not observed. The absence of this velocity dependence at very low ion velocities is consistent with resonant charge exchange theory because at larger freezing distances the level shift depends only weakly on the distance [12,13,14]. This suggests that the overestimation of the surface density by the characteristic velocity method, as demonstrate here for energies of a few keV, will not be present for noble gas ions at low enough initial energies ($\ll 1$ keV). However, further investigations in this low-energy regime are required before definite conclusions can be drawn.

References

- 1 D.P. Smith, J. Appl. Phys. 38 (1967) 340.
- 2 H.H. Brongersma, P.M. Mul, Chem. Phys. Lett. 14 (1972) 380.
- 3 H. Niehus, W. Heiland, E. Taglauer, Surf. Sci. Rep. 17 (1993) 213.
- 4 E. Taglauer, "Ion scattering Spectroscopy", in Ion Spectroscopies for Surface Analysis, Eds. A.W. Czanderna, D.M. Hercules, Plenum Press, New York, 1991.
- 5 L.C.A. van den Oetelaar, H.E. van Benthem, J.H.J.M. Helwegen, P.J.A. Stapel, H.H. Brongersma, Surf. Interface Anal. 26 (1998) 537.
- 6 Oxides: H.H. Brongersma, P.A.C. Groenen, J.-P. Jacobs, in *Science of Ceramic Interfaces II*, p. 113-182, Ed. J. Nowotny, Material Science Monographs 81, Elsevier Science B.V., Amsterdam, 1994.
Polymers: T.G. Vargo, J.A. Gardella, R.L. Schmitt, K.J. Hook, T.J. Hook, L. Salvati, *Low-Energy Ion Scattering Spectrometry of Polymer Surface Composition and Structure*, in Surface Characterisation of Advanced Polymers. Ed. L. Sabbatini, P.G. Zamboni, 1993.
Catalysts: L.C.A. van den Oetelaar, O.W. Nooij, S. Oerlemans, A.W. Denier van der Gon, H.H. Brongersma, J. Phys. Chem. B 102 (1998) 3445-3455.
Liquids: G. Andersson, H. Morgner, Surf. Sci. 405 (1998) 138.
- 7 R. Souda, M. Aono, Nucl. Instr. Meth. B 15 (1986) 114.
- 8 M.J. Ashwin, D.P. Woodruff, Surf. Sci. 244 (1991) 247.

- 9 M. Beckschulte, E. Taglauer, Nucl. Instr. Meth. B 78 (1993) 29.
- 10 A.W. Denier van der Gon, M.F.F.K. Jongen, H.H. Brongersma, U. van Slooten, A. Manenschijn, Appl. Surf. Sci. 111 (1997) 64.
- 11 R. Cortenraad, A.W. Denier van der Gon, H.H. Brongersma, G. Gaertner, A. Manenschijn, Appl. Surf. Sci. 146 (1999) 69.
- 12 R. Cortenraad, A.W. Denier van der Gon, H.H. Brongersma, S.N. Ermolov, V.G. Glebovsky, G. Gärtner, A. Manenschijn, to be published.
- 13 R. Brako, D.M. Newns, Rep. Prog. Phys. 52 (1989) 655.
- 14 J. Los, J.J.C. Geerlings, Phys. Rep. 190 (1990) 134.
- 15 M.L. Yu, N.D. Lang, Nucl. Instr. and Meth. B14 (1986) 403.
- 16 J.K. Norskov, B.L. Lundqvist, Phys. Rev. B. 19 (1979) 5661.
- 17 D.A. Gorodetskii, Y.P. Melnik, Surf. Sci. 62 (1977) 647.
- 18 E. Koch, W. Huisl (eds), "Gmelin Handbook of Inorganic and Organometallic Chemistry, Tungsten Supplement Volume A 6a", Springer-Verlag, Berlin, 1991.
- 19 R. Cortenraad, A.W. Denier van der Gon, H.H. Brongersma, Surf. Interface Anal. 29 (2000) 524.
- 20 A.P. Janssen, P. Akhter, C.J. Harland, J.A. Venables, Surf. Sci. 93 (1980) 453.
- 21 G. Eng, H.K.A. Kan, Appl. Surf. Sci. 8 (1981) 81.
- 22 H. Oechsner, Fresenius J. Anal. Chem. 355 (1996) 419.
- 23 H.D. Hagstrum, Phys. Rev. 96 (1954) 336.
- 24 D.P. Woodruff, Nucl. Instr. Meth. 194 (1982) 639.
- 25 E.C. Goldberg, R. Monreal, F. Flores, H.H. Brongersma, P. Bauer, Surf. Sci. 440 (1999) L875.
- 26 D.J. Godfrey, D.P. Woodruff, Surf. Sci. 105 (1981) 438.
- 27 D.J. Godfrey, D.P. Woodruff, Surf. Sci. 105 (1981) 459.
- 28 M.L. Yu, N.D. Lang, Nucl. Instr. and Meth. B14 (1986) 403.
- 29 R.Cortenraad, A.W. Denier van der Gon, H.H. Brongersma, G. Gaertner, A. Manenschijn, to be published.
- 30 H.D. Hagstrum: *Inelastic Ion-Surface Collisions*, Editors H.H. Tolk, J.C. Tully (Academic Press, New York, 1977), p. 1.
- 31 S.N. Mikhailov, R.J.M. Elfrink, J.-P. Jacobs, L.C.A. van den Oetelaar, P.J. Scanlon, H.H. Brongersma, Nucl. Instr. Meth. B93 (1994) 148.
- 32 M. Tsukada, S. Tsuneyuki, N Shima, Surf. Sci. 164 (1985) L811.
- 33 S. Tsuneyuki, M. Tsukada, Phys. Rev. B 34 (1986) 5758.

7

Surface Analysis of Thermionic Dispenser Cathodes

Abstract

Surface analysis of thermionic Ba dispenser cathodes with various refractory metal substrates (W, Re, Ir, and Os/Ru) was performed by means of low-energy ion scattering and Auger electron spectroscopy. It was found that the Ba-O complex responsible for the low work functions of the cathodes has similar properties on the different substrates: the atomic Ba/O ratio is close to unity on all cathodes, with the O atoms positioned in a plane below the Ba atoms. The bonding between the Ba and O atoms as observed in the low-energy Auger spectra is also almost identical on all cathodes. However, a significant difference in the absolute Ba-O coverage was observed for the various cathodes.

The dipole moments of the Ba-O dipoles are similar for all cathodes, and the work functions of the cathode are thus determined by the work functions of the substrates and the number of dipoles, i.e. the Ba-O densities. It was found that the work functions are 2.02, 1.93, 1.89 and 1.85 eV for the cathodes with the W, Re, Ir and Os/Ru substrates respectively, where the Ba-O coverage increases with decreasing work function. For all substrates the density of Ba-O dipoles is below the value that would result in the lowest work function. The work functions of the cathodes are thus limited by the density of Ba-O dipoles on the surface. This density is determined by the strength of the bonding of the O atoms in the Ba-O complex with the substrate atoms. The results are discussed with respect to previous experimental and theoretical investigations of cathode surfaces.

7.1 Introduction

Thermionic dispenser cathodes are widely used in devices which require high-density electron beams, such as the cathode-ray tubes used in television-sets. The basic dispenser cathodes consist of a porous tungsten matrix impregnated with a compound containing barium and oxygen (I-cathode) [1]. During cathode operation at a true temperature of 1030°C a submonolayer of barium and oxygen is formed on the cathode substrate. This electropositive Ba-O layer counteracts the surface dipole and results in a low cathode work function of approximately 2.0 eV. These W-cathodes are capable of electron emission densities in the order of $3 \text{ A}\cdot\text{cm}^{-2}$ at a true temperature of 1030°C (see figure 7.1). Improvement of the emission capabilities by almost one order of magnitude ($\approx 10 \text{ A}\cdot\text{cm}^{-2}$) was obtained by coating the surface of the W matrix by a thin layer of refractory metals like Re, Os, or Ir [2]. The best results have been obtained so far for cathodes with a Ba-scandate complex in the toplayer, which results in emission densities exceeding $300 \text{ A}\cdot\text{cm}^{-2}$ for Philips scandate cathodes [3].

Many theoretical and experimental investigations have been devoted to understanding the details of the operation of dispenser cathodes and related model systems [4]. However, many properties are still subject of discussion, for example the Ba-O geometry, the Ba/O ratio, and the chemical nature of the Ba atoms (metallic or oxidic). Moreover, it has not yet been indisputably established how the different substrates influence the cathode performance. In this paper we report on our investigations of the surfaces of various dispenser cathodes. The aim of this work was to compare the different cathodes and gain insight into the relation between the surface properties and the work functions of the cathodes. We have investigated the Ba and O coverages, the Ba-O geometry, and the Ba-O bonding using a combination of low-energy ion scattering (LEIS) and Auger electron spectroscopy (AES). Furthermore we studied the role of the O present on the surface, and show that the presence of the Ba and O is equally important. The importance of the O atoms has been underestimated so far because most cathode studies reported in the literature focussed on the Ba coverage.

The outline of this paper is as follows: We start by briefly discussing the types of cathodes investigated, and the surface analysis techniques used here (section 7.2). In the first section of the results we then show how the ion scattering can give information about the outermost atomic layer of the surface (section 7.3.1). Subsequently, we will show that the quantification of the surface density using LEIS at low work functions surfaces, e.g. I-cathodes, is not straightforward and requires a correction for the influence of the cathode work function on the ion scattering signal (section 7.3.2). Next, the surface coverages of the various cathodes derived from the combined LEIS and AES measurements are presented, where we show that the differences in the coverages among the various cathodes determined the differences in work functions (section 7.3.3). The origin of the differences between the cathodes is discussed in sections 7.3.4 and 7.3.5, where we focus on the role which the surface oxygen and the substrate material play in the emission capabilities of the cathodes. Finally, we briefly summarise our findings (section 7.4).

7.2 Experimental

The cathodes investigated in this study were Ba dispenser cathodes as used in Philips cathode-ray tubes. The cathodes consist of a porous W base (porosity 20%) with a diameter of 1 mm, and are impregnated with a 4:1:1 mixture of BaO:CaO:Al₂O₃. Various cathode types were investigated: the uncoated W-cathode, and different top-layer cathodes where the surface of the W matrix was coated by Re, Ir, or Os(80%)/Ru(20%) top-layers with thicknesses varying between 50 nm and 500 nm. These coatings were especially prepared for these investigations

by sputtering or by laser ablation deposition (LAD). During all investigations the cathodes were at the operating temperature of 965 °C Mo-Brightness, corresponding to a true temperature of 1030 °C. The heating was performed by the built-in 0.65 Watt heater unit. After the cathode activation, which consisted of operating the cathodes for 2 hours at a temperature of approximately 100°C above the operating temperature, the cathodes were operated for approximately 50 hours in UHV in order to ensure that the cathodes were fully activated and stable during the surface analysis.

The surface analysis of the various dispenser cathodes was performed in the UHV set-up MiniMobis which has a base pressure of $1 \cdot 10^{-10}$ mbar [5,6]. This set-up is dedicated to in-situ investigations of thermionic dispenser cathodes and related low-work function model systems. Instrumentation is available for low-energy ion scattering (LEIS), Auger electron spectroscopy (AES), low-energy electron diffraction (LEED), and electron emission density measurements. The outermost atomic layer of the cathodes was studied by LEIS [7,8,9,10], where a differentially pumped ion gun was used to direct He^+ , Ne^+ and Ar^+ noble gas ions with an initial energy between 2 keV and 5 keV perpendicular onto the surface. The ions that backscattered over an angle of 136° were energy selected by a cylindrical mirror analyser (CMA) and detected using a microchannelplate-based detector [6]. Due to the high electron affinity of the noble gas ions, ions that penetrate beyond the outermost atomic layer are almost certainly neutralised and do not contribute to the ion scattering signal [8]. The energy spectrum of the backscattered ions thus represents a mass spectrum of the outermost atomic layer. The ion beam had a full width at half maximum of 0.4 mm, and therefore the ion scattering signal was averaged over a large fraction of the cathode surface. The Ba-impregnate in the pores did not contribute to the ion scattering signal, because ions that are scattered from atoms in the pores are not detected due to the geometric shielding caused by the roughness and the depth of the pores [9,11]. The ion scattering thus only yields information about the emitting surface. All ion scattering measurements were performed using an ion flux not exceeding $1 \cdot 10^{12}$ ions $\cdot\text{cm}^{-2}\cdot\text{s}^{-1}$ since a higher flux influenced cathode operation [12] (see chapter 8).

In addition to the ion scattering, Auger analysis was used during cathode operation to determine the Ba and O coverages. For the Auger analysis a grazing incidence electron gun was used, where the electron beam was directed onto the cathode surface at an angle of approximately 10° with the surface. The Auger electrons were analysed by the same CMA as used for the ion scattering, but with a reversed polarity of the pass energy. Like the ion scattering, the Auger analysis was also averaged over a large fraction of the cathode surface. Here, the grazing incidence minimised the contribution from the pores because the incident electrons did not penetrate into the pores, as evidenced by the absence of any Ba or O signals in the AES spectrum after sputter-removal of the outermost Ba-O layer. This grazing incidence thus enabled a more accurate investigation of the emitting surface compared to the more commonly used perpendicular incidence geometry.

The Ba and O densities for the LEIS and the AES analysis were calibrated by adsorbing Ba and O atoms on a flat well-ordered W(110) single crystal [13,14]. Calibration of the Ba signals was performed by adsorbing various Ba coverages on the W(110) crystal, and measuring the work function as a function of the coverage [15]. The work function minimum of $\phi=1.8$ eV was assigned to a Ba density $n_{\text{Ba}}=2.6 \cdot 10^{14}$ atoms $\cdot\text{cm}^{-2}$, according to detailed studies of the Ba/W(110) system reported in the literature [16,17] (see also chapter 5). The O signal was calibrated by saturating the W(110) crystal with oxygen (1000 L O_2) at room temperature, which resulted in a (1x1) O structure on the crystal as was verified by LEED

($n_O=1.41 \cdot 10^{15}$ atoms \cdot cm $^{-2}$) [18,19]. This calibration method for the Auger analysis based on the use of well-defined overlayers of O and Ba on a clean substrate enabled a direct determination of the Ba and O sensitivities, which is more accurate than the use of sensitivity factors from literature [20]. It is also more accurate than calibration using compound samples which requires correction for contributions from deeper layers due to the differences in mean free paths of the Auger electrons from Ba and O, as is the case when for example bulk BaO is used for calibration [21,22].

Because we used a flat surface without pores for the calibration of the Ba and O densities, a correction was performed for the porosity of the W cathode matrix. It was found that the ion scattering W signal from the sputter-cleaned W substrate (no Ba-O complex) was equal to 83% of the W signal from a flat W poly-crystal, which is consistent with the bulk porosity of the W matrix of 20 %. Note that the sputter-removal of the Ba-O layer induced atomic roughness and disorder on the W substrate which resulted in a decrease of the ion scattering signal compared to a well-ordered surface [9,11]. Here we have corrected for the influence of the surface roughness based on investigations of this subject reported elsewhere [23] (see chapter 4). The Ba and O densities presented in this paper thus represent the densities of the emitting surface, i.e. the surface on top of the individual grains (see section 7.3.3).

The emission characteristics of the cathodes were measured in-situ in a close-spaced diode configuration, by positioning the cathodes directly under a Ta anode at a distance of approximately 300 μ m [3,24,25]. The emission current densities were measured as a function

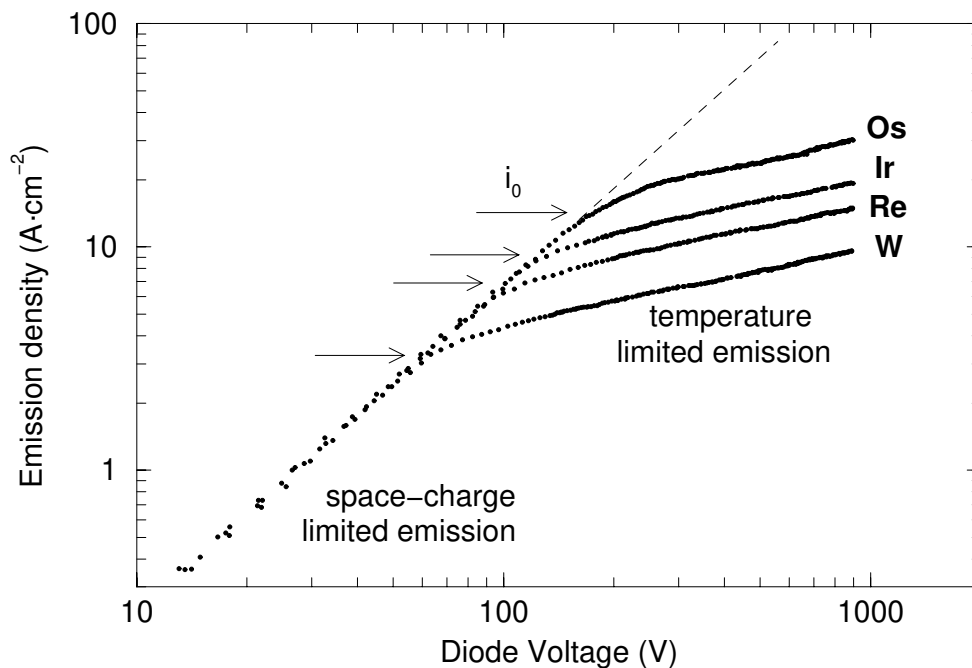


Figure 7.1. Emission measurements of the various cathodes at a true temperature of 1030°C. The electron density is shown versus the applied diode voltage. The arrows mark the i_0 values for the different cathodes used to determine the effective work function. (Note, the Os/Ru cathode is marked as Os.). The dashed line represents the emission for pure space-charge limited emission.

of the diode voltage, which was applied using a high-voltage saw-tooth pulser (50 Hz) with an amplitude of 1 kV and a pulse width of 50 μ s. Figure 7.1 shows typical IV-curves for the different cathodes measured at the operating temperature $T=1030^\circ\text{C}$. The effective work functions ϕ of the cathodes were derived from these curves using the Richardson equation [3]:

$$i_0 = A_R T^2 \cdot \exp(-\phi/kT) \quad (7.1)$$

Here the Richardson constant $A_R=120 \text{ A}\cdot\text{cm}^{-2}\cdot\text{K}^{-2}$, and the current density i_0 is taken from the knee in the IV curves where the deviation from the space-charge limited emission starts (indicated by the arrows in figure 7.1) [3]. The resulting work functions for the different cathodes are summarised in table 7.1. Before and after the surface analysis, emission measurements were performed to verify that the investigations did not influence the cathode operation.

7.3 Results and discussions

7.3.1 The outermost atomic layer

Figure 7.2 shows 5 keV Ne^+ spectra of the W-cathode (solid curve) and the Os/Ru-cathode (dashed curve) at the operating temperature. The spectrum of the W-cathode is shifted up for clarity, where the shift of the baseline is indicated by the short dashed line. In the spectrum of the W-cathode a clear W peak is visible, while no clear peak due to the substrate atoms is visible for the Os/Ru-cathode. The substrate atoms are only probed by the incident ions if no

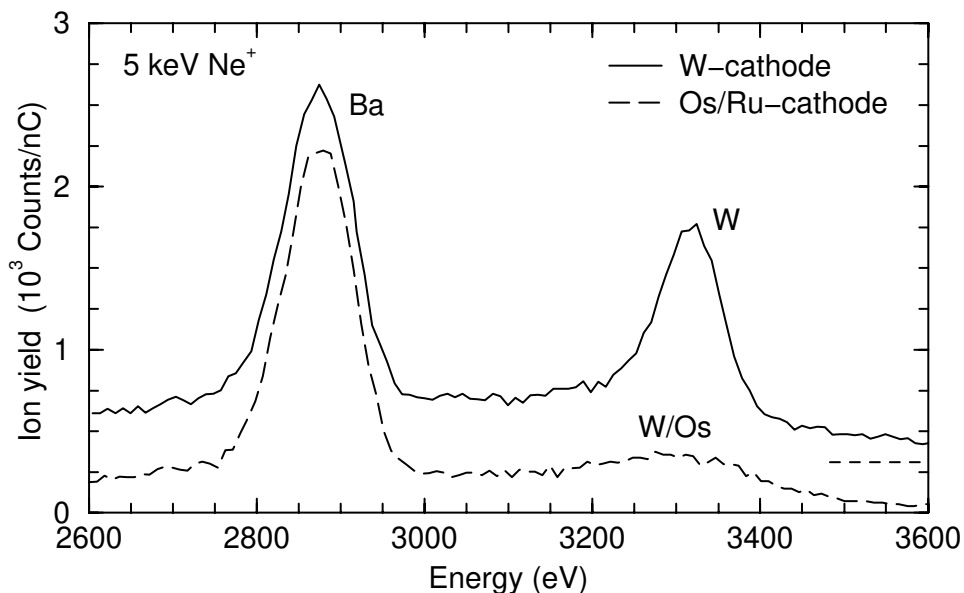


Figure 7.2. LEIS 5 keV Ne^+ spectra of the W-cathode (solid curve) and the Os/Ru-cathode (dashed curve). The baseline of the W-cathode is shifted up for clarity, as is indicated by the short dashed line. The spectra were taken at the operating temperature using an ion flux of $1\cdot 10^{12} \text{ ions}\cdot\text{cm}^{-2}\cdot\text{s}^{-1}$.

Ba-O complex is present on top, and it is thus evident that the surface coverage by the Ba-O complex is more complete for the Os/Ru-cathode than for the W-cathode. A direct quantitative comparison of these spectra is not possible due to the influence of the cathode work function on the neutralisation of the ions (see section 7.3.2).

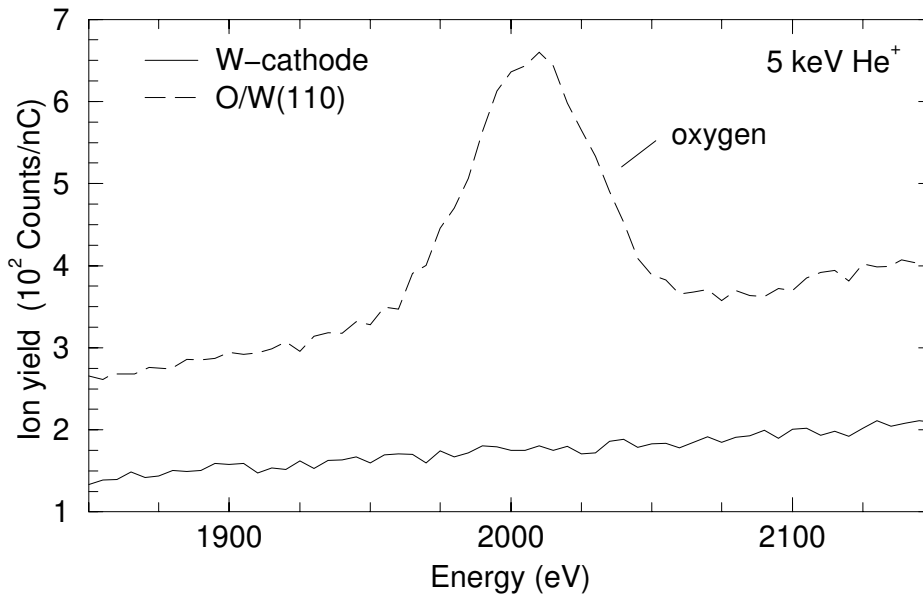


Figure 7.3. LEIS 5 keV He^+ spectra of the W-cathode at the operating temperature and the O/W(110) reference system. On all cathodes the O signal is below the detection limit during operation.

In order to investigate the presence of oxygen in the outermost layer, He^+ ions were used. Figure 7.3 shows a 5 keV He^+ spectrum of the W-cathode at operating temperature (solid curve), and for comparison also a 5 keV He^+ spectrum of the O/W(110) reference system with a density of $n_{\text{O}}=1.41 \cdot 10^{15}$ atoms $\cdot\text{cm}^{-2}$ (dashed curve). No O peak is observed in the spectrum of the W-cathode, or the other cathode types, and we conclude that no oxygen is present in the outermost atomic layer of the cathodes at the operating temperature. The O atoms present on the cathode surface must thus be shielded from the incident ions by the Ba atoms positioned in a plane above the O atoms. These observations are in agreement with results from previous ion scattering investigations by Denier van der Gon et al. of specially prepared W-cathodes with a diameter of 3-4 mm, where also no O was observed at the operating temperature [26]. Other ion scattering investigations by Baun [27] and by Marrian et al. [28,29] showed small O peaks. However, these investigations were performed with the cathodes at room temperatures using a simultaneous combination of He^+ and Ne^+ ions. The sputtering rate of the heavy Ne^+ ions is much higher than for the light He^+ ions. Therefore, a possible explanation for the O peaks in the spectra is that first the Ba atoms are removed by the Ne^+ ions, consequently exposing the O atoms for detection by the He^+ ions.

In the literature several Ba-O geometries have been proposed: the Ba atoms directly on top of the O atoms (upright Ba-O axis) [30,31,32], the O atoms in a plane below the Ba plane, but in the middle between two Ba atoms (tilted Ba-O axis) [33,34], and the Ba and O atoms in the same plane (in-plane Ba-O axis) [35,36]. Our He^+ results are consistent with the Ba atoms

above the O atoms, and in addition suggest that all O atoms present on the surface are covered by Ba atoms. If the O atoms are positioned in the middle between two Ba atoms which are approximately 6 Å apart (see section 7.3.3), the O would be detected by the ion scattering even if the O plane is 1-2 Å below the Ba plane [33]. Moreover, the on-top geometry is in agreement with theoretical calculations of the influence of the geometry on the work function of the cathodes performed by Mueller, where it was concluded that the low work functions of the cathodes can only be obtained if the Ba atoms are positioned directly above the O atoms [37].

7.3.2 Ion scattering at low work functions

The quantification of the surface compositions of the cathodes using LEIS is not straightforward because the low work functions strongly influence the neutralisation of the ions [26,29,38,39,40]. Consequently, the signal intensity in the ion scattering is not simply proportional to the surface density. In previous work we have reported on the neutralisation mechanisms for noble gas ions at low-work function surfaces [15], and also discussed how to correct for the influence of the work function on the neutralisation in order to perform a quantitative analysis of low-work function systems [41] (see chapters 5 and 6). Here, we only briefly summarise how the work function influences the quantification of the LEIS signals.

The ion scattering signal S_k for species k is proportional to the surface density n_k and the ion fraction P_k^+ , which is defined as the probability that an incident ion leaves the surface as an ion after the interaction with the surface. The ion fraction can be expressed as [42,43,44]:

$$P^+ = \exp\left(-v_c \cdot \left(\frac{1}{v_i} + \frac{1}{v_f}\right)\right) \quad (7.2)$$

Here, $1/v_i$ and $1/v_f$ are the reciprocal ion velocities on the incident and outgoing trajectory, and the characteristic velocity v_c is a measure for the neutralisation rate during the interaction. The characteristic velocity depends on the ion-target combination and the type of neutralisation mechanism [45]. Moreover, at surfaces with a low work function, such as for the cathodes, the characteristic velocity increases strongly with decreasing work function [5,15].

In order to perform a quantitative analysis of the various cathodes with different work functions the ion scattering signal was measured on each cathode as a function of the initial energy of the ions, thereby varying $(1/v_i + 1/v_f)$ [44,45]. Figure 7.4 shows the logarithm of the measured Ba signal S_{Ba} as a function of $(1/v_i + 1/v_f)$ for Ne^+ ions scattered from the Ba atoms on the W-cathode and on the Os/Ru-cathode, where the area of the Ba peak is taken as a measure for the Ba signal intensity. The measured signal S_{Ba} is corrected for the energy dependencies of the analyser transmission (T), the detection efficiency (ϵ), and the differential scattering cross-section (σ) [6]. It is evident that without any correction for the influence of the neutralisation, the relative Ba signals and thus the coverages of these cathodes would depend on the initial energy of the ions used in the investigation: for low energies (≈ 2 keV) the W-cathode seems to have a higher coverage, while at high energies (≈ 5 keV) the Os/Ru-cathode seems to have the highest coverage. The characteristic velocities v_c , represented by the slopes of the linear fits, are different for both cathodes due to the difference in neutralisation rate caused by the difference in the cathode work functions [15]. The derived characteristic velocities for scattering from the Ba atoms on the different cathodes are shown in figure 7.5 versus the work function using Ne^+ ions (left ordinate scale) and Ar^+

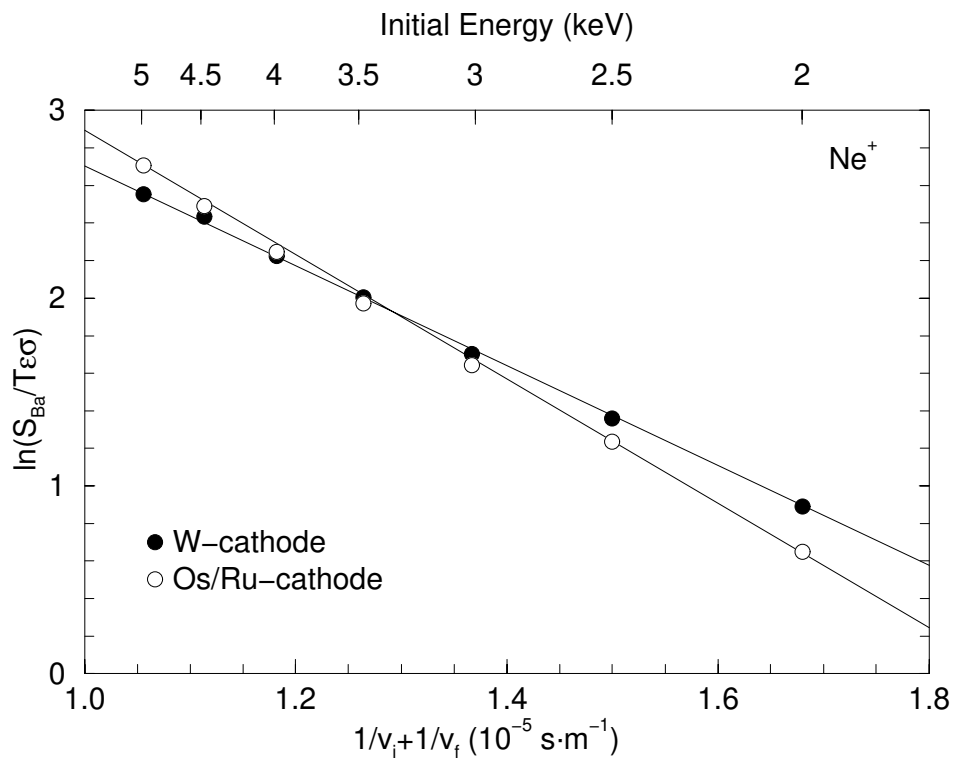


Figure 7.4. Characteristic velocity plots for the W-cathode (filled circles) and the Os/Ru-cathode (open circles) using Ne^+ ions. The logarithm of the Ba signal is shown versus $(1/v_i + 1/v_f)$. The initial energy scale is shown on the top axis.

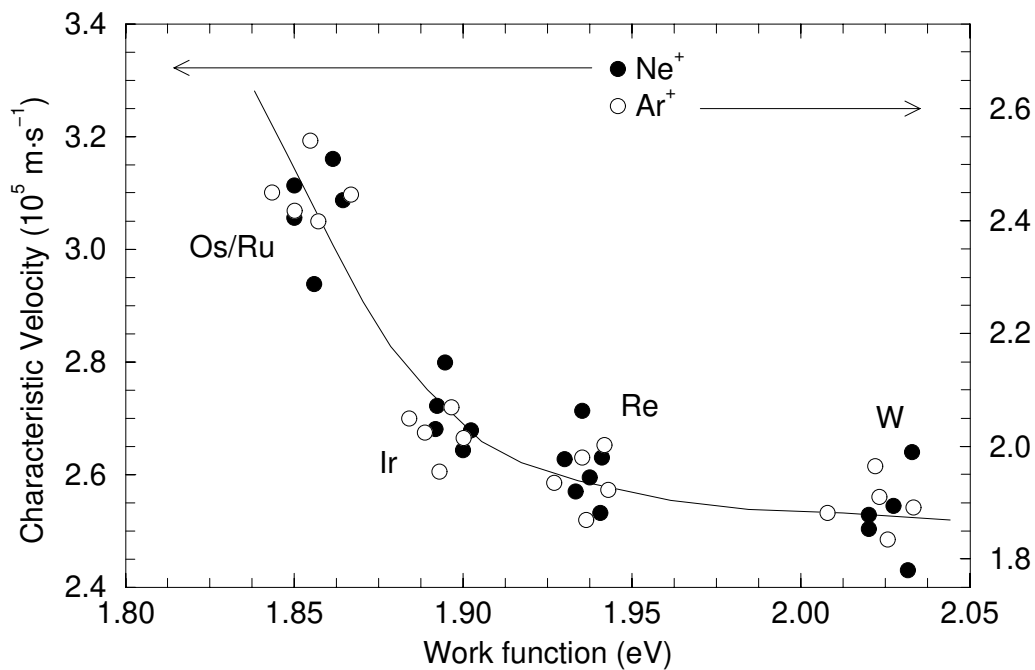


Figure 7.5. The characteristic velocities for Ba on the different cathodes versus the work function using Ne^+ ions (left ordinate scale) and Ar^+ ions (right ordinate scale). The work functions are derived from the emission measurements.

ions (right ordinate scale). For each substrate type various cathodes were studied to investigate the reproducibility. It is observed that the absolute increase in the characteristic velocity with decreasing work function is identical for Ne^+ and Ar^+ ions, which is consistent with the additional neutralisation mechanisms for noble gas ions at low work functions [15].

The neutralisation probability thus increases from the W-cathode to the Os/Ru cathode, and a correction for the neutralisation differences is required in order to perform a quantitative comparison of the Ba densities. The correction method has been described elsewhere [41], and takes into account the difference in ion fractions of ions scattered from surfaces with different work functions (see chapter 6). This correction has been used in the quantification of the LEIS signals in the following section.

7.3.3 Coverage versus work function

The Ba densities of the various cathodes determined by the ion scattering are shown in figure 7.6 versus the work function as determined by the diode configuration (filled circles). The error bars represent the spread in the Ba densities for the different cathodes and different ions used, and show the reproducibility of the cathode preparation, activation and measurements. The Ba densities shown here represent the densities on top of the individual grains, where a correction for the porosity of the cathode matrix was performed by dividing the Ba densities derived through calibration by the Ba/W(110) system by a factor 0.83 (see section 7.2). The Ba density increases with decreasing work function, which is consistent with the qualitative

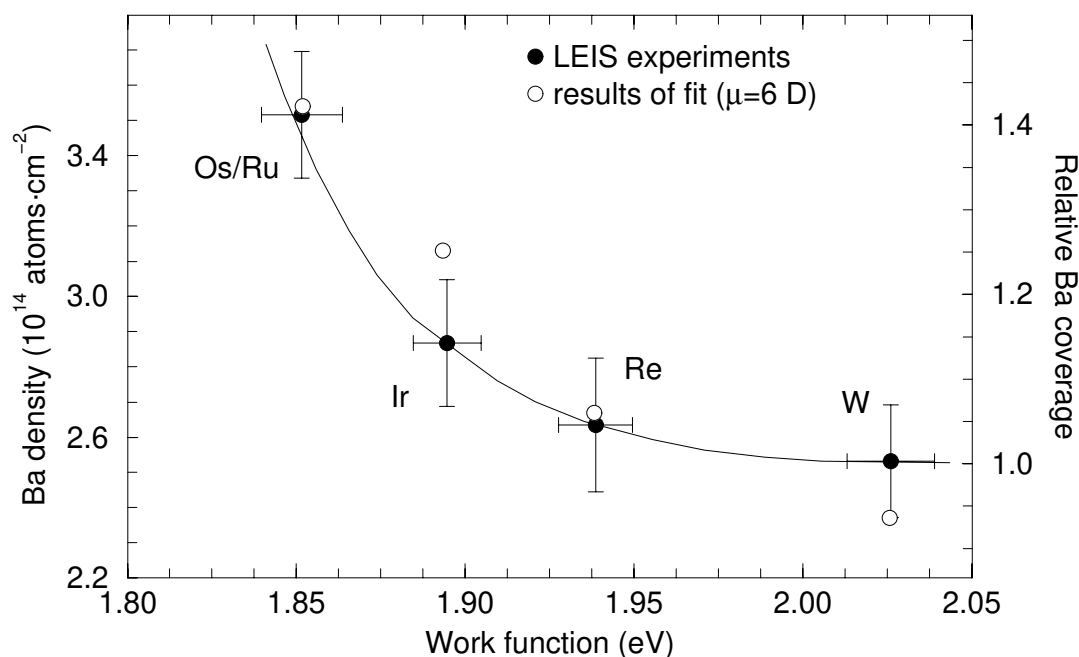


Figure 7.6. The Ba densities of the various cathode derived from the ion scattering versus the work function (filled circles). The right ordinate scale represent the Ba coverage relative to the coverage of the W-cathode. The open circles represent the fitted Ba densities assuming an identical dipole moment μ for all cathodes, and using the dipole moment as a fitting parameter ($\mu=6$ D).

observation of the stronger substrate LEIS signal for the higher work function cathode as demonstrated in figure 7.2 for the W-cathode and the Os/Ru-cathode. The upper limit of the O density in the outermost atomic layers of the cathodes, i.e. the O atoms not covered by Ba atoms, can be estimated from the noise level in the spectrum in figure 7.3 as $n_{\text{O}} < 4 \cdot 10^{13}$ atoms/cm².

Although many investigations have focussed on the Ba-O coverage of dispenser cathodes, only few studies have actually quantified the surface densities of the Ba and O atoms using AES or XPS techniques [49,51]. Most studies only give the Auger peak ratios of the cathodes [22,28,46], or state, for example, that the Ba-O coverage is close to a monolayer [27,35,57]. The few quantitative studies have yielded higher densities than derived in this work. For example van Veen found Ba densities of $n_{\text{Ba}} = 3.8 \cdot 10^{14}$ atoms·cm⁻² and $n_{\text{Ba}} = 5.8 \cdot 10^{14}$ atoms·cm⁻² for the W-cathode and the Os/Ru cathode respectively [51]. The XPS technique used by van Veen has a much larger information depth than the LEIS, which may result in contributions from the pores where multiple layers of Ba are present, and this would then result in an overestimation of the surface Ba coverage. In addition, corrections for the large information depth and the various sensitivity factors, as used in standard quantification of XPS signals, complicates the quantitative analysis of the outermost layers. We believe that the use of model systems for calibration purposes as performed in the present work results in more reliable absolute coverages. In addition, the data we present in the remainder of the paper are consistent with the lower Ba densities derived in this work.

On each cathode the atomic Ba/O ratio was determined from Auger analysis, where we used the areas of the Ba peak (600eV) and O peak (503 eV) in the direct Auger spectrum as a measure for the signal intensities. The Ba and O Auger sensitivities were calibrated using the Ba/W(110) and O/W(110) systems respectively. The derived atomic Ba/O ratios are shown in table 7.1 for the various cathodes, and it is found that these atomic ratios are close to unity for all cathodes. Here we did not yet make any correction for the fact that the O atoms are situated below the Ba atoms. However, the mean free path of the Auger electrons from the O atoms is approximately $\lambda = 10$ Å, while the diameter of the Ba atoms is of the order of $d_{\text{Ba}} = 2.8$ Å [47]. Moreover, the Auger electrons have to leave the O atoms at an angle of approximately 45° to be detected, and can thus pass between the Ba atoms situated above the O atoms since for a density of $n_{\text{Ba}} = 3 \cdot 10^{14}$ atoms·cm⁻² the interatomic Ba distance is approximately 6 Å. Therefore, we estimate that the attenuation of the oxygen signal is no more than 10-15%, which results in an average atomic Ba/O ratio for the cathodes of 1.04 ± 0.06 . In combination with the results

Substrate	ϕ_{cath} (eV)	ϕ_{substr} (eV)	n_{Ba} ($10^{14} \cdot \text{cm}^{-2}$)	$n_{\text{Ba}} \text{ optim.}$ ($10^{14} \cdot \text{cm}^{-2}$)	Ba/O ratio	Ba-O bond 68 eV/73 eV
W	2.02±0.01	4.5	2.53±0.16	3-4	0.89±0.04	0.57±0.04
Re	1.93±0.01	4.8	2.63±0.19	5	0.94±0.03	0.58±0.04
Ir	1.89±0.01	5.4	2.86±0.18	6	0.91±0.05	0.61±0.05
Os/Ru	1.85±0.01	5.7	3.51±0.18	6	0.96±0.06	0.65±0.03

Table 7.1. Properties of the various cathodes. ϕ_{cath} : cathode work function. ϕ_{substr} : substrate work function. n_{Ba} : Ba density derived by LEIS. $n_{\text{Ba}} \text{ optim.}$: optimal Ba density corresponding to the work function minimum of the particular substrate. Ba/O ratio: atomic Ba/O ratio derived by AES, before correction for the position of the O atoms below the Ba atoms. Ba-O bond: peak ratio of the 68 eV and 73 eV peaks in the low-energy Auger spectrum.

of our He^+ investigations we can conclude that every O atom on the surface is covered by a Ba atom, and all Ba atoms on the surface are bound to O atoms. This is consistent with previous investigations where we have shown that Ba atom cannot be present on the surface at the operating temperature if it is not bound to an O atom [12] (see chapter 8).

Reports in the literature about the atomic Ba/O ratio vary between $\text{Ba/O} \approx 1$ [27,32,48,49] and $\text{Ba/O} \approx 0.5-0.7$ [47,50,51]. The spread in the reported Ba/O ratios is most likely due to the fact that many different methods were used to calibrate the Ba and O Auger signals and to correct for their respective sensitivities. Ba/O ratios smaller than unity can be caused by contributions from the pores where a large concentration of O is associated with the impregnate [48,49]. Most studies that have found Ba/O ratios smaller than unity have attributed the O in excess of the Ba-O stoichiometry to parts of the substrate only covered by O atoms. However, for fresh cathodes operated for only a few hundred hours it is unlikely that O atoms on the surface are not covered by Ba atoms since an ample supply of Ba is available in the pores, and the Ba supply from the pores to the surface is very fast [12]. Our He^+ results of the various fresh cathodes do not show any significant parts of the surface covered only by O atoms. However, as the cathodes age, the pores near the surface become depleted of Ba, resulting in a lower Ba resupply rate which then leads to parts of the cathode substrate only covered by O atoms ($\text{Ba/O} < 1$) [49,52].

The O present on the surface is important because the Ba-O bond results in a stronger bonding of the Ba atoms compared to the Ba-substrate bond. This increases the residence time of the Ba atoms on the surface so that the complete substrate can be covered by the Ba-O complex [53,54,55,56]. Without this Ba-O bond the residence time is not sufficient to cover the surface by diffusion because the Ba atoms evaporate too quickly [12]. Differences in the bonding between the Ba and O atoms for different substrates can be derived from the low-energy Auger spectrum of the cathodes [57,58,59], as demonstrated in figure 7.7 for the Os/Ru-cathode. The signal in this derivative spectrum is normalised to the “Ba” peak near 73 eV,

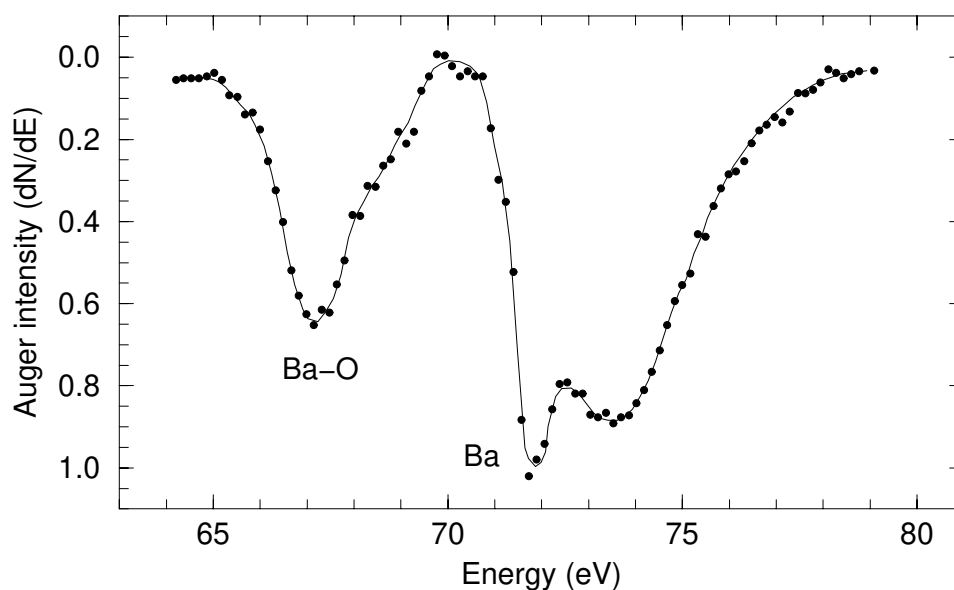


Figure 7.7. Low-energy Auger spectrum of the Os/Ru-cathode. The peak marked “Ba-O” is a measure for the Ba-O bonding, and the peak marked “Ba” is a measure for the Ba density.

which is due to transitions involving electrons in the Ba levels: Ba 4d-Ba 5p-Ba 6s. The peak marked “Ba-O” near 68 eV is caused by electrons occupying levels involved in the Ba-O bonding: Ba 4d-Ba 5p-O 2p [58]. The direct comparison of the low-energy Auger spectra for the different cathodes showed that the ratio of the 68 eV/73 eV peaks is similar for all cathodes (see table 7.1). Comparable 68 eV/73 eV values have also been reported in previous cathode investigations [22,28,35]. Therefore, we conclude that the bonding between the Ba and O atoms is almost independent of the substrate type, and cannot explain the differences in the work functions for the various cathodes. Note that the presence of the Ba-O bond in the Auger spectra does not imply that the Ba and O atoms are present on the surface in the form of BaO. Instead, the Ba is bound to O which is adsorbed on the substrate [27,32,57].

Thus far we have found that on the different substrates the atomic Ba/O ratio and the Ba-bonding are almost identical, and only the absolute value of the coverage varies significantly between the substrates. When alkali or earth-alkali atoms are adsorbed on metal substrates an optimum coverage exists which corresponds to the work function minimum for that particular system; a lower or higher than optimum coverage results in a higher work function. To investigate whether the Ba-O coverages on the different substrates studied here are below or above the optimum coverage we made use of the influence of the work function on the neutralisation of the ions. When the cathode temperature is increased the Ba-O coverage decreases [51], which results in a work function increase or decrease for a coverage below or above the optimal coverage, respectively. We have observed that the increase in the temperature results in a decrease in the characteristic velocity v_c for the cathodes, and this implies that the work function increases as a result of the higher temperature and decreasing Ba-O density. Therefore, we conclude that all cathodes studied here have coverages below the optimum coverage for the corresponding substrates. In table 7.1 we show estimated optimal Ba densities (“ n_{Ba} optimum”) for the different cathodes, based on studies reported in the literature of Ba adsorption on the different substrate types (W: [16,17,60], Re: [54,61], Ir: [62], Os/Ru: [62]). Comparison of the Ba densities derived in this work and the optimal coverage for the different substrates indeed show that the cathode coverages are below the optimal coverages.

The minimum in the work function-versus-coverage curve for the alkali and earth-alkali atoms adsorbed on metal substrates is caused by mutual depolarisation due to interaction between the dipoles. For coverages below the optimal coverage the depolarisation is negligible, and the total work function decrease compared to the clean substrate due to the Ba-O adsorption is in first order approximation equal to the sum of the individual Ba-O dipoles. The work function of the various cathodes φ_{cath} depends on the work function of the clean substrate φ_{substr} , the Ba-O density n and the dipole moment μ of the individual dipoles according to [16,17]:

$$\varphi_{\text{cath}} = \varphi_{\text{substr}} - 4\pi \cdot e \cdot n \cdot \mu \quad (7.3)$$

The similarity of the Ba/O ratio and the Ba-O bonding for the various cathodes suggests that the work function difference between the cathodes is determined by the difference in substrate work function φ_{substr} and the difference in dipole density n , and that the dipole moment μ is similar for the various cathodes. In order to test this hypothesis we have derived the Ba-O densities for the different cathodes using the dipole moment μ as a fitting parameter, and taking the work functions of the cathodes and of the substrates from our emission measurements and from the literature [31,63] respectively. The resulting densities for the various cathodes are shown in figure 7.6 as the open circles. Here, the dipole moment was

fitted as $\mu=6$ D for all cathodes, which is consistent with dipole moments reported in the literature [17]. It is evident that the thus derived Ba-O densities are in good agreement with the densities derived by the ion scattering analysis. This also strongly suggests that the Ba-O complex is similar on the various cathodes with an identical dipole moment of the Ba-O dipoles independent of the substrate.

7.3.4 The role of the surface oxygen

Most investigations of the surface composition of dispenser cathodes reported in the literature have focussed on the Ba coverage. However, in investigations of the influence of ion bombardment on the dispenser cathodes reported elsewhere, we have shown that Ba and O play an equally important role [12]. Here, we show that the Ba-O coverage of a certain cathode type is determined by the extent to which that particular substrate can maintain a certain O coverage at the operating temperature.

The importance of oxygen is demonstrated by studying the reactivation of the dispenser cathodes after the Ba-O complex has been removed at room temperature by 3 keV Ar^+ ion bombardment. In figure 7.8 the Ba (filled circles) and O (open circles) coverages as determined by AES analysis are shown during the reactivation at 1030 °C for the W-cathode (a) and the Os/Ru cathode (b). The Ba densities of the cathodes after full reactivation (≈ 150 s) are taken from the ion scattering in section 7.3.3. A detailed discussion of the resupply process is given in ref. [12], where figure 7.8b is also presented, and where it is shown that the reactivation rate for the Ba atoms and for the O atoms is limited by the O resupply rate (see chapter 8).

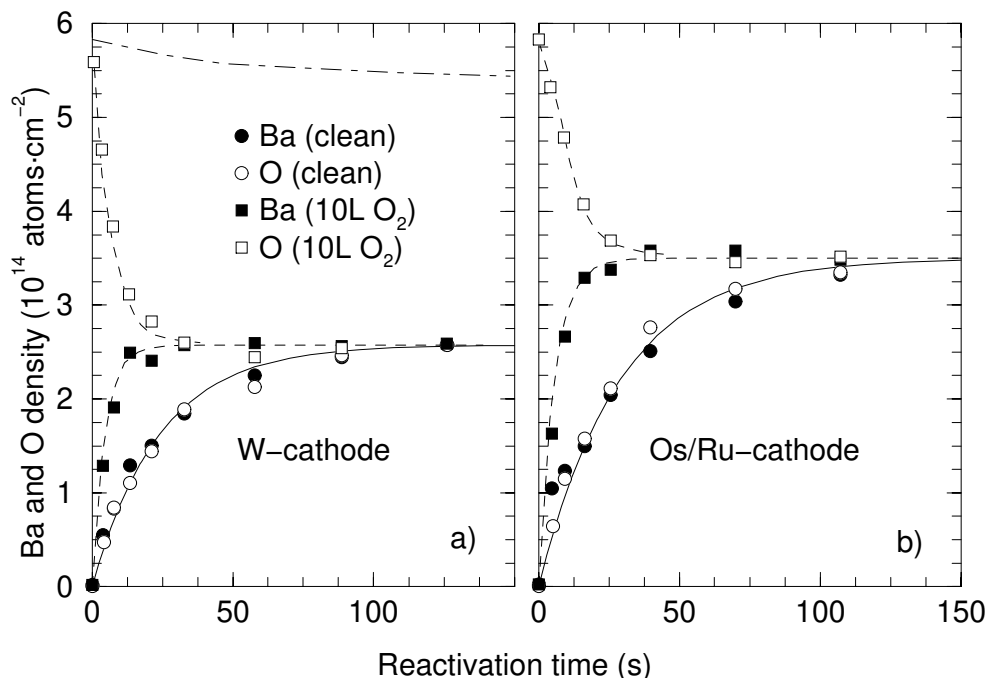


Figure 7.8. Reactivation of sputter-cleaned cathode: a) W-cathode, b) Os/Ru cathode. The reactivation after pre-oxidation is represented by the squares. The dash-dotted curve represent the O coverage on the unimpregnated cathode.

In addition, the reactivation of pre-oxidised substrates was studied, where the sputter-cleaned substrates were saturated by oxygen (10 L) at room temperature before the reactivation. Figure 7.8 also shows the reactivation of the pre-oxidised substrates (squares), where the O coverage directly after the O exposure was determined by LEIS using 5 keV He⁺ ions. It is evident that if O is already present on the surfaces, the Ba reactivation rate is enhanced; the reactivation rate is no longer limited by the slow O resupply, but is determined by the much faster Ba resupply [12].

Next, we focus on the O coverage during the reactivation of the pre-oxidised substrates. It is seen that the oxygen in excess of the O coverage after full reactivation is lost at the same rate as the Ba is resupplied. To investigate the influence of the cathode temperature we sputter-cleaned an unimpregnated W-cathode (no Ba-compound in the pores) at room temperature and also exposed it to 10 L oxygen. Figure 7.8 shows that the O coverage of the unimpregnated cathode (dash-dotted line) during operation at 1030 °C decreases only slightly over the time required for the reactivation. Furthermore, no loss of O was also observed while heating the O/W(110) reference system to the same temperature. The desorption of the O atoms must thus be induced by the presence of the Ba atoms. The most plausible explanation is that the O is lost by desorption of the Ba-O complex as a whole due to the electrostatic repulsion between adjacent Ba-O dipoles. This electrostatic interaction weakens the O-substrate bond compared to the situation where no Ba atoms are bound to the O atoms. Investigations of Ba adsorbed on W substrates have shown that the binding energy of the Ba atoms decreases with increasing coverage due to an increase in the electrostatic repulsion between the Ba dipoles [16,17]. A strong O-substrate bond implies that a large electrostatic repulsion can be tolerated before desorption of the Ba-O complex takes place.

7.3.5 The role of the cathode substrate

Since the discovery by Zalm et al. [2] that the emission of the dispenser cathodes can be enhanced by coating the surface of the W matrix by an Os layer with a high work function, many investigations have focussed on preparing cathodes with an as high as possible work function of the non-covered substrate [64,65,66,67]. The search for substrates with a high work function is based on reports about the paradoxical effect that the minimum work function at the optimal Ba-O coverage is lower for a high work function of the non-covered substrate [2]. To demonstrate the influence of the substrate work function, figure 7.9 shows the electron emission of cathodes with different substrates relative to the emission of the W-cathode (left ordinate scale). The solid line represents an average value for the different substrates taken from the literature [31,32,63], while the filled circles represent our emission measurements. Figure 7.9 also shows the substrate work functions as open circles (right ordinate scale). A reasonable correlation is observed between the substrate work function and the work function and corresponding emission of the cathodes [31,32,63]. Indeed, the work functions of the cathodes used in these investigation decrease with increasing substrate work function (see table 7.1). However, in figure 7.9 it is also evident that the Pt and Au substrates with high work functions show poor emission compared to the W-cathode.

Apparently, a high work function substrate is no guarantee for a low work function cathode. The most important property of the substrate is that it can maintain a large Ba-O coverage during cathode operation, in order to obtain a low work function. The bonding of the Ba-O dipoles to the substrates is thus of vital importance for the emission properties of the cathodes. When the Ba-O bonding to the substrate is weak, the electrostatic repulsion results in a low Ba-O coverage and high work function during cathode operation.

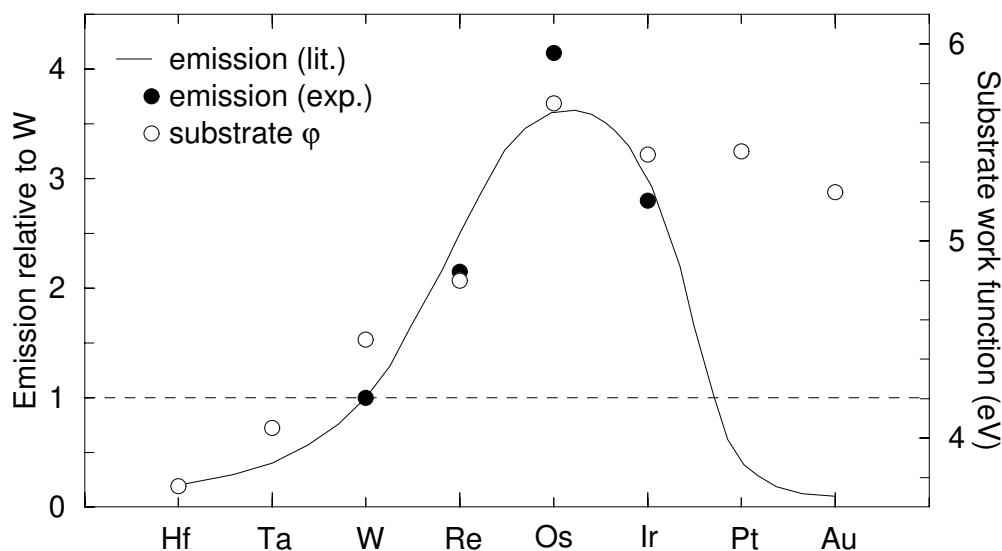


Figure 7.9. The influence of the substrate material on the cathode performance. Left ordinate scale: electron emission relative to the W-cathode, where the solid curve represents an average emission value taken from the literature, and the filled circles represent the emission data in this work. Right ordinate scale: work functions of the various substrates (open circles). A reasonable correlation is observed between the substrate work functions and the electron emission.

Green [32] theoretically studied the bonding between the O atoms in the Ba-O complex and different transition metals, and qualitatively explained the emission trends for the different transition metal substrates as shown by the solid curve in figure 7.9. He found that the strength of the bond between the O atoms and the substrate is determined by the orientation and the number of unoccupied d-orbitals of the substrate atoms. The W atoms have a single vacant d-orbital protruding normal to the surface, which bonds with a filled O orbital. The Ir, Os and Re atoms have two vacant d-orbital lobes available and oriented suitably for bonding with the two O orbitals. Hence, two bonds are formed, giving a stronger total bond and a larger heat of adsorption. This is consistent with desorption experiments by Forman, where it was concluded that the binding energy of the dipoles on an Os/Ru substrate is higher than on a W substrate: 5.4 eV and 4.8 eV respectively [56,68]. Moreover, Haas et al. showed that the work function decreases with an increasing O 2p binding energy [59].

In contrast, for Pt no suitable vacant orbitals exist, and only partially filled orbitals are responsible for the, therefore, weak bonding. The increase in the Ba-O coverage from the W-substrate to the Os/Ru-substrate, as observed in figure 7.6, is consistent with this theory, and is thus caused by the orientation and the occupancy of the d-orbitals of the substrate atoms. The low emission of the cathodes with a Pt substrate is therefore most probably caused by the low Ba-O coverage due to the weak bonding with the substrate, which is consequently insufficient to compensate for the high work function of the non-covered Pt substrate.

We conclude that a low work function cathode requires a strong bonding of the Ba-O complex. Although many studies have focussed on obtaining a high substrate work function, only few have investigated the O-substrate bond [31,32,59]. Here, we emphasise that the bonding of the O atoms in the Ba-O complex with the substrate atoms determines the Ba-O

coverage of the cathode, and a strong O-substrate bond is thus crucial for the emission capabilities of the cathodes.

7.4 Conclusions

Surface analysis of thermionic dispenser cathodes with W, Re, Ir and Os/Ru substrates revealed that the Ba-O complex responsible for the low work functions of the cathodes is present in a similar form on all cathodes. At the operating temperature the Ba atoms can only be present on the surface when bound to O atoms, which results in an atomic Ba/O ratio close to unity with the Ba atoms positioned above the O atoms.

The work functions of the cathodes are determined by the work functions of the clean non-covered surfaces and the Ba-O coverages. The Ba-O coverage during cathode operation depends on the number and the orientation of the unoccupied d-orbitals of the substrate atoms. If the bonding is weak, the electrostatic repulsion between the Ba-O dipoles leads to desorption of the Ba-O complex, and results in a low coverage and high work function. From the W substrate to the Os/Ru substrate the bonding increases, and consequently so does the Ba-O coverage. The increase in coverage is sufficient to compensate for the higher substrate work functions, and thus results in a decreasing work function from the W-cathode to the Os/Ru-cathode. Further improvement of the emission capabilities of the cathodes can thus be obtained by enhancing the bond between the O atoms in the Ba-O complex and the substrate atoms. We emphasise that the results obtained here also show that a high work function of the substrate is not an as important property as has been previously assumed.

The emission limit of the cathodes can be estimated from investigations of model systems. When the Ba and O adsorption are performed in a controlled manner, the work function minimum of the Ba-O-substrate system under investigation can be derived. For example, investigations of Ba and O adsorption on W substrates have shown that at the optimal coverage a work function of the order of $\phi=1.8$ eV is possible [16,17,52,69]. Hence, for the W-cathode the emission densities can be increased one order of magnitude if the bonding between the O atoms in the Ba-O complex and the substrate atoms is enhanced.

Acknowledgements

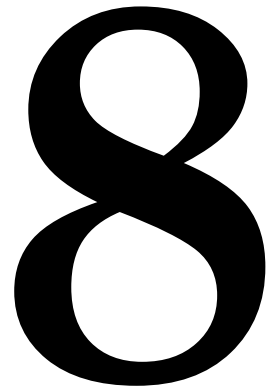
We would like to thank Georg Gärtner (Philips Forschungslaboratorien, Aachen) en Albert Manenschijn (Philips Display Components, Eindhoven) for all the support and the discussions. We also would like to thank Wolfgang Mueller for the discussion about the influence of the Ba-O geometry on the cathode work function.

References

- 1 R.E. Thomas, J.W. Gibson, G.A. Haas, R.H. Abrahams, *IEEE Trans. Elec. Dev.* 37 (1990) 850.
- 2 P. Zalm, A.J.A. van Stratum, *Philips Tech. Rev.* 27 (1966) 69.
- 3 G. Gaertner, P. Geittner, H. Lydtin, A. Ritz, *Appl. Surf. Sci.* 111 (1997) 11.
- 4 see for example the published proceeding of the cathode conferences:
Tri-Service Cathode Workshop: *Appl. Surf. Sci.* volumes 2,8,16, 24.
International Vacuum Electron Sources Conference: *Appl. Surf. Sci.* volumes 111, 146.
- 5 R. Cortenraad, A.W. Denier van der Gon, H.H. Brongersma, G. Gaertner, A. Manenschijn, *Appl. Surf. Sci.* 146 (1999) 69.
- 6 R. Cortenraad, A.W. Denier van der Gon, H.H. Brongersma, *Surf. Interface Anal.* 29 (2000) 524.
- 7 D.P. Smith, *J. Appl. Phys.* 38 (1967) 340.
- 8 H.H. Brongersma, P.M. Mul, *Chem. Phys. Lett.* 14 (1972) 380.
- 9 E. Taglauer, "Ion scattering Spectroscopy", in *Ion Spectroscopies for Surface Analysis*, Eds. A.W. Czanderna, D.M. Hercules, Plenum Press, New York, 1991.
- 10 H. Niehus, W. Heiland, E. Taglauer, *Surf. Sci. Rep.* 17 (1993) 213.
- 11 G.C. Nelson, *J. Appl. Phys.* 47 (1976) 1253.
- 12 R. Cortenraad, A.W. Denier van der Gon, H.H. Brongersma, G. Gaertner, D. Raasch, A. Manenschijn, to be published.
- 13 S.N. Ermolov, R. Cortenraad, V.N. Semenov, A.W. Denier van der Gon, S.I. Bozhko, H.H. Brongersma, V.G. Glebovsky, *Vacuum* 53 (1999) 83-86.
- 14 R. Cortenraad, S.N. Ermolov, V.N. Semenov, A.W. Denier van der Gon, V.G. Glebovsky, S.I. Bozhko, H.H. Brongersma, accepted for publication in *J. Crystal Growth*.
- 15 R. Cortenraad, A.W. Denier van der Gon, H.H. Brongersma, S.N. Ermolov, V.G. Glebovsky, submitted for publication.
- 16 D.A. Gorodetskii, Y.P. Melnik, *Surf. Sci.* 62 (1977) 647.
- 17 E. Koch, W. Huisl (eds), "Gmelin Handbook of Inorganic and Organometallic Chemistry, Tungsten Supplement Volume A 6a", Springer-Verlag, Berlin, 1991.
- 18 A. Elbe, G. Meister, A. Goldmann, *Surf. Sci.* 371 (1997) 438.
- 19 K.E. Johnson, R.J. Wilson, S. Chiang, *Phys. Rev. Lett.* 71 (1993) 1055.
- 20 L.E. Davis, *Handbook of Auger Electron Spectroscopy*, Physical Electronics Industries, Eden Prairie, MN, 1978.
- 21 A. Shih, C. Hor, G.A. Haas, *Appl. Surf. Sci.* 2 (1979) 258.
- 22 D. Brion, J.C. Tonnerre, A.M. Shroff, *Appl. Surf. Sci.* 16 (1983) 55.
- 23 R. Cortenraad, S.N. Ermolov, B. Moest, A.W. Denier van der Gon, V.G. Glebovsky, H.H. Brongersma, accepted for publication in *Nucl. Instr. Meth.*
- 24 J. Hasker, *Appl. Surf. Sci.* 16 (1983) 220
- 25 C.E. Maloney, C.S. Fang, *Appl. Surf. Sci.* 24 (1985) 407.
- 26 A.W. Denier van der Gon, M.F.F.K. Jongen, H.H. Brongersma, U. van Slooten, A. Manenschijn, *Appl. Surf. Sci.* 111 (1997) 64.
- 27 W.L. Baun, *Appl. Surf. Sci.* 4 (1980) 374.
- 28 C.R.K. Marrian, A. Shih, G.A. Haas, *Appl. Surf. Sci.* 16 (1983) 1.
- 29 C.R.K. Marrian, A. Shih, G.A. Haas, *Appl. Surf. Sci.* 24 (1985) 372.

- 30 D. Norman, R.A. Tuck, H.B. Skinner, P.J. Wadsworth, Phys. Rev. Lett. 58 (1987) 519.
- 31 H.B. Skinner, R.A. Tuck, P.J. Dobson, J. Phys. D 15 (1982) 1519.
- 32 M.C. Green, report RADC-TR-81-211, Rome Air Development Center, Air Force Systems Command, New York, 1981.
- 33 A. Shih, D.R. Mueller, L.A. Hemstreet, IEEE Trans. Elec. Dev. 36 (1989) 194.
- 34 L.A. Hemstreet, S.R. Chubb, W.E. Pickett, Phys. Rev. B 40 (1989) 3592.
- 35 G.A. Haas, A. Shih, C.R.K. Marrian, Appl. Surf. Sci. 16 (1983) 139.
- 36 J.W. Gibson, R.E. Thomas, Appl. Surf. Sci. 16 (1983) 163.
- 37 private communications W. Mueller; to be published
- 38 M.J. Ashwin, D.P. Woodruff, Surf. Sci. 244 (1991) 247.
- 39 M. Beckschulte, E. Taglauer, Nucl. Instr. Meth. B 78 (1993) 29.
- 40 R. Souda, M. Aono, Nucl. Instr. Meth. B 15 (1986) 114.
- 41 R. Cortenraad, A.W. Denier van der Gon, H.H. Brongersma, S.N. Ermolov, V.G. Glebovsky, submitted for publication
- 42 H.D. Hagstrum, Phys. Rev. 96 (1954) 336.
- 43 H.D. Hagstrum: *Inelastic Ion-Surface Collisions*, Editors H.H. Tolk, J.C. Tully (Academic Press, New York, 1977), p. 1.
- 44 L.C.A. van den Oetelaar, H.E. van Benthem, J.H.J.M. Helwegen, P.J.A. Stapel, H.H. Brongersma, Surf. Interface Anal. 26 (1998) 537.
- 45 S.N. Mikhailov, R.J.M. Elfrink, J.-P. Jacobs, L.C.A. van den Oetelaar, P.J. Scanlon, H.H. Brongersma, Nucl. Instr. Meth. B93 (1994) 148.
- 46 C.E. Maloney, H.L. Zang, Appl. Surf. Sci. 21 (1985) 50.
- 47 J. Hasker, H.J.H. Stoffelen, Appl. Surf. Sci. 24 (1985) 330.
- 48 G. Eng, H.K.A. Kan, K.T. Luey, Appl. Surf. Sci. 16 (1983) 181.
- 49 G.A. Haas, C.R.K. Marrian, A. Shih, Appl. Surf. Sci. 24 (1985) 430.
- 50 D. Brion, J.C. Tonnerre, A.M. Shroff, Appl. Surf. Sci. 20 (1985) 429.
- 51 N.J.A. van Veen, Appl. Surf. Sci. 29 (1987) 113.
- 52 R. Forman, Appl. Surf. Sci. 2 (1979) 258.
- 53 E.S. Rittner, R.H. Ahlert, W.C. Rutledge, J. Appl. Phys. 28 (1957) 156.
- 54 Kh.I. Lakh, Z.V. Stasyuk, Soviet Phys.-Tech. Phys. 27 (1982) 848.
- 55 R. Forman, Appl. Surf. Sci. 17 (1984) 429.
- 56 R. Forman, Appl. Surf. Sci. 29 (1987) 127.
- 57 R. Forman, J. Appl. Phys. 47 (1976) 5272.
- 58 G.A. Haas, C.R.K. Marrian, A. Shih, Appl. Surf. Sci. 16 (1983) 125.
- 59 G.A. Haas, A. Shih, D. Mueller, R.E. Thomas, Appl. Surf. Sci. 59 (1992) 227.
- 60 V.K. Medvedev, T.P. Smereka, Sov. Phys. Solid State, 15 (1973) 507.
- 61 D.A. Gorodetskii, A.N. Knysh, Surf. Sci. 40 (1973) 651.
- 62 A.P. Makarov, O.K. Kultashev, Appl. Surf. Sci. 111 (1997) 56.
- 63 R.A. Tuck, Vacuum 33 (1983) 715.
- 64 C.S. Fang, W.S. Tse, Appl. Surf. Sci. 33/34 (1988) 1189.
- 65 C.S. Fang, C.E. Maloney, Appl. Phys. A. 50 (1990) 603.
- 66 R.E. Thomas, J.W. Gibson, Appl. Surf. Sci. 29 (1987) 49.
- 67 M.C. Green, H.B. Skinner, R.A. Tuck, Appl. Surf. Sci. 8 (1981) 13.
- 68 R. Forman, Appl. Surf. Sci. 25 (1986) 13.
- 69 K.G. Eyink, B.C. Lamartine, W.V. Lampert, T.W. Haas, Appl. Surf. Sci. 20 (1985) 215.

Dynamic Behaviour of Thermionic Dispenser Cathodes under Ion Bombardment



Abstract

We have investigated the surface coverage and electron emission of thermionic dispenser cathodes during 3 keV Ar^+ ion bombardment, thereby simulating the bombardment of the cathodes by residual gases that takes place in cathode-ray tubes as used in television-sets. During the ion bombardment at the operating temperature of 1030°C, a dynamic equilibrium is established between the sputter removal and resupply mechanisms of the Ba and O atoms that form the dipole layer on the cathode substrate. We have demonstrated that the performance of the cathodes under ion bombardment is governed by the O removal and resupply rates. It was found that the Ba resupply rate is almost an order of magnitude higher than the O resupply rate, but that the Ba atoms can only be present on the surface bound to O atoms. Therefore, the Ba/O ratio is approximately equal to unity during the ion bombardment. Based on the investigations of the removal and resupply processes, we proposed a model that accurately describes the surface coverage and electron emission during the ion bombardment, including the dependence of the ion flux and cathode temperature.

8.1 Introduction

Oxide cathodes consisting of the oxides of earth alkali elements (Ba, Sr, Ca) have been employed for many years as electron sources in cathode-ray tubes used in television-sets [1,2]. These cathodes consists of a thick oxide layer with a low work function of approximately 1.3 eV, and can deliver continuous electron emission densities of the order of $1 \text{ A}\cdot\text{cm}^{-2}$ at an operating temperature of 700-800°C.

With the introduction of large high-quality tubes and high-definition television, the demand arose for higher emission densities exceeding the capabilities of the oxide cathodes. Emission densities of 1 to 2 orders of magnitude higher than the limit of the oxide cathodes can be obtained from thermionic Ba dispenser cathodes, which are also used in high-power microwave tubes. These dispenser cathodes consist of a porous W matrix impregnated with a BaO containing compound [3]. Figure 8.1 shows a secondary electron microscope image of the porous matrix, showing the individual W granulates and the impregnated pores. During cathode operation a Ba-O monolayer is formed on the substrate with a Ba/O ratio approximately equal to unity [4] (see chapter 7). This electropositive dipole layer results in a work function of approximately 2eV. Because this work function is higher than the very low work function of the oxide cathode, the dispenser cathode is operated at a temperature of 1000°C to compensate for the higher work function. Note that there is thus a fundamental difference between the oxide and dispenser cathode: the low work function of the dispenser cathode is obtained by a monolayer Ba-O complex, while the low work function of the oxide cathode is due to a thick oxide layer.

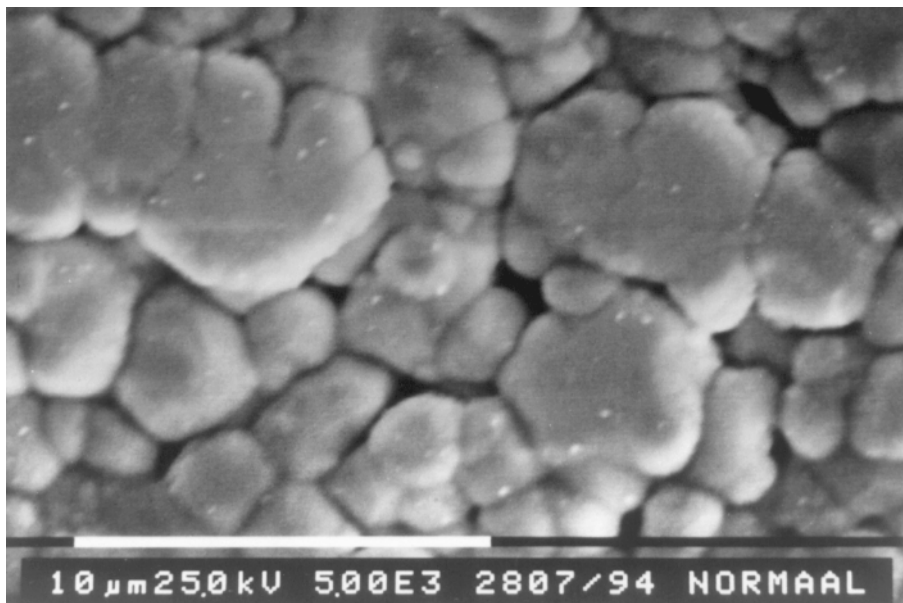


Figure 8.1. Secondary electron microscope image of the dispenser cathode, showing the porous matrix and the impregnated pores.

The Ba-O complex responsible for the low work function can be removed from the surface by thermal evaporation or through ion bombardment by residual gases in the tube. Residual gas atoms, ionised by the high density electron beam, are accelerated onto the cathode surface due to the electric fields present in the electron gun. The impinging rest gas ions sputter the Ba and

O atoms from the surface. In order to maintain the near monolayer Ba-O complex essential for the emission properties, the loss of the Ba-O complex is replenished by surface diffusion from the pores. However, because the required diffusion length is of the order of 10 μm for the dispenser cathodes, ion bombardment can strongly influence the emission densities. In addition to removal of the Ba-O complex, the ion bombardment can also damage the substrate of the cathode. Substrate damage is especially important for top-layer dispenser cathodes, where the emission is further enhanced by coating the W matrix by an additional metal (e.g. Os, Re, Ir) or metal/oxide (e.g. Re/Sc₂O₃) layer of the order of 300-500nm [5]. While the removal of the Ba-O complex can be restored by resupply from the pores, damage to the coating leads to gradual and permanent long-term emission degradation.

The low resistivity of the Ba dispenser cathodes to the ion bombardment is an important drawback of these cathode types. The importance of ion bombardment resistivity is most evident for the scandate cathode which has a coating containing a Ba-scandate complex. Although the scandate cathode has an enormous emission potential of up to 400 A·cm⁻², its breakthrough for applications has not been possible so far due to its strong susceptibility to ion bombardment damage and emission degradation [5].

In order to solve the problem of the low ion bombardment resistivity of the dispenser cathode, especially for scandate cathodes, more insight is needed in the behaviour of the cathodes during the bombardment. Although several studies have been reported on this topic, most of the studies have focussed on studying merely the influence of the bombardment on the electron emission [6]. From these emission measurement one often indirectly draws conclusions about the surface composition. Here, we have combined surface analysis techniques with emission measurements in order to investigate the surface composition and electron emission during the ion bombardment of thermionic dispenser cathodes. We will show that the generally accepted belief that the Ba removal and resupply rates determine the behaviour of dispenser cathodes during ion bombardment is incorrect. Instead, we show that if an ample supply of Ba is present in the pores, the O removal and resupply rates actually determine the Ba-O surface coverage and electron emission under bombardment.

The outline of this paper is as follows. First we give a brief description of the experimental techniques used to determine the surface composition and electron emission (section 8.2). Subsequently, a demonstration of the dynamic behaviour of the dispenser cathodes during the bombardment is presented (section 8.3.1). In order to come to a full description of the dynamic behaviour, we then separately discuss the Ba-O removal and resupply processes (section 8.3.2 and 8.3.3 respectively). The surface coverage and electron emission at the dynamic equilibrium as a function of the incident ion flux and cathode temperature are subsequently discussed (section 8.3.4). Furthermore, the experimentally determined coverage and emission are compared to a model that describes the Ba-O coverage during the ion bombardment, and is based on the separately determined removal and resupply rates. In addition to the influence of the ion bombardment on the Ba-O adlayer, we also investigated the damage to the cathode substrate that leads to unrecoverable long-term emission degradation (section 8.3.5). Finally, an ion bombardment experiment in an O₂ background pressure is performed in order to emphasise the importance of the O resupply during the ion bombardment (section 8.3.6). The main conclusions of this work are summarised in section 8.4.

8.2 Experimental

The two main constituent of the residual gas present in the cathode-ray tubes are Ar and N₂. When ionised, the ions are directed onto the cathode surface with an average kinetic energy of the order of 3 keV due to the electric fields in the electron gun. Thus, in order to simulate the ion bombardment that takes place in cathode-ray tubes, the dispenser cathodes are bombarded by 3 keV Ar⁺ ions (similar behaviour for N₂). The ion bombardment is performed in a UHV set-up using a differentially pumped ion gun. The ion beam is directed perpendicular onto the cathode, delivering a uniform ion dose over its surface. The dispenser cathodes used in the investigations were experimental Philips Os/Ru-I cathodes, where the surface of the W matrix with a diameter of 1 mm is coated with Os(80%)/Ru(20%) toplayers of 20 nm to 500 nm. (The coating on which the Ba-O complex is adsorbed will further be referred to as the substrate.) The matrix is impregnated with a 4:1:1 mixture of BaO, CaO, and Al₂O₃. The Os/Ru-I cathode is capable of emission densities of the order of 10-20 A·cm⁻² at its operating temperature of 1030°C.

The surface composition during the ion bombardment was analysed by two different methods. The composition of the outermost atomic layer of the surface was analysed using low-energy ion scattering (LEIS) by detecting the Ar⁺ ions that have backscattered from the cathode surface [7,8,9,10]. Because of the high electron affinity of the Ar⁺ noble gas ions, the neutralisation probability during an interaction with the surface atoms is very high. Ions that penetrate into the cathode beyond the outermost atoms, have multiple interactions and are therefore almost certainly neutralised. Here, we have measured the Ar⁺ ions that have backscattered over an angle of 136°. These ions were energy analysed by a cylindrical mirror analyser (CMA) and detected using a micro-channelplates based detector [11]. The energy spectrum thus obtained represents a mass spectrum of the outermost atomic layer during the bombardment.

In addition to analysing the backscattered Ar⁺ ions, Auger electron spectroscopy (AES) was used to determine the Ba and O coverage during the ion bombardment. For the Auger analysis a grazing incidence electron gun is used, where the electron beam is directed onto the surface at an angle of approximately 10° with the cathode surface. The grazing incidence minimised the contribution from the pores, and thus enabled a more accurate investigation of the emitting surface compared to perpendicular incidence. The Auger electrons were analysed by the same CMA as used for the ion scattering, but with a reversed polarity of the pass energy.

The electron emission of the cathodes during the ion bombardment was determined in a separate setup employing a close spaced diode configuration [5,12,13], with a distance of approximately 300 μm between the cathode and the anode. The ion beam was directed onto the cathode through a circular hole in the anode with a diameter of 2 mm. A high-voltage saw-tooth pulser was used to apply a diode voltage of 800 V, and the electron emission was determined in the saturation regime. The emission current was continuously monitored before, during, and after the ion bombardment.

8.3 Results and discussion

8.3.1 The dynamic equilibrium

A demonstration of the dynamic behaviour of the dispenser cathodes during the ion bombardment is given in figure 8.2. This example shows the emission of an Os/Ru cathode bombarded at operating temperature of 1030°C by a flux of $6 \cdot 10^{13}$ ions·cm⁻²·s⁻¹ Ar⁺ ions. The

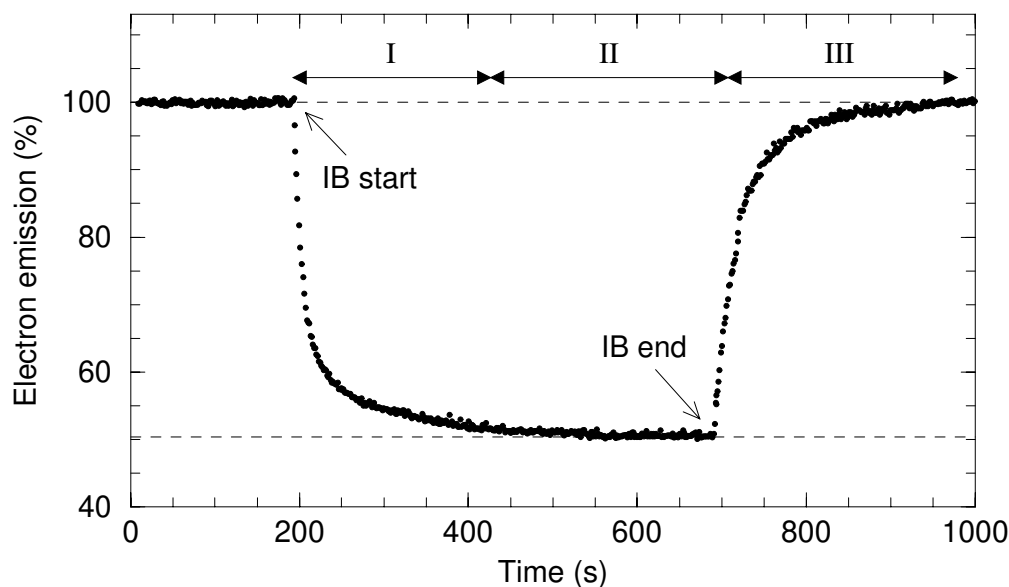


Figure 8.2. The dynamic behaviour of the emission of an Os/Ru dispenser cathode during ion bombardment with an ion flux of $6 \cdot 10^{13}$ ions \cdot cm $^{-2}$ \cdot s $^{-1}$ Ar $^{+}$ ions at an operating temperature of 1030°C. The emission is normalised to the emission in the absence of ion bombardment. I: formation of the equilibrium, II: the dynamic equilibrium, III: recovery after ion bombardment is stopped.

emission is normalised to the emission during operation in UHV in the absence of ion bombardment. Three stages can be identified in the figure: the formation of the dynamic equilibrium (I), the dynamic equilibrium (II), and the recovery after the ion bombardment is stopped (III). At the equilibrium the emission complex removal rate equals the resupply rate, and the surface coverage and emission are constant.

The removal rate depends on the incident ion flux F and the number of atoms removed per incident ion. The resupply is governed by surface diffusion of Ba and O atoms, and depends on the cathode temperature. The equilibrium coverage under ion bombardment thus depends on the ion flux to which the surface is subjected, and the temperature at which the cathode is operated. This is illustrated in figure 8.3 which shows ion scattering spectra under the dynamic equilibrium for different ion fluxes F at a fixed operating temperature of 1030°C. At a very low ion flux (a) no substrate atoms are observed in the outermost layer, indicating a complete coverage of the substrate. With increasing ion flux the removal rate increases, while the resupply rate determined by the temperature remains constant (b and c). Consequently, the substrate is no longer completely covered by the Ba-O complex and substrate peaks due to Ru, W and Os appear in the ion scattering spectra. These spectra serve as qualitative examples to demonstrate the change in surface coverage with increasing ion flux. Quantitative analysis is not straightforward due to the dependence of the neutralisation probability of the Ar $^{+}$ ions on the work function, as is discussed elsewhere [14,15].

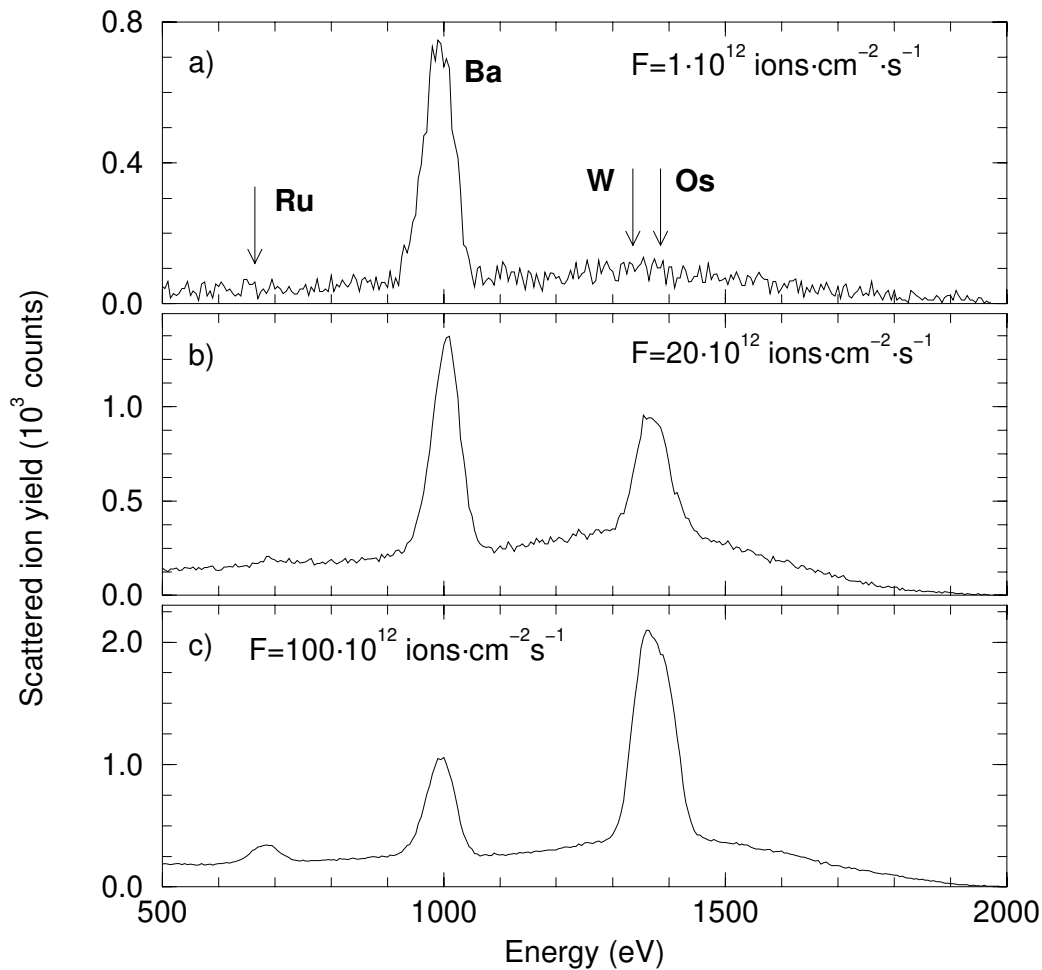


Figure 8.3. Ion scattering spectra at the dynamic equilibrium obtained by analysing the backscattered Ar^+ ions. At low ion flux the substrate is completely covered by the Ba-O complex. With increasing flux the intensities of the peaks due to the substrate atoms increase. The W and Os contributions are convoluted into a single peak, but can be resolved by peak fitting.

8.3.2 The sputtering process

Here, we will determine the probability that the Ba and O atoms constituting the emission complex are removed by the impinging ions. Only a small fraction of the adatoms are sputtered directly from the surface due to a collision between the adatom and an incident ion. Most incident ions do not have a hard collision with the outermost Ba atoms, but rather penetrate into the cathode substrate beyond the adlayer. The collisions of the ions with the substrate atoms initiate linear collision-chains of the substrate atoms as sketched in figure 8.4 [16,17]. If a chain of collisions is directed towards the surface, an atom in the outermost layer may be emitted from the surface since it cannot transfer its energy to a subsequent atom. Thus, the actual sputtered atom is only indirectly coupled to the incident ion. The sputter yield Y , which is defined as the number of atoms removed per incident ion, depends on the details of the bombardment, such as the ion type and the incident energy and angle of the ions [18,19].

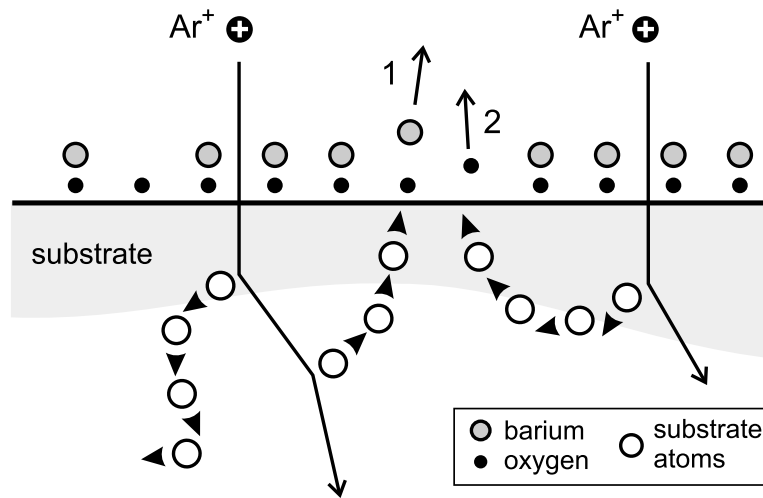


Figure 8.4. Schematic representation of the collision-chains of substrate atoms initiated by the incident ions. The Ba atoms are removed first (1), and the O atoms below can only be removed if the Ba atoms were removed by previous sputtering events (2).

To determine the sputter yield for the removal of the Ba and O adatoms, the cathode surface is bombarded by 3keV Ar⁺ ions at room temperature and thus no resupply of the Ba-O complex is possible. Figure 8.5 shows the Ba and O coverage as a function of the applied ion dose measured by the ion scattering and Auger analysis, where the coverages are normalised to the initial coverages of the undamaged cathode. We emphasise that the initial increase in the ion scattering signal is caused by a decrease in the neutralisation probability, resulting from the increase in work function associated with the Ba removal. The dependence of the neutralisation probability on the work function is discussed elsewhere in detail [14] (see chapter 5). Above a dose of $3 \cdot 10^{14}$ ions·cm⁻², indicated by the arrow, the neutralisation probability is constant and the ion scattering signal is proportional to the coverage.

The sputter yield Y for Ba can be determined from the signal decrease as a function of the applied dose. The decrease of the Ba density n when the surface is bombarded by an ion flux F can be expressed as:

$$\left. \frac{dn}{dt} \right|_{IB} = -\frac{n}{n_{max}} \cdot F \cdot Y = -\frac{n}{\tau_{IB}} \quad (8.1)$$

Here n_{max} is the maximum density corresponding to full surface coverage, and τ_{IB} is the time constant for Ba removal by the ion bombardment (IB). Assuming that the sputter yield Y is independent of the coverage, the Ba coverage $n(d)$ as a function of the applied ion dose $d=F \cdot t$ obeys:

$$n(d) = n_0 \cdot \exp(-Y \cdot d/n_{max}) \quad (8.2)$$

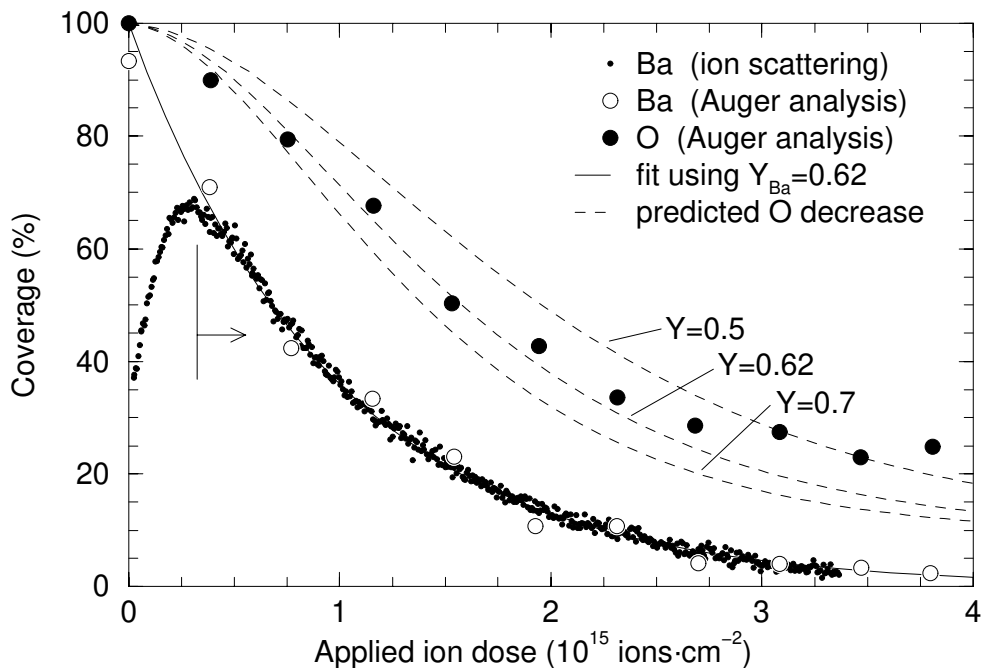


Figure 8.5. Decrease of the Ba and O coverage during 3 keV Ar^+ bombardment at room temperature. The solid curve shows a fit to the Ba decrease using a sputter yield $Y=0.62$, and the middle dashed curve shows the decrease in O assuming the same sputter yield and a step-by-step removal process. The other dashed curves with $Y=0.5$ and $Y=0.7$ are shown to indicate the accuracy of the fit.

The density n_0 represent the surface density of the Ba-O complex in the absence of ion bombardment (at $t=0$). The sputter yield can be deduced from the decay constant of the ion scattering and Auger signal (solid curve). For the maximum Ba density we used $n_{max}=6 \cdot 10^{14}$ atoms·cm⁻², according to investigations of Ba adsorption of W substrates [20,21]. The obtained sputter yield is $Y=0.62 \pm 0.07$. This is in good agreement with previously determined sputter yields by Denier van der Gon et al. ($Y=0.63$) [14] and Gaertner et al. [22] ($Y=0.58$), which were deduced directly from ion scattering investigations and indirectly from emission measurement, respectively.

The decrease in the O coverage is slower than that of Ba coverage, indicating that the Ba-O complex is not removed as a whole. This is not surprising since the O atoms are situated in a plane below the Ba atom [14,15,23,24], and are predominantly removed after the Ba atoms in the outermost atomic layer have been removed by previous sputtering events. However, it is not unlikely that a small fraction of the O atoms are removed via sputtering of the Ba-O complex as a whole. The middle of the dashed curves in figure 8.5 shows the expected signal decrease assuming an identical sputter yield for Ba and O, and a step-by-step removal of the complex. The other dashed curves indicate the influence of the value of the sputter yield for O on the fit. When the Ba is almost completely removed, the O becomes more difficult to remove by the ion bombardment because the O atoms are more tightly bound to the substrate. We conclude that the Ba and O adatoms are removed step-by-step with approximately the same sputter yield. Although these sputter yields were determined at room temperature, the

same values apply during the operating temperature since the thermal energy is negligible compared to the binding energy of the adatoms and to the kinetic energy of the incident ions.

8.3.3 The resupply process

The Ba-O resupply during the ion bombardment is investigated here by studying the reactivation of the cathodes after the Ba-O complex has been removed by sputtering at room temperature. The reactivation procedure is studied at various temperatures between 800°C and 1200°C. The surface coverage during the reactivation is monitored by AES. Figure 8.6 shows the Ba coverage (filled circles) and O coverage (open circles) as a function of the reactivation time for cathode temperatures of 920°C (a) and 1030°C (b). At low reactivation temperatures, of the order of 900°C, the Ba resupply is faster than the O resupply in the initial reactivation (see figure 8.6a). However, as the coverage increases, the Ba resupply approaches and follows the O resupply. When the temperature is increased, the initial faster Ba resupply becomes less significant (see figure 8.6b). At high reactivation temperatures, of the order of 1100°C, the Ba and O resupply curves are identical.

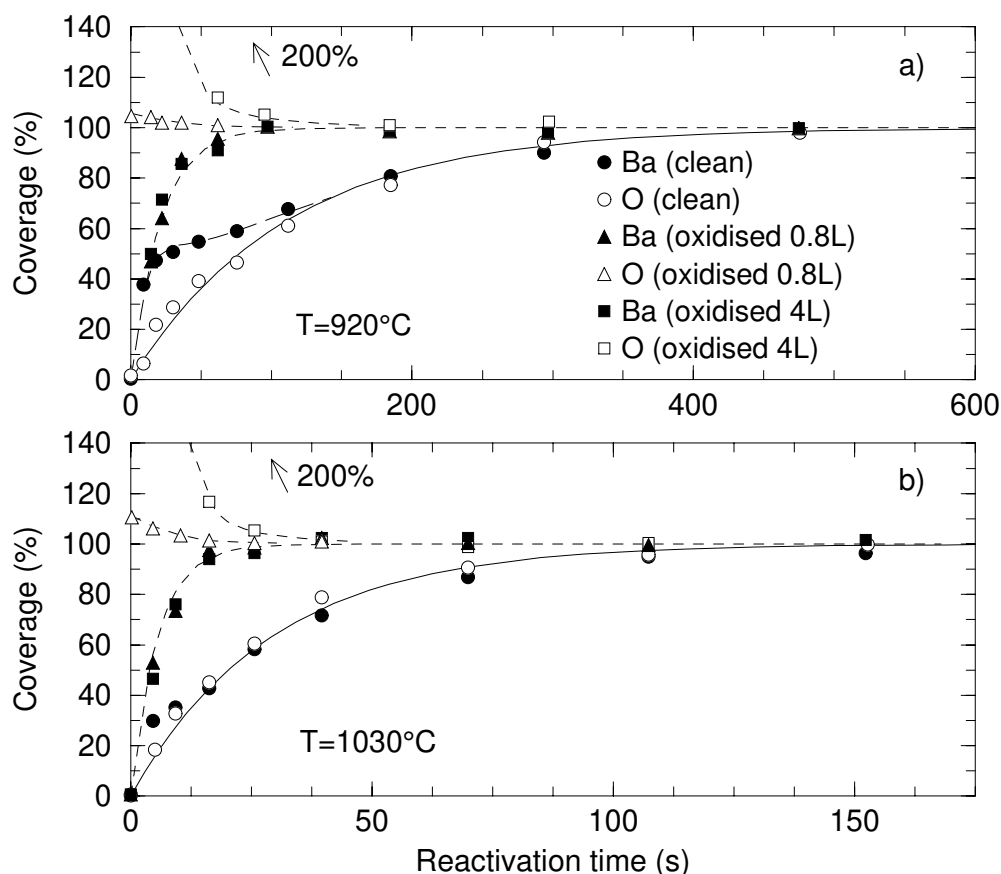


Figure 8.6. Reactivation of the dispenser cathodes after removing the Ba-O complex by ion bombardment (circles), and after pre-oxidation of the sputter-cleaned substrates (triangles and squares). The top panel (a) and bottom panel (b) show the reactivation at temperatures of 920°C and 1030°C respectively. The Ba and O coverages are normalised to the coverages when the cathodes are operated in UHV.

To investigate the role of the oxygen in the resupply process, the reactivation procedure was also performed on pre-oxidised substrates. After the removal of the Ba-O layer by sputtering, the substrates were exposed to oxygen prior to reactivation. Figure 8.6 also shows the reactivation of the pre-oxidised substrates for an initial coverage of $n_O=100\%$ (squares) and $n_O=200\%$ (triangles), which were prepared by 0.8 L and 4 L oxygen exposure at room temperature respectively. The dramatic influence of the O is apparent: the resupply of Ba on the pre-oxidised substrates is much faster than that for the clean substrates, and is comparable to the initial fast Ba resupply as is most obvious at low reactivation temperatures (see figure 8.6a). Moreover, it is observed that the excess oxygen compared to the O coverage during operation is lost at approximately the same rate as the Ba resupply takes place.

These observations can be explained as follows. The initial fast resupply of Ba at low reactivation temperatures is caused by Ba diffusion across the clean cathode substrate. The average diffusion length $\langle l \rangle$ of the Ba atoms is determined by its diffusion rate D and residence time τ , which represents the time the Ba spends on the surface before it is thermally desorbed. The substrate area $\langle l \rangle^2$ that can be covered by the Ba adatoms is limited by the residence time, and is given by [25,26,27]:

$$\langle l \rangle^2 = D \cdot \tau = D_0 \tau_0 \cdot \exp\left(\frac{(Q - E_d)}{kT}\right) \quad (8.3)$$

Here Q and E_d are the activation energies for desorption and diffusion, respectively, and are further referred to as desorption and diffusion energy, respectively. The effective diffusion length for Ba on the clean substrate is evidently insufficient to cover the substrate completely [28]. This is most clearly seen in figure 8.6a, where it is observed that the Ba diffusion across the clean substrate results in a maximum coverage of approximately 50%. The limited Ba coverage of the clean substrate is attributed to the fact that the desorption energy Q strongly decreases with increasing coverage due to mutual depolarisation between the Ba adatoms [29].

Surface coverage beyond the limit of the diffusion length for Ba on the clean substrate requires the presence of oxygen on the surface. The interaction between the Ba and O atoms increases the desorption energy due to the stronger Ba-O-substrate bond compared to the Ba-substrate bond [30,31,32,33,34]. Consequently, the diffusion length for Ba is higher in the presence of O, but the Ba resupply rate depends on the arrival of O on the substrate. On the pre-oxidised substrates, the Ba resupply rate is determined by the diffusion rate of Ba on the oxidised surface, and is not limited by the slower O resupply.

When the temperature is increased, the Ba and O resupply rates increase (see figure 8.6b). Because the desorption energy is higher than the diffusion energy ($E_d/Q \approx 0.1-0.2$), the factor $(Q-E_d)$ in eq. (8.3) is positive. Thus, when the temperature is increased the diffusion length decreases. For reactivation temperatures higher than approximately 1000°C, the extent to which the Ba can cover the clean substrate is negligible and the Ba resupply is only possible in the presence of O. Therefore, in figure 8.6b almost no initial fast Ba resupply is observed compared to the slower O resupply.

Evidence for the Ba-O bonding in the resupply process is presented in figure 8.7. Here, low-energy Auger spectra are shown for the reactivation at a temperature of 920 °C after a reactivation time of 20 s (a) and 200 s (b). Both spectra show two Auger peaks: the peak near 73 eV is due to Auger transitions involving the electron of the Ba levels (Ba 4d-Ba 5p-Ba 6s), while the peak near 68 eV is caused by transitions from the electrons involved in the Ba-O

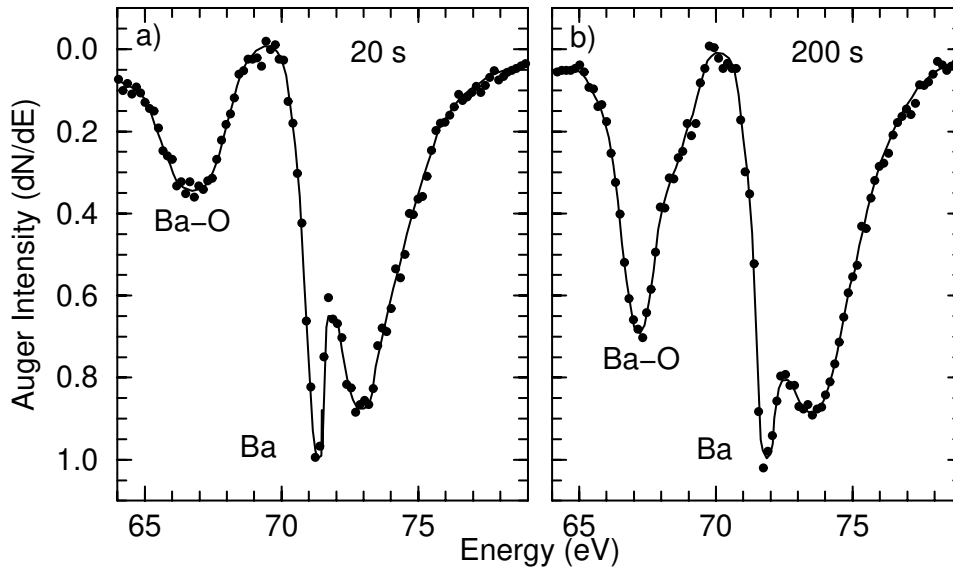


Figure 8.7. Low-energy Auger spectra during the reactivation at 920°C: (a) after 20 s reactivation, (b) after 200 s reactivation. The peak at 68 eV is a measure for the Ba-O bond, and the peak at 73 eV is a measure for the Ba density.

bonding (Ba 4d-Ba 5p-O 2p) [35,36,37]. The intensities of the 73 eV and 68 eV peaks are thus a measure for the Ba density and the Ba-O bonding respectively. The peaks in figure 8.7 are normalised to the intensity of the 73 eV peaks. In figure 8.7 it is evident that in the initial reactivation (a), where the Ba diffuses across the clean substrate, there are fewer Ba-O bonds than for coverages where the Ba resupply depends on the O resupply (b). We emphasise that the Ba-O bond evidenced here enhances the residence time of the Ba atoms, but the Ba and O adatoms are supplied as individual atoms. Concluding from the observed Ba-O bond that the dipole complex is supplied in the oxidic form BaO is incorrect.

From the observations above we conclude that the resupply of the Ba-O emission complex is limited by the O resupply. The resupply of O atoms is thus equally important as the resupply of Ba atoms, since without the Ba-O bond the cathode substrate can not be sufficiently covered by the dipole complex. The role of O has been underestimated in most studies of dispenser cathodes, where one in general focuses on the Ba adatoms.

The activation energy for resupply of the Ba-O complex can now be determined from the temperature dependence of the O resupply. The diffusion rate of the adatoms is proportional to the concentration gradient (Fick's first law). Therefore, we introduce the time constant τ_{res} for resupply as:

$$\left. \frac{dn}{dt} \right|_{res} = \frac{n - n_0}{\tau_{res}} \quad (8.4)$$

The time constant τ_{res} depends on the reactivation temperature. The O coverage during the reactivation is thus given by:

$$n(t) = n_0 \cdot (1 - \exp(-t/\tau_{res})) \quad (8.5)$$

The solid curves in figures 8.6a and 8.6b represent the results of fitting eq. (8.5) to the O resupply, where τ_{res} was used as a fitting parameter. The temperature dependence of τ_{res} is shown in figure 8.8 (open circles). The figure also shows the time constant from the emission recovery after the ion bombardment stop (filled circles), which will be discussed in section 8.3.4. The activation energy for resupply is found to be $E_{res}=(2.1\pm 0.1)$ eV, which is in good agreement with the activation energies for recovery determined by Manenschijn et al. [38] ($E_{res}=2.2$ eV) and Gaertner et al.[6] ($E_{res}=2.0$ eV) determined from emission measurements.

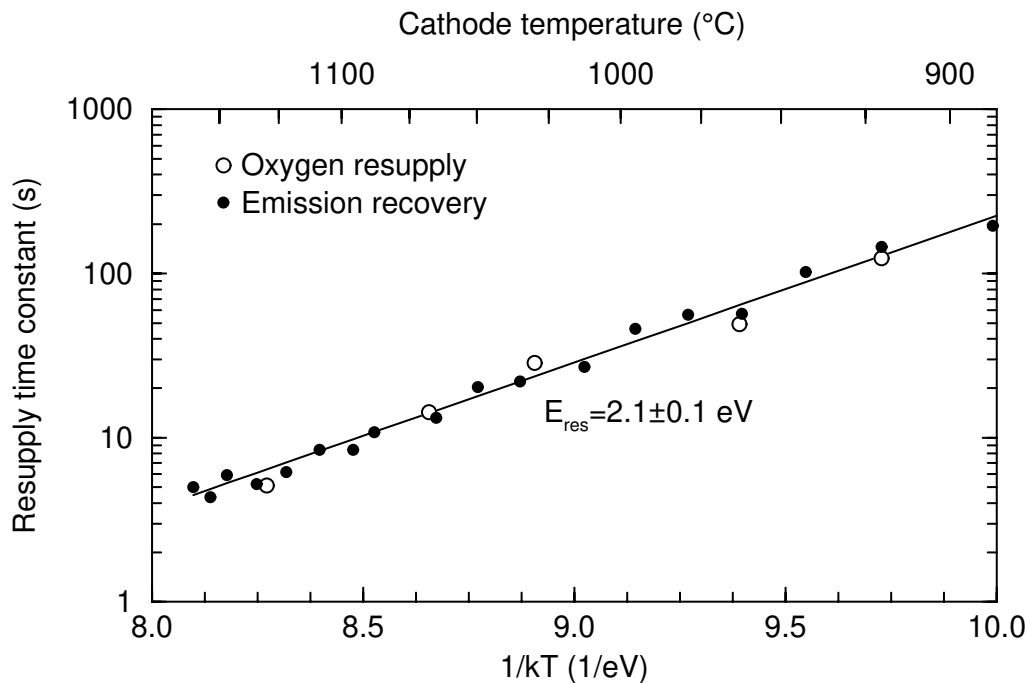


Figure 8.8. The time constants for O resupply (open circles) and emission recovery (filled circles) versus the temperature. The O resupply rates were determined by the Auger analysis. The time constants for the emission recovery were determined from the emission increase immediately after the ion bombardment was stopped.

In order to investigate whether the activation energy for the O resupply is determined by the diffusion of O across the substrate, or by the formation of free O in the pores, reactivation of the cathodes was studied after O₂ exposure. The cathode was first exposed to 100 L O₂ at room temperature, and subsequently the substrate was cleaned by the ion bombardment. However, an ample supply of O is now present in the pores as follows from the results below. Reactivation was subsequently studied at a temperature of 1030°C. This procedure was performed for an Os/Ru cathode, as well as unimpregnated W matrix where no BaO containing compound was present in the pores. It was found that the time constants for the O resupply for the impregnated and unimpregnated cathode were $\tau_{res}=9$ s and $\tau_{res}=7$ s

respectively. Reactivation without O_2 exposure gives a time constant for the O resupply of $\tau_{res}=21$ s (see figure 8.6b). The O resupply is thus faster by approximately a factor of 2.5 if O is abundantly present in the pores. We therefore conclude that the limiting factor in the O resupply is the formation of free O in the pores. Moreover, the activation energy for the resupply derived here is much larger than the activation energy for O diffusion across a W substrate, which is of the order of 1 eV [25,26,39]. This indicates that for the resupply more energy is required than merely the diffusion of O from the pores to the surface. The activation energy for the resupply thus represents the activation energy for the formation of free O in the pores. Although the value of the activation energy is in agreement with previous reported studies, the assignment of the activation energy to the formation of O represents a new interpretation which can only be made on the basis of the present surface coverage measurements.

8.3.4 Coverage and emission at dynamic equilibrium

The surface coverage at dynamic equilibrium is determined by the removal and resupply rates, and thus depends on the incident ion flux and the cathode temperature. The surface coverage at equilibrium is shown in figure 8.9 as a function of the ion flux for different cathode temperatures (filled symbols). In addition, figure 8.10 shows the equilibrium coverage as a function of the cathode temperature for a fixed ion flux of $3 \cdot 10^{13}$ ions \cdot cm $^{-2}$ \cdot s $^{-1}$. Here, we did not differentiate between the Ba and O coverages because it is observed that the Ba/O ratio is constant during the ion bombardment. As discussed in the previous section, the Ba atoms

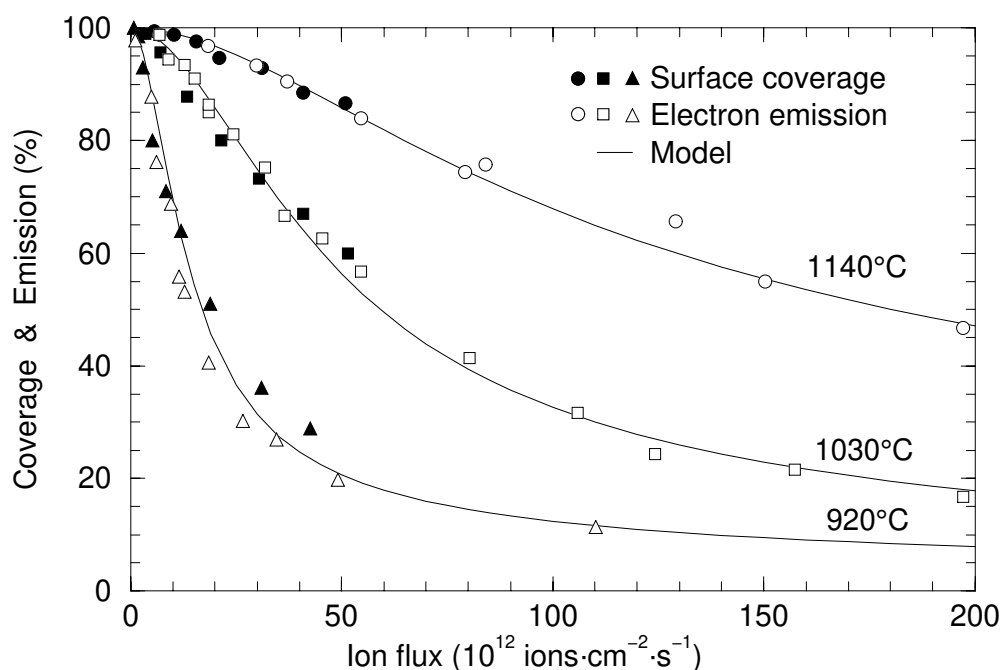


Figure 8.9. The Ba-O surface coverage (filled circles) and electron emission (open circles) versus the ion flux for different cathode temperatures. The solid curves represent the results of the derived model based on the time constant for O removal and resupply (see text).

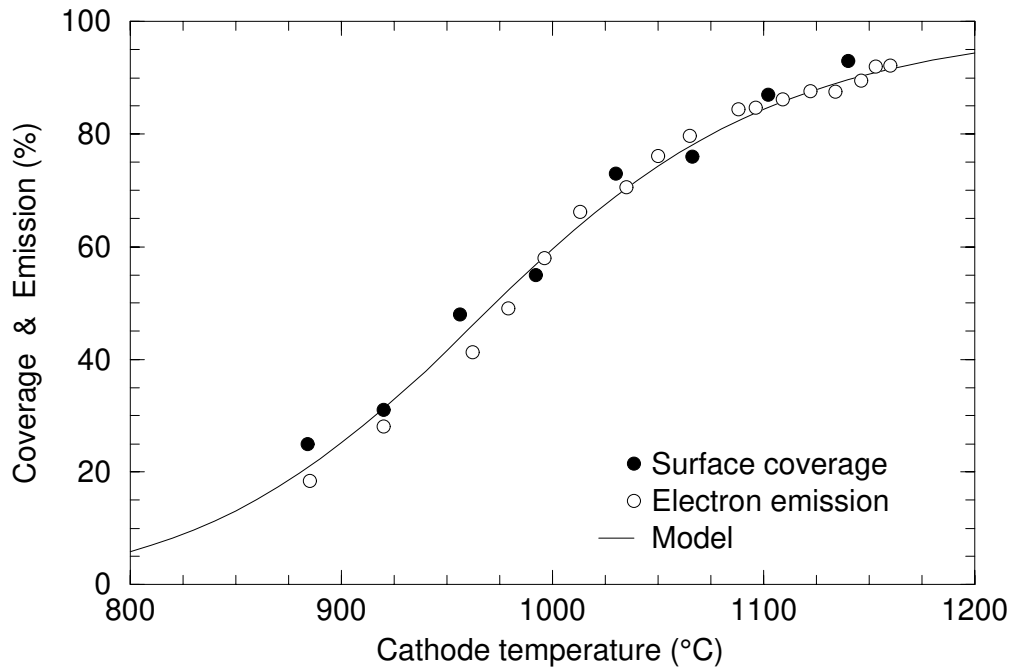


Figure 8.10. The Ba-O surface coverage (filled circles) and the electron emission (open circles) versus the cathode temperature for a fixed ion flux of $30 \cdot 10^{12}$ ions \cdot cm $^{-2}$ \cdot s $^{-1}$ Ar $^{+}$ ions. The solid curve represents the results of the derived model based on the time constants for O removal and resupply.

removed by the ion bombardment are resupplied very fast, but can only be present on the surface bound to O atoms. Therefore, the Ba/O ratio is approximately equal to unity during the ion bombardment, independent of the ion flux or cathode temperature.

The electron emission during the ion bombardment, as determined in the diode configuration, is also shown in figures 8.9 and 8.10 (open symbols). It is observed that the decrease in electron emission is identical to the decrease in coverage. This “one to one” relation between emission and coverage indicates that each Ba-O site can be regarded as an individual emission site, and that the total emission equals the sum of the local emission sites. Moreover, it confirms that the fraction of the surface covered during the ion bombardment has the correct Ba-O arrangement required for optimum emission. Note that this one-to-one relation between emission and coverage has been assumed in previous investigation of the emission degradation of dispenser cathodes under ion bombardment [22], but this is the first time it has been actually been verified experimentally.

A model that describes the surface coverage and electron emission during the ion bombardment can be derived using the insight gained from the separate investigations of the removal and resupply processes. Combining equations (8.1) and (8.4) for the removal and the recovery rate respectively, the dependence of the equilibrium coverage n_{eq} on the time constants for removal τ_{IB} and resupply τ_{res} is given by:

$$\frac{n_{eq}}{n_0} = \frac{1}{1 + \frac{\tau_{res}}{\tau_{IB}}} \quad (8.6)$$

Since the one-to-one relation between coverage and emission has been proven above, this equation can also be used to describe the emission during the dynamic equilibrium. The O coverage determines also the Ba coverage, and thus the time constants for O removal and resupply must be used in eq. (8.6). In order to verify that the O resupply rates should also be applied for the modelling of the emission, we have determined the time constants for the emission recovery after the ion bombardment has been stopped. These time constants are compared to the O resupply rates derived from the reactivation studies in figure 8.8 (filled circles). The good agreement between the time constants confirms the O resupply determines the emission recovery if sufficient Ba is generated.

The time constants for the O removal in the model cannot be deduced straightforward using the derived sputter yield for O in section 8.3.2. In the removal process the Ba and O atoms are removed in a step-by-step manner, which means that O can only be sputtered if the Ba atoms are not present on top. The Ba atoms thus form a protective layer over the O atoms. In order to remove an O atom, collision-chains induced by the incident ions have to hit the surface at the same O position twice within the time it takes for the Ba removed in the first event to be resupplied on top of the O atom. The probability for the same position to be hit twice is proportional to the incident ion flux, and the probability for the Ba to be resupplied between those two events depends on the temperature. The probability to remove O from the surface thus depends on both the ion flux and temperature. In figure 8.11 the effective sputter yield for the O removal is shown versus the ion flux for two different cathode temperatures. The

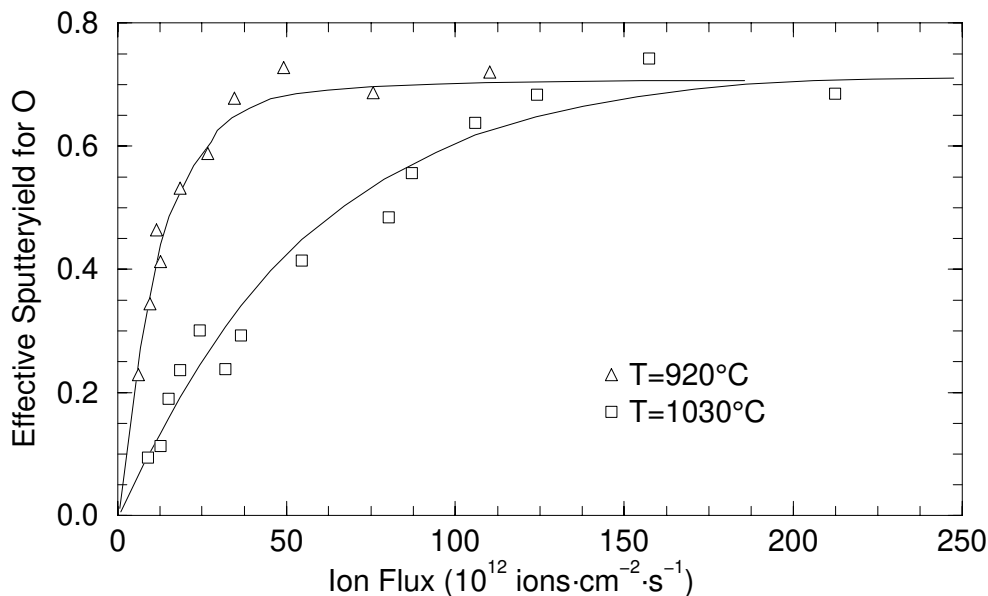


Figure 8.11. Effective sputter yield of O as a function of the ion flux for different cathode temperatures. The sputter yields were derived from the emission decrease at the start of the ion bombardment.

effective sputter yield has been determined from the slope of the initial decrease of the electron emission immediately after the start of the ion bombardment, when the resupply of O is negligible since $n \approx n_0$ (see figure 8.2). Here, we made use of the one-to-one relation between emission and coverage. In the figure it is observed that at low ion flux the effective sputter yield for O is much smaller than the sputter yield determined at room temperature ($Y=0.62$) due to the protective function of the Ba atoms. However, as the flux increases the finite Ba resupply rate is not sufficiently high to protect the O layer, and the effective sputter yield increases to the value of approximately $Y=0.6-0.7$, comparable to the value for Y determined in section 8.3.2. When the cathode temperature increases, the protective function of the Ba layer can be maintained up to a higher ion flux due to the faster Ba resupply. This dynamic protective function of the Ba atoms and is crucial for the performance of dispenser cathodes under ion bombardment, and although this effect has been investigated previously using emission measurements [6], a thorough investigation including a surface analysis as performed here has, to our knowledge, never been reported before.

These effective sputter yields for O derived from figure 8.11 are used in combination with the O resupply rates in eq. (8.6) to model the behaviour of the dispenser cathode under ion bombardment. The results of the model are shown in figures 8.9 and 8.10 by the solid curves. An excellent agreement between the model and the experimentally determined coverage and emission during ion bombardment is observed. We emphasise that no additional fitting has been performed. Thus, we conclude that the behaviour of the cathode surface during ion bombardment can be accurately described by the derived model including the O removal and resupply rates.

8.3.5 Ion bombardment induced substrate damage

In the previous section we discussed the protective function of the Ba atoms against the removal of O atoms by the ion bombardment. In a similar manner, the Ba-O complex protects the coating of the top-layer cathodes against the removal of substrate atoms by the collision-chains. However, unlike the O atoms, loss of substrate atoms cannot be resupplied and thus leads to unrecoverable long-term emission degradation for top-layer cathodes [6]. The fraction of the surface not covered by O is also not covered by Ba, and if the collision-chains reach the surface at such positions, substrate atoms can be sputtered from the surface. The protection efficiency of the adlayer thus depends on the O coverage, and is therefore indirectly related to the incident ion flux and the cathode temperature.

Here, we investigate the damage to the substrate during ion bombardment for Os/Ru cathodes with a specially prepared thin Os/Ru layer of approximately 100 nm. To determine the protection efficiency of the adlayer the cathodes are exposed to a certain fixed ion dose, which is delivered to the cathode at a varying ion flux during operation at 1030°C. After the applied ion dose, a depth profile of the substrate is made using 3 keV Ar^+ ions with the cathode at room temperature. In order to study the damage to the substrate inflicted by the ions, and determine the protection efficiency of the Ba-O layer, the depth profiles of the cathodes exposed to the ion bombardment are then compared to depth profiles of reference cathodes not exposed to any ion bombardment. Note that the time over which the ion bombardment dose is applied depends on the ion flux. To correct for any possible change in the substrate due to the (varying) extended time at operating temperature, the reference cathodes were operated simultaneously with the bombardment experiments.

The approach is demonstrated in figure 8.12, where the depth profiles of the reference substrate (a) and the damaged substrate (b) are presented for a dose of $d=900 \cdot 10^{15}$ ions·cm⁻² at

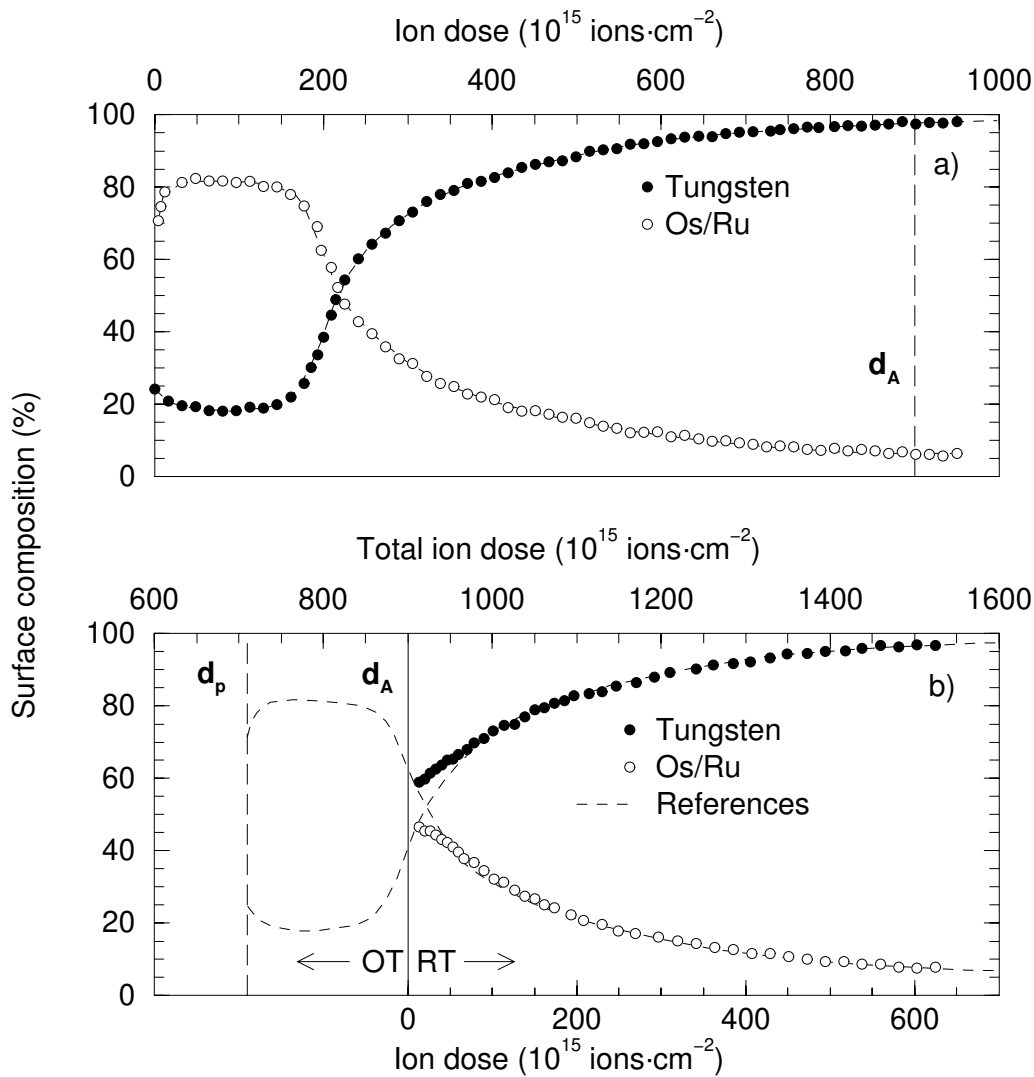


Figure 8.12. Depth profiles of the reference cathode (a) and cathode exposed to ion bombardment (b). Due to the ion bombardment the Os/Ru toplayer is removed, exposing the W matrix below. The ion dose applied during cathode operation is indicated by d_A . The shift required to fit the damage depth profiles by the reference profiles is indicated by d_p .

a flux of $F=3 \cdot 10^{12}$ ions·cm⁻²·s⁻¹. Both profiles show the surface composition versus the applied ion dose, where the composition is determined by the ion scattering analysis. It is evident from the reference depth profile in figure 8.12a that as the Os/Ru toplayer is removed, the underlying W matrix is exposed. The fixed ion dose applied in these experiments at a varying flux is indicated in figure 8.12a by the dashed vertical line at $d_A=900 \cdot 10^{15}$ ions·cm⁻². The initial increase in the Os/Ru composition at the start of the depth profiles in figures 8.12 is due to the removal of WO_x present on the substrate. The WO_x segregates to the surface during cathode operation and covers approximately 10-15% of the substrate, as is discussed elsewhere [40,41]. Figure 8.12b shows the depth profile of the damaged substrate, where the bottom axis of the figure shows the ion dose used for the depth profile of the remaining damaged substrate, while the top axis shows the total ion dose including the ion bombardment at operating temperature. The dashed curves represent the reference profiles from figure 8.12a,

shifted along the dose-axis to fit the damaged depth profile. The vertical dashed line indicates the required shift of $d_p=710\cdot 10^{15}$ ions \cdot cm $^{-2}$, which represents the ion dose that did not affect the substrate due to the protective function of the adlayer. In case of perfect protection, the substrate is unaffected by the ion bombardment during operation and the depth profile would equal the reference profile shifted over the applied dose ($d_p=d_A$). If no protection takes place, the remaining depth profile after the applied dose d_A would be equal to the profile to the right of the dashed line in figure 8.12a ($d_p=0$). The extent to which the substrate is protected from the ion bombardment can thus be derived from the shift d_p required to fit the reference profile to the damaged profile. Therefore we introduce the protection factor P as:

$$P = \frac{d_p}{d_A} \quad (8.7)$$

(Note that in previous ion bombardment studies [6,22] the term dynamic shielding factor is used. However, this might suggest that the substrate is shielded from the incident ions by the Ba-O complex, which is not the case.) The thus determined protection factor is shown versus the ion flux at which the dose d_A is applied in figure 8.13 (open circles). The coverage of the Ba-O complex during the ion bombardment at the corresponding ion flux is also shown (filled circles). In addition, the figure shows the protection efficiency ε_p of the remaining adlayer (dashed curve), which is derived by dividing the protection factor P by the remaining Ba-O coverage. It is observed that even for complete coverage the protection is not perfect since the substrate is damaged at a very low ion flux ($P\approx 0.8$). This imperfect protection at low ion dose

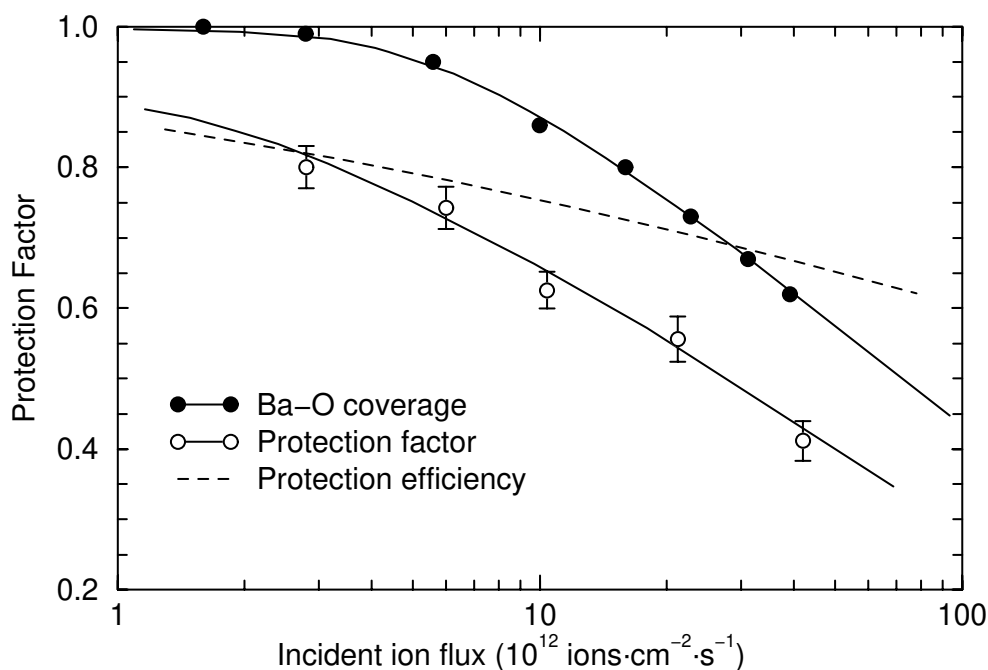


Figure 8.13. The protection factor (open circles) and protection efficiency (dashed curve) as a function of the ion flux, derived from the ion bombardment simulations (see text). The Ba-O coverages at the dynamic equilibrium are also shown for comparison (filled circles).

has previously been reported by Gärtner et al. in investigations of the influence of ion bombardment on the emission of Scandate cathodes with a Re/Sc₂O₃ coating [5]. The protection efficiency of the adlayer is smaller than unity because in a fraction of the collision-chains the outermost substrate atom is not able to transfer its energy to the Ba-O complex on top, and thus is sputtered from the surface [16,17]. Although the Ba/O ratio is equal to unity and every O is protected by a Ba atom, this is not the case for the substrate atoms. Even for complete coverage of the substrate by the Ba-O complex there is not a Ba-O complex on top of every substrate atom [20]. Therefore, the protective function of the remaining Ba-O is not perfect. Furthermore, the protection efficiency decreases with increasing ion flux because a large flux increases the surface roughness. For rough surfaces the sputter yield increases [42], and so does the probability to sputter second layer atoms. Consequently, the protection efficiency decreases with increasing ion flux.

In first order approximation the protection efficiency of the adlayer can be taken to be $\epsilon_p=0.7-0.8$. The protection factor of the adlayer is then proportional to the surface coverage according to $P=\epsilon_p \cdot \theta$. This implies that if one determines the surface coverage or electron emission during the ion bombardment, one can estimate the protection factor of the Ba-O layer for any given flux at any given temperature. This provides a fast method to estimate the protection during accelerated lifetime tests of dispenser cathodes, where the lifetime ion dose that the cathodes receive in cathode-ray tubes is given at a higher flux than in the actual tubes in order to have acceptable timeframes for the investigations. Due to the higher ion flux, the coverage and the resulting protection factor are smaller than is the case in the real tubes at lower flux. When investigating the influence of the ion bombardment on the cathode substrate, the difference in the protection factor must be corrected for. This correction can be performed if one knows the surface coverages (or electron emission) for the fluxes used in the tube and in the accelerated lifetime test: the protection factor scales with the surface coverage. Note that in the cathode-ray tubes the ion dose is not uniformly distributed across the surface, but is peaked in the centre of the cathode.

8.3.6 Ion bombardment in oxygen background

It has been shown that the surface coverage during ion bombardment is determined by the removal and resupply rate of O atoms. The limited rate of Ba resupply when it is governed by the O resupply, compared to the potential resupply rate of Ba when O is already present has been demonstrated in figure 8.6. The decrease in Ba-O coverage and damage to the substrate due to the ion bombardment can be diminished by increasing the O resupply rate. To substantiate this conclusion we performed an ion bombardment experiment in an O₂ background pressure in order to enhance the O resupply rate. Figure 8.14 shows the Ba coverage during ion bombardment in UHV (closed circles) and in an O₂ background (open circles) using a flux of $F=20 \cdot 10^{12}$ ions·cm⁻²·s⁻¹ at a cathode temperature of 920°C. The partial oxygen pressures were 1·10⁻¹² mbar and 5·10⁻⁹ mbar respectively. It is obvious that the ion bombardment in the O₂ background results in a smaller decrease in the Ba coverage. For the O₂ background the coverage is $n_{Ba}(O_2)=(68 \pm 3)$ % compared to $n_{Ba}(UHV)=(45 \pm 2)$ % in UHV. The solid curve for the UHV bombardment shows the coverage as a function of time, deduced by combining eqs. (8.1) and (8.4) with the above determined time constants for removal τ_{IB} and resupply $\tau_{res}(UHV)$. The solid curve for the bombardment in an O₂ background was deduced in a similar manner, but using the time constant for resupply $\tau_{res}(O_2)$ as a fitting parameter. (The solid curve for the O₂ background has been slightly shifted to the right for clarity.) The thus derived time constant for resupply in O₂ gives $\tau_{res}(UHV)/\tau_{res}(O_2)=2.6$.

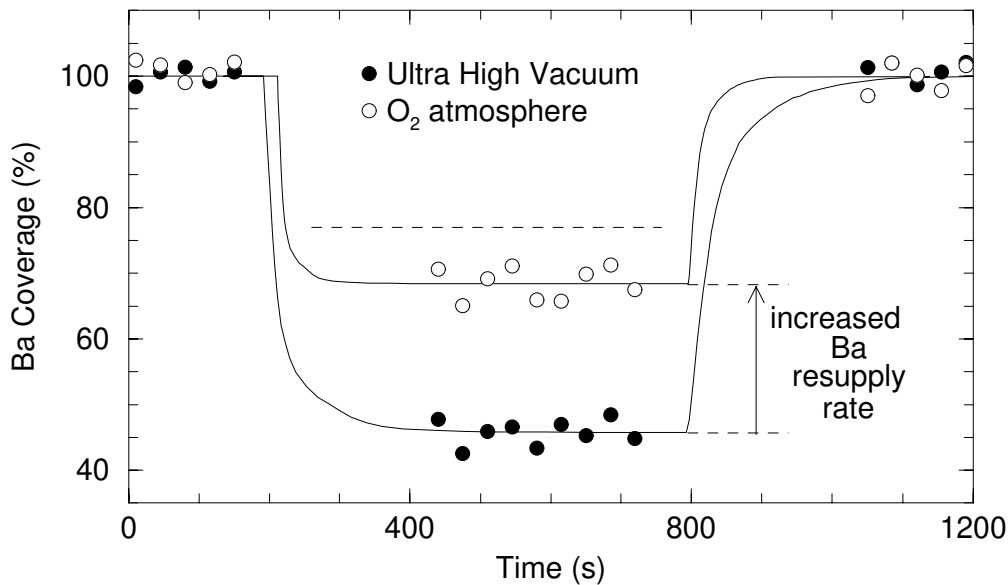


Figure 8.14. Ion bombardment in UHV (filled circles) and an O_2 background (open circles) using a flux of $F=2 \cdot 10^{13}$ ions \cdot cm $^{-2}$ \cdot s $^{-1}$ at a cathode temperature of 920°C. The partial oxygen pressures were $1 \cdot 10^{-12}$ mbar and $5 \cdot 10^{-9}$ mbar respectively. The solid curves represent the results of the derived model, and the dashed line represents the situation for an infinite fast O resupply.

We can estimate an upper limit of the improvement due to the increased O resupply from the results in figure 8.6, where it has been observed that the resupply of Ba on the oxidised substrate is enhanced by approximately a factor of 4 compared to the Ba resupply on the clean substrate. Therefore, for an infinitely fast O resupply, the time constant for resupply of the Ba-O complex is determined by the Ba resupply rate and can be decreased by a factor of 4 compared to O limited Ba-O resupply rate on a clean substrate ($\tau_{res} = \tau_{res}(UHV)/4$). In this case the Ba coverage in figure 8.14 would equal $n_{Ba}=77\%$ as indicated by the dashed line, which represents the maximum Ba coverage possible at this flux and temperature, and is limited by the Ba resupply rate. We can thus conclude that enhancement of the O resupply rate improves the performance of the cathode during ion bombardment. Moreover, the increased coverage diminishes the damage to the substrate and thus increases cathode lifetime. The protection factor P for the substrate increases by approximately the same fraction as the surface coverage is increased. An increase in cathode performance has also been observed by Gärtner et al. [43] during O_2 poisoning investigations. However we emphasise that above a certain O_2 pressure the poisoning by the excess O leads to a increase in the work function and a decreased electron emission.

8.4 Conclusions

In this paper we have studied and modelled the surface coverage and electron emission of dispenser cathodes during ion bombardment. All the results presented here clearly demonstrate for the first time the crucial role of O in the surface coverage of the dispenser cathodes. Many cathode studies reported in the literature have mainly focussed on the Ba coverage, and have underestimated the importance of O. However, Ba can only cover the

cathode substrate if it is bound to O present on the surface. During cathode operation, with or without ion bombardment, the Ba/O ratio equals unity. The surface coverage during the ion bombardment is thus determined by the O removal and resupply rates, as long as an ample supply of the Ba is available in the pores.

The Ba atoms in the outermost layer protect the O atoms situated below from the ion bombardment. In order to remove an O atom, collision-chains initiated by the incident ions must reach the surface at the same position twice within the time required to replace the Ba atom sputtered by the first collision-chain. The probability to remove the O atoms is thus determined by the ion flux, which determines the probability that a collision-chain reaches the surface twice at the same position, and the cathode temperature, which determines how fast the lost Ba is replaced.

Any O removed from the surface must be resupplied by diffusion from the pores. The O resupply is not in the form of BaO as has been suggested in many studies, but by individual O atoms. Although the surface diffusion of O itself is fast, the O resupply rate is limited by the formation of free O in the pores. The resistivity of the cathodes against ion bombardment is thus determined by the O resupply rate. Indeed, cathodes with a fine-grained matrix show improved ion bombardment resistivity due to smaller diffusion distances [44,45]. The decisive proof of the importance of the O resupply was given by performing an ion bombardment experiment in an O₂ background pressure. Due to the externally enhanced O resupply, the ion bombardment resistivity and the Ba-O coverage during the bombardment increased significantly.

The O resupply is not only important for maintenance of the Ba-O layer, it also indirectly influences the ion bombardment-induced damage to the cathode substrate. The Ba-O layer protects the substrate from the ion bombardment, where the protection factor is in a first order approximation proportional to the surface coverage during the ion bombardment. The protection of the substrate by the Ba-O layer is very important for coated cathodes, where damage to the substrate leads to unrecoverable emission degradation. The importance of ion bombardment resistivity is most evident for the scandate cathode which has a coating containing a Ba-Scandate complex. Although the scandate cathode has an enormous emission potential of up to 400 A·cm⁻², its breakthrough for application has not been possible so far due to its strong susceptibility to ion bombardment damage and emission degradation. The scandate cathode does not have a Sc resupply mechanism, so when the Ba-scandate complex is sputtered from the surface the emission enhancement by this complex is no longer present. Based on the evidence of O resupply presented here, a possible approach to increase the resistivity to ion bombardment is to increase the O resupply rate so the Ba-scandate complex is better protected from the ion bombardment. Hasker et al. have indicated that the Sc₂O₃ complex regulated the O concentration on the surface [46]. Definite conclusions about the role of the complex in the O resupply requires similar experiments as performed here for Os/Ru cathodes on scandate cathodes.

Acknowledgements

We would like to thank Georg Gärtner (Philips Forschungslaboratorien, Aachen) and Albert Manenschijn (Philips Display Components, Eindhoven) for all the support and the discussions. We also would like to thank Detlef Raasch (Philips Forschungslaboratorien, Aachen) for the assistance with the emission measurements during ion bombardment.

References

- 1 J.P. Blewett, J. Appl. Phys. 10 (1939) 668.
- 2 S. Yamamoto, J. Vac. Soc. Japan 40 (1997) 423.
- 3 R.E. Thomas, J.W. Gibson, G.A. Haas, R.H. Abrahams, IEEE Trans. Elec. Dev. 37 (1990) 850.
- 4 R. Cortenraad, A.W. Denier van der Gon, H.H. Brongersma, G. Gaertner, A. Manenschijn, to be published.
- 5 G. Gaertner, P. Geittner, H. Lydtin, A. Ritz, Appl. Surf. Sci. 111 (1997) 11.
- 6 G. Gaertner, P. Geittner, D. Raasch, A. Ritz, D.U. Wiechert, Appl. Surf. Sci. 146 (1999) 12.
- 7 H.H. Brongersma, P.M. Mul, Surf. Sci. 35 (1973) 393.
- 8 H.H. Brongersma, T.M. Buck, Nucl. Instr. and Meth. 149 (1978) 569.
- 9 H. Niehus H, W. Heiland, E. Taglauer, Surf. Sci. Rep. 17 (1993) 213.
- 10 J.W. Rabalais (Ed), "*Low Energy Ion-Surface interaction*", Wiley Series in Ion Chemistry and Physics, John Wiley & Sons, 1994.
- 11 R. Cortenraad, A.W. Denier van der Gon, H.H. Brongersma, Surf. Interface Anal. 29 (2000) 524.
- 12 J. Hasker, Appl. Surf. Sci. 16 (1983) 220
- 13 C.E. Maloney, C.S. Fang, Appl. Surf. Sci. 24 (1985) 407.
- 14 A.W. Denier van der Gon, M.F.F.K. Jongen, H.H. Brongersma, U. van Slooten, A. Manenschijn, Appl. Surf. Sci. 111 (1997) 64.
- 15 R. Cortenraad, A.W. Denier van der Gon, H.H. Brongersma, to be published.
- 16 R. Kelly, in "*Ion Bombardment Modification of Surfaces: Fundamentals and Applications*", eds. O. Auciello, R. Kelly, Elsevier, Amsterdam 1984.
- 17 R. Behrisch (ed.), "*Sputtering by Particle Bombardment I, II, III*", Springer Series Topics in Applied Physics, Vol. 47, 52, 64, Springer Verlag, Berlin 1981, 1983, 1991.
- 18 K. Wittmaack, Surf. Sci. 53 (1975) 626.
- 19 H. Oechsner, Z. Physik 261 (1973) 27.
- 20 D.A. Gorodetskii, Y.P. Melnik, Surf. Sci. 62 (1977) 647.
- 21 E. Koch, W. Huisl (eds), "*Gmelin Handbook of Inorganic and Organometallic Chemistry, Tungsten Supplement Volume A 6a*", Springer-Verlag, Berlin, 1991.
- 22 G. Gaertner, P. Geittner, D. Raasch, D.U. Wiechert, Appl. Surf. Sci. 146 (1999) 22.
- 23 R. Cortenraad, A.W. Denier van der Gon, H.H. Brongersma, G. Gaertner, A. Manenschijn, Appl. Surf. Sci. 146 (1999) 69.
- 24 D. Norman, R.A. Tuck, Phys. Rev. Lett. 58 (1987) 519.
- 25 A.G. Naumovets, Y.S. Vedula, Surf. Sci. Rep. 4 (1985) 365.
- 26 A. King, J. Vac. Sci. Technol. 17 (1980) 241.
- 27 D. Jones, D. McNeely, L.W. Swanson, Appl. Surf. Sci. 2 (1979) 232.
- 28 N.J.A. van Veen, Appl. Surf. Sci. 29 (1987) 113.
- 29 A.G. Naumovets, V.V. Poplavsky, Y.S. Vedula, Surf. Sci. 200 (1988) 321.
- 30 R.E. Thomas, Appl. Surf. Sci. 24 (1985) 538.
- 31 R. Forman, Appl. Surf. Sci. 2 (1979) 258.
- 32 R. Forman, Appl. Surf. Sci. 17 (1984) 429.
- 33 R. Forman, Appl. Surf. Sci. 29 (1987) 127.

- 34 K.I. Lakh, Z.V. Stasuk, *Sov. Phys. Tech. Phys.* 27 (1982) 848.
- 35 G.A. Haas, C.R.K. Marrian, A. Shih, *Appl. Surf. Sci.* 16 (1983) 125.
- 36 G.A. Haas, A. Shih, C.R.K. Marrian, *Appl. Surf. Sci.* 16 (1983) 139.
- 37 C.R.K. Marrian, A. Shih, G.A. Haas, *Appl. Surf. Sci.* 16 (1983) 1.
- 38 A. Manenschijn, P. v.d. Heide, S. Deckers, 1994 Tri-Service/NASA Cathode Workshop, Cleveland, Conference Record, 177.
- 39 G. Ehrlich, *CRC Crit. Rev. Solid State Mat. Sci.* 10 (1982) 391.
- 40 R. Cortenraad, S.N. Ermolov, A.W. Denier van der Gon, H.H. Brongersma, V.G. Glebovsky, to be published.
- 41 D.S. Chen, I. Lindau, M.H. Hecht, A.J. Viescas, *Appl. Surf. Sci.* 13 (1982) 321.
- 42 U. Littmark, W. Hofer, *J. Mater. Sci.* 13 (1978) 2577.
- 43 Private communications with G. Gärtner.
- 44 S. Kimura, T. Higuchi, Y. Ouchi, E. Uda, O. Nakamura, *Appl. Surf. Sci.* 111 (1997) 60.
- 45 T. Higuchi, O. Nakamura, S. Matsumoto, E. Uda, *Appl. Surf. Sci.* 146 (1999) 51.
- 46 J. Hasker, H.J.H. Stoffelen, *Appl. Surf. Sci.* 24 (1985) 330.

Summary

In this thesis a combination of low-energy ion scattering (LEIS) and Auger electron spectroscopy (AES) was used to study the surfaces of thermionic dispenser cathodes, which are used as electron sources in cathode-ray tubes. The objective of the surface analysis was to investigate the relation between the surface properties and the electron emission capabilities of various types of dispenser cathodes. Furthermore, the dynamic behaviour of the dispenser cathodes during bombardment by noble gas ions was studied, thereby simulating the bombardment by ionised residual gases occurring in real cathode-ray tubes.

To be able to perform the ion scattering analysis of the cathode surfaces with work functions of the order of 2 eV, a systematic investigation of the neutralisation mechanisms of noble gas ions at low-work function surfaces was carried out prior to the analysis of the cathodes. These investigations were required because reports about LEIS studies of low-work function surfaces are sporadic, and the influence of the work function on the neutralisation probability of noble gas ions at low work functions was not yet completely understood. Here, the neutralisation studies were performed using cathode model systems consisting of sub-monolayers of Ba adsorbed on W and Re single crystals. The crystals used as substrates for these model systems were especially prepared by the group of prof.dr. Vadim Glebovsky (Chernogolovka, Russia) using the electron-beam floating zone melting (EFBZM) technique, which resulted in crystals with a near-perfect crystallographic structure.

Using these cathode model systems, the neutralisation probabilities of noble gas ions during the interaction with the surface were determined over a work function range from 6 eV to just below 2 eV. It was found that at high work functions (above approximately 3 eV) the neutralisation probability of the noble gas ions is independent of the work function, but does depend on the ion-target combination. For noble gas ions scattered from alkali and earth-alkali atoms, like Ba, the collision-induced neutralisation mechanism is the dominant mechanism at high work functions. The results of the investigations also show that Auger neutralisation is much less dominant as is commonly assumed. At work functions below approximately 3 eV the noble gas ions are additionally neutralised by resonant electron transfer from the levels near the Fermi level of the metal substrate to the first excited level of the ions. This resonant mechanism is not available at high work functions because the first excited level is situated above the Fermi level at the distance where the neutralisation takes place. The neutralisation probability due to the resonant neutralisation is governed by the macroscopic work function and increases exponentially with decreasing work function.

In addition to the investigation of the neutralisation mechanisms, the consequences of the resonant neutralisation for the quantification of the composition of low-work function surfaces were discussed. The correction for the influence of the work function on the neutralisation probability was performed using the characteristic velocity method through investigating the dependence of the ion scattering signal on the energy of the ions. It was demonstrated that an additional correction is required for the influence of the ion velocity on the work function

threshold of the resonant neutralisation, since otherwise the surface density of the species under investigation is overestimated. The insights gained from the fundamental neutralisation studies are of relevance for all LEIS investigations of low-work function systems.

These newly gained neutralisation insights were applied for a quantitative comparison of the surface composition of various types of cathodes with different work functions. The composition of the Ba-O complex for top-layer cathodes with W, Re, Ir, and Os/Ru substrates was investigated, and it was for the first time established what the exact influence of the substrate material is on the work function of the cathodes during operation. The substrate material of course determines the work function of the clean non-covered surface and, most important, also determines the Ba-O coverage during cathode operation. The Ba-O coverage for the various cathodes depends on the bond between the O in the Ba-O complex and the substrate atoms. For a large coverage, and thus a low work function, a strong bond is required to overcome the electrostatic repulsion between the Ba-O dipoles. If only a weak bond exists, part of the Ba-O dipoles are desorbed due to this repulsion, resulting in a low coverage. The bond strength is determined by the orientation and the number of unoccupied d-orbitals of the substrate atoms and increases from the W, Re, Ir to the Os/Ru cathodes. Therefore, the coverage increases and the work function increases in that order of substrates. Thus far, it was commonly believed that the higher the work function of the non-covered substrate, the lower the work function of the cathodes during operation. However, here it has been shown that the bond between the O atoms in the Ba-O complex and the substrate atoms, is more important than the work function of the substrate. Despite the differences in absolute coverages among the cathodes, the Ba-O complex is similar on all cathodes. Because the Ba atoms can only reside on the cathode surface when bound to O atoms, the atomic Ba/O ratio is close to unity for all cathodes with the Ba atoms situated above the O atoms.

During operation of the dispenser cathodes a dynamic equilibrium exists between the processes that remove the Ba-O complex, i.e. thermal desorption and ion bombardment, and the resupply process of the Ba and O atoms from the pores of the matrix. The influence of the ion bombardment on the surface composition and the electron emission at the dynamic equilibrium was investigated. It was shown that the ion bombardment removes the Ba and O atoms in a step-by-step manner, first the outermost Ba atoms and subsequently the underlying O atoms, if the Ba has not yet been resupplied. Furthermore, we have shown that in the resupply process the Ba and O atoms arrive at the surface as individual atoms, and not in the form of BaO as is often suggested. The Ba resupply is approximately 4 times faster than the O resupply, but the residence time of the Ba atoms on the clean substrate is too short to result in a large enough diffusion length to cover the surface. However, when the Ba atoms are bound to O atoms, the residence time is sufficient to result in complete coverage. The resupply of the Ba-O complex is thus limited by the slow O resupply from the pores. The activation energy for the O resupply is determined by the production of free O in the pores, and is not limited by the O diffusion rate. Using the insight from these investigations a model was derived that describes the surface coverage and electron emission during the ion bombardment, and includes the influence of the cathode temperature and the incident ion flux.

In conclusion, these studies have revealed new insights into the operating mechanism of thermionic dispenser cathodes. From the surface analysis, the difference in electron emission capabilities of various dispenser cathodes could be explained. Furthermore, an accurate model for the description of the dynamic behaviour of the cathode during ion bombardment was derived. To a large extent these new insights are related to a better understanding of the role of oxygen in the operation of the cathodes.

Samenvatting

In dit proefschrift staat beschreven hoe een combinatie van lage-energie ionen verstrooiing (LEIS) en Auger elektronen spectroscopie is toegepast om het oppervlak te onderzoeken van thermische dispenser kathodes, zoals die worden gebruikt in beeldbuizen. Het doel van dit onderzoek was om het verband tussen de eigenschappen van het oppervlakte van de kathodes en de elektronen emissie te analyseren. Daarnaast is er onderzoek verricht naar het dynamisch gedrag van de kathodes tijdens edelgas ionen bombardement, zoals dat gebeurt in beeldbuizen.

Om het oppervlak van de kathodes te kunnen onderzoeken met behulp van LEIS is er eerst onderzoek verricht naar de neutralisatiemechanismen van edelgas ionen aan oppervlakken met een lage uittreearbeid. Dit onderzoek was vereist omdat LEIS studies van oppervlakken met een lage uittreearbeid zeldzaam zijn, en omdat de neutralisatiemechanismen van edel gas ionen bij lage uittreearbeid nog niet helemaal begrepen werden. In dit werk zijn deze neutralisatiemechanismen onderzocht met behulp modelsystemen bestaande uit Ba atomen geadsorbeerd op W en Re éénkristallen. Deze kristallen zijn gegroeid in de groep van prof.dr. Vadim Glebovsky (Chernogolovka, Rusland) met behulp van de electron-beam floating zone melting (EBFZM) techniek.

Met behulp van deze modelsystemen is de neutralisatiewaarschijnlijkheid van de edel gas ionen onderzocht over een uittreearbeidbereik van 6 eV tot 2 eV. Er is aangetoond dat voor een uittreearbeid groter dan ongeveer 3 eV de neutralisatiewaarschijnlijkheid onafhankelijk is van de uittreearbeid, maar sterk afhangt van het type ion en het oppervlakte atoom. Voor alkali and aard-alkali atomen is de neutralisatie tijdens de botsing tussen het ion en het oppervlakte atoom het dominante mechanisme bij hoge uittreearbeid. In dit mechanisme vindt de neutralisatie van het ion plaats door een resonante ladingsoverdracht van de valentieband van het substraat naar het grondniveau van het ion. De resultaten van dit onderzoek laten ook zien dat het Auger neutralisatiemechanisme veel minder belangrijk is dan tot nu toe werd aangenomen.

Voor een uittreearbeid lager dan ongeveer 3 eV kunnen de edelgas ionen geneutraliseerd worden door een resonante ladingsoverdracht naar het eerste aangeslagen niveau van het ion. Dit mechanisme is niet beschikbaar voor een hoge uittreearbeid omdat dan het eerste aangeslagen niveau boven het Fermi niveau ligt als het ion zich op korte afstand van het oppervlak bevindt. Het resonante mechanisme kan worden beschreven met behulp van de resonante ladingsoverdracht theorie, waaruit volgt dat de neutralisatiewaarschijnlijkheid bepaald wordt door de macroscopische uittreearbeid en exponentieel toeneemt met afnemende uittreearbeid.

Naast het onderzoek van de neutralisatiemechanismen, is ook de invloed van de resonante neutralisatie op een kwantitatieve analyse van de samenstelling van oppervlakken met een lage uittreearbeid onderzocht. De correctie voor de invloed van de uittreearbeid op de neutralisatiewaarschijnlijkheid is uitgevoerd met de zogenaamde karakteristieke snelheid methode, waarin de neutralisatiewaarschijnlijkheid bepaald wordt uit de afhankelijkheid

van het LEIS signaal van de kinetische energie van de ionen. Behalve de correctie voor de invloed van de uittreearbeid, is er ook nog een correctie nodig voor de snelheid van het ion. Indien deze extra correctie niet wordt toegepast zal dit leiden tot een overschatting van de oppervlaktedichtheid. De inzichten die zijn verkregen uit dit onderzoek zijn van belang voor alle LEIS studies aan oppervlakken met een lage uittreearbeid.

De inzichten verkregen uit het neutralisatie onderzoek zijn toegepast voor de kwantitatieve analyse van de oppervlaktesamenstelling van verschillende type kathodes met verschillende uittreearbeid. De samenstelling van het Ba-O complex is onderzocht voor kathodes met een W, Re, Ir en Os/Ru substraat. Er is aangetoond wat de precieze invloed is van het substraat materiaal op de uittreearbeid van de kathodes. De keuze van het substraat materiaal bepaalt de uittreearbeid van het onbedekte substraat, maar veel belangrijker, bepaalt de Ba-O bedekking van de kathode. Deze bedekking wordt namelijk bepaald door de binding van het O atoom in het Ba-O complex met de substraat atomen. Voor een hoge Ba-O bedekking, en dus een lage uittreearbeid, is een sterke band vereist om de elektrostatische repulsie tussen de Ba-O dipolen te overwinnen. Als de band zwak is, zal deze repulsie leiden tot desorptie van een deel van het Ba-O complex en een lage uittreearbeid tot gevolg hebben. De sterkte van de band tussen de O atomen en de substraat atomen wordt bepaald door de oriëntatie en het aantal d-orbitals van de substraat atomen. Deze sterkte neemt toe van de W, Re, Ir naar de Os/Ru kathodes, en dus resulteert in een toename van de Ba-O bedekking en een afname van de uittreearbeid in die volgorde. Ondanks het verschil in absolute bedekking tussen de verschillende kathodes, zijn de eigenschappen van het Ba-O complex vergelijkbaar op alle kathodes. Omdat de Ba atomen alleen aanwezig kunnen zijn op het oppervlak als ze gebonden zijn aan O atomen is de Ba/O verhouding ongeveer 1, met de Ba atomen direct boven de O atomen gepositioneerd.

Tijdens het gebruik van de kathodes in beeldbuizen is er een dynamische evenwicht tussen processen die het Ba-O complex verwijderen (thermische desorptie en ionen bombardement) en processen die voor de aanlevering van Ba and O atomen zorgen. De invloed van het ionen bombardement op de samenstelling van het oppervlak en op de elektronen emissie is onderzocht. Door het ionen bombardement wordt het Ba-O complex stap-voor-stap verwijderd; eerst het buitenste Ba atoom, en dan het onderliggende O atoom. De aanlevering van het Ba-O complex vindt plaats door individuele aanlevering van Ba en O atomen. De snelheid waarmee de Ba atomen aangeleverd worden is ongeveer 4 keer zo hoog als de snelheid waarmee de O atomen worden aangeleverd. Echter, de Ba atomen kunnen alleen het oppervlak bedekken als ze gebonden zijn aan O atomen. Daarom wordt de aanlevering van het Ba-O complex bepaald door de langzamere aanlevering van de O atomen. De activeringsenergie van de O aanlevering wordt bepaald door het vrijmaken van de O atomen uit het impregnaat in de poriën van de kathode, en niet door de O diffusie over het oppervlak. Met behulp van de inzichten uit het onderzoek van de verwijderings- en aanleverings- processen van het Ba-O complex is er een model ontwikkeld dat de bedekking en emissie van de kathodes tijdens het ionen bombardement beschrijft.

Samenvattend, uit dit onderzoek zijn vele nieuwe inzichten in het functioneren van thermische dispenser kathodes naar voren gekomen. Door de oppervlakte analyse van verschillende kathodes is er meer begrip van de invloed van het type kathode substraat. Daarnaast, is er ook een nauwkeurig model ontwikkeld dat het invloed van het ionen bombardement in beeldbuizen beschrijft. Voor een groot deel zijn de nieuwe inzichten te wijten aan een beter begrip van de rol die de O atomen spelen.

Publications

Chapter 2

Influence of Analyser Transmission and Detection Efficiency on the Energy Dependence of Low-Energy Ion Scattering Signals

R. Cortenraad, A.W. Denier van der Gon, H.H. Brongersma.
Surf. Interface Anal. 29 (2000) 524.

Chapter 3

Growth, Characterisation, and Surface Cleaning Procedures of High-Purity W Single Crystals

R. Cortenraad, S.N. Ermolov, V.N. Semenov, A.W. Denier van der Gon, V.G. Glebovsky, S.I. Bozhko, H.H. Brongersma.

Accepted for publication in J. Crystal Growth.

Electron-Beam Growing and Purification of W Crystals

R. Cortenraad, S.N. Ermolov, V.N. Semenov, A.W. Denier van der Gon, V.G. Glebovsky, S.I. Bozhko, E.D. Stinov, H.H. Brongersma.

Accepted for publication in Vacuum.

Study of High-Purity W Single Crystals by LEIS, AES, LEED, and X-ray Diffraction

R. Cortenraad, S.N. Ermolov, A.W. Denier van der Gon, V.N. Semenov, H.H. Brongersma, V.G. Glebovsky, S.I. Bozhko.

Izvestiya Akademii Nauk, Fizicheskaya Seria 64 N4 (2000) 691. (in Russian)

Chapter 4

Crystal-Face Dependence of Low-Energy Ion Scattering Signals

R. Cortenraad, S.N. Ermolov, B. Moest, A.W. Denier van der Gon, V.G. Glebovsky, H.H. Brongersma.

Accepted for publication in Nucl. Instr. and Meth. B.

Chapter 5

Work Function Dependent Neutralisation of Low-Energy Noble Gas Ions

R. Cortenraad, A.W. Denier van der Gon, H.H. Brongersma, S.N. Ermolov, V.G. Glebovsky.
Submitted for publication (Phys. Rev. B).

Chapter 6

On the Quantification of the Surface Composition of Low-Work Function Surfaces using Low-Energy Ion Scattering

R. Cortenraad, A.W. Denier van der Gon, H.H. Brongersma, S.N. Ermolov, V.G. Glebovsky.
Submitted for publication. (Surf. Interface Anal.)

Chapter 7

Quantitative LEIS Analysis of Thermionic Dispenser Cathodes

R. Cortenraad, A.W. Denier van der Gon, H.H. Brongersma, G. Gärtner, A. Manenschijn.
Appl. Surf. Sci. 146 (1999) 69.

Study of Low-Work Function Thermionic Cathodes by Low-Energy Ion Scattering

R. Cortenraad, A.W. Denier van der Gon, H.H. Brongersma, G. Gärtner, A. Manenschijn,
S.N. Ermolov, V.N. Semenov, V.G. Glebovsky, S.I. Bozhko.
Izvestiya Akademii Nauk, Fizicheskaya Seria 64 N4 (2000) 658. (in Russian)

Surface Analysis of Thermionic Dispenser Cathodes

R. Cortenraad, A.W. Denier van der Gon, H.H. Brongersma, G. Gärtner, A. Manenschijn.
Submitted for publication. (Appl. Surf. Sci.)

Chapter 8

Dynamic Behaviour of Thermionic Dispenser Cathodes under Ion Bombardment

R. Cortenraad, A.W. Denier van der Gon, H.H. Brongersma, G. Gärtner, D. Raasch,
A. Manenschijn.
Submitted for publication. (J. Appl. Phys)

Other publications

A Round Robin Experiment of Elemental Sensitivity Factors in Low-Energy Ion Scattering

H.H. Brongersma, M. Carrere, R. Cortenraad, A.W. Denier van der Gon, et al.
Nucl. Instr. and Meth. B, 142 (1998) 377.

In-Situ Analysis by Low-Energy Ion Scattering

A.W. Denier van der Gon, R. Cortenraad, W.P.A. Jansen, M.A. Reijme, H.H. Brongersma.
Nucl. Instr. and Meth. B, 161-163 (2000) 56.

Tungsten Oxide Segregation in Rhenium Films on Tungsten Substrates

R. Cortenraad, S.N. Ermolov, A.W. Denier van der Gon, V.G. Glebovsky, H.H. Brongersma.
In preparation.

Dankwoord

Op deze plaats wil ik graag iedereen bedanken die op de één of andere manier heeft bijgedragen aan het tot stand komen van dit proefschrift.

Allereerst wil ik mijn copromotor Arnoud Denier van der Gon bedanken voor de directe begeleiding en de vele discussies die we de afgelopen jaren gevoerd hebben. Ook mijn promotor Hidde Brongersma wil ik bedanken voor de vrijheid die hij me heeft gegeven voor het uitvoeren van dit promotie onderzoek. Behalve de wetenschappelijke begeleiding op de TUE wil ik ook graag Georg Gärtner en Albert Manenschijn bedanken voor hun uitstekende steun vanuit Philips. De interesse die zij toonden in alle aspecten van dit onderzoek deden mij bijzonder deugd. Naast de wetenschappelijke begeleiding was dit proefschrift natuurlijk nooit tot stand gekomen zonder de technische ondersteuning van Gerard Wijers, Rein Rumphorst, Wijnand Dijkstra en Erwin Timmerman. Als er aan de vacuüm opstelling gesleuteld moest worden stond Gerard altijd voor me klaar, de bako in de ene hand en de waterpomptang in de andere. Iemand die ook altijd klaar stond was Rein; hij was altijd de eerste ter plekke als er leedvermaak was. Behalve de directe ondersteuning in de groep zijn er ook vele technici van de CTD die hun steentje hebben bijgedragen: Jos de Laat, Piet van den Hoogen, Theo Maas, Erwin Dekkers, en Peer Brinkgreve. Voorts wil ik ook de afstudeerders Paul Schenkel en Toussaint Janken bedanken voor hun bijdrage aan dit proefschrift. I am also very grateful to my friends from the Russian connection, Vadim Glebovsky and Sergey Ermolov, for all the support they have given in the past years.

Het plezier waarmee ik dit promotieonderzoek heb verricht is natuurlijk ook voor een groot deel te danken aan de sfeer binnen de groep Fysica van Oppervlakken en Grenslagen (FOG). Met name mijn collega-promovendi en post-docs Leon en Ronald van den Oetelaar, Will Ceelen, Camiel Rouweler, Barry Moest, Mireille Reijme, Marco de Ridder, Marc Ponjée, Wim Jansen, Frank Janssen, George Tanasa (alias Georg Constanza), Juan Amir, Jean-Michel Wulveryck, Gunther Andersson en Coralie Gallis wil ik bedanken voor hun bijdrage aan deze sfeer. Daarnaast droegen natuurlijk ook de overige vaste medewerkers Kees Flipse en Rob van Welzenis, en de Calipso-crew Jos Maas, Minna Viitanen en Arie Knoester bij aan de sfeer in de groep. Rob de Kluijver (alias Bor) wil ik ook bedanken voor zijn, zelden onopgemerkte, aanwezigheid.

Tenslotte maak ik van deze gelegenheid maar meteen gebruik om sommige personen, die ik niet met naam zal noemen, mijn excuses aan te bieden voor de vlees- en schaafwonden, de gebroken brillen, en de blauwen plekken ten gevolge van de door mij georganiseerde fietstripjes in binnen- en buitenland.

Curriculum Vitae

René Cortenraad werd op 4 juli 1972 geboren in Maastricht. Na het behalen van het atheneum diploma aan het Jeanne d'Arc college te Maastricht, startte hij in september 1990 met de studie Technische Natuurkunde aan de Technische Universiteit Eindhoven (TUE). Zijn afstudeeronderzoek werd verricht op de Radiologie afdeling van het Academisch Ziekenhuis Maastricht, waar hij onderzocht welke factoren van belang zijn bij het bepalen van de stroomsnelheden van het bloed met behulp van Magnetic Resonance Imaging (MRI). In december 1995 behaalde hij zijn ingenieursdiploma. Aansluitend begon hij als assistent in opleiding met zijn promotieonderzoek in de groep Fysica van Oppervlakken en Grenslagen (FOG) van prof.dr. H.H. Brongersma aan de TUE. In een samenwerkingsproject met Philips heeft hij onderzoek verricht aan de buitenste atoomlaag van kathodes die gebruikt worden als elektronenbron in beeldbuizen. De resultaten van dit onderzoek staan beschreven in dit proefschrift.

